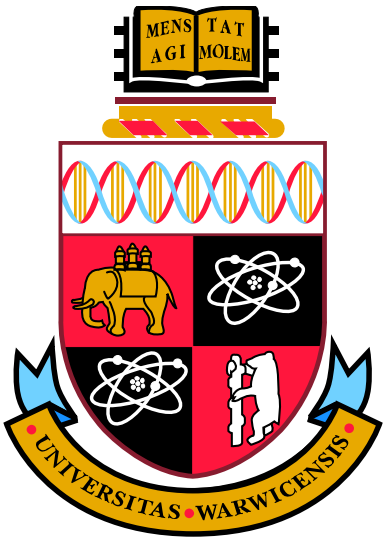

Optical and Magnetic Resonance Studies of Point Defects in CVD Diamond

by

Ulrika Francine Stephanie D'Haenens-Johansson

Thesis

Submitted to the University of Warwick

for the degree of

Doctor of Philosophy

Department of Physics

April 2011

THE UNIVERSITY OF WARWICK

Contents

List of Tables

List of Figures

Acknowledgments

I would first like to thank Dr. Mark Newton for his excellent supervision, patience and humorous teaching methods during the course of my PhD. You struck the perfect balance between seriousness and light-heartedness. I am indebted to Prof. Malcolm Cooper and Prof. Robin Ball for providing great laboratory facilities.

I am thankful to the extended Warwick Diamond Group members: Dr. Chris Welbourn, Prof. Michael Baker and Dr. Jim Butler, for thought provoking discussions. I would also like to thank others who have helped further my understanding of diamond physics: Dr. Philip Martineau, Dr. Riz Khan, Dr. Daniel Twitchen, Dr. Jon Goss, Prof. Junichi Isoya and Prof. Gordon Davies. I must also thank Mr. DuPriest and Mr. Boardman for their inspiring teaching.

I would like to thank both the Diamond Trading Company (DTC) and the EPSRC for financial support. Element Six, Ltd. and DTC are thanked for kindly providing exciting diamond samples to study. Additionally, Chris Kelly and Laura Hutton are thanked for their help with sample preparation.

I am extremely grateful for having been a part of "Team Diamond." I have been very lucky to work (and play!) with such a fantastic team: Stephanie (for all our conference adventures), Andy ("Aaaaaandy...?"), bouncy Brad, mysterious Bianca, Ben (the best editor *ever*), Robin, Solveig and Chris H.

Thank you to all my other friends: Lieke, Lisa, Ruth and Lindsay for our legendary cooking nights. James, Jon and Tom, who have been with me through the undergraduate years and the "thesis experience." Jen, for our wonderful friendship and sneaky shopping trips. My Swedish friends Aiysha and Khadijah for always being there for me. The Circle, in particular Charlotte, Fiorella, and Giorgio – you are the ultimate cross-Atlantic cheerleaders!

Finally, I would like to thank my family for their love and support, and for their perseverance in trying to understand the unfamiliar field that I study. Also, I must acknowledge that my mother once helped me conduct an experiment by systematically pressing a button on a spectrometer – thank you! I dedicate this thesis to my parents; I hope that I have made you proud.

Declaration and published work

I declare that the work presented in this thesis is my own except where stated otherwise, and was carried out entirely at the University of Warwick, during the period of July 2007 to April 2011, under the supervision of Dr. M. E. Newton. The research reported here has not been submitted, either wholly or in part, in this or any other academic institution for admission to a higher degree.

Some parts of the work reported and other work not reported in this thesis have been published or have been submitted for publication, as listed below:

Published papers

1. B. Naydenov, F. Reinhard, A. Lämmle, V. Richter, R. Kalish, U. F. S. D'Haenens-Johansson, M. E. Newton, F. Jelezko, and J. Wrachtrup, *Increasing the coherence time of single electron spins in diamond by high temperature annealing*, Appl. Phys. Lett. **97**, 242511 (2010).

2. U. F. S. D'Haenens-Johansson, A. M. Edmonds, M. E. Newton, J. P. Goss, P. R. Briddon, J. M. Baker, P. M. Martineau, R. U. A. Khan, D. J. Twitchen, and S. D. Williams, *EPR of a defect in CVD diamond involving both silicon and hydrogen that shows preferential alignment*, Phys. Rev. B **82**, 155205 (2010).

Papers submitted for publication

1. A. M. Edmonds, U. F. S. D'Haenens-Johansson, R. J. Cruddace, M. E. Newton, K.- M. C. Fu, C. Santori, R. U. A. Khan, P. M. Martineau, D. J. Twitchen, and M. Markham, *How is a nitrogen-vacancy color center produced in as-grown CVD synthetic diamond?* Nature Materials (to be submitted, April 2011).

2. U. F. S. D'Haenens-Johansson, A. M. Edmonds, B. L. Green, M. E. Newton, G. Davies, P. M. Martineau, R. U. A. Khan, and D. J. Twitchen, *Optical*

properties of the neutral silicon split-vacancy center in diamond, Phys. Rev. B (submitted, February 2011).

Conference presentations and seminar

1. U. F. S. D'Haenens-Johansson, A. M. Edmonds, M. E. Newton, G. Davies, P. M. Martineau, R. U. A. Khan, and D. J. Twitchen, *Optical properties of silicon-related defects in diamond*, Condensed Matter and Materials Physics CMMP10, University of Warwick, Coventry, United Kingdom, oral presentation (2010).

2. U. F. S. D'Haenens-Johansson, *EPR of silicon-related defects in CVD diamond*, Gordon Research Conference: Defects in Semiconductors, Colby-Sawyer College, New Hampshire, United States of America, oral presentation (2010).

3. U. F. S. D'Haenens-Johansson, S. Liggins, A. M. Edmonds, M. E. Newton, J. Isoya, P. M. Martineau, and D. J. Twitchen, *Spin-lattice relaxation times for (Si-V)^0 and (Si-V)$^-$ during optical excitation*, The 61st De Beers Diamond Conference, P10, University of Warwick, Coventry, United Kingdom, poster presentation (2010).

4. U. F. S. D'Haenens-Johansson, M. E. Newton, P. M. Martineau, R. U. A. Khan, D. J. Twitchen, and S. D. Williams, *Investigation of the charge states of the silicon split-vacancy centre in CVD diamond*, The 61st De Beers Diamond Conference, P9, University of Warwick, Coventry, United Kingdom, poster presentation (2010).

5. U. F. S. D'Haenens-Johansson, A. M. Edmonds, M. E. Newton, P. M. Martineau, R. U. A. Khan, and D. J. Twitchen, *Spin polarisation of the silicon-vacancy defect in CVD diamond*, Rank Prize Funds Symposium on Diamond Photonics, Storrs Hall, Windermere, United Kingdom, oral presentation (2010).

6. U. F. S. D'Haenens-Johansson, A. M. Edmonds, M. E. Newton, J. P. Goss, P. R. Briddon, J. M. Baker, P. M. Martineau, R. U. A. Khan, D. J. Twitchen,

and S. D. Williams, *EPR studies of a new defect in CVD diamond involving both silicon and hydrogen which shows preferential alignment*, Hasselt Diamond Workshop 2010 - SBDD XV, 10.3, Cultuurcentrum Hasselt, Hasselt, Belgium, oral presentation (2010).

7. U. F. S. D'Haenens-Johansson, M. E. Newton, A. M. Edmonds, J. P. Goss, J. M. Baker, P. M. Martineau, R. U. A. Khan, and D. J. Twitchen, *Silicon in diamond: the silicon divacancy complex*, Oxford CAESR Symposium, Talk 8, University of Oxford, Oxford, United Kingdom, oral presentation (2010).

8. U. F. S. D'Haenens-Johansson, A. M. Edmonds, S. Liggins, M. E. Newton, P. M. Martineau, R. U. A. Khan, and D. J. Twitchen, *EPR of silicon related defects in CVD diamond*, United States Naval Research Laboratory, Washington D.C., United States of America, seminar (2009).

9. U. F. S. D'Haenens-Johansson, A. M. Edmonds, M. E. Newton, P. M. Martineau, D. J. Twitchen, and S. D. Williams, *Spin polarisation of the neutral silicon split-vacancy defect in diamond*, The 60$^{\text{th}}$ De Beers Diamond Conference, O26, University of Warwick, Coventry, United Kingdom, oral presentation (2009).

10. U. F. S. D'Haenens-Johansson, A. M. Edmonds, B. L. Cann, and M. E. Newton, *Preferentially oriented defects in CVD diamond*, The 60$^{\text{th}}$ De Beers Diamond Conference, P22, University of Warwick, Coventry, United Kingdom, poster presentation (2009).

11. B. L. Cann, U. F. S. D'Haenens-Johansson, S. Felton, A. M. Edmonds, R. J. Cruddace, M. E. Newton, H. Murphy, J. Dodson and D. J. Twitchen, *A reliable method for the detection of* < 1 *ppb single substitutional nitrogen in single crystal CVD diamond*, The 60$^{\text{th}}$ De Beers Diamond Conference, P27, University of Warwick, Coventry, United Kingdom, poster presentation by B. L. Cann (2009).

12. U. F. S. D'Haenens-Johansson, A. M. Edmonds, S. Felton, M. E. Newton, P. M. Martineau, R. U. A. Khan, D. J. Twitchen, and S. D. Williams, *A new*

EPR active silicon- and hydrogen-related defect, BRSG: Frontiers of Magnetic Resonance, P13, University of Warwick, Coventry, United Kingdom, poster presentation (2008).

13. U. F. S. D'Haenens-Johansson, A. M. Edmonds, S. Felton, M. E. Newton, P. M. Martineau, R. U. A. Khan, D.J. Twitchen, and S. D. Williams, *A new EPR active silicon- and hydrogen-related defect*, SUSSP-64 and COST P15 Training School and 4th European EPR Federation Summer School in Advanced Techniques in EPR, 33, University of St. Andrews, St. Andrews, United Kingdom, poster presentation (2008).

14. U. F. S. D'Haenens-Johansson, A. M. Edmonds, S. Felton, M. E. Newton, P. M. Martineau, R. U. A. Khan, D. J. Twitchen, and S. D. Williams, *A new EPR active silicon- and hydrogen-related defect*, Gordon Research Conference: Defects in Semiconductors, 33, Colby-Sawyer College, New Hampshire, United States of America, poster presentation (2008).

15. U. F. S. D'Haenens-Johansson, *Investigating defects in diamond using EPR*, DRIVE Diamond Polishing Workshop, University of Warwick, Coventry, United Kingdom, oral presentation (2008).

16. U. F. S. D'Haenens-Johansson, A. M. Edmonds, S. Felton, M. E. Newton, P. M. Martineau, R. U. A. Khan, D. J. Twitchen, and S. D. Williams, *A new EPR active silicon- and hydrogen-related defect*, The 59$^{\text{th}}$ De Beers Diamond Conference, P24, University of Oxford, Oxford, United Kingdom, poster presentation (2008).

U. F. S. D'Haenens-Johansson

April 2011

Abstract

This thesis reports research conducted on point defects in single crystal diamond utilising the complementary techniques of electron paramagnetic resonance (EPR), optical absorption and photoluminescence (PL) spectroscopy. Intentional silicon-doping of chemical vapour deposition (CVD) diamond allowed the production of samples grown on differently oriented substrates and containing distinct silicon isotopic abundances.

The EPR spectrum of the neutral charge state of the silicon split-vacancy centre in diamond, (Si-V)^0, has been characterised in the literature. Evidence for the assignment of the 1.31 eV zero phonon line (ZPL) seen in absorption and PL to the $^3A_{2g} \rightarrow {}^3A_{1u}$ transition arising at (Si-V)^0 is presented. Reversible charge transfer between the negatively charged centre, (Si-V)$^-$ (ZPL at 1.68 eV), and (Si-V)^0 enabled the determination of calibration factors relating defect concentrations to their respective ZPL intensities. Preferential alignment of trigonal centres, such as (Si-V), in CVD material grown on {110}-substrates has been observed. The formation of (Si-V) centres during CVD synthesis and via irradiation and annealing of silicon-doped diamond was studied.

Variable temperature EPR spectroscopy under illumination was used to investigate the optical spin polarisation (SP) of the (Si-V)^0 $^3A_{2g}$ ground state. Two different mechanisms for the SP are considered; selective intersystem crossing of (Si-V)^0, and photoionisation of (Si-V)$^-$. The properties of (Si-V)^0 are compared to those of the extensively studied negatively charged nitrogen vacancy centre, (N-V)$^-$. The effective spin-lattice relaxation and spin polarisation rates for both centres during continuous illumination are explored using pulsed EPR methods.

A new defect, labelled WAR3, with spin $S = \frac{1}{2}$ was observed in silicon-doped diamond and characterised using multifrequency EPR. Analysis of the data revealed that WAR3 is the neutral charge state of a silicon divacancy complex decorated by a hydrogen atom, (Si-V$_2$:H)^0. The experimentally derived ^{29}Si and ^{1}H hyperfine parameters are in good agreement with the values calculated using the spin-density-functional technique, confirming this model and ruling out a non-planar structure.

Glossary and abbreviations

A	Hyperfine interaction term
A_s	Isotropic component of the hyperfine interaction
A_p	Anisotropic component of the hyperfine interaction
AFC	Automatic frequency control
B	Applied magnetic field
B_m	Magnetic field modulation amplitude
B_r	Position (in magnetic field) of a resonance line
B_1	Magnetic field component of microwave radiation
CVD	Chemical vapour deposition
D	Zero-field interaction term
E	Energy
EM	Electro-magnetic
EPR	Electron paramagnetic resonance
FTIR	Fourier transform infra-red spectroscopy
g_e	g value for the free-electron
g_n	Nuclear g value
$\mathscr{H}$	Spin Hamiltonian term(s)
HPHT	High-pressure high-temperature
I	Nuclear spin
IR	Infra-red
k_B	Boltzmann constant
L	Orbital angular momentum
M	Magnetisation
M_S	Projection of electron spin (S) on z-axis
m_I	Projection of nuclear spin (I) on z-axis
m_e	Mass of electron
MP-CVD	Microwave-plasma chemical vapour deposition

N_s	Single substitutional nitrogen defect
NIR	Near infra-red
NMR	Nuclear magnetic resonance
(N-V)	Nitrogen-vacancy defect
(N-V-H)	Nitrogen-vacancy-hydrogen defect
p	Probability of energy level occupation
P	Quadrupole interaction term
$P_{\mu w}$	Microwave power
PL	Photoluminescence
ppm	Parts per million carbon atoms
ppb	Parts per billion carbon atoms
Q	Quality factor
S	Electronic spin
SHQ	Super high Q
SIMS	Secondary ion mass spectroscopy
Si_s	Single substitutional silicon
(Si-V)	Silicon split-vacancy defect
(Si-V:H)	Silicon split-vacancy defect decorated with hydrogen
(Si-V_2)	Silicon divacancy defect
(Si-V_2:H)	Silicon divacancy defect decorated with hydrogen
T	Temperature
τ_1	Spin-lattice relaxation time
τ_2	Spin-spin relaxation time
UV	Ultra-violet
(V-H)	Vacancy-hydrogen defect
ZPL	Zero phonon line

Γ	Half-width at half-maximum linewidth
γ_e	Gyromagnetic ratio
θ/ϕ	Angle
λ_h	Hybridisation ratio

λ_{SO}	Russel-Saunders spin-orbit coupling term
μ	Magnetic dipole
μ_B	Bohr magneton
μ_n	Nuclear magneton
μ_s	Absorption coefficient
ν	Microwave frequency
ν_m	Magnetic field modulation frequency
τ	Lifetime
ω_0	Larmor frequency

$\langle hkl \rangle$	A general hkl direction
$[hkl]$	A specific hkl direction
$\{hkl\}$	A general hkl plane
(hkl)	A specific hkl plane

"*Diamonds are a girl's best friend.*"

- Marilyn Monroe

Chapter 1

Introduction

> "Diamond has aroused intense interest in the historian and the folklorist, the industrialist and the man of wealth, the scientist and the technologist, the speculator and the investor, the craftsman and the aesthete..."
>
> — S. Tolansky [1]

1.1 Diamond through the ages

Diamond has long fascinated mankind due to its combination of superlative physical properties which have led to a variety of uses through history, ranging from magical amulets to rigorously developed technological applications. The origin of its name is the ancient Greek word "adamas" (*ἀδάμας*), meaning unconquerable, arising from the belief that the material was indestructible to blows and fire. This observation is not scientifically accurate, since, though diamond is the hardest natural material (defining the upper limit of the Mohs hardness scale, with a value of 10), it is brittle and oxidises in air at temperatures $\gtrsim 700\,^{\circ}\mathrm{C}$ [2]. References to diamond, often unintentionally humorous, are scattered through written records from sources such as *Natural History* by Pliny the Elder (Gaius Plinius Secundus, AD 23-79) [3], the *Bible* [4] and *The Travels of Sir John Mandeville* [5]. A historical perspective of diamond is presented by Tolansky [1]. Diamonds were first discovered in alluvial river deposits in India around 880 BC, but the modern diamond era commenced in 1869, when the Star of South Africa (with an uncut mass of 83 carats[1]) was found near the site that would become the Kimberley diamond mines, South Africa [1]. This discovery led to the diamond rush, which

[1] A carat is the unit of mass used for diamonds, where 1 carat = 200 mg.

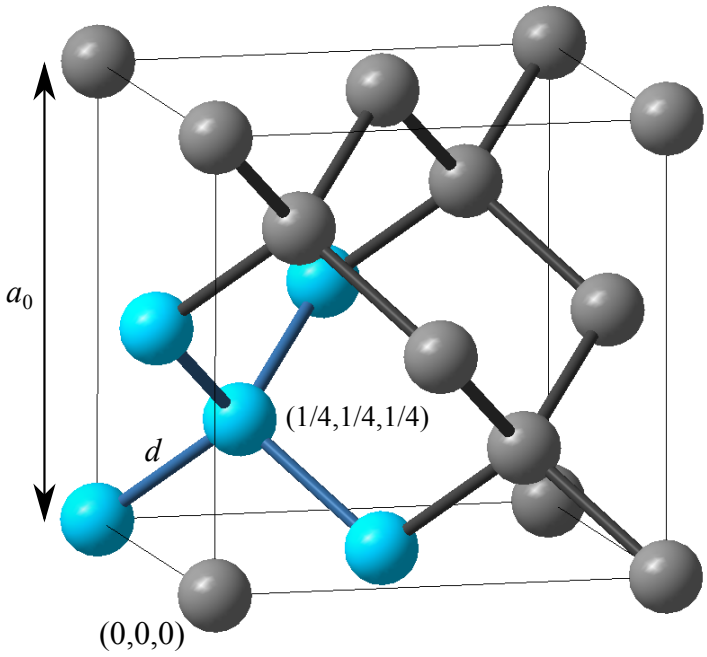

Figure 1-1: The unit cell of diamond, consisting of an arrangement of carbon atoms which adopt a face-centred Bravais lattice structure (Fd3 m space group) with a two atom basis at (0,0,0) and $(\frac{1}{4}, \frac{1}{4}, \frac{1}{4})$. The cubic unit cell constant $a_0 = 0.357\,\text{nm}$, whilst the average C–C bond length $d = 0.154\,\text{nm}$ [6]. The five highlighted atoms emphasise the tetrahedral symmetry of diamond.

has influenced the course of history of several African nations.

Diamond's highest profile application is as gemstones for jewellery. It is widely touted as "the king of gems," prized for its great optical clarity, sparkle, hardness (often confused with indestructibility) and rarity. The whole industry is supported by clever marketing which emphasises these properties and informs the consumer of the remarkable journey that each stone has travelled to reach the customer.

Diamond is an allotrope of carbon, where each atom is covalently bonded to four nearest neighbour atoms in a tetrahedral arrangement, illustrated in Fig. 1-1. It is the metastable state of carbon at atmospheric pressures and temperatures; the stable state is the far less glamorous graphite, from which we get pencil lead (Fig. 1-2). The conditions necessary for natural diamond formation are temperatures of 1000 – 1300 °C, pressures of ~ 4-6 GPa, and undetermined time periods [7]. These conditions are met either at a depth of ~ 200 km below the earth's crust, from which they were brought up to the surface by volcanic erruption, or at meteorite impact sites. Since the 1870's most diamond mining has been based in continental

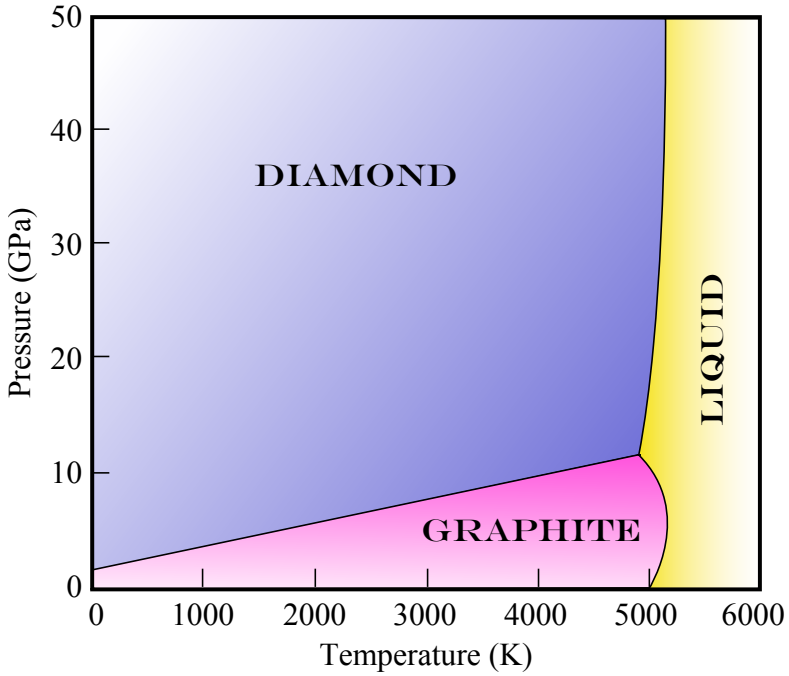

Figure 1-2: Carbon phase diagram, based on that compiled by Bundy *et al.* [9].

Africa, but deposits in other locations such as Russia, Canada and Australia have also helped fulfill the world demand for gem-quality diamond, which was estimated to be $39 billion in 2009 [8].

There is also a wide range of industrial applications which exploit its impressive combination of properties (Table 1-1). Historically limited to uses in cutting and grinding by the scarcity and value of homogeneous and large stones, there has been a great leap in application development stemming from advances in the laboratory synthesis of diamond. The production of man-made diamond was first reported in 1955, when F.P. Bundy *et al.* from General Electric converted a carbon source to diamond using a high-pressure high-temperature process (HPHT) [10], mimicking some of the key conditions for natural diamond formation. An alternative synthesis technique is chemical vapour deposition (CVD) [11–14], a process which has gained momentum due to its inherent increased control of defect incorporation and its ability to coat complex geometric shapes. Unlike HPHT, CVD employs low pressures, ranging from 1 Torr (133 Pa) to 1 atm (10^5 Pa). The method is based on the activation of a plasma consisting of a complex gaseous mixture of a hydrocarbon (such as methane) in an excess of hydrogen above a suitable substrate, resulting in the deposition of diamond on its surface. A vari-

Table 1-1: A selection of some of the extreme properties of diamond, at room temperature.

Properties
Wide band-gap with an indirect band-gap energy $E_g \sim 5.47\,\mathrm{eV}$ [15]
High breakdown field, $\sim 100\,\mathrm{V}\,\mu\mathrm{m}^{-1}$ [16]
Good insulator, with a resistivity $> 10^{13}\,\Omega\,\mathrm{cm}$ [6]
Can be doped, High electronic mobility, $4500\,\mathrm{cm}^2\,\mathrm{V}^{-1}\,\mathrm{s}^{-1}$ [15]
High hole mobility, $3800\,\mathrm{cm}^2\,\mathrm{V}^{-1}\,\mathrm{s}^{-1}$ [15]
Unrivalled thermal conductivity, $2500\,\mathrm{W}\,\mathrm{m}^{-1}\,\mathrm{K}^{-1}$ [17] (5 times that of copper)
Low linear thermal expansion, $0.8(\pm 0.1) \times 10^{-6}\,\mathrm{K}$ [6]
High acoustic wave velocity, $\sim 18\,\mathrm{km}\,\mathrm{s}^{-1}$ [18]
Highest Young's modulus, 1223 GPa [18]
Extreme Knoop hardness, $\sim 90\,\mathrm{GPa}$ [6]
Low coefficient of friction, ~ 0.1 [6]
Chemically inert and resistent to acidic or alkaline solutions, except for those which act as oxidising agents at high temperatures [6]
Biologically compatible since it consists of carbon [6]

ety of substrates can be used, although it is common to use silicon wafers when synthesising polycrystalline diamond and (natural, HPHT or CVD) diamond for single crystal diamond deposition. Diamond synthesis will be reviewed in §2.1 in this thesis.

1.2 The properties and applications of diamond

To understand the unique properties of diamond (Table 1-1) the atomic and electronic structure and defect incorporation need to be considered. Both diamond and graphite are allotropes of carbon, yet they do not share many physical properties. This is a direct result of the different type of bonding found in these materials. The atomic configuration of carbon is $1s^2 2s^2 2p^2$, where the $2s$ and $2p$ orbitals are usually either sp^2 or sp^3 hybridised. Graphite consists of sp^2 hybridised carbon atoms, where strong covalent bonds are formed between carbon atoms in a layer with a hexagonal lattice pattern. The separate layers are attracted to each other by weak van der Waals forces. Other materials such as graphene and carbon nanotubes also have sp^2 hybridised carbon bonds. Meanwhile, the carbon orbitals in diamond are sp^3 hybridised, resulting in three-dimensional tetrahedrally

coordinated covalent bonding (Fig. 1-1). Even though the electron promotion is energetically expensive [19], the electron sharing results in complete electron shells that render the process ultimately energetically favourable.

The large distance between the occupied bonding and unoccupied anti-bonding orbitals results in an electronic structure dominated by a wide band-gap, with an indirect band-gap energy of $E_g \sim 5.47\,\mathrm{eV}$ [15]. This creates a material that is optically transparent in the terahertz to ultraviolet regime, making it a superb optical window for technological devices. The densely packed three-dimensional network of covalent bonds, which are much stronger than the alternative ionic or hydrogen bonds, coupled with the light atomic mass of carbon, results in the material's outstanding strength, mechanical hardness, chemical inertness and radiation hardness. Furthermore, the lattice is able to support the rapid travel of lattice vibrations, giving it a high thermal conductivity and high acoustic wave velocity. Weak phonon scattering also results in high electron and hole carrier mobilities. The supreme hardness, thermal conductivity and wear resistance have led to the production of diamond materials to be used as cutting, drilling or abrasive tools. Furthermore, the combination of properties make diamond an ideal material for uses in high power and high frequency electronics [20, 21].

Recent advances in diamond synthesis enable a heightened control of impurity incorporation. By tailoring the impurity concentrations it is possible to maintain certain preferred properties while modifying those that are less desirable, unveiling its potential for further exciting applications. For example, intrinsic diamond is an excellent insulator, with an electrical resistivity greater than $10^{13}\,\Omega\,\mathrm{cm}$ [6]. However, heavy doping with boron ($> 3 \times 10^{20}\,\mathrm{cm}^{-3}$), a p-type dopant, can result in metallic behaviour [22]. For a comparison between diamond and the competitor materials for uses in electronic devices see Ref. [21]. The combination of the high chemical inertness and the conductivity of boron-doped diamond has also been exploited for the development of electrodes for electrochemical purposes [23, 24]. Moreover, diamond's ability to accommodate a wide variety of optically active colour centres, such as the nitrogen-vacancy centre, renders it a candidate for quantum information processing devices, greatly stimulating research into selective defect production and the synthesis of high quality single crystal material [25–29].

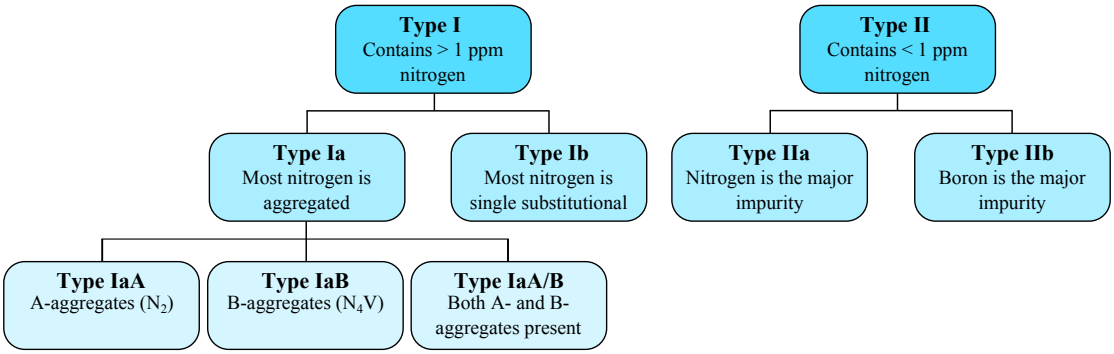

Figure 1-3: The classification scheme for diamonds [59].

An excellent review on the properties and applications of synthetic diamond has been produced by Balmer *et al.* [30].

1.3 Defects in diamond

Defects are defined as entities which cause an interruption in the lattice periodicity of the crystal, and are classified as either surface, line or point defects. The nomenclature reflects whether the imperfect region is bounded in the atomic scale in one, two or three dimensions, respectively. In this thesis only point defects will be investigated. They are often grouped into three categories [31, 32]:

Impurities – An atom other than carbon occupies one of the regular (substitutional) lattice sites.

Vacancies – A carbon atom is missing from a lattice site.

Interstitials – An atom is located at a site other than a substitutional lattice site. The interstitial can be a carbon atom (if its vacancy remains it is a Frenkel pair defect) or another element.

It is noteworthy that complex defects involving all three aspects can also form in diamond, producing a rich field of study.

There are several different impurities which can incorporate into diamond, based on elements such as (but not limited to) hydrogen [33, 34], nitrogen [35–41], silicon [42–48], nickel [49–54], cobalt [54–56] or boron [57, 58]. A selection of point defects which are relevant to this thesis will be reviewed in §2.2.

Nitrogen is frequently found in diamond and its content has been been used to create a classification system [59–62], summarised in Fig. 1-3. The scheme is based on the intensity of the defect-induced one-phonon absorption measured using infrared (IR) spectroscopy, which is proportional to defect concentration. Type I diamonds contain sufficiently high concentrations of nitrogen to be detected by IR techniques (> a few ppm, parts per million host atoms), a class which is further split into type Ia or type Ib, depending on whether the nitrogen centres are present in a mainly aggregated [59] or single substitutional form [35], respectively. The aggregated nitrogen impurities are then differentiated by whether they form dinitrogen centres (A-centres [36], type IaA) or a complex consisting of four substitutional nitrogen atoms surrounding a vacant lattice site (B-centres [37], type IaB). If both aggregate defects are present in a single sample it is known as a type IaA/B. This type of diamond usually also contains the N3 centre (3N + V) [59]. Diamonds which do not have sufficiently high nitrogen concentrations to be detectable by IR are classed as type II. Furthermore, if these diamonds do not conduct they are type IIa, whilst if they conduct, due to a significant concentration of boron, they are type IIb.

1.4 Motivation for research

Due to the significant impact that defects have on the physical properties of diamond both the scientific and industrial community have shown considerable interest in research which enables their chemical and structural identification. Any information which elucidates defect incorporation, formation mechanisms and stability, either during the synthesis or as a result of treatments, is also key for the tailoring of the material properties and the advancement of commercial application development. Furthermore, the presence of certain defects provides an insight into the processes that an unfamiliar diamond may have been subjected to and hence are useful to the gem industry, which strives to differentiate between gem-quality natural, synthetic and treated diamonds [63–66].

In this thesis impurity complexes in CVD and HPHT synthetic diamond have been investigated using a range of optical and paramagnetic techniques. It is

the destruction of the lattice symmetry by the presence of these defects which gives rise to spectroscopic features observable using these tools. Defects introduce a dipole moment in the lattice, permitting characteristic absorption in the one-phonon region of the infrared optical spectrum [67]. Furthermore, the defects may introduce electronic levels in the band-gap of diamond, such that electronic dipole transitions can be detected at energies less than ~ 5.47 eV using either optical absorption or photoluminescence. For centres with unpaired electrons, known as paramagnetic defects, it is also possible to probe the atomic scale environment by careful analysis of induced magnetic dipole transitions using both continuous wave and pulsed electron paramagnetic resonance (EPR). Continuous wave EPR benefits from being not only extremely sensitive and quantitative, allowing the determination of defect concentrations down to $\lesssim 0.1$ ppb (where 1 ppb is one part per billion host atoms) [68], but also providing a wealth of information regarding the elemental constituents and geometry of complexes. Meanwhile, pulsed EPR permits the study of paramagnetic defect spin relaxation mechanisms.

Interest in silicon-related defects in diamond initially arose due to their presence in CVD material, with a zero phonon line at 1.68 eV being commonly used as a spectroscopic marker by the gemmological laboratories [64, 65]. Excitement about the centre responsible for this line, the silicon split-vacancy in the negative charge state ((Si-V)$^-$) [42, 43], has been heightened by its potential use as a single photon source for quantum information processing devices [69, 70]. Hence, this thesis will focus on novel research conducted to characterise and identify silicon-related defects in diamond.

1.5 Thesis outline

The remainder of this thesis is laid out as follows:

Chapter 2 – The development of the HPHT and CVD diamond synthesis to date is reviewed, emphasising the current understanding of defect incorporation. Background information pertaining to selected defects in diamond is also examined.

Chapter 3 – The theoretical aspects underpinning the EPR, absorption and

photoluminescence techniques utilised in this thesis are explained. Furthermore, the mathematical formulism of defect symmetry and its effect on their electronic (and thus spectroscopic) properties is also included.

Chapter 4 – The different pieces of equipment and their setups used are introduced.

Chapter 5 – The EPR spectrum for the neutral charge state of the silicon split-vacancy centre in diamond, (Si-V)^0, has previously been conclusively identified [48]. In this chapter the optical analogue for the defect is determined. The photochromic and thermochromic behaviour of (Si-V)^0 and (Si-V)$^-$ centres are investigated, enabling the calculation of coefficients which allow the quantification of defect concentrations by analysis of the integrated intensities of their respective absorption features. The silicon split-vacancy is shown to have a non-statistical distribution over crystallographically equivalent orientations in homoepitaxial CVD diamond synthesised on {110}-oriented substrates, demonstrating its incorporation as a unit. Analysis of the preferential orientation for (Si-V)^0 provides information on the nature of the electronic dipole transition responsible for its optical spectrum.

Chapter 6 – Further work on the (Si-V)^0 complex is presented. Optical excitation is used to spin polarise its ground state, preferentially populating specific spin levels and destroying the Boltzmann population distribution which would otherwise govern the system. The behaviour and nature of the spin polarisation process for both (Si-V)^0 and its lead competitor, the negatively charged nitrogen-vacancy centre, are explored using continuous wave and pulsed EPR techniques, and a critical comparison of their properties is made.

Chapter 7 – The step-by-step process leading to the identification of a previously unreported EPR-active complex containing both silicon and hydrogen is demonstrated. Its thermal stability, formation and preferential orientation are studied.

Chapter 8 – The conclusions from each results chapter are summarised and key

future experiments are suggested.

References

[1] S. Tolansky, *The History and Use of Diamond* (The Shenval Press, 1962).

[2] P. John, N. Polwart, C. E. Troupe, and J. I. B. Wilson, Diam. Relat. Mater. **11**, 861 (2002).

[3] Pliny the Elder, *Natural History*, vol. Book XXVII (AD77-79).

[4] *The Holy Bible, Exodus XXVIII* (????).

[5] J. Mandeville, *The Travels of Sir John Mandeville* (1356).

[6] J. E. Field, in *The Properties of Natural and Synthetic Diamond*, edited by J. E. Field (Academic Press, Cambridge, 1992), chap. 18, pp. 667 – 700.

[7] J. W. Harris, in *The Properties of Natural and Synthetic Diamond* (Academic Press, London, 1992), chap. 9, pp. 345–393.

[8] *What Countries Produce Gem Diamonds? - Diamond Production Map* (Geology.com website, 2010), http://geology.com/articles/gem-diamond-map/.

[9] F. P. Bundy, W. A. Bassett, M. S. Weathers, R. J. Hemley, H. K. Mao, and A. F. Goncharov, Carbon **34**, 141 (1996).

[10] F. P. Bundy, H. T. Hall, H. M. Strong, and R. H. Wentorf, Nature **176**, 51 (1955).

[11] W. G. Eversole and N. Y. Kenmore, *Synthesis of diamond*, US Patent 3030187 (1962).

[12] W. G. Eversole and N. Y. Kenmore, *Synthesis of diamond*, US Patent 3030188 (1962).

[13] J. E. Butler and R. L. Woodin, Phil. Trans. R. Soc. Lond. A **342**, 209 (1993).

[14] J. E. Butler, Y. A. Mankelevich, A. Cheesman, J. Ma, and M. N. R. Ashfold, J. Phys.- Condens. Mat. **21**, 364201 (2009).

[15] C. Nebel and J. Ristein, *Thin-Film Diamond I - Semiconductors and Semimetals* (San Diego, 2003), vol. 76, chap. Preface.

[16] C. Beuille, E. Dutarde, H. Schneider, M. C. Castex, E. Lefeuvre, J. Achard, and F. Silva, in *Proc. 33rd IEEE Power Electronics Specialists Conf.* (Milton, 2002), pp. 1764–1768.

[17] J. W. Vandersande, in *Properties and Growth of Diamond*, edited by G. Davies (INSPEC, London, 1994), no. 9 in EMIS Datareview Series, pp. 33–35.

[18] S.-F. Wang, Y.-F. Hsu, J.-C. Pu, J. C. Sung, and L. G. Hwa, Mater. Chem. Phys. **85**, 432 (2004).

[19] G. Davies and T. Evans, Proc. R. Soc. Lond. A **328**, 413 (1972).

[20] S. Hadlington, IEE Review **51**, 30 (2005).

[21] C. J. H. Wort and R. S. Balmer, Mater. Today **11**, 22 (2008).

[22] J.-P. Lagrange, A. Deneauville, and E. Gheeraert, Diam. Relat. Mater. **7**, 1390 (1998).

[23] A. L. Colley, C. G. Williams, U. F. S. D'Haenens-Johansson, M. E. Newton, P. R. Unwin, N. R. Wilson, and J. V. Macpherson, Anal. Chem. **78**, 2539 (2006).

[24] R. G. Compton, J. S. Foord, and F. Marken, Electroanalysis **15**, 1349 (200.).

[25] L. Childress, M. V. Gurudev Dutt, J. M. Taylor, A. S. Zibrov, F. Jelezko, J. Wrachtrup, P. R. Hemmer, and M. D. Lukin, Science **314**, 281 (2006).

[26] M. V. Gurudev Dutt, L. Childress, L. Jiang, E. Togan, J. Maze, F. Jelezko, A. S. Zibrov, P. R. Hemmer, and M. D. Lukin, Science **316**, 1312 (2007).

[27] P. Hemmer and J. Wrachtrup, Science **324**, 473 (2009).

[28] R. Hanson, Nat. Mater. **8**, 368 (2009).

[29] B. B. Buckley and D. D. Awschalom, Nature **461**, 1217 (2009).

[30] R. S. Balmer, J. R. Brandon, S. L. Clewes, H. K. Dhillon, J. M. Dodson, I. Friel,

P. N. Inglis, T. D. Madgwick, M. L. Markham, T. P. Mollart, et al., J. Phys.-Condens. Mat. **21**, 364221 (2009).

[31] M. Lannoo and M. Bourgoin, *Point Defects in Semiconductors I - Theoretical Aspects* (Springer, Berlin, 1981).

[32] B. Henderson, *Defects in Crystalline Solids*, The Structures and Properties of Solids 1 (Edward Arnold, London, 1972).

[33] B. Dischler, C. Wild, W. Müller-Sebert, and P. Koidl, Physica B **185**, 217 (1993).

[34] J. P. Goss, J. Phys.-Condens. Mat. **15**, R551 (2003).

[35] W. Smith, P. P. Sorokin, I. L. Gelles, and G. J. Lasher, Phys. Rev. **115**, 1546 (1959).

[36] G. Davies, J. Phys. C: Solid State **9**, L537 (1976).

[37] Davies, in *Chemistry and Physics of Carbon*, edited by P. L. Walker and P. A. Thrower (Marcel Dekker, New York, 1977), vol. 13, pp. 1–143.

[38] J. H. N. Loubser and J. A. van Wyk, Diamond Research **11**, 11 (1977).

[39] N. R. S. Reddy, N. B. Manson, and E. R. Krausz, J. Lumin. **38**, 46 (1987).

[40] D. A. Redman, S. Brown, R. H. Sands, and S. C. Rand, Phys. Rev. Lett. **67**, 3420 (1991).

[41] A. T. Collins, J. Phys.-Condens. Mat. **14**, 3743 (2002).

[42] C. D. Clark, H. Kanda, I. Kiflawi, and G. Sittas, Phys. Rev. B **51**, 16681 (1995).

[43] J. P. Goss, R. Jones, S. J. Breuer, P. R. Briddon, and S. Öberg, Phys. Rev. Lett. **77**, 3041 (1996).

[44] K. Iakoubovskii and A. Stesmans, Phys. Status Solidi a **186**, 199 (2001).

[45] K. Iakoubovskii, A. Stesmans, K. Suzuki, J. Kuwabara, and A. Sawabe, Diam. Relat. Mater. **12**, 511 (2003).

[46] J. P. Goss, P. R. Briddon, M. J. Rayson, S. J. Sque, and R. Jones, Phys. Rev. B **72**, 035214 (2005).

[47] J. P. Goss, P. R. Briddon, and M. J. Shaw, Phys. Rev. B **76**, 075204 (2007).

[48] A. M. Edmonds, M. E. Newton, P. M. Martineau, D. J. Twitchen, and S. D. Williams, Phys. Rev. B **77**, 245205 (2008).

[49] A. T. Collins, J. Phys. D Appl. Phys. **15**, 1431 (1982).

[50] J. E. Lowther, Phys. Rev. B **51**, 91 (1995).

[51] V. Nadolinny and A. Yelisseyev, Diam. Relat. Mater. **3**, 1196 (1994).

[52] V. A. Nadolinny, A. P. Yelisseyev, O. P. Yuryeva, and B. N. Feygelson, Appl. Magn. Reson. **12**, 543 (1997).

[53] V. A. Nadolinny, A. P. Yelisseyev, J. M. Baker, M. E. Newton, D. J. Twitchen, S. C. Lawson, O. P. Yuryeva, and B. N. Feigelson, J. Phys.-Condens. Mat. **11**, 7357 (1999).

[54] K. Iakoubovskii and A. T. Collins, J. Phys.- Condens. Mat. **16**, 6897 (2004).

[55] A. M. Zaitsev, Phys. Rev. B **61**, 12909 (2000).

[56] M. Benabdesselam, P. Iacconi, E. Gheeraert, H. Kanda, D. Lapraz, and D. Briand, Radiat. Prot. Dosim. **100**, 329 (2002).

[57] A. T. Collins and A. W. S. Williams, J. Phys. C: Solid State **4**, 1789 (1971).

[58] A. Deneuville, in *Thin-Film Diamond I - Semiconductors and Semimetals*, edited by C. Nebel and J. Ristein (Elsevier, San Diego, 2003), vol. 76, chap. 4, pp. 183 – 238, 1st ed.

[59] A. T. Collins, Physica B **185**, 284 (1993).

[60] J. F. H. Custers, Physica **18**, 489 (1952).

[61] R. Robertson, J. J. Fox, and A. E. Martin, P. Phys. Soc. Lond. A **232**, 463 (1934).

[62] R. Robertson, J. J. Fox, and A. E. Martin, P. Phys. Soc. Lond. A **157**, 579 (1936).

[63] C. M. Welbourn, M. Cooper, and P. M. Spear, Gems. Gemol. **32**, 156 (1996).
[64] W. Wang, T. Moses, R. C. Linares, J. E. Shigley, M. Hall, and J. E. Butler, Gems. Gemol. **39**, 268 (2003).
[65] P. M. Martineau, S. C. Lawson, A. J. Taylor, S. J. Quinn, D. J. F. Evans, and M. J. Croder, Gems. Gemol. **40**, 2 (2004).
[66] R. U. A. Khan, P. M. Martineau, B. L. Cann, M. E. Newton, H. K. Dhillon, and D. J. Twitchen, Gems. Gemol. **46**, 18 (2010).
[67] M. Lax and E. Burstein, Phys. Rev. **97**, 39 (1955).
[68] B. L. Cann, Ph.D. thesis, University of Warwick (2009).
[69] C. L. Wang, C. Kurtsiefer, H. Weinfurter, and B. Burchard, J. Phys. B-At. Mol. Opt. **39**, 37 (2006).
[70] E. Neu, D. Steinmetz, J. Riedrich-Möller, S. Gsell, M. Fischer, M. Schreck, and C. Becher, New J. Phys. **13**, 025012 (2011).

Chapter 2

Literature review

2.1 Diamond synthesis methods

Synthetic diamond has been produced since the 1950s, spurring the commercialisation of diamond for industrial applications. In order to appreciate defect formation in diamond it is crucial to have at least a basic understanding of the main growth methods employed: the high-pressure high-temperature and chemical vapour deposition techniques. The literature pertaining to these procedures will be reviewed in this section.

2.1.1 High-Pressure High-Temperature (HPHT)

In 1772 Lavoisier demonstrated that diamond could burn when exposed to strong focused light in a closed glass vessel, producing "fixed air" (carbon dioxide) [1]. He noted the resemblance between charcoal and diamond, though he did not go as far as to state that they were elementally identical. Further experiments by Tennant in 1797 finally led to the conclusion that diamond is an allotrope of carbon [1]. First attempts to create diamond focused on subjecting graphitic material to temperatures and pressures similar to those used in its natural formation [2–8], classed as *high-pressure high-temperature* (HPHT) synthesis methods. However, reaching the diamond stabile region for carbon (see Fig. 1-2) is insufficient to instigate a conversion between graphite and diamond [8]. The is due to the fact that the reaction is not simply a thermodynamic problem; the chemical kinetics of the process need to be considered too. The kinetic barrier to rearrange the bonding of the sp^2 hybridised source material to sp^3 hybridised diamond needs to be overcome [9, 10].

The first published reports of successful diamond synthesis were made by Gen-

eral Electric in the 1950s [11], whose advances in instrumentation enabled them to explore higher temperature and pressure regions for sustained periods of time. However, the diamonds produced were very small, having dimensions ranging from less than 100 μm to $\sim$ 1 mm. Further work by the team at the company eventually led to the discovery that molten "solvent/catalysts" could be utilised to break apart the carbonaceous source material, thereby allowing carbon atoms to be transported along a temperature gradient in the mixture, which then crystallise to diamond form in local regions with lower temperatures [10, 12]. Often a "seed" diamond is located in the low temperature region, and layer-by-layer growth both upward and outward can occur, allowing the formation of large diamonds [13]. In the solubility gradient method the difference in the solubility stems from the allotropic difference between the carbon source material and the diamond. One of the key gains with the catalyst activated HPHT method is that synthesis can occur at lower temperatures and pressures (still within the diamond stability region), and the necessary pressure is dictated by the melting point of the solvent/catalyst. The solvent/catalyst can take many forms. It is usually molten metals of group VIII elements, although other metals such as manganese, chromium, tantalum and niobium can also be used [10]. Alloys such as FeNi and FeCo are generally used for commercial production owing to their lower melting points [10], whilst non-metallic solvent/catalysts are rarely utilised due to their low yield [10]. Various carbonaceous materials can be used as the starting source [14–16], and successful experiments have been carried out with graphite, diamond, hydrocarbons, etc. – even peanut butter! The efficiency of a catalytic HPHT synthesis method depends on several factors, though mainly on the melting point of the catalyst, the surface wetting characteristics with graphite, and the stability of any possible metal carbide structures which may form [10]. The conditions vary depending on the size, geometry and numbers of diamonds to be made, but generally pressures of 5 – 6 GPa and temperatures of 1300 – 1400 °C are applied. The procedure and equipment used for HPHT synthesis have been reviewed elsewhere and will thus not be discussed further [10, 17–19].

The morphology of HPHT synthetic diamond differs from that of natural diamonds, where the latter typically show octahedral {111} growth or a combination

of octahedral and more complex growth [20, 21]. Meanwhile, HPHT diamond generally exhibits cube-octahedral growth, where cube faces lie perpendicular to a ⟨100⟩-orientation [22]. Small dodecahedral {110}, trapezohedral ({113} or {115}) and {117} faces have also been reported for HPHT material [22–25]. The relative development of these faces depends on the solvent/catalyst chosen and the temperature and pressure used [13].

During synthesis impurities may be incorporated into the lattice, both intentionally or unintentionally, with the uptake differing for each type of sector [10]. One of the most common impurities in diamond is nitrogen (§2.2.3.1), which may be present in single substitutional or, if permitted by the synthesis time and temperature, in A-aggregated (nearest-neighbour dinitrogen) forms [26, 27]. Doping occurs mainly due to the availability of air in the growth capsule. Unless steps are taken, standard synthesis conditions will yield nitrogen concentrations in the range 100 – 300 ppm (parts per million carbon atoms) [25, 28]. The solubility of nitrogen is highest in the {111} sectors at usual growth temperatures [29]. Relative to this sector the nitrogen concentrations in the {100} sector is ~ 50%, and both {110} and {113} sectors contain an order of magnitude less nitrogen. In summary, the concentrations of nitrogen, [N], for the different sectors can be expressed as $[N]_{\{111\}} > [N]_{\{100\}} \gg [N]_{\{110\}} \approx [N]_{\{113\}}$ [10, 29], though the order can be affected by the overall nitrogen concentration of the diamond [29]. If nitrogen is the main dopant, the sectors with high concentrations will be yellow, giving HPHT diamonds a characteristic colour zoning [13].

There are two main methods used to limit and control nitrogen doping of HPHT diamond. A *nitrogen getter*, a material with a strong affinity for nitrogen (e.g. aluminium, titanium or zirconium), may be added to the solvent/catalyst mixture [23, 26, 30]. A significant amount of the nitrogen will be "trapped" by this substance. However, it is noteworthy that the nitrogen getter itself might be incorporated into the diamond. Alternatively, the high-temperature degassing method may be used, whereby air in the growth capsule is removed at temperatures below the diamond stability region and purged with a gas of choice [31, 32]. The ability to replace the gas provides growers with the opportunity to dope the resulting diamond with specific impurities in a controlled fashion. For instance

nitrogen, silicon, boron, or phosphorus doping can be achieved using N_2, SiH_4, B_2H_6, or PH_4, respectively. Furthermore, higher purity diamond can be produced using methane. For more details on the doping of HPHT diamond the reader is referred to the review article by Burns and Davies [10].

2.1.2 Chemical Vapour Deposition (CVD)

During HPHT diamond synthesis (§2.1.1) scientists try to reproduce the extreme temperature and pressure parameters at which diamond is the stable phase of carbon. Conversely, an increasingly popular technique for diamond production, known as *chemical vapour deposition* (CVD), enables growth under conditions where diamond is metastable with respect to graphite. This means that although diamond is kinetically stable, it is thermodynamically unstable. The method relies on the fact that, once formed, there is a large kinetic barrier to convert diamond into graphite. The CVD process is based on a gas phase chemical reaction involving a hydrocarbon gas in an excess of hydrogen occurring above a surface (the *substrate*), resulting in carbon atoms being added one-at-a-time onto this surface. The growth parameters are optimised to ensure that the formation of a tetrahedrally (sp^3) bonded carbon lattice is favoured over sp^2 bonded graphitic material, or that the latter material is selectively etched. The reactions occur at very low pressures of $10 - 50$ Torr, with the substrate being held at a temperature of $700 - 900\,^{\circ}$C during the active growth period. One of the main advantages of the CVD procedure over the HPHT method is its superior flexibility in terms of the size and geometry of diamonds produced. CVD diamond has been successfully synthesised in a wide range of forms: ultrananocrystalline [33–35], nanocrystalline [35–37], polycrystalline plates and wafers [38], and large single crystals [39–41]. Furthermore, intentional doping can be controlled via the addition of gases containing the intended impurity atom.

The first CVD growth of diamond was reported by Eversole, of the Union Carbide Corporation, in 1958 (patented in 1962, [42, 43]). These early experiments were beleaguered by high levels of graphite co-deposition and low growth rates ($\sim 0.1\,\mu$m per hour). A breakthrough in the development of this technique occurred in 1968, when Angus *et al.* noted that the presence of excess atomic hy-

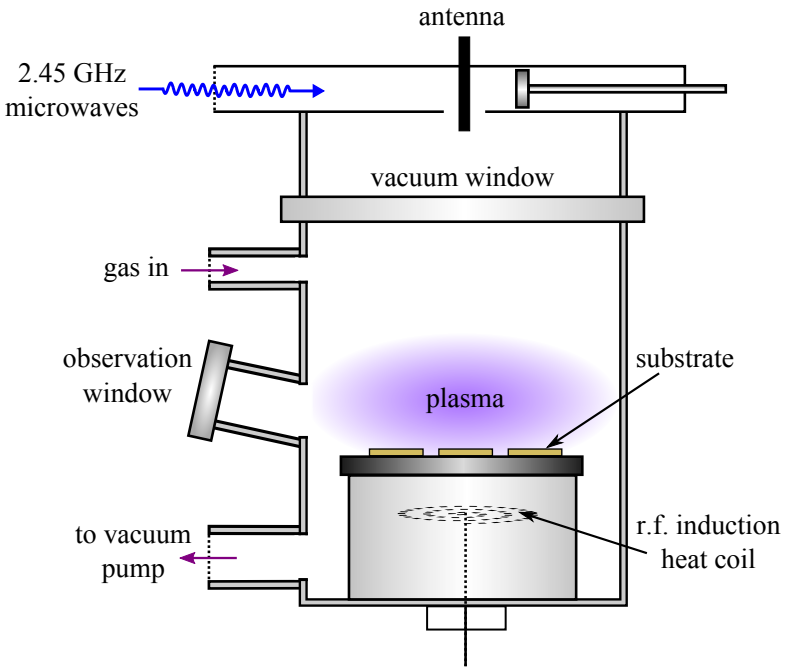

Figure 2-1: Illustration of a 2.45 GHz ASTeX microwave CVD reactor used to grow synthetic diamond [55]. The source gas molecules, usually a gas-phase hydrocarbon in an excess of hydrogen, are dissociated in a plasma which is generated using incident microwaves. They can then react with the diamond substrates, resulting in layer-by-layer diamond growth. Depending on the reactor and the growth chemistry, the useable growth area may vary in diameter between 2 – 20 cm [56].

drogen in the reactor resulted in the preferential etching of graphitic material [44]. Consequently the precursor gas (e.g. CH_4) is heavily diluted in H_2, with a typical mixing ratio of 1%vol. [45]. All CVD techniques require a means to activate the gas phase carbon-containing precursor molecules, and are thus classified accordingly. Activation can occur using thermal methods (e.g. a hot filament), electric discharge (e.g. direct currents, radio frequencies or microwaves), or a combustion flame [45, 46]. The CVD single crystal materials investigated in this thesis were grown using microwave plasma CVD reactors. Thus, the key steps to this specific process will be outlined, though broadly speaking the same basic elements apply to the other methods as well. For more detail regarding the various forms of CVD growth, equipment and theory the reader is directed to the several review articles found in the literature [45–54].

Figure 2-1 illustrates a typical microwave plasma CVD apparatus, based on a 2.45 GHz ASTeX commercial reactor [55]. Single crystal CVD diamond films can only be grown homoepitaxially; growth on non-diamond surfaces such as, for

example, silicon wafers will result in a polyscrystalline diamond coating instead. First, the reaction chamber is purged with hydrogen gas, hydrogen-terminating and stabilising the substrate surface as the temperature is increased. Once the substrate has reached the temperature at which growth will occur, the hydrocarbon gas species (and any additional gases used for doping) are introduced. In a microwave plasma CVD system discharge is created by coupling microwave power (with a frequency of $\sim 2.45\,\mathrm{GHz}$ [57]) to the chamber via a dielectric window. The microwaves dissociate the hydrogen molecules into atomic hydrogen and create carbon-containing radicals, which react both amongst themselves, and with the surface of the growing diamond. The role of the atomic hydrogen is twofold. It not only effectively etches sp^2 material from the growing surface, but also abstracts hydrogen atoms, producing the radical sites necessary for the deposition of carbon. Due to the substantially higher hydrogen concentration in the chamber, relative to the carbon source gas, the radical sites will also frequently recombine with incident hydrogen atoms. High quality growth is easier to achieve on {100}-oriented substrates, though growth on {110}, {111} and {113} sectors has also been accomplished [58–60].

Most research efforts on CVD are currently focused on maximising the growth control and rates, improving purity, and understanding point and extended defect incorporation [46, 59–62]. The processes occurring in the gas phase and on the surface are complex and acutely sensitive to even minute changes to various parameters, such as the surface orientation [58–60] and smoothness [56], the hydrocarbon-to-hydrogen ratio [61, 63–67], the substrate temperature [68], the plasma density [67, 68] and the impurities present [69].

The CVD technique provides greater control over the available atmospheric dopants than the HPHT method. Nevertheless, impurity doping can occur due to their presence in the gas sources or the reactor components. Nitrogen is frequently incorporated into the growing diamond due to the use of impure source gases or the presence of leaks in the reactor. Intentional doping can also be instigated via the addition of N_2 to the gas mixture. Nitrogen is mainly incorporated in a substitutional form, but may also be involved in complexes with vacancies and/or hydrogen (§2.2.3). Studies of the incorporation efficiency (the fraction of the

nitrogen atoms, relative to the carbon atoms, present in the gas phase which are incorporated into the lattice) of {100} growing faces have measured values in the region of $7.5 \times 10^{-5} - 2 \times 10^{-4}$ [70, 71], depending on the specific growth parameters used. Its efficiency also depends on the orientation of the sector, increasing threefold on {111} faces [68].

High concentrations of nitrogen (> 100 ppb, parts per billion host atoms) have been shown to promote the formation of non-diamond materials, hence deteriorating the optical properties of the resulting specimen, whilst even low concentrations (~ 1 ppb) can affect its electronic properties [72, 73]. Improvements in the purification of the source gases and increased control over the growth chemistry has enabled the production of high purity CVD diamond with nitrogen levels $\lesssim 0.1$ ppb [74]. Nevertheless, depending on the properties required, the presence of nitrogen can also be advantageous. Intentional nitrogen-doping can be utilised to increase the growth rate. For instance, adding 2 – 5 ppm of nitrogen into the gases can increase this rate by a factor of ~ 2.5, with the resulting single crystal diamond having a moderate (~ 100 ppb) concentration of substitutional nitrogen [71]. Furthermore, it has also been shown to improve the growth rate, surface morphology and to stabilise the {100} texture of polycrystalline diamond, spurring research into its effect in single crystal material [70, 75–77].

Silicon is also a common contaminant of CVD diamond (§2.2.4) due to the presence of silicon-containing reactor components, which may be chemically or plasma etched [78, 79]. Also, polycrystalline CVD material is often grown on silicon wafers. Silicon has been demonstrated to incorporate more efficiently than nitrogen into diamond [80], and is also sector dependent [81]. Nevertheless, improved control in CVD synthesis has resulted in growth of diamond without observable silicon-related impurities [82]. Furthermore, intentional doping can be achieved via the addition of silicon-containing gases, such as silane, to the growth mixture [80]. Codoping with both nitrogen and silicon can improve the optical properties of the resulting specimen without sacrificing the catalytic enhancement of the growth rate attributed to nitrogen [80], although the interplay between the impurities is not yet understood.

CVD diamond can also be doped using other impurities, such as boron [83],

phosphorus [84], and oxygen [74, 85, 86]. The relative control available in CVD synthesis renders it an attractive process to investigate defect formation and enables tailoring of the material to yield specific combinations of properties for technological applications.

2.2 Selected defects in diamond

This section provides a brief introduction of the properties and models for a selection of defects in diamond. Owing to the wide variety of extended and point defects predicted, detected and characterised to date, only those which are relevant to the work presented in this thesis will be discussed.

2.2.1 Vacancies in diamond

The dominant absorption feature (also visible in luminescence) in electron, neutron or γ-ray irradiated diamond is the GR1 (General Radiation 1) zero phonon line (ZPL) doublet at 1.665 eV and 1.673 eV (744 nm and 741 nm) [87, 88]. In absorption GR1 is often accompanied by a series of lines in the 2.88 – 3.04 eV spectral region, labelled GR2-GR8. Due to the strong absorption in the red region of the visible spectrum by the GR1 band, samples with high concentrations of this centre may be blue-green in colour. The strength of GR1 is directly proportional to the irradiation dose and is only produced when the particles have sufficient energy to cause atomic displacements [87–89], suggesting that it is related to vacancies or interstitials.

Extensive theoretical analysis of isolated vacant lattice sites in diamond [90–93], combined with uniaxial stress data for the 1.673 eV ZPL [94], led to the assignment of GR1 to a transition between a doubly degenerate ground state (^1E) and a triply degenerate excited state ($^1T_2$) at a tetrahedral (T_d) neutral vacancy, V^0. Both the states undergo dynamic Jahn-Teller distortions, resulting in the observed T_d symmetry [93, 95, 96]. Furthermore, the GR2-GR8 lines have been attributed to zero phonon excited state transitions originating at V^0 [97–99]. The ground state of the centre is diamagnetic (S = 0) and so cannot be studied using EPR. However, the $^5A_2$ excited state of V^0 has been identified by van

Wyk *et al.* utilising continuous wave EPR and electron nuclear double resonance (ENDOR) experiments under continuous illumination with an Hg arc-lamp [100]. The thermal stability of GR1 has also been studied. At room temperature the vacancies are immobile, annealing out at temperatures ~ 600 °C [87]. Davies *et al.* established the activation energy for the migration of V^0 to be 2.3 ± 0.3 eV [101].

The negatively charged vacancy in diamond, V^-, has been identified using both optical absorption and EPR spectroscopy [102, 103]. A ZPL at 3.149 eV (394 nm), known as ND1, accompanied by a phonon-assisted structure at energies about 3.4 eV was first reported by Pringsheim and Voreck [104] and subsequently studied in greater detail by Dyer and du Preez [105]. The line has been attributed to a transition between the $^4A_2$ ground and $^4T_1$ excited states of a tetrahedral centre using uniaxial stress [102, 106]. The ground state and symmetry assignment was confirmed by identification of the $S = \frac{3}{2}$ spin state of the ground state by Isoya *et al.* using EPR and ENDOR experiments [103, 107]. V^- does not produce a photoluminescence spectrum. Instead, the centre de-excites via the emission of a charge (of undetermined sign), resulting in photoconductivity [108]. Charge transfer between V^0 and V^- has been reported [101, 105, 106], with illumination reducing the intensity of the latter band, whilst increasing that of the former. The process can be reversed by heating the samples to 500 °C or leaving them overnight in the dark. Annealing studies by Davies *et al.* suggest that vacancy diffusion is dominated by V^0, with V^- converting to V^0 prior to migrating through the lattice [101].

Centres consisting of multiple vacancies have also been observed in diamond. The nearest-neighbour divacancy centre in the neutral charge state, V_2^0, has been produced in irradiated diamond which has subsequently been annealed at temperatures where the vacancy is mobile [87, 109, 110]. This defect starts to anneal out upon prolonged annealing at temperatures above ~ 800 °C [110]. Both the TH5 optical absorption band at 2.3-2.8 eV, which was attributed to V_2^0 [87, 109], and the R4/W6 EPR centre in diamond were observed simultaneously [110, 111]. It was hence proposed by Lea-Wilson *et al.* that the EPR spectrum was the $S = 1$ $^3A_{2g}$ ground state of V_2^0, as theorised by Coulson and Larkins [109, 111]. This model was confirmed by Twitchen *et al.* [110], who carried out a detailed charac-

terisation of the R4/W6 centre and were able to correlate its concentration with the intensity of the TH5 band. Interestingly, the symmetry of the R4/W6 centre was observed to change from D_{3d} (predicted by Coulson [109]) to C_{2h} at low temperatures [110].

There has been renewed interest in extended vacancy defects due to the suggestion by Hounsome *et al.* that their presence may be responsible for the brown colouration often observed in natural and synthetic diamond [112–114]. Furthermore, HPHT treatment of such material has been shown to reduce the saturation of the colour, at times resulting in colourless diamond [56, 115, 116]. This development was particularly noted by the gem trade, where the value of a diamond is strongly influenced by its colour.

Positron annihilation spectroscopy (PAS) results imply the presence of vacancy clusters in brown diamond [117–119]. Moreover, these types of defects have been directly observed by transmission electron microscopy (TEM) [120]. Density functional theory (DFT) calculations predict that the most stable form of vacancy clusters consists of a disk on a {111} plane [113, 114]. They become unstable when they contain more than ~200 vacancy members, instead relaxing into loops [114]. The calculated absorption spectrum for the disks is consistent with the observed spectrum for brown diamond [114]. It has also been suggested that hydrogen may be involved in these clusters [114].

The temperature required to remove the brown colour differs between natural (~1900 °C [116]) and CVD (1400 – 1600 °C [121]) diamonds. The origin of the disparity has not yet been established, although it is possibly related to the different concentrations of hydrogen present in the two types of material [114]. The calculated thermal stability of vacancy disks, up to ~2000 °C [114], is comparable to the treatment temperature necessary to observe colour changes in type IIa natural diamond [116].

An understanding of the geometries, thermal stabilities and formation mechanisms of single vacancies and multi-vacancy defects in diamond is highly relevant due to their involvement in the formation of vacancy-impurity complexes in intrinsic and treated material. In the following sections the key impurity atoms studied in this thesis, and their vacancy-related centres, will be outlined.

2.2.2 Hydrogen in diamond

Hydrogen has been observed in natural, HPHT and CVD diamond, and can reach concentrations as high as 1 atomic percent [122, 123]. It is commonly detected by FT-IR in natural diamond, where sharp absorption lines at 3107 cm^{-1} and 1405 cm^{-1} have been attributed to carbon-hydrogen stretching and bending mode vibrations, respectively [124–127]. Hydrogen's effect on diamond growth and properties can be far-reaching. For example, Zeisel [128] and Chevallier [129] *et al.* demonstrated that hydrogen can passivate electrically active defects such as boron acceptors in doped diamond. Hydrogen-related defects are frequently encountered in CVD diamond, an unsurprising observation due to the prevalence of hydrogen in the reactor and its crucial role during the technique's characteristic layer-by-layer growth [46, 47]. Generally, as-grown HPHT diamond does not contain observable concentrations of hydrogen-related centres. Nevertheless, Kiflawi *et al.* detected the 3107 cm^{-1} absorption line upon HPHT annealing HPHT synthetics at temperatures above 2100 °C [130]. These data were interpreted to mean that hydrogen was originally incorporated into the as-grown material, but further annealing was necessary to form the defect responsible for the 3107 cm^{-1} line [130]. Additionally, intentional hydrogen implantation of the graphite source material has been shown to affect the graphitic/diamond conversion during HPHT synthesis, resulting in a higher mass yield (up to 46%) of diamond than when using unimplanted graphite [131].

The shortage of experimental data pertaining to isolated interstitial hydrogen in diamond has hindered its direct inspection, whereupon research efforts have instead been directed towards the study of the exotic atom muonium. Muonium consists of an electron bound to an antimuon, where the latter is also known as a positive muon μ^+. A muon μ^- is a negatively charged, spin $S = \frac{1}{2}$, elementary lepton particle; μ^+ is the corresponding antiparticle. Since the mass of a muon is much larger (~ 209 times) than the electron mass, muonium can be taken to be a light pseudo-isotope of hydrogen, resulting in comparable chemical properties [132]. The reader is referred to Ref. [132] for a direct comparison between some characteristics of muonium and hydrogen in vacuum. By extension, it is assumed that both atoms will exhibit similar electronic structures when implanted in solids

[132]. Two distinct states of muonium have been observed in diamond [132–135]: "normal" muonium (Mu) has an isotropic spectrum and is thus assigned to a tetrahedral interstitial site, whilst "anomalous" muonium (Mu*) is axially symmetric and is situated at a bond-centred site. Muon-spin-rotation (μSR) experiments used to study muonium and *ab initio* theoretical work based on the Hartree-Fock method have demonstrated that anomalous muonium is the most stable state for muons in diamond [132–135]. Hence, it is concluded that hydrogen is more stable at a bond-centred site than in a tetrahedral cage-centred position. A comprehensive review which highlights and compares the key theoretical developments in research on hydrogen in diamond has been prepared by Goss [123], which also considers complexes of hydrogen with alternative impurities.

This section will not attempt to review all research done on hydrogen-related centres in diamond. Instead, it will focus on some of the work conducted on hydrogen-related centres with unknown structures, and those of identified defects which do not contain any other impurity atoms. Complexes with conclusively verified structures which consist of hydrogen and either nitrogen or silicon impurities will be discussed in §2.2.3 and §2.2.4, respectively.

2.2.2.1 The 1405 cm^{-1} and 3107 cm^{-1} optical absorption lines

Runciman and Carter suggested that the 1405 cm^{-1} and 3107 cm^{-1} bands arose from bending and stretching mode vibrations, respectively, of either C-H or N-H bonds at a centre, with the stretching mode vibration resulting in a stronger peak intensity. Woods and Collins noted that the 3107 cm^{-1} band is always accompanied by a weak peak at $\sim$3098 cm^{-1} [126]. Data for the relative intensities and positions of the peaks led them to identify the 3107 cm^{-1} and 3098 cm^{-1} lines as ^{12}C-H and ^{13}C-H and stretching mode vibrations, respectively. Similar ^{14}N:^{15}N substitutions experiments conducted by Kiflawi *et al.* did not result in a shift in the 3107 cm^{-1} absorption band, which would be consisted with its assignment to C-H vibrations [130]. However, as pointed out by Chevallier *et al.* [136], this does not rule out the involvement of nitrogen in the defect.

Uniaxial stress investigations by Cruddace [137] of the 3107 cm^{-1} (first attempted by Runciman and Carter [125] and Davies *et al.* [138]) and 1405 cm^{-1}

lines revealed that they originate from $A \rightarrow A$ and $A \rightarrow E$ transitions, respectively, of a trigonal centre (details on symmetry and the nature of transitions can be found in §3.2). A tentative assignment to a (N:H-C) defect has been made [137, 139]. Theoretical modelling by Goss *et al.* has determined the stable structure of the (N:H-C) centre to be that of a hydrogen atom located near a bond centre between a carbon atom (to which it is bonded) and a nearest-neighbour substitutional nitrogen atom [139]. This results in a centre with a very small ($< 0.1\,\mathrm{cm}^{-1}$) ^{15}N isotopic shift [139], consistent with the behaviour observed for the $3107\,\mathrm{cm}^{-1}$ line. However, uniaxial stress and annealing studies by Liggins contradict the assignment, instead attributing a line at $3324\,\mathrm{cm}^{-1}$ to the (N:H-C) centre, in good agreement with the theoretical data of Goss [32, 139]. Therefore, the structure of the defect responsible for the $3107\,\mathrm{cm}^{-1}$ and $1405\,\mathrm{cm}^{-1}$ lines is still uncertain. For a review on the work conducted on these lines the reader is directed to Liggins [32].

2.2.2.2 H1, H2 and the vacancy-hydrogen centre

An EPR-active centre ($S = \frac{1}{2}$), known as H1, has been observed in hydrogen-containing polycrystalline CVD diamond, annealing out in the temperature range 1400-1500 °C [140–145]. H1 consists of a broad (0.4-0.8 mT) EPR signal at $g = 2.0028$ with a pair of weak hyperfine satellites which were assigned to the involvement of hydrogen [141]. The origin of the spectral structure was refined by Holder *et al.* [142], who suggested that the satellites arise from "forbidden" $\Delta m_{\mathrm{I}} = \pm 1$ nuclear spin flip transitions of the hydrogen nucleus during EPR (the theory of transition selection rules, probabilities and forbidden transitions is outlined in §3.1.4). Analysis of the hyperfine satellites, coupled with defect modelling using the Hartree-Fock approach, led Zhou *et al.* to conclude that H1 results from a point defect with a single hydrogen located ~ 1.9 Å away from the unpaired electron [143]. Their experimentally extracted hyperfine parameters were subsequently confirmed by Talbot-Ponsonby *et al.* [144] and Iakoubovskii *et al.* [146]. High concentrations of H1 are detected in polycrystalline CVD material, where there is an abundance of grain boundaries, surfaces and other discontinuities in the diamond lattice. Zhou *et al.* proposed that H1 is a centre composed of a lattice vacancy and a hydrogen atom bonded to a nearest neighbour carbon atom [143],

though the number of vacancies involved in the centre is unclear. This defect has not been observed in CVD diamond of good structural quality, in which other hydrogen-related defects have been detected [144].

Glover *et al.* detected, at room temperature, a $S = 1$ EPR complex with C_{3v} symmetry, and assigned it to the negatively charged vacancy-hydrogen centre, $(V{-}H)^-$ [147]. However, this model was challenged by Shaw *et al.* [148, 149], who noted that an alternative structure, the negatively charged divacancy-hydrogen complex, $(V_2{-}H)^-$ is also compatible with the data reported. The experimentally observed symmetry of the EPR defect at room temperature was accounted for by a prediction that the hydrogen atom quantum tunnels between the three equivalent carbon sites neighbouring the negatively charged divacancy [148, 149]. *Ab initio* pseudopotential calculations with all-electron wavefunction reconstruction, combined with DFT calculations, were employed by Shaw *et al.* to estimate hyperfine parameters for both $(V{-}H)^-$ and $(V_2{-}H)^-$ [148, 149]. Comparison between the theoretical and experimental values indicate a significantly better agreement with the $(V_2{-}H)^-$ model. Nevertheless, the accuracy of their calculated hyperfine parameters was reduced by the small magnitudes of the values in question. Hence, neither the $(V{-}H)^-$ nor the $(V_2{-}H)^0$ structures can be conclusively linked to the EPR centre.

An additional $S = \frac{1}{2}$ EPR-active defect, labelled H2, has been reported to have similar parameters to H1, but with a smaller line width [143]. The detailed structure for this centre has not yet been hypothesised, but experimental evidence indicates a propensity for the complex to form close to grain boundaries in polycrystalline material [143, 144]. Zhou *et al.* has tentatively suggested that the centre is based on the hydrogenation of one or more vacancies, with the hydrogen atom lying ~ 2.3 Å away from a carbon dangling bond [143].

2.2.3 Nitrogen-related defects

The optical properties of diamond are largely dominated by nitrogen impurities in the lattice, which can exist in many forms [150]. Only the following nitrogen-related centres will be considered here: single substitutional nitrogen (N_s), A-centre (N_2), B-centre ($N_4{-}V$), N3 (($N_3{-}V$), nitrogen-vacancy (N-V), and nitrogen-

vacancy-hydrogen (N-V-H). Due to the prevalence of nitrogen in diamond, it has historically been used to classify the material, as introduced in §1.3. Diamond with nitrogen concentrations which are sufficiently high to be detected using infrared (IR) absorption are termed type I, a class which is further divided into those which mainly have aggregated (type Ia) or isolated (type Ib) nitrogen. Moreover, subgroups for type Ia diamond exist; depending on whether the specimen contains mainly A-centres (type IaA), B-centres (type IaB), or appreciable concentrations of both (type IaAB). Finally, if nitrogen concentrations are too low to detect by IR spectroscopy ($\lesssim 1$ ppm) the material is considered to be type IIa, whilst if boron is present at a higher concentration than nitrogen it is termed a type IIb diamond.

2.2.3.1 Aggregated nitrogen

Nitrogen aggregates typically only form under HPHT conditions, which can be provided either in a laboratory or during natural post-growth annealing in the upper mantle prior to its eruption, and are thus not observed in as-grown CVD diamond. The A-centre was identified as the neutral charge state of a complex composed of two nearest-neighbour substitutional impurities, and is present in measurable concentrations in $\sim 98\%$ of all natural diamonds [151]. Its concentration can be calculated by analysis of the IR spectra, which include a vibrational mode at $1280\,\mathrm{cm}^{-1}$ [152, 153]. The positive charge state of the centre, $(N_2)^+$, has been identified by EPR and ENDOR experiments (known as the W24 centre) [154].

Chrenko *et al.* showed that HPHT annealing of type Ib diamond at temperatures in the range $1600 - 2000\,^{\circ}\mathrm{C}$ resulted in the aggregation of dispersed isolated nitrogen atoms and the formation of A-centres [27]. Their data indicated that the aggregation process was significantly more favourable than the diffusion of the nitrogen out of the diamond. Furthermore, investigations by Collins revealed that the efficiency of aggregation could be enhanced by the presence of vacancies and nitrogen-vacancy complexes [115, 155], leading to an alternative aggregation sequence which could be activated at annealing temperatures of only $\sim 1500\,^{\circ}\mathrm{C}$.

The B-centre is a more complex aggregate form, consisting of four substitutional nitrogen atoms surrounding a single vacant site, (N_4–V) [150]. Vibrational

bands at 1332, 1171, 1093, 1003 and 780 cm^{-1} have been assigned to the centre [156]. A method for deconvolving the spectra for the A- and B-centres has been presented by Davies [152]. Although sometimes present in untreated natural diamond, it is also possible to create B-centres during extended HPHT anneals at 2000 – 2500 °C [157]. However, the exact formation mechanism, which involves A-centres, is still unclear.

The N3 defect, with a ZPL at 2.985 eV (415 nm) is frequently observed in type Ia diamond [87, 158]. It has been attributed to a transition between a $^2A_1$ (or $^2A_2$) ground state and a ^2E excited state of a trigonal defect [87, 159]. The intensity of N3 has been correlated with the concentration of the P2 EPR defect in diamond [160–164]. Analysis of EPR and ENDOR data has allowed the assignment of the N3/P2 defect to a complex consisting of a vacancy surrounded by three nearest-neighbour nitrogen atoms and a carbon with a dangling bond [161, 164].

A more detailed discussion of nitrogen aggregates can be found in the review articles by Woods [157], Kiflawi and Lawson [165], and Jones and Goss [156] (and references therein).

2.2.3.2 Isolated substitutional nitrogen

The neutral charge state of single substitutional nitrogen, N_s^0, was first identified by Smith *et al.* using EPR [166]. The spectra observed for this spin $S = \frac{1}{2}$ defect, commonly labelled P1, were characterised by a nearly isotropic g-factor of 2.0024 ± 0.0005 and hyperfine structure arising from nitrogen and ^{13}C hyperfine interactions. They suggested that P1 was a substitutional atom bonded to the four nearest-neighbour carbon atoms, with an unpaired electron localised at one of the C–N bonds, producing a bond length extension. This distortion leads to a symmetry lowering from tetrahedral (T_d) to trigonal ($C_{3\mathrm{v}}$) symmetry. This particular C–N bond has been calculated to be ~30% longer than that for an undistorted C–C bond [167], in reasonable agreement with the experimentally determined bond length estimated by Tucker *et al.* [154]. Additionally, a detailed ENDOR study of P1 by Cox *et al.* enabled the accurate determination of the hyperfine and quadrupole parameters for ^{14}N and the hyperfine parameters for ^{15}N and ^{13}C [168], further corroborating the assignment of P1 to N_s^0.

The C_{3v} symmetry of N_s^0 was originally explained by a Jahn-Teller distortion [166], which was supported by theoretical cluster calculations by Messmer and Watkins [169], who predicted an orbitally degenerate T_2 ground state. Thermally induced reorientation of N_s^0, with an activation energy of 0.7 ± 0.1 eV, was reported by Loubser and Ryneveld [170], in apparent agreement with the Jahn-Teller distortion model. However, this model was refuted by subsequent theoretical work by Bachelet *et al.* [171], Kajihara *et al.* [172], and Briddon and Jones [167], whose data indicated that the ground state for N_s^0 was the antibonding A_1 state. As this state is orbitally nondegenerate it is incompatible with a Jahn-Teller distortion. Instead, the centre's symmetry lowering arises from the bonding-antibonding occupancy of one of the C–N bonds. The relaxation of the neighbouring carbon atoms is significant [154, 167], and is responsible for the deep donor level associated with N_s^0, which is positioned ~ 1.7 eV below the conduction band [173].

N_s^0 produces an absorption continuum which starts at ~ 1.7 eV and rises in intensity up to the fundamental absorption edge (~ 5.5 eV) [173]. The absorption has been attributed to photoconductivity from the donor level into the conduction band [173]. If the absorption by N_s^0 is the dominant feature in the visible spectral range, resulting colour of the diamond will be canary yellow. Uniaxial stress measurements by Koppitz *et al.* revealed that the continuum can be decomposed into two separate broad bands, with peaks at 3.3 eV (376 nm) and 3.9 eV (318 nm) [174]. Furthermore, a band at 4.6 eV (270 nm) has been correlated with the N_s^0 concentration [175].

The concentration of N_s^0 centres in a diamond can also be measured using IR absorption spectroscopy. The defect's spectrum has a maximum at 1130 cm^{-1} and a sharp peak associated with a local vibrational mode at 1344 cm^{-1} [26, 176]. The N_s^0 concentration ($[N_s^0]$, in ppm) can be determined from the measured absorption coefficient for the 1130 cm^{-1} peak ($\mu_s(1130\,cm^{-1})$ [177]:

$$[N_s^0] = 25(\pm 5) \times \mu_s(1130 cm^{-1}) \tag{2-1}$$

If there is a suitable acceptor nearby (e.g. boron), N_s^0 can donate an electron, converting to the positively charged single substitutional nitrogen defect, N_s^+. Unlike N_s^0, for N_s^+ the nitrogen atom sits on a lattice site, resulting in T_d symmetry. N_s^+ is diamagnetic and is hence EPR-inactive. Nevertheless, it pro-

duces a characteristic IR absorption spectrum, with lines at 1332 cm^{-1}, 1046 cm^{-1} and 950 cm^{-1} [178]. A relationship between the N_s^+ concentration ($[N_s^+]$, in ppm) and the 1332 cm^{-1} absorption coefficient ($\mu_s(1332\,cm^{-1})$) was derived by Lawson *et al.*[178]:

$$[N_s^+] = 5.5(\pm 0.5) \times \mu_s(1332 cm^{-1}) \quad (2\text{-}2)$$

It is noteworthy that other centres may absorb at 1332 cm^{-1}, so positive identification of N_s^+ requires the detection of the other peaks.

Further information on both charge states of single substitutional nitrogen can be found in Refs. [32, 179].

2.2.3.3 Nitrogen-vacancy

The nitrogen vacancy ((N-V)) centre consists of a substitutional nitrogen atom located next to a vacant lattice site, resulting in a point defect with C_{3v} symmetry and a principal axis aligned along a ⟨111⟩ direction. It can be found in as-grown CVD diamond and created in natural, CVD and HPHT diamond by various treatments. Two charge states for the (N-V) exist: the neutral ($(N\text{-}V)^0$) or negative ($(N\text{-}V)^-$) charge states, and can be present simultaneously in a single sample [180].

The formation mechanism for (N-V) in as-grown single crystal CVD diamond is not well understood [56], though recent evidence by Edmonds *et al.* for the preferential alignment (defined in §5.4.2) of (N-V) in material homoepitaxially deposited on a {110}-oriented substrate indicates that its incorporation as a unit during growth is possible [181]. NV centres can be created after the growth of natural or synthetic diamond via a simple two-step process. First, the diamond is irradiated with high energy particles, such as electrons, introducing a significant concentration of vacancies into the lattice. Vacancy formation by irradiation is discussed in §2.2.1. The sample is then annealed at temperatures in the region of ~ 600 – 900 °C, activating the diffusion of vacancies [87], whereupon they can be trapped by substitutional nitrogen impurities, creating (N-V) defects. There are several variations to this process (such as starting by nitrogen implantation), but the key elements are that nitrogen atoms and vacancies must be present, followed by annealing under conditions where the vacancies can be mobilised. The centre anneals out at ~ 1500 °C and is reportedly involved in the enhanced aggregation

of A-centres in type Ib diamond [115].

The first observation of (N-V) was reported by du Preez [182], who detected a zero phonon line at 1.945 eV (637 nm) by optical absorption in a nitrogen-containing diamond which had been irradiated and annealed. Davies and Hamer conducted a detailed uniaxial stress study of the line and determined that it arose from an $A \rightarrow E$ transition at a trigonal centre [183]. Due to its production in irradiated and annealed diamond it was suggested that this centre was (N-V). An $S = 1$ centre with C_{3v} symmetry, displaying a large zero-field splitting (2.878 ± 0.005 GHz), and involving an atom which has a nearly 100% $I = 1$ isotopic abundance, was investigated using EPR by Loubser and van Wyk in a diamond showing 1.945 eV absorption [184]. The EPR and optical centres were thus both attributed to (N-V) [184], a model whose credence was established by subsequent studies by Reddy *et al.* [185] and Redmann *et al.* [186].

A ZPL at 2.156 eV (575 nm) is often observed simultaneously with the 1.945 eV line [187, 188]. Uniaxial stress measurements of this line revealed that the centre responsible was also trigonal, and the nature of the transition was established to be $E \rightarrow A$ [188]. Consideration of the similarities between the two defects led Collins and Lawson to suggest that the 2.156 eV centre was also a nitrogen-vacancy complex [187]. Mita demonstrated that the relative intensities of the 1.945 eV and 2.156 eV ZPLs depended on the dose of the neutron irradiation used to create the centres [189]. At low doses the former ZPL dominated, but as the dose was increased there came a point (which will be sample dependent) after which the latter line abruptly appeared. As the dose was further increased, the 2.156 eV absorption strength increased, correlating with a decrease in that of the 1.945 eV line [189]. This led Mita to suggest that they arose from two different charge states of (N-V); the 1.945 eV and 2.156 eV lines were assigned to $(\text{N-V})^-$ and $(\text{N-V})^0$, respectively. The relative concentrations of these centres is determined by the availability of N_s^0, which acts as a donor according to $(\text{N-V})^0 + N_s^0 \rightarrow (\text{N-V})^- + N_s^+$ [180, 190].

The (N-V) centres are discussed in greater detail in §6.1.1.

2.2.3.4 Nitrogen-vacancy-hydrogen

An $S = \frac{1}{2}$ defect which displayed nitrogen and ^{1}H hyperfine structure was observed in a single crystal CVD sample by Glover *et al.* [191]. Analysis of the data, greatly facilitated by the availability of a sample doped using a ^{15}N-enriched (90%) nitrogen source, led to the defect being attributed to the nitrogen-vacancy-hydrogen (N-V-H) complex in the negative charge state, $(\text{N-V-H})^{-}$. The hypothesised model consisted of a hydrogen atom bonded to the nitrogen atom, so that the impurity atoms and the vacancy were all connected by a common $\langle 111 \rangle$-axis, giving the C_{3v} symmetry observed experimentally.

However, subsequent theoretical calculations by several groups conflicted with this static model [123, 148, 149, 192], predicting that it was unstable. Instead, they suggested that the hydrogen was bonded directly to one of the carbon atoms neighbouring the vacancy. This configuration has monoclinic I (C_{1h}) symmetry, in apparent disagreement with the EPR data [191]. However, the calculation also predicted that the hydrogen atom tunnels between the three different C_{1h} configurations at a timescale (τ) which is sufficiently rapid in comparison to the timescale of the EPR measurements reported ($\sim 10^{-10}$ s), resulting in the observation of a time averaged configuration with C_{3v} symmetry [192]. Experimental evidence for the dynamic model of (N-V-H) was reported by Edmonds, who carried out multifrequency EPR investigations at temperatures between $8 - 750$ K, revealing a transition- and frequency-dependent line broadening effect [81]. It was noted that even at cryogenic temperatures it was not possible to slow down the tunnelling rate sufficiently in order to observe $(\text{N-V-H})^{-}$ with C_{1h} symmetry [81, 191]. It was thus suggested that, for the temperature range investigated, τ is primarily determined by temperature-independent quantum mechanical tunnelling [81]. Supplementary computational work by Edmonds *et al.* enabled the calculation of the spin Hamiltonian parameters for the static configuration and the simulation of spectra which agreed with the experimental spectra [193]. Their experimentally derived parameters for the static structure agreed with those predicted from theoretical calculations by Goss *et al.* (unpublished, but stated in Ref. [193]). Also, the timescale for the interconversion between the different C_{1h} configurations was extracted from the data, giving $\tau = 2.5(\pm 0.4) \times 10^{-8}$ s [193], which is only two or-

ders of magnitude greater than that predicted by Kerridge *et al.* [192]. Thus, the dynamic model for $(\text{N-V-H})^-$ has been established.

The characteristic time for optical measurements is significantly shorter than for EPR experiments, and may be as short as $\sim 10^{-10}$ s [192]. Hence, it has been suggested that optical absorption transitions from (N-V-H) centres will appear to arise from defects with C_{1h} [192]. A local vibrational mode at 3123 cm^{-1} is frequently observed in nitrogen-doped CVD diamond [39, 56]. Isotopic substitution experiments using deuterium indicated that the centre responsible for the line was hydrogen-related [136, 194]. Cruddace conducted a uniaxial stress study of the line, and found that it arose from an $A \rightarrow A$ transition at a defect with C_{1h} symmetry [137]. Thus, consideration of all these traits for the 3123 cm^{-1} line led to the suggestion that it was related to (N-V-H), although the specific charge state was not established [137]. Both the neutral ($(\text{N-V-H})^0$) and negative charge states are probable candidates as they are predicted to be IR active (it is noteworthy that $(\text{N-V-H})^0$ is not going to be EPR-active). The positive charge state, $(\text{N-V-H})^+$, is also possible, though it is only expected in material with a high concentration of shallow acceptors unlike the samples used in these studies [32].

Evidence for the assignment of the 3123 cm^{-1} local vibrational mode to $(\text{N-V-H})^0$ was presented by Cann *et al.*, who induced charge transfer between the centre responsible for the optical absorption line and the $(\text{N-V-H})^-$ centre, where the concentration of the latter was monitored using EPR [74, 195, 196]. Heating diamonds containing (N-V-H) complexes at 850 K in the dark produced an increase in the $(\text{N-V-H})^-$ concentration and a decrease in the intensity of the 3123 cm^{-1} line. The effect could be reversed by illuminating the material with strong ultraviolet light. Hence, it was suggested that the 3123 cm^{-1} line originated at $(\text{N-V-H})^0$. Further studies by Liggins [32], where the conversion between the two charge states was modelled using first order kinetics, was used to calculated a conversion factor, given in:

$$[(\text{N-V-H})^0] = 200(\pm 15) \times I(3123\text{cm}^{-1}) \tag{2-3}$$

where the concentration of $(\text{N-V-H})^0$, $[(\text{N-V-H})^0]$, is given in ppb and $I(3123\,\text{cm}^{-1})$ is the integrated intensity of the 3123 cm^{-1} line. It was noted that the height of the line was strongly dependent on the resolution used for the measurements and

thus quantitative analysis should instead consider the area under the line [32].

The optical analogue for $(N\text{-}V\text{-}H)^-$ has not yet been identified, though local vibrational modes at 2727 cm^{-1} and 2806 cm^{-1} demonstrate the same thermo- and photochromic behaviour observed for $(N\text{-}V\text{-}H)^-$ [32]. Uniaxial stress experiments of these lines did not result in a clear splitting and thus the symmetry of their respective defects could not be analysed. Nevertheless, out of the two lines it was the 2727 cm^{-1} which showed the most promise, as the line became asymmetric under stress, suggesting that it might split under different conditions. Further experiments are necessary in order to verify whether this line might potentially be attributed to the $(N\text{-}V\text{-}H)^-$ complex.

2.2.4 Silicon-related defects

From purely thermodynamical considerations silicon is not soluble in diamond and hence silicon-related impurities are not expected to form in diamond [197]. Nevertheless, non-equilibrium growth conditions present opportunities for its incorporation. For instance, silicon is frequently introduced unintentionally into CVD diamond as a consequence of chemical [78] and plasma [78, 79] etching of silicon-containing components in the synthesis chamber (e.g. silica windows). Similarly, HPHT diamond can be intentionally doped during growth by using SiC as a starting material [198] or by adding silicon to the graphite in the growth cell [199]. Furthermore, post-growth implantation with Si^+ ions will result in the creation of silicon-related centres in diamond [200]. Silicon is rarely observed in natural diamond and its presence, though it does not rule out natural origin, is often taken to be indicative of synthetic (in particular CVD) diamond [56, 201]. Silicon is usually identified in diamond by the detection of a zero phonon line at 1.68 eV (737 nm) [199, 200, 202]. In view of this, the investigations which were used to conclusively attribute the line to the negatively charged silicon split-vacancy defect in diamond, $(Si\text{-}V)^-$, will be used as an introduction to other silicon-related defects.

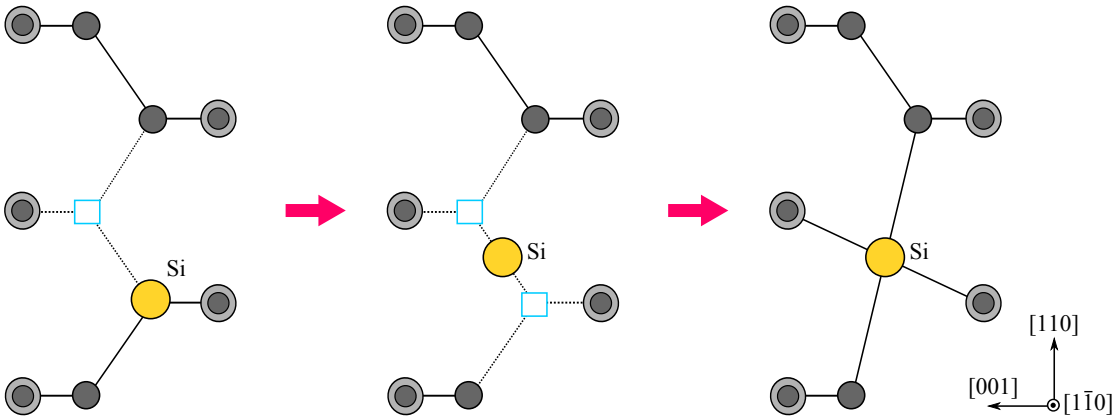

Figure 2-2: Cross-sectional view of the $(1\bar{1}0)$ mirror plane of a silicon-vacancy complex in diamond. A structure with a substitutional silicon atom next to a vacancy is predicted to be unstable [202], instead relaxing into a bond-centred position between two nearest-neighbour vacant sites. The resulting complex with D_{3d} symmetry is known as the silicon-split vacancy centre. The large yellow atoms, grey atoms and light blue squares represent silicon, carbon and vacancies, respectively.

2.2.4.1 The silicon split-vacancy and its related complexes

The 1.68 eV band in diamond was first detected in the cathodoluminescence spectrum of polycrystalline CVD diamond by Vavilov *et al.* [200]. To investigate the nature of the centre they implanted natural diamond with silicon, whereupon the line was created. Thus they proposed that it was silicon-related, suggesting a complex based on two interstitial silicon atoms. This model was subsequently disproved [199, 202]. The involvement of silicon was conclusively determined by Clark *et al.* [199], who were able to resolve the centre's 12-line fine structure. The twelve lines were divided into three groups of four equally intense lines whose relative strengths agree with the ratios of the abundance of the natural isotopes of silicon (^{28}Si, ^{29}Si, ^{30}Si). A minimum of four energy levels are required to describe the multiplicity of the lines; this is in accordance with a transition from an orbitally twofold degenerate ground state, split by 0.20 meV, to a doublet excited state split by 1.07 meV [199]. The defect was found to be extremely stable, surviving annealing temperatures up to 2200 °C [203]. Electron irradiation of CVD diamond followed by annealing above 700 °C usually leads to substantial growth of the 1.68 eV feature (if there is a suitable concentration of donors). This is indicative of the optical centre involving a vacancy,[203, 204] as vacancies become

mobile at ~600 °C [101].

Goss *et al.* employed spin-polarised local density functional cluster theory to verify that the 1.68 eV luminescence centre in diamond arises from a silicon-vacancy complex [202]. Silicon was predicted to be unstable when placed in a lattice site next to a vacancy, spontaneously relaxing into a split-vacancy position, where the atom lies at the centre of a nearest-neighbour divacancy (D_{3d} symmetry), a configuration known as a paired or double semivacancy [205], illustrated in Fig. 2-2. The silicon-vacancy complex was predicted to have a deep acceptor $(-/0)$ level at around $E_v + 1.4$ eV [206], such that in the negatively charged state a $^2E_g \rightarrow {}^2E_u$ internal optical transition can occur. Calculations suggest that the optical transition for $(\text{Si-V})^-$ would result in a band at 1.86 eV [202], in reasonable agreement with the experimental value. The splitting of the doublets has been attributed to a Jahn-Teller effect [202], which would affect the observed symmetry of the centre. Uniaxial stress studies were incomplete and unable to parameterise the system responsible for the 1.68 eV ZPL [207, 208]. The binding energy and dissociation barrier for the complex have been estimated to be 4.1 eV and 6.4 eV, respectively [206, 209]. The high barrier is in accordance with the high thermal stability exhibited by $(\text{Si-V})^-$. Hence, the optical analogue for $(\text{Si-V})^-$ is generally accepted to be the 1.68 eV band. Despite the prediction that $(\text{Si-V})^-$ has an $S = \frac{1}{2}$ ground state [202, 209], it has not yet been conclusively identified by EPR, possibly due to linewidth broadening due to the proposed Jahn-Teller distortion [81]. An EPR-active defect labelled KUL8 was suggested to be the $(\text{Si-V})^-$ centre by Iakoubovskii *et al.*[210, 211], but due to absence of data for the ^{29}Si hyperfine structure, the assignment can only be taken to be speculative. Furthermore, the KUL8 defect has not been observed in other silicon-containing diamonds which show strong 1.68 eV absorption [81, 82].

The silicon split-vacancy centre in the neutral state, $(\text{Si-V})^0$, is predicted to have a $^3A_{2g}$ ground state by Goss *et al.* by theory and was confirmed by EPR studies [202, 206, 209]. The EPR centre KUL1, first reported by Iakoubovskii *et al.*, was shown to increase in concentration in material with higher levels of silicon doping [212], and was subsequently suggested to be the $(\text{Si-V})^0$ complex [213]. Their data was able to resolve hyperfine satellites that were attributed to the $I = \frac{1}{2}$

^{29}Si isotope of silicon [212, 213], yet they concluded that the centre did not have six equivalent nearest-neighbour carbon atoms surrounding the silicon atom which are required for the D_{3d} symmetry predicted by Goss *et al.* [202]. More detailed EPR analysis of the KUL1 centre using improved single crystal CVD diamond intentionally doped with silicon with either natural or ^{29}Si-enriched isotopic abundances enabled Edmonds *et al.* to conclusively confirm its assignment to (Si-V)^0 [82]. These new studies showed that KUL1 has an approximately isotropic ^{29}Si hyperfine interaction, and near 100% localisation of the unpaired electron probability density on six equivalent carbon nearest-neighbour atoms as predicted by theory. A line at 1.31 eV (946 nm), visible in absorption and photoluminescence, has been observed in silicon-containing diamond and has been correlated with (Si-V)^0 [201, 214, 215]. Nevertheless, the optical analogue of the (Si-V)^0 centre has not yet been unambiguously determined.

Another EPR-active defect frequently observed in silicon-doped diamond is the KUL3 centre, characterised by monoclinic-I (C_{1h}) symmetry and $S = \frac{1}{2}$ [82, 212, 213]. In addition to ^{29}Si hyperfine splitting, indicating the involvement of silicon, further splitting due to an $I = \frac{1}{2}$ nucleus with 100% abundance was apparent [212]. On account of the profusion of hydrogen present in the CVD synthesis environment it was suggested that the nucleus in question was hydrogen [212]. Goss *et al.* had predicted a structure for a (Si-V) complex decorated by a hydrogen atom, where the hydrogen atom is located in a bond-centred position between the (Si-V) unit and a nearest-neighbour carbon atom [209]. In its neutral charge state the centre, (Si-V:H)^0, should have an effective spin $S = 1$, rendering it EPR-active [209]. Edmonds *et al.* were able to conclusively assign KUL3 to (Si-V:H)^0 by the determination of accurate ^{29}Si and ^{1}H hyperfine parameters which agreed with those predicted by Goss *et al.* [82, 209].

Further discussion of the silicon-vacancy complexes and their properties can be found in Chapters 5–7.

2.2.4.2 Substitutional silicon

The ability to create (Si-V) centres by irradiation and annealing methods indicates that alternative forms of silicon must have been present in the as-grown

material. Furthermore, secondary ion mass spectroscopy (SIMS) measurements on silicon-doped CVD diamond has demonstrated that the detected $(\text{Si-V})^{(0/-)}$ and $(\text{Si-V:H})^0$ concentrations do not account for the total silicon content [81, 82]. Various theoretical calculations suggest that silicon may incorporate substitutionally (Si_s) into diamond [197, 206, 209, 216], being stable only in its neutral charge state, Si_s^0 [206].

Si_s will distort the lattice, occupying a volume which otherwise would contain 1.6 ± 0.5 host atoms [206, 216]. The Si–C bonds are predicted to have a length of ~ 1.71 Å, which is 12% longer than an undistorted C–C bond in diamond, yet 9% shorter than a bond in cubic silicon carbide [209]. Due to the lattice dilation it might be possible to detect an increase in the lattice constant of a heavily silicon-doped sample, compared to an ideal crystal structure [209].

Direct detection of Si_s^0 is complicated by the prediction that it is EPR-inactive, invisible to electronic-optical spectroscopy, and electrically indistinguishable from the host [209]. Nonetheless, an extensive theoretical modelling study carried out by Goss *et al.* indicates that the centre is IR-active, producing several T_2 modes of vibration [209]. A mode has been proposed at $1333\,\text{cm}^{-1}$ [209], in good agreement with a peak observed at $1338\,\text{cm}^{-1}$ in silicon doped material [217]. However, this line has not yet been correlated with silicon content in diamond. Furthermore, silicon isotope substitution experiments may not be able to establish whether the line is silicon related since calculations suggest that the motion of the vibration will be mainly localised on the neighbouring atoms [209]. Another T_2 mode of vibration has been predicted to exist around $430\,\text{cm}^{-1}$ [209]. Unlike the $1333\,\text{cm}^{-1}$ line, the vibration is thought to be partly localised on the silicon atom, and an isotopic shift of $\sim 3\,\text{cm}^{-1}$ has been predicted if ^{28}Si is replaced by either ^{29}Si or ^{30}Si [209]. These line positions should mainly be considered to be guides in the search for an IR-feature for Si_s^0 around the one-phonon maximum; the approach used by Goss *et al.* was unable to predict precise line positions [209]. Hence, detailed experimental investigations are necessary to rule out a simply fortuitous agreement between theoretical and observed peak positions.

The formation of silicon aggregates and silicon interstitial defects was also considered in the study Goss *et al.* [209], who concluded that both structures are

highly unlikely to form or remain stable in diamond.

References

[1] S. Tennant, Philos.T. R. Soc. Lond. **87**, 123 (1797).

[2] J. E. Hannay, Proc. Roy. Soc. Lond. **30**, 188 (1880).

[3] H. Moissan, C. R. Acad. Sci., Paris, **118**, 320 (1894).

[4] H. Moissan, C. R. Acad. Sci., Paris, **123**, 206 (1896).

[5] H. Moissan, C. R. Acad. Sci., Paris, **123**, 210 (1896).

[6] C. A. Parsons, Proc. R. Soc. Lond. A **79**, 532 (1907).

[7] C. A. Parsons, Phil. Trans. R. Soc. Lond. A **220**, 67 (1920).

[8] P. W. Bridgman, J. Chem. Phys. **15**, 92 (1947).

[9] G. Davies and T. Evans, Proc. R. Soc. Lond. A **328**, 413 (1972).

[10] R. C. Burns and G. J. Davies, in *The Properties of Natural and Synthetic Diamond*, edited by J. E. Field (Academic Press, London, 1992), chap. 10, pp. 395–422.

[11] F. P. Bundy, H. T. Hall, H. M. Strong, and R. H. Wentorf, Nature **176**, 51 (1955).

[12] H. P. Bovenkerk, F. P. Bundy, H. T. Hall, H. M. Strong, and R. H. Wentorf, Nature **184**, 1094 (1959).

[13] C. M. Welbourn, M. Cooper, and P. M. Spear, Gems. Gemol. **32**, 156 (1996).

[14] R. H. J. Wentorf, J. Phys. Chem. **69**, 3063 (1965).

[15] E. M. Yakovlev, O. A. Voronov, and A. V. Rakhamina, Sverkhtverdye Materialy **6**, 8 (1984).

[16] E. M. Yakovlev, O. A. Voronov, and A. V. Rakhamina, Sverkhtverdye Materialy **9**, 3 (1987).

[17] G. Muncke, in *The Properties of Diamond*, edited by J. E. Field (Academic Press, London, 1979), chap. 15, pp. 473–499.

[18] R. J. Wedlake, in *The Properties of Diamond*, edited by J. E. Field (Academic Press, London, 1979), chap. 16, pp. 501–535.

[19] H. M. Strong, Am. J. Phys. **57**, 794 (1989).

[20] I. Sunagawa, J. Cryst. Growth **1977**, 214 (1977).

[21] I. Sunagawa, in *Materials Science of the Earth's Interior*, edited by I. Sunagawa (Terra, Tokyo, 1984), p. 303.

[22] H. Kanda, T. Ohsawa, O. Fukunaga, and I. Sunagawa, J. Cryst. Growth **94**, 115 (1989).

[23] H. M. Strong and R. M. Chrenko, J. Phys. Chem. **75**, 1838 (1971).

[24] M.-L. T. Rooney, J. Cryst. Growth **116**, 15 (1992).

[25] R. C. Burns, J. O. Hansen, R. A. Spits, M. Sibanda, C. M. Welbourn, and D. L. Welch, Diam. Relat. Mater. **8**, 1433 (1999).

[26] R. M. Chrenko, H. M. Strong, and R. E. Tuft, Philos. Mag. **23**, 313 (1971).

[27] R. M. Chrenko, R. E. Truft, and H. M. Strong, Nature **270**, 141 (1977).

[28] R. C. Burns, S. Kessler, M. Sibanda, C. M. Welbourn, and D. L. Welch, Proc. 3rd NIRIM Int. Symp. Advanced Materials pp. 105–111 (1996).

[29] R. C. Burns, V. Cvetkovic, C. N. Dodge, D. J. F. Evans, M.-L. T. Ronney, P. M. Spear, and C. M. Welbourn, J. Cryst. Growth **104**, 257 (1990).

[30] R. H. J. Wentorf, J. Phys. Chem. **75**, 1833 (1971).

[31] C. V. H. Strömann, F. Tshisikhawe, O. J. Hansen, and R. C. Burns, *Synthesis of diamond*, International Patent WO2006061672 (2006).

[32] S. Liggins, Ph.D. thesis, University of Warwick (2011).

[33] D. M. Gruen, X. Pan, A. R. Krauss, S. Liu, and C. M. Luo, J. amd Foster, J. Vac. Sci. Technol. A **12**, 1491 (1994).

[34] D. M. Gruen, Annu. Rev. Mater. Sci. **29**, 211 (1999).

[35] J. E. Butler and A. V. Sumat, Chem. Vapor. Depos. **14**, 145 (2008).
[36] T. P. Ong and R. P. H. Chang, Appl. Phys. Lett. **55**, 2063 (1989).
[37] H. Windischmann and G. F. Epps, J. Appl. Phys. **68**, 5665 (1990).
[38] K. J. Gray and H. Windischmann, Diam. Relat. Mater. **8**, 903 (1999).
[39] W. Wang, T. Moses, R. C. Linares, J. E. Shigley, M. Hall, and J. E. Butler, Gems. Gemol. **39**, 268 (2003).
[40] C. S. Yan, Y. K. Vohra, H. K. Mao, and R. J. Hemley, P. Nat. Acad. Sci. USA **99**, 12523 (2002).
[41] G. Bogdan, K. De Court, W. Deferme, K. Haenens, and M. Nesládek, Phys. Status Solidi a **203**, 3063 (2006).
[42] W. G. Eversole and N. Y. Kenmore, *Synthesis of diamond*, US Patent 3030187 (1962).
[43] W. G. Eversole and N. Y. Kenmore, *Synthesis of diamond*, US Patent 3030188 (1962).
[44] J. C. Angus, H. A. Will, and W. S. Stanko, J. Appl. Phys. **1968**, 2915 (39).
[45] P. W. May, Phil. Trans. R. Soc. Lond. A **358**, 473 (2000).
[46] J. E. Butler, Y. A. Mankelevich, A. Cheesman, J. Ma, and M. N. R. Ashfold, J. Phys.- Condens. Mat. **21**, 364201 (2009).
[47] J. E. Butler and R. L. Woodin, Phil. Trans. R. Soc. Lond. A **342**, 209 (1993).
[48] J. C. Angus and C. C. Hayman, Science **241**, 913 (1988).
[49] J. C. Angus, A. Argoita, R. Gat, Z. Li, M. Sunkara, L. Wang, and Y. Wang, Philos. T. R. Soc. A **342**, 195 (1993).
[50] J. E. Butler and H. Windischmann, MRS Bulletin (USA) **23**, 22 (1998).
[51] A. Argoitia, C. S. Kovach, and J. Angus, in *Handbook of Industrial Diamonds and Diamond Films*, edited by M. A. Prelas, G. Popovici, and L. K. Bigelow (Marcel Dekker, New York, 1998), chap. 20, pp. 797–819.
[52] S. L. Girshick, in *Handbook of Industrial Diamonds and Diamond Films*, edited by M. A. Prelas, G. Popovici, and L. K. Bigelow (Marcel Dekker, New York, 1998), chap. 22, pp. 851–864.
[53] M. A. Cappelli, in *Handbook of Industrial Diamonds and Diamond Films*, edited by M. A. Prelas, G. Popovici, and L. K. Bigelow (Marcel Dekker, New York, 1998), chap. 23, pp. 865–886.
[54] T. A. Railkar, W. P. Kang, H. Windischmann, A. P. Malshe, H. A. Naseem, J. L. Davidson, and W. D. Brown, in *Critical Reviews in Solid State and Materials Sciences* (Taylor & Francis, 2000).
[55] P. K. Bachmann, in *Handbook of Industrial Diamonds and Diamond Films*, edited by M. A. Prelas, G. Popovici, and L. K. Bigelow (Marcel Dekker, New York, 1998), chap. 21, pp. 821–850.
[56] P. M. Martineau, S. C. Lawson, A. J. Taylor, S. J. Quinn, D. J. F. Evans, and M. J. Croder, Gems. Gemol. **40**, 2 (2004).
[57] M. Kamo, Y. Sato, S. Matsumoto, and N. Setaka, J. Cryst. Growth **62**, 642 (1983).
[58] L. F. Sutcu, C. J. Chu, M. S. Thompson, R. H. Hauge, J. L. Margrave, and M. P. D'Evelyn, J. Appl. Phys. **71**, 5930 (1992).
[59] C. Findeling-Dufour, A. Vignes, and Gicquel, Diam. Relat. Mater. **4**, 429 (1995).
[60] F. Silva, J. Achard, X. Bonnin, A. Michau, A. Secroun, K. De Corte, S. Felton, M. Newton, and A. Gicquel, Diam. Relat. Mater. **17**, 1067 (2008).
[61] J. Achard, A. Tallaire, R. Sussman, F. Silva, and A. Gicquel, J. Cryst. Growth **284**, 396 (2005).
[62] F. Silva, J. Achard, X. Bonnin, A. Michau, A. Tallaire, O. Brinza, and A. Gicquel,

Phys. Status Solidi a **203**, 3049 (2006).
[63] H. Watanabe, D. Takeuchi, S. Yamanaka, H. Okushi, K. Kajimura, and T. Sekiguchi, Diam. Relat. Mater. **8**, 1272 (1999).
[64] H. Okushi, Diam. Relat. Mater. **10**, 281 (2001).
[65] H. Okushi, H. Watanabe, R. S., S. Yamanaka, and D. Takeuchi, J. Cryst. Growth **237-239**, 1269 (2002).
[66] M. Kasu and N. Kobayashi, Diam. Relat. Mater. **12**, 413 (2003).
[67] T. Teraji and T. Ito, J. Cryst. Growth **271**, 409 (2004).
[68] A. Tallaire, J. Achard, F. Silva, R. S. Sussmann, and A. Gicquel, Diam. Relat. Mater. **14**, 249 (2005).
[69] L. Bergman, M. T. McClure, J. T. Glass, and R. J. Nemanich, J. Appl. Phys. **76**, 3020 (1994).
[70] R. Samlenski, C. Haug, R. Brenn, C. Wild, R. Locher, and P. Koidl, Appl. Phys. Lett. **67**, 2798 (1995).
[71] A. Tallaire, A. T. Collins, D. Charles, J. Achard, R. Sussmann, A. Gicquel, M. E. Newton, A. M. Edmonds, and R. J. Cruddace, Diam. Relat. Mater. **15**, 1700 (2006).
[72] A. Secroun, A. Tallaire, J. Achard, G. Civrac, H. Schneider, and A. Gicquel, Diam. Relat. Mater. **16**, 953 (2007).
[73] A. Secroun, P. Brinza, A. Tardieu, J. Achard, F. Silva, X. Bonnin, K. De Corte, A. Anthonis, M. E. Newton, J. Ristein, et al., Phys. Status Solidi A **204**, 4298 (2007).
[74] B. L. Cann, Ph.D. thesis, University of Warwick (2009).
[75] S. Jin and T. D. Moustakas, Appl. Phys. Lett. **65**, 403 (1994).
[76] G. Z. Cao, J. J. Chermer, J. P. van Exkenvort, W. A. L. M. Elst, and L. J. Giling, J. App. Phys. **79**, 1357 (1996).
[77] W. Müller-Sebert, E. Wörner, F. Fuchs, C. Wild, and P. Koidl, Appl. Phys. Lett. **68**, 759 (1996).
[78] J. Barjon, E. Rzepka, F. Jomard, J. M. Laroche, D. Ballutaud, T. Kociniewski, and J. Chevallier, Phys. Status Solidi A **202**, 2177 (2005).
[79] L. H. Robins, L. P. Cook, E. N. Farabaugh, and A. Feldman, Phys. Rev. B **39**, 13367 (1989).
[80] S. D. Williams, D. J. Twitchen, P. M. Martineau, G. A. Scarsbrook, and I. Friel, *High colour diamond*, UK Patent GB2428690 B (2010).
[81] A. M. Edmonds, Ph.D. thesis, University of Warwick (2008).
[82] A. M. Edmonds, M. E. Newton, P. M. Martineau, D. J. Twitchen, and S. D. Williams, Phys. Rev. B **77**, 245205 (2008).
[83] G. A. Scarsbrook, P. M. Martineau, T. D. J., A. J. Whitehead, and M. A. Cooper, *Boron doped diamond*, International Patent WO03052174 (2003).
[84] S. Koizumi, M. Kamo, Y. Sato, H. Ozaki, and T. Inuzuka, Appl. Phys. Lett. **71**, 1065 (1997).
[85] Y. Liou, A. Inspektor, R. Weimer, D. Knight, and R. Messier, J. Mater. Res. **5**, 2305 (1990).
[86] S. Kapoor, M. A. Kelly, and S. B. Hagström, J. Appl. Phys. **77**, 6267 (1995).
[87] C. D. Clark, R. W. Ditchburn, and H. B. Dyer, Proc. Soc. London, Ser. A **237**, 75 (1956).
[88] C. D. Clark, R. W. Ditchburn, and Dyer, Proc. R. Soc. A **234**, 363 (1956).
[89] C. D. Clark, P. J. Kemmey, and E. W. J. Mitchell, Discuss. Faraday Soc. **31**, 96 (1961).

[90] C. A. Coulson and M. J. Kearsley, Proc. R. Soc. Lond. A **241**, 433 (1957).
[91] T. Yamaguchi, J. Phys. Soc. Jpn. **17**, 1359 (1962).
[92] C. A. Coulson and F. Larkins, J. Phys. Chem. Solids **32**, 2245 (1971).
[93] F. P. Larkins, J. Phys. Chem. Solids **32**, 2123 (1971).
[94] C. D. Clark and J. Walker, Proc. R. Soc. L **334**, 241 (1973).
[95] Lowther, J. Phys. C Solid State **8**, 3448 (1975).
[96] Stoneham, Solid State **21**, 339 (1977).
[97] J. Walker, L. A. Vermeulen, and C. D. Clark, Proc. R **341**, 253 (1974).
[98] C. Foy and G. Davies, J. Phys. C: Solid State **13**, L25 (1980).
[99] A. T. Collins, J. Phys. C Solid State **14**, 289 (1981).
[100] J. A. van Wyk, O. D. Tucker, M. E. Newton, J. M. Baker, G. S. Woods, and P. Spear, Phys. Rev. B **52**, 12657 (1995).
[101] G. Davies, S. C. Lawson, A. T. Collins, A. Mainwood, and S. J. Sharp, Phys. Rev. B **46**, 13157 (1992).
[102] G. Davies and E. C. Lightowlers, J. Phys. C Solid State **3**, 638 (1970).
[103] J. Isoya, H. Kanda, Y. Uchida, S. C. Lawson, S. Yamasaki, H. Itoh, and Y. Morita, Phys. Rev. B **45**, 1436 (1992).
[104] P. Pringsheim and R. C. Voreck, Z. Phys. **133**, 2 (1952).
[105] H. B. Dyer and L. D. du Preez, J. Chem. Phys. **42**, 1898 (1965).
[106] G. Davies, Nature **269**, 498 (1977).
[107] D. J. Twitchen, D. C. Hynt, V. Smart, M. E. Newton, and J. M. Baker, Diam. Relat. Mater. **8**, 1572 (1999).
[108] R. G. Farrer and L. A. Vermeule, J. Phys. C: Solid State **5**, 2762 (1972).
[109] C. A. Coulson and F. P. Larkins, J. Phys. Chem. Solids **30**, 1963 (1969).
[110] D. J. Twitchen, M. E. Newton, J. M. Baker, T. R. Anthony, and W. F. Banholzer, Phys. Rev. B **59**, 12900 (1999).
[111] M. A. Lea-Wilson, J. N. Lower, and J. A. van Wyk, Philos. Mag. B **72**, 81 (1995).
[112] L. S. Hounsome, R. Jones, P. M. Martineau, M. J. Shaw, P. R. Briddon, S. Öberg, A. T. Blumenau, and N. Fujita, Phys. Status Solidi A **202**, 2182 (2005).
[113] L. S. Hounsome, R. Jones, P. M. Martineau, D. Fisher, M. J. Shaw, P. R. Briddon, and S. Oberg, Phys. Rev. B **73**, 125203 (2006).
[114] L. S. Hounsome, R. Jones, P. M. Martineau, D. Fisher, M. J. Shaw, P. R. Briddon, and S. berg, Phys. Status Solidi C **4**, 2950 (2007).
[115] A. T. Collins, J. Phys. C: Solid State **13**, 2641 (1980).
[116] R. C. Burns, D. Fisher, and R. A. Spits, *High temperature/high pressure colour change of diamond*, International Patent WO0172406 (2004).
[117] A. Pu, T. Bretagahnon, D. Kerr, and Dannefaer, Diam. Relat. Mater. **9**, 1450 (2000).
[118] V. Avalos and S. Dannefaer, Physica B **340**, 76 (2003).
[119] J. M. Mäki, F. Tuomisto, C. Kelly, D. Fisher, and P. Martineau, Physica B **401**, 613 (2007).
[120] U. Bangert, R. Barnes, M. H. Gass, A. L. Bleloch, and I. S. Godfrey, J. Phys.-Condens. Mat. **21**, 364208 (2009).
[121] D. J. Twitchen, P. M. Martineau, and G. A. Scarsbrook, *Coloured diamond*, International Patent WO20040202821 (2004).
[122] B. Dischler, C. Wild, W. Müller-Sebert, and P. Koidl, Physica B **185**, 217 (1993).
[123] J. P. Goss, J. Phys.-Condens. Mat. **15**, R551 (2003).
[124] R. M. Chrenko, R. McDonald, and K. A. Darrow, Nature **213**, 474 (1967).
[125] W. A. Runciman and T. Carter, Solid State Commun. **9**, 315 (1971).

[126] G. S. Woods and A. T. Collins, J. Phys. Chem. Solids **44**, 471 (1983).
[127] F. De Weerdt and I. N. Kupriyanov, Diam. Relat. Mater. **11**, 714 (2002).
[128] R. Zeisel, C. E. Nebel, and M. Stutzmann, Appl. Phys. Lett. **74**, 1875 (1999).
[129] J. Chevallier, L. A., D. Ballutaud, B. Theys, F. Jomard, A. Deneuville, M. Bernard, E. Gheeraert, and E. Bustarret, Diam. Relat. Mater. **10**, 399 (2001).
[130] I. Kiflawi, D. Fisher, H. Kanda, and G. Sittas, Diam. Relat. Mater. **5**, 1516 (1996).
[131] W. Kindlein, R. Livi, N. M. Balzarettu, and J. A. H. da Jornada, Diamond and Related Materials **9**, 22 (2000).
[132] E. Holzschuh, W. Kündig, P. F. Meier, and B. D. Patterson, Phys. Rev. A **25**, 1272 (1982).
[133] S. F. J. Cox and M. C. R. Symons, Chem. Phys. Lett. **126**, 516 (1986).
[134] T. A. Claxton, A. Evans, and M. C. R. Symons, J. Chem. Soc., Faraday Trans. 2 **82**, 2031 (1986).
[135] T. L. Estle, S. Estreicher, and D. S. Marynick, Hyperfine Interactions **32**, 637 (1986).
[136] J. Chevallier, F. Jomard, Z. Teukam, S. Koisumi, H. Kanda, Y. Sato, A. Deneuville, and M. Bernard, Diamond and Related Materials **11**, 1566 (2002).
[137] R. Cruddace, Ph.D. thesis, University of Warwick (2007).
[138] G. Davies, A. T. Collins, and P. Spear, Solid State Commun. **49**, 433 (1984).
[139] J. P. Goss, R. Jones, M. I. Heggie, C. P. Eweis, P. R. Briddon, and Öberg, Phys. Rev. B **65**, 115207 (2002).
[140] I. Watanabe and K. Sugata, Jpn. J. Appl. Phys. **27**, 1808 (1988).
[141] J. Jia, H. an Shinar, L. D. P., and M. Pruski, Phys. Rev. B **48**, 17595 (1993).
[142] S. L. Holder, L. G. Rowan, and J. J. Krebs, Appl. Phys. Lett. **64**, 1091 (1994).
[143] X. Zhou, G. D. Watkins, K. M. McNamara Rutledge, R. P. Messmer, and S. Chawla, Phys. Rev. B **54**, 7881 (1996).
[144] D. F. Talbot-Ponsonby, M. E. Newton, J. M. Baker, G. A. Scarsbrook, R. S. Sussmann, A. J. Whitehead, and S. Pfenninger, Phys. Rev. B **57**, 2264 (1998).
[145] S. V. Nistor, M. Stefan, V. Ralchenko, A. Khomich, and D. Schoemaker, J. Appl. Phys. **87**, 8741 (2000).
[146] K. Iakoubovskii, A. Stesmans, K. Suzuki, A. Sawabe, and T. Yamada, Phys. Rev. B **66**, 113203 (2002).
[147] C. Glover, M. E. Newton, P. M. Martineau, S. Quinn, and D. J. Twitchen, Phys. Rev. Lett. **92**, 135502 (2004).
[148] M. J. Shaw, P. R. Briddon, J. P. Goss, M. J. Rayson, A. Kerridge, A. H. Harker, and A. M. Stoneham, Phys. Rev. Lett. **95**, 105502 (2005).
[149] M. J. Shaw, P. R. Briddon, J. P. Goss, M. J. Rayson, A. Kerridge, A. H. Harker, and A. M. Stoneham, Phys. Rev. Lett. **95** (2005).
[150] Davies, in *Chemistry and Physics of Carbon*, edited by P. L. Walker and P. A. Thrower (Marcel Dekker, New York, 1977), vol. 13, pp. 1–143.
[151] G. Davies, J. Phys. C: Solid State **9**, L537 (1976).
[152] G. Davies, Nature **290**, 40 (1981).
[153] W. Kaiser and W. L. Bond, Phys. Rev. **115**, 857 (1959).
[154] O. D. Tucker, M. E. Newton, and J. M. Baker, Phys. Rev. B **50**, 15586 (1994).
[155] A. T. Collins, J. Phys. C Solid State **11**, L417 (1978).
[156] R. Jones and J. P. Goss, in *Properties, Growth and Applications of Diamond*, edited by M. H. Nazaré and A. J. Neves (INSPEC, London, 2001), no. 26 in EMIS Datareview Series, pp. 127–129.
[157] G. S. Woods, in *Properties and Growth of Diamond*, edited by G. Davies (INSPEC,

London, 1994), no. 9 in EMIS Datareview Series, pp. 98–100.
[158] B. Walter, Ann. Phys. Chem. **45**, 505 (1891).
[159] C. D. Clark, G. W. Maycraft, and E. W. Mitchell, J. Appl. Phys. **33**, 378 (1962).
[160] W. V. Smith, I. L. Gelles, and P. P. Sorokin, Phys. Rev. Lett. **2**, 39 (1959).
[161] J. H. N. Loubser and A. C. Wright, Diamond Research pp. 16–20 (1973).
[162] G. Davies, C. M. Welbourn, and J. H. N. Loubser, Diamond Research pp. 23–30 (1978).
[163] J. A. van Wyk, J. Phys. C Solid State **15**, L981 (1982).
[164] J. A. van Wyk and J. H. N. Loubser, J. Phys.-Condens. Mat. **5**, 3019 (1993).
[165] I. Kiflawi and S. C. Lawson, in *Properties, Growth and Applications of Diamond*, edited by M. H. Nazaré and A. J. Neves (INSPEC, London, 2001), no. 26 in EMIS Datareview Series, pp. 130–133.
[166] W. Smith, P. P. Sorokin, I. L. Gelles, and G. J. Lasher, Phys. Rev. **115**, 1546 (1959).
[167] P. R. Briddon and R. Jones, Physica B **185**, 179 (1993).
[168] A. Cox, M. E. Newton, and J. M. Baker, J. Phys.- Condens. Mat. **6**, 551 (1994).
[169] R. P. Messmer and G. D. Watkins, Phys. Rev. B **7**, 2568 (1973).
[170] J. H. N. Loubser and W. P. v. Ryneveld, Brit. J. Appl. Phys. **18**, 1029 (1967).
[171] G. B. Bachelet, G. A. Baraff, and Schlüter, Phys. Rev. B **24**, 4736 (1981).
[172] S. A. Kajihara, A. Antonelli, and J. Bernholc, Phys. Rev. Lett. **66**, 2010 (1991).
[173] R. G. Farrer, Solid State Commun. **7**, 685 (1969).
[174] J. Koppitz, O. F. Schirmer, and M. Seal, J. Phys. C Solid State **19**, 1123 (1986).
[175] H. B. Dyer, F. A. Raal, L. Du Preez, and J. H. N. Loubser, Philos. Mag. **11**, 763 (1965).
[176] A. T. Collins, M. Stanley, and G. S. Woods, J. Phys. D Appl. Phys. **20**, 969 (1987).
[177] G. S. Woods, J. A. van Wyk, and A. T. Collins, Philos. Mag. B **62**, 589 (1990).
[178] S. C. Lawson, D. Fisher, D. C. Hunt, and M. E. Newton, J. Phys.- Condens. Mat. **10**, 6171 (1998).
[179] M. E. Newton, in *Properties, Growth and Applcations of Diamond*, edited by M. H. Nazaré and A. J. Neves (INSPEC, London, 2001), no. 26 in EMIS Datareview Series, pp. 136–141.
[180] A. T. Collins, J. Phys.-Condens. Mat. **14**, 3743 (2002).
[181] A. M. Edmonds, U. F. S. D'Haenens-Johansson, R. J. Cruddace, M. E. Newton, K.-M. C. Fu, C. Santori, R. U. A. Khan, P. M. Martineau, D. J. Twitchen, and M. Markham, submitted to Nature Materials.
[182] L. du Preez, Ph.D. thesis, University of Witwatersrand (1965).
[183] G. Davies and M. F. Hamer, Proc. R. Soc. Lond. A **348**, 285 (1976).
[184] J. H. N. Loubser and J. A. van Wyk, Diamond Research **11**, 11 (1977).
[185] N. R. S. Reddy, N. B. Manson, and E. R. Krausz, J. Lumin. **38**, 46 (1987).
[186] D. A. Redman, S. Brown, R. H. Sands, and S. C. Rand, Phys. Rev. Lett. **67**, 3420 (1991).
[187] A. T. Collins and S. C. Lawson, J. Phys.- Condens. Mat. **1**, 6929 (1989).
[188] G. Davies, J. Phys. C: Solid State **12**, 2551 (1979).
[189] Y. Mita, Phys. Rev. B **53**, 11360 (1996).
[190] T. A. Kennedy, J. S. Colton, J. E. Butler, R. C. Linares, and P. J. Doering, Appl. Phys. Lett. **83**, 4190 (2003).
[191] C. Glover, M. E. Newton, P. Martineau, D. J. Twitchen, and J. M. Baker, Phys. Rev. Lett. **90**, 185507 (2003).

[192] A. Kerridge, A. H. Harker, and A. M. Stoneham, J. Phys.- Condens. Mat. **16**, 8743 (2004).

[193] A. M. Edmonds, M. E. Newton, P. M. Martineau, and D. J. Twitchen, in *The 60th Diamond Conference Abstract Book* (2009), p. P21.

[194] F. Fuchs, C. Wild, K. Schwarz, and P. Koidl, Diamond and Related Materials **4**, 652 (1995).

[195] R. U. A. Khan, P. M. Martineau, B. L. Cann, M. E. Newton, H. K. Dhillon, and D. J. Twitchen, Gems. Gemol. **46**, 18 (2010).

[196] R. U. A. Khan, P. M. Martineau, B. L. Cann, M. E. Newton, and D. J. Twitchen, J. Phys.- Condens. Mat. **21**, 6171 (2009).

[197] P. Bicai and X. Shangda, Phys. Rev. B **49**, 11444 (1994).

[198] S. M. Hong, H. Kanda, and G. Li, Chin. Sci. Bull. **41**, 208 (1996).

[199] C. D. Clark, H. Kanda, I. Kiflawi, and G. Sittas, Phys. Rev. B **51**, 16681 (1995).

[200] V. S. Vavilov, A. A. Gippus, A. M. Zaitsev, B. V. Deryagin, B. V. Spitsyn, and A. E. Aleksenko, Sov. Phys. Semiconduct. **14**, 1078 (1980).

[201] C. M. Breeding and W. Wang, Diam. Relat. Mater. **17**, 1335 (2008).

[202] J. P. Goss, R. Jones, S. J. Breuer, P. R. Briddon, and S. Öberg, Phys. Rev. Lett. **77**, 3041 (1996).

[203] C. D. Clark and C. B. Dickerson, Surf. Coat. Tech. **47**, 336 (1991).

[204] A. T. Collins, L. Allers, C. J. Wort, and G. A. Scarsbrook, Diam. Relat. Mater. **3**, 932 (1994).

[205] B. J. Masters, Solid State Comm. **9**, 283 (1971).

[206] J. P. Goss, P. R. Briddon, M. J. Rayson, S. J. Sque, and R. Jones, Phys. Rev. B **72**, 035214 (2005).

[207] S. W. Brown and S. C. Rand, J. Appl. Phys. **78**, 4069 (1995).

[208] H. Sternschulte, K. Thonke, J. Gerster, W. Limmer, R. Sauer, J. Spitzer, and P. C. Mnzinger, Diam. Relat. Mater. **4**, 1189 (1995).

[209] J. P. Goss, P. R. Briddon, and M. J. Shaw, Phys. Rev. B **76**, 075204 (2007).

[210] K. Iakoubovskii and A. Stesmans, Phys. Rev. B **66**, 195207 (2002).

[211] K. Iakoubovskii, A. Stesmans, M. Nésladek, and G. Knuyt, Phys. Status Solidi A **193**, 448 (2002).

[212] K. Iakoubovskii and A. Stesmans, Phys. Status Solidi a **186**, 199 (2001).

[213] K. Iakoubovskii, A. Stesmans, K. Suzuki, J. Kuwabara, and A. Sawabe, Diam. Relat. Mater. **12**, 511 (2003).

[214] L. Allers and A. T. Collins, J. Appl. Phys. **77**, 3879 (1995).

[215] D. J. F. Evans, C. F. Kelly, P. Leno, P. M. Martineau, and A. J. Taylor, in *The 57th Diamond Conference* (2006), p. 38.

[216] J. P. Goss, P. R. Briddon, M. J. Rayson, S. J. Sque, and R. Jones, Phys. Rev. B **73**, 199904 (pages 1) (2006).

[217] P. M. Martineau, *private communication* (2007).

Chapter 3

Theory

3.1 Electron Paramagnetic Resonance

Electron paramagnetic resonance (EPR) is a powerful tool for identifying paramagnetic defects in crystalline solids by exploiting the interaction of electromagnetic radiation with the magnetic moments of electrons. Point defects will often have an even number of electrons which are paired with their spins antiparallel to each other, resulting in diamagnetic, rather than paramagnetic, behaviour. In order for a defect to be paramagnetic it has to contain one or more unpaired electrons, resulting in a net spin moment. The strength of the EPR signal for a centre in a specimen enables the determination of the defect concentration since the signal intensity is directly proportional to the number of spins of that species in the sample. Furthermore, EPR can be used to establish the symmetry and environment of the detected spins.

3.1.1 The magnetic moment of an electron

A magnetic dipole is produced by a classical particle with mass m and charge q, rotating about a point in a circular path with radius r at a speed v. The motion of the charged particle will result in an effective electrical current i which gives rise to a point magnetic dipole with a magnetic moment $\boldsymbol{\mu}_d$. $|\boldsymbol{\mu}_d|$ is equal to iA, where A is the area enclosed by the orbiting charge, and the dipole moment is normal to the plane where the rotation takes place. i is given by $qv/2\pi r$. The magnitude of the magnetic moment for an electron with mass m_e and charge $-e$ is thus [1]

$$|\boldsymbol{\mu}_d| = iA = \frac{ev\pi r^2}{2\pi r} = \frac{em_e vr}{2m_e} \tag{3-1}$$

where $m_e vr$ is the magnitude of the total orbital angular momentum of the electron about the axis of rotation.

Quantum mechanically, the orbital angular momentum, represented by the operator $\hat{\mathbf{L}}$, is quantised and can be expressed as an integer multiple of $\hbar$, the reduced Planck's constant. Each multiple has an orbital magnetic moment of magnitude $\beta_e = |\gamma_e \hbar|$, where γ_e is the gyromagnetic ratio. However, electrons also posses an intrinsic property known as spin angular momentum (commonly referred to as *spin*), with an operator $\hat{\mathbf{S}}$, which also gives rise to a magnetic moment. The total angular momentum $\hat{\mathbf{J}}$ is thus given by $\hat{\mathbf{J}} = \hat{\mathbf{L}} + \hat{\mathbf{S}}$ and Eq. 3-1 can be rewritten as [1]

$$\hat{\boldsymbol{\mu}} = \gamma_e \hbar \hat{\mathbf{J}} \tag{3-2}$$

where $\hat{\boldsymbol{\mu}}$ is the quantum mechanical operator for the magnetic moment. For an electron in an s-orbital $|\hat{\mathbf{L}}| = 0$, so $\hat{\mathbf{J}} = \hat{\mathbf{S}}$. Then

$$\hat{\boldsymbol{\mu}} = -\frac{e\hbar}{2m_e c} g_e \hat{\mathbf{S}} = -g_e \mu_B \hat{\mathbf{S}} \tag{3-3}$$

where μ_B is the Bohr magneton and g_e is the free-electron Zeeman (correction) factor. The value for g_e has been determined to be $g_e = 2.0023193043617(15)$ [2].

3.1.2 Electron spin and resonance conditions

Classically the energy E of a magnetic moment in a magnetic field $\mathbf{B}$ is given by

$$E = -\hat{\boldsymbol{\mu}} \cdot \mathbf{B} = -\mu B \cos\theta \tag{3-4}$$

where θ is the angle between $\hat{\boldsymbol{\mu}}$ and $\mathbf{B}$. The minimum energy $-|\mu B|$ occurs when $\hat{\boldsymbol{\mu}}$ is parallel to $\mathbf{B}$ and $\theta = 0$; the maximum energy $+|\mu B|$ occurs when $\hat{\boldsymbol{\mu}}$ is antiparallel to $\mathbf{B}$ and $\theta = \pi$. Quantum mechanically a system with one unpaired electron and no orbital momentum contribution will be described by the *Hamiltonian* [1]

$$\mathscr{H} = -\hat{\boldsymbol{\mu}} \cdot \mathbf{B} = g\mu_B \hat{\mathbf{S}} \cdot \mathbf{B} \tag{3-5}$$

where g is the g-factor, which is a dimensionless measure of the moment of the system. The energy thus depends on the spin eigenstates $|M_S\rangle$, using Dirac notation. $M_S = -S, -S+1, ..., S+1$ with a multiplicity $2S+1$ for a particle with spin S. Hence the eigenstates of an electron, which has a spin $S = 1/2$, are given by $|M_S\rangle = |\pm 1/2\rangle$. Applying the magnetic field lifts the degeneracy of the spin states of the electron, which can then be probed using EPR techniques. For a single

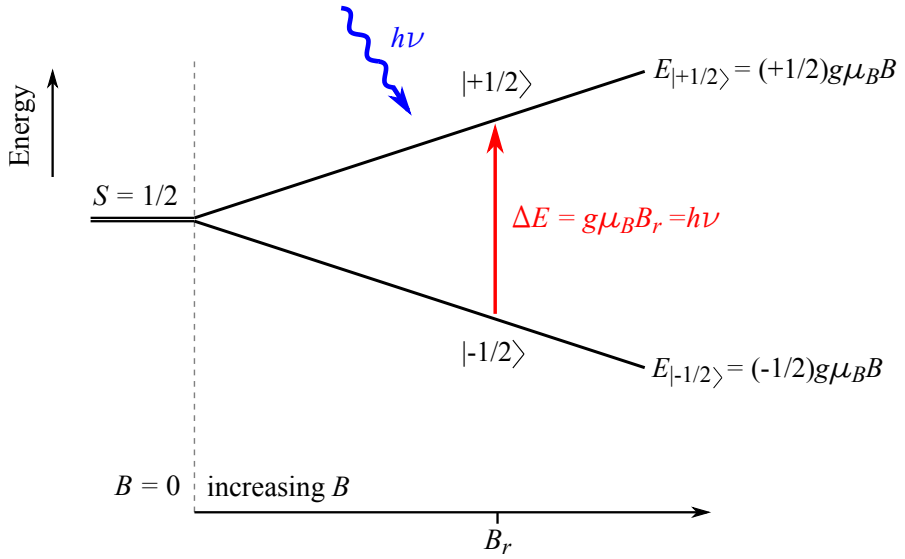

Figure 3-1: Energy levels for a single unpaired electron ($S = 1/2$) subjected to an increasing magnetic field, B. The Zeeman effect lifts the degeneracy of the $|\pm 1/2\rangle$ spin states, separating them by $\Delta E = g\mu_B B$. At resonance ($B = B_r$) ΔE is equal to the energy of the applied radiation, $h\nu$, and absorption occurs, inducing a transition between the spin states.

unpaired electron the energies of the two spin state energy levels, also known as *electronic Zeeman levels*, are $\pm\frac{1}{2}g\mu_B B$. An energy-level scheme for this spin system as a function of the applied magnetic field is illustrated in Fig. 3-1.

Magnetic dipole transitions between two Zeeman levels may be induced when the energy of a photon ($h\nu$) of the applied electromagnetic radiation is equal to the energy difference between the levels, expressed mathematically by the *resonance condition* [1]:

$$\Delta E = g\mu_B B_r = h\nu \tag{3-6}$$

where h is Planck's constant and B_r is the magnetic field at which resonance occurs. Furthermore, conservation of spin angular momentum requires that $|\Delta M_S| = 1$, even for $S > 1/2$, since the photon has one unit of angular momentum [1].

There are two approaches to detecting resonant energy absorption by a paramagnetic sample: either B is kept constant such that ΔE is fixed and ν is varied until resonant absorption can occur, or B is swept while ν remains unchanged. Experimentally the latter case is easier to achieve and consequently the continuous-wave (CW) EPR spectrometers used for this work follow that principle. They will be discussed in detail in §4.1.

If the magnetic field experienced by each spin species was simply the externally applied magnetic field the EPR spectrum would consist of a single line with $g = g_e$. However, the complexity of EPR spectra increases due to additional interactions between the unpaired electrons and the environment, resulting in shifts or further splittings of the energy levels.

3.1.3 The spin Hamiltonian

The *effective spin Hamiltonian* $\mathscr{H}$ is used to characterise a paramagnetic species by considering the separate contributions of each interaction that the *effective spin* of the system is subjected to. The effective spin is a concept used to simplify analysis, it does not need to be the actual spin of the system if there are multiple unpaired spins. For instance, a centre with two unpaired electrons (spins $s_1 = \frac{1}{2}$ and $s_2 = \frac{1}{2}$) which interact appreciably can be represented by a spin triplet ($S = 1$) and a spin singlet ($S = 0$) state, which are separated in energy. The effective spin of the system is defined by the spin which generates the multiplicity needed for the state considered. The eigenstates of the effective spin Hamiltonian are the lowest-energy eigenstates of the full Hamiltonian; using $\mathscr{H}$ further simplifies analysis. $\mathscr{H}$ is usually written as the sum of the separate Hamiltonians for the different interactions [1]:

$$\mathscr{H} = \underbrace{\mu_B \hat{\mathbf{S}} \cdot \underline{\mathbf{g}} \cdot \mathbf{B}}_{1} + \underbrace{\hat{\mathbf{S}} \cdot \underline{\mathbf{D}} \cdot \hat{\mathbf{S}}}_{2} + \sum_j [\underbrace{\hat{\mathbf{S}} \cdot \underline{\mathbf{A}}_j \cdot \hat{\mathbf{I}}_j}_{3} - \underbrace{\mu_n g_{n_j} \hat{\mathbf{I}}_j \cdot \mathbf{B}}_{4} + \underbrace{\hat{\mathbf{I}}_j \cdot \underline{\mathbf{P}}_j \cdot \hat{\mathbf{I}}_j}_{5}] + \text{higher order terms}, \tag{3-7}$$

where $\hat{\mathbf{S}}$ is the effective electron spin operator and $\hat{\mathbf{I}}_j$ is the effective nuclear spin operator for the j^{th} nuclei. The different terms are related to the following:

1. Electronic Zeeman and spin-orbit interactions
2. Zero-field (electron-electron) interaction, $S \geq 1$
3. Hyperfine interaction between electrons and nuclei, $I > 0$
4. Nuclear Zeeman interaction, $I > 0$
5. Nuclear quadrupole interaction, $I \geq 1$

The interactions and their variables will be discussed in §3.1.3.1-§3.1.3.5.

3.1.3.1 Electronic Zeeman and spin-orbit interactions

The production of Zeeman levels due to the interaction between the applied magnetic field **B** and the magnetic moment of the unpaired electrons for a system with a single unpaired electron has been introduced in §3.1.2, where the spin was associated with the free electron Zeeman factor g_e. An electron may also posses orbital angular momentum. Equation 3-3 can be generalised to include both effects, giving

$$\hat{\boldsymbol{\mu}} = -\mu_B(\hat{\mathbf{L}} + g_e\hat{\mathbf{S}}) \tag{3-8}$$

The strong covalent bonding and sp^3-hybridisation of diamond destroys the spherical symmetry of the free atom orbitals and quenches the orbital angular momentum. Therefore, to the first order the ground states of paramagnetic centres have zero orbital angular momentum and the g-factor $g \approx g_e$. However, the *spin-orbit interaction* admixes the ground state with certain excited states, removing the quenching effect and introducing a small amount of orbital angular momentum to the ground state.

The coupling between the spin and the orbital angular momentum can be described by *Russel-Saunders coupling*, where the spin-orbit interaction is treated like a perturbation and spin-spin interactions are ignored. Hence, the Zeeman and spin-orbit coupling contributions to the effective spin Hamiltonian are [1]

$$\mathscr{H} = \mathscr{H}_{\mathrm{Ze}} + \mathscr{H}_{\mathrm{SO}} = \mu_B\mathbf{B}\cdot(\hat{\mathbf{L}} + g_e\hat{\mathbf{S}}) + \lambda_{\mathrm{SO}}\hat{\mathbf{L}}\cdot\hat{\mathbf{S}} \tag{3-9}$$

where λ_{SO} is the Russel-Saunders spin-orbit coupling term. Using perturbation theory the following expression for the spin Hamiltonian may be derived [1]:

$$\mathscr{H} = \mu_B\mathbf{B}\cdot(g_e\underline{\mathbf{1}} + 2\lambda_{\mathrm{SO}}\underline{\boldsymbol{\Lambda}})\cdot\hat{\mathbf{S}} + \lambda_{\mathrm{SO}}^2\hat{\mathbf{S}}\cdot\underline{\boldsymbol{\Lambda}}\cdot\hat{\mathbf{S}} \tag{3-10}$$

$$= \mu_B\mathbf{B}\cdot\underline{\mathbf{g}}\cdot\hat{\mathbf{S}} + \hat{\mathbf{S}}\cdot\underline{\mathbf{D}}\cdot\hat{\mathbf{S}} \tag{3-11}$$

where the 3×3 $\underline{\mathbf{g}}$-matrix is defined by

$$\underline{\mathbf{g}} = g_e\underline{\mathbf{1}} + 2\lambda_{\mathrm{SO}}\underline{\boldsymbol{\Lambda}} \tag{3-12}$$

and $\underline{\mathbf{1}}$ is the 3×3 identity matrix. Equation 3-12 explicitly shows that the spin-orbit coupling introduces a shift in $\underline{\mathbf{g}}$ from the free electron value and a possible

anisotropy. Furthermore, the spin-orbit coupling contributes to the *zero-field splitting matrix*

$$\underline{\mathbf{D}} = \lambda_{\mathrm{SO}}^2 \underline{\mathbf{\Lambda}} \tag{3-13}$$

which will be discussed further in §3.1.3.2. The remaining term, $\underline{\mathbf{\Lambda}}$, is the 3×3 spin-orbit coupling matrix, where the ij^{th} element is given by [1]

$$\Lambda_{ij} = -\sum_{g \neq e} \frac{\langle \psi_g | \hat{\mathbf{L}}_i | \psi_e \rangle \langle \psi_e | \hat{\mathbf{L}}_j | \psi_g \rangle}{(E_e - E_g)} \tag{3-14}$$

ψ_g and ψ_e are the wavefunctions for the ground and excited states with energies E_g and E_e, respectively.

3.1.3.2 Zero-field interaction

In the absence of a magnetic field electron-electron ($S \geq 1$) interactions can cause splittings in the energy levels. The *zero-field splitting* is represented by the spin Hamiltonian:

$$\mathscr{H}_{\mathrm{zf}} = \hat{\mathbf{S}} \cdot \underline{\mathbf{D}} \cdot \hat{\mathbf{S}} \tag{3-15}$$

which was first seen in Eq. 3-11. The zero-field splitting matrix $\underline{\mathbf{D}}$ represents an electric potential V and is therefore chosen to be traceless as it must satisfy Laplace's equation, $\nabla^2 V = 0$. It is conventionally written using Cartesian coordinates (x, y and z), where D_z is the principal value and has the largest magnitude. $|D_x| > |D_y|$ if $|D_x| \neq |D_y|$, resulting in a set that is ordered in energy. $\mathscr{H}_{\mathrm{zf}}$ can then be written as [1]

$$\mathscr{H}_{\mathrm{zf}} = D\left(S_z^2 - \frac{1}{3}S(S+1)\right) + E(S_x^2 - S_y^2) \tag{3-16}$$

where $D = \frac{3}{2}D_z$ and $E = \frac{1}{2}(D_x - D_y)$. There are three types of interactions which contribute to $\mathscr{H}_{\mathrm{zf}}$: the anisotropic exchange interaction, dipole-dipole interactions and the spin-orbit interactions. The latter interaction was described in §3.1.3.1.

For a paramagnetic species with two or more unpaired electrons the electrons will interact, leading to a coupling of their wavefunctions. The Hamiltonian for the *exchange interaction* is given by

$$\mathscr{H}_{\mathrm{ex}} = \hat{\mathbf{s}}_1 \cdot \underline{\mathcal{J}} \cdot \hat{\mathbf{s}}_2 \tag{3-17}$$

$\underline{\mathcal{J}}$ is a 3×3 matrix which considers the Coulombic interaction between electrons 1 and 2 ($|\hat{\mathbf{s}}_1| = \frac{1}{2}$ and $|\hat{\mathbf{s}}_2| = \frac{1}{2}$). The coupled functions can either be symmetric or antisymmetric with respect to the exchange of the electrons, with the combinations determining the effective spin S and $(2S+1)$ multiplicity (degeneracy) of the states [1]. It is the sign of the exchange coupling which determines which state lies lower in energy and is thus the ground state. If there is no spin-orbit coupling the exchange interaction is isotropic and all levels within a spin multiplet will shift equally.

For an $S = 1$ system the *anisotropic magnetic dipole-dipole interaction* is described by [1]

$$\mathscr{H}_{\text{dip}}(r) = \left(\frac{\mu_0}{4\pi}\right) g_1 g_2 \mu_B^2 \left(\frac{\hat{\mathbf{s}}_1 \cdot \hat{\mathbf{s}}_2}{r^3} - \frac{3(\hat{\mathbf{s}}_1 \cdot \mathbf{r})(\hat{\mathbf{s}}_2 \cdot \mathbf{r})}{r^5}\right) \tag{3-18}$$

where the two unpaired electrons are separated by the vector $\mathbf{r}$ ($r^2 = x^2 + y^2 + z^2$). g_1 and g_2 are their g-factors; generally $g_1 = g_2 = g$ is assumed. If a total spin operator $\hat{\underline{\mathbf{S}}} = \hat{\underline{\mathbf{s}}}_1 + \hat{\underline{\mathbf{s}}}_2$ is used the equation can be rewritten in the following matrix form [1]:

$$\mathscr{H}_{\text{dip}} = \frac{\mu_0}{8\pi}(g\mu_B)^2 \begin{bmatrix} \hat{S}_x & \hat{S}_y & \hat{S}_z \end{bmatrix} \cdot \begin{bmatrix} \left\langle \frac{r^2-3x^2}{r^5} \right\rangle & \left\langle -\frac{3xy}{r^5} \right\rangle & \left\langle -\frac{3xz}{r^5} \right\rangle \\ \left\langle -\frac{3xy}{r^5} \right\rangle & \left\langle \frac{r^2-3y^2}{r^5} \right\rangle & \left\langle -\frac{3yz}{r^5} \right\rangle \\ \left\langle -\frac{3xz}{r^5} \right\rangle & \left\langle -\frac{3yz}{r^5} \right\rangle & \left\langle \frac{r^2-3z^2}{r^5} \right\rangle \end{bmatrix} \cdot \begin{bmatrix} \hat{S}_x \\ \hat{S}_y \\ \hat{S}_z \end{bmatrix} = \hat{\mathbf{S}} \cdot \underline{\mathbf{D}} \cdot \hat{\mathbf{S}} \tag{3-19}$$

where the equations in the angled brackets, $\langle ... \rangle$, give the expectation values of the spatial part of the electronic wavefunction.

Therefore, in the case of a purely dipolar interaction the terms in Eq. 3-16 are expressed by

$$D = \left(\tfrac{\mu_0}{4\pi}\right) \tfrac{3}{4} g^2 \mu_B^2 \left\langle \tfrac{r^2-3z^2}{r^5} \right\rangle \quad \text{and} \quad E = \left(\tfrac{\mu_0}{4\pi}\right) \tfrac{3}{4} g^2 \mu_B^2 \left\langle \tfrac{y^2-x^2}{r^5} \right\rangle \tag{3-20}$$

These terms can reveal information regarding both the symmetry and dimensions of the centre being examined. If the centre has axial symmetry ($x \equiv y$) the rhombic E term vanishes; for cubic symmetry ($x \equiv y \equiv z$) $D = 0$. Furthermore, if the dipolar interaction dominates $\underline{\mathbf{D}}$ the distance between the spins can be measured from $|\underline{\mathbf{D}}|$.

3.1.3.3 Hyperfine interaction

Hyperfine structure in EPR spectra is produced by the coupling of the electron (S) and nuclear (I) spins for paramagnetic species involving elemental isotopes with $I \neq 0$. The Hamiltonian for the *hyperfine interaction* of j nuclei is

$$\mathscr{H}_{\text{hyp}} = \sum_j \hat{\mathbf{S}} \cdot \underline{\mathbf{A}}_j \cdot \hat{\mathbf{I}}_j \tag{3-21}$$

where $\underline{\mathbf{A}}$ is the 3×3 hyperfine matrix. The hyperfine splitting is a measure of the electron density of the unpaired electron(s) localised at the nuclei of the defect and nearby nuclei. This is a direct interaction and can be separated into isotropic and anisotropic parts.

The isotropic component of the hyperfine interaction arises purely from electrons in s-orbitals localised at the nuclei and is known as the *Fermi* or *contact interaction*. The unpaired s-electron spin density arises from the polarisation of the filled electron shells through an exchange interaction with the partly filled states, an effect known as the "core polarisation" effect [3]. The isotropic hyperfine parameter is given by [1]

$$A_s = \frac{2\mu_0}{3} g_e \mu_B g_n \mu_n |\psi(0)|^2 \tag{3-22}$$

where g_n is the nuclear g-factor, μ_n is the nuclear magneton ($\mu_n = e\hbar/2m_n c$ and m_n is the mass of a proton) and $\psi(0)$ is the electronic wavefunction at the nucleus. The probability density of a p-electron being localised at the nucleus is zero and thus does not contribute to the isotropic hyperfine interaction.

A magnetic dipole interaction between the nuclei and the unpaired electron analogous to the electron-electron magnetic dipolar interaction discussed in §3.1.3.2 produces the dominant contribution to the anisotropic portion of the hyperfine interaction. Its Hamiltonian is thus [1]

$$\mathscr{H}_{\text{dip}}(r) = -g_e \mu_B g_n \mu_n \left(\frac{\hat{\mathbf{S}} \cdot \hat{\mathbf{I}}}{r^3} - \frac{3(\hat{\mathbf{S}} \cdot \mathbf{r})}{r^5} \right) \tag{3-23}$$

There are also indirect hyperfine interactions such as spin polarisation, hyperconjugation and distant dipolar coupling which can contribute to the hyperfine splitting. However these contributions are much weaker than those arising from

direct interactions and will therefore not be discussed further. The reader is directed to Hunt [4], Abragam and Bleaney [3], and Weil and Bolton (§9.2.4-§9.2.6 and §9.2.9 in Ref. [1]) for details on these interactions.

If $\underline{\mathbf{A}}$ is axially symmetric it is conventionally split into parallel ($A_\parallel$) and perpendicular ($A_\perp$) components such that

$$\underline{\mathbf{A}} = \begin{bmatrix} A_\perp & 0 & 0 \\ 0 & A_\parallel & 0 \\ 0 & 0 & A_\parallel \end{bmatrix} \tag{3-24}$$

Here the coordinate system has been rotated so that $A_\parallel$ is parallel to the principal axis of the centre.

$A_\parallel$ and $A_\perp$ can be measured experimentally, enabling the determination of the isotropic (A_s) and anisotropic (A_p) hyperfine parameters using the following relationships [1]:

$$A_s = \frac{1}{3}(A_\parallel + 2A_\perp) \tag{3-25}$$

$$A_p = \frac{1}{3}(A_\parallel - A_\perp) \tag{3-26}$$

Applying the method described by Morton and Preston [5] it is possible to estimate the localisation of the unpaired electron(s) on a nucleus once A_s and A_p have been found.

It is standard to assume that the unpaired electron wavefunction Ψ is governed by the *linear combination of the atomic orbitals* (LCAO) centred on the nuclei of the atoms in and near the point defect. This approximation is appropriate for diamond due to its strong, highly directional covalent bonding structure. Defects in diamond usually involve 2*s*- and 2*p*-type atomic orbitals for carbon or nitrogen, or 3*s*- and 3*p*-type for Si, etc, and consequently Ψ is an *sp*-hybrid. Considering only this case, the unpaired electron wavefunction can be written as

$$\Psi = \sum_j \eta_j \psi_j = \sum_j \eta_j [\alpha_j (\psi_s)_j + \beta_j (\psi_p)_j] \tag{3-27}$$

where ψ_j is an atomic orbital on the j^{th} site. Normalisation requires:

$$\alpha_j^2 + \beta_j^2 = 1 \quad \text{and} \quad \sum_j \eta_j^2 = 1 \tag{3-28}$$

Table 3-1: Published [8] values for the natural abundance, nuclear spin (I) and nuclear g-factor for isotopes with non-zero nuclear spin of selected elements involved in defects in diamond. Also tabulated are a and b, defined as the values for the isotropic (A_s) and anisotropic (A_p) hyperfine parameters if 100% of the unpaired electron density was localised on the s- and p-orbitals, respectively [5].

Nucleus	Natural Abundance	I	g_n	a (MHz)	b (MHz)
^{1}H	99.9885(70)	1/2	5.5857		
^{2}H	0.0115(70)	1	0.8574		
^{13}C	1.07(8)	1/2	1.4048	3777	107.4
^{14}N	99.636(20)	1	0.40376	1811	55.52
^{15}N	0.364(20)	1/2	-0.5664	-2540	-77.88
^{29}Si	4.685(8)	1/2	-1.1106	-4594	-114.2

α, β and η can then be related to A_s and A_p by [6]

$$A_s \simeq \frac{8\pi}{3} g\mu_B g_n \mu_n \alpha_j^2 \eta_j^2 |\psi_s|^2 = a\alpha_j^2\eta_j^2 \tag{3-29}$$

and

$$A_p \simeq \frac{2}{5} g\mu_B g_n \mu_n \beta_j^2 \eta_j^2 \left\langle \frac{1}{r^3} \right\rangle_p = b\beta_j^2\eta_j^2 \tag{3-30}$$

where a and b are the values that A_s and A_p would have for 100% occupancy of the s- and p-orbitals, respectively. These values have been calculated for several nuclei; a selected summary can be seen in Table 3-1. The fraction of the unpaired electron localised in the ψ_j atomic orbital is then given by η_j^2. The *hybridisation ratio* λ_h can also be calculated since $\lambda_h = (\beta/\alpha)^2$, and $\lambda_h = 3$ for an undistorted sp^3 orbital in diamond [7]. This method should be seen as a starting point for the theoretical interpretation of hyperfine data; there are several sources of error and omitted factors which may influence the results [7].

3.1.3.4 Quadrupole interaction

If a nucleus with spin $I \geq 1$ experiences an electric field gradient an interaction may arise between the field and the nuclear electric quadrupole moment. The electric field gradient is a result of the anisotropic electric charge distribution on the paramagnetic species and its immediate neighbours [3]. It can orient the nuclear charge distribution and hence change both the electrostatic energy and

the direction of the nuclear spin angular momentum [1, 9]. The spin Hamiltonian related to the energy of the alignment for j nuclei is given by [1]

$$\mathscr{H}_{\mathrm{Q}} = \sum_{j} \hat{\mathbf{I}}_j \cdot \underline{\mathbf{P}}_j \cdot \hat{\mathbf{I}}_j \tag{3-31}$$

where the 3×3 matrix $\underline{\mathbf{P}}$ is the *nuclear quadrupolar coupling matrix*. $\underline{\mathbf{P}}$ represents an electric potential and is thus traceless to satisfy Laplace's equation. Equation 3-31 can be rewritten in terms of Cartesian coordinates (x, y, z, where z is the principal axis) so that [3]

$$\hat{\mathbf{I}} \cdot \underline{\mathbf{P}} \cdot \hat{\mathbf{I}} = P_x I_x^2 + P_y I_y^2 + P_z I_z^2 \tag{3-32}$$

where $P_x + P_y + P_z = 0$. Equation 3-32 can be expressed as [3]

$$\hat{\mathbf{I}} \cdot \underline{\mathbf{P}} \cdot \hat{\mathbf{I}} = P_{\parallel} \left[\left(I_z^2 - \frac{1}{3} I\{I+1\} \right) + \frac{1}{3} \eta \left(I_x^2 - I_y^2 \right) \right] \tag{3-33}$$

where $P_{\parallel} = 3P_z/2$ and $\eta = (P_x - P_y)/P_z$. η is known as the *asymmetry parameter* and describes the deviation of the field gradient from axial symmetry about the principal axis z; for axial symmetry $\eta = 0$. $P_{\parallel}$ is given by [3]

$$P_{\parallel} = \frac{3eQq_{\mathrm{efg}}}{4I(2I-1)} = \frac{3eQ}{4I(2I-1)} \frac{\partial^2 V}{\partial z^2} \tag{3-34}$$

where $q_{\mathrm{efg}} = (\partial^2 V / \partial z^2)$ is the electric field gradient and V is the potential. Q is the quadrupole moment of the nucleus, which describes the electrical shape of the nucleus and is a fixed number for each isotopic species [1]. Q can be negative or positive; if the distribution is "elongated" $Q > 0$ and if it is "flattened" $Q < 0$. $Q = 0$ for $I < 1$ [4]. Since s-orbitals are spherically symmetric they will not contribute to the electric field gradient, while p- and d-orbitals will have non-zero contributions, with the effect from p-orbitals being stronger than that from d-orbitals with the same quantum numbers [1].

3.1.3.5 Nuclear Zeeman interaction

The *nuclear Zeeman interaction* is a consequence of the interaction between the nuclear magnetic moment ($I > 0$) and the applied magnetic field $\mathbf{B}$. The spin Hamiltonian contribution from the nuclear Zeeman interaction is expressed by [1]:

$$\mathscr{H}_{\mathrm{nZe}} = -\mu_n g_{n_j} \hat{\mathbf{I}}_j \cdot \mathbf{B} \tag{3-35}$$

This expression is analogous to that for the electronic Zeeman effect (§3.1.3.1). The negative sign is included to ensure that for the stable configuration the nuclear moment is aligned parallel to $\mathbf{B}$.

The nuclear Zeeman effect can be difficult to observe in EPR spectra as it is a factor of m_e/m_n smaller than the electronic Zeeman effect. Furthermore, the positions of the resonance lines for allowed EPR transitions ($|\Delta M_S| = 1$ and $|\Delta m_I| = 0$, see §3.1.4) are unaffected since all levels with the same magnitude of m_I are shifted equally by the nuclear Zeeman interaction. However, analysis of *forbidden transitions* (§3.1.4) can reveal information about the value of g_n and the related nuclear species. Forbidden transitions, which occur for $|\Delta M_S| = 1$ and $|\Delta m_I| = 1$, are the result of an admixture of the $|M_S, m_I\rangle$ and $|M_S, m_I \pm 1\rangle$ states arising from cross terms in the spin Hamiltonian [3]. Comparison between the positions of the forbidden lines relative to the allowed lines in an EPR spectrum can be used to determine the sign of g_n relative to g and estimate its value [3].

3.1.4 Transition probabilities and selection rules

The Hamiltonian describing the interaction between a magnetic moment $\hat{\boldsymbol{\mu}}$ and a static magnetic field $\mathbf{B}$ in the absence of any other interaction was given by Eq. 3-5 in §3.1.2. If an oscillatory magnetic field $\mathbf{B}_1$ is applied there will be an additional perturbation. In EPR experiments the oscillating magnetic field is the time-varying magnetic component of the applied microwave radiation. Thus

$$\mathscr{H}_1 = -\hat{\boldsymbol{\mu}}\cdot\mathbf{B}_1 \tag{3-36}$$

The effect can be evaluated using time-dependent perturbation theory [1]. The probability of a transition between an initial and final state ($|\psi_i\rangle$ and $|\psi_f\rangle$, respectively) is proportional to the square of the matrix element of the perturbation between the two states, i.e. $\propto |\langle\psi_i|\mathscr{H}_1|\psi_f\rangle|^2$. Therefore, if the eigenvalues of a spin system are known the relative intensities of the possible transitions can be calculated.

Consider the Hamiltonian of the microwave radiation induced perturbation if $\mathbf{B}_1 \perp \mathbf{B}$, letting $\mathbf{B}_1 \| x$ and $\mathbf{B} \| z$ (identical results would be achieved with $\mathbf{B}_1$ anywhere in the plane perpendicular to $\mathbf{B}$). The Hamiltonian can be expressed as

$\mathscr{H}_1 = g\mu_B B_1 S_x$. By operating the $\mathscr{H}_1$ on the spin states (represented by $|M_S, m_I\rangle$) the general energy matrix is given by [1]

$$\begin{aligned} \langle M_S, m_I|\mathscr{H}_1|M'_S, m'_I\rangle &\propto \langle M_S, m_I|\hat{S}_x|M'_S, m'_I\rangle \\ &\propto \langle M_S, m_I|M'_S \pm 1, m'_I\rangle \end{aligned} \tag{3-37}$$

From the orthogonality of the functions it can be shown that the matrix element is only non-zero when $m'_I = m_I$ and $M'_S = M_S \pm 1$ [1]. Therefore the selection rules for EPR transitions with $\mathbf{B}_1 \perp \mathbf{B}$ are

$$\Delta M_S = \pm 1 \quad \text{and} \quad \Delta m_I = 0 \tag{3-38}$$

These selection rules are only applicable for the strong field approximation, $g\mu_B B \gg |A|$, where the hyperfine parameter A is assumed to be isotropic [1, 9].

The hyperfine interaction will contribute terms which include ladder operators, since $S_\pm = S_x \pm iS_y$ and $I_\pm = I_x \pm iI_y$ [1], which give rise to off-diagonal terms in the energy matrix. Additional terms with ladder operators would be added if there is an anisotropic g-value or if the magnetic field B is applied at an angle $\theta \neq 0$ to the principal axis (here the z-axis). A consequence of the first-order admixture of the states $|M_S, m_I\rangle$ by the off-diagonal terms in the Hamiltonian is that *forbidden transitions*, where $\Delta M_S = \pm 1$ and $\Delta m_I \pm 1$, become weakly allowed. These transitions are also known as double electron-nuclear spin flip transitions since both the electronic and nuclear spins "flip." Their intensity will depend on the value of θ, being strongest for $\theta = 45°$ and vanishing for $\theta = 0, 90°$ [3]. Second-order admixtures can result in transitions with $\Delta M_S = \pm 1$ and $\Delta m_I \pm 2$ having appreciable intensity [3].

3.1.5 Spin relaxation and the Bloch equations

3.1.5.1 Magnetisation in a static magnetic field, B

For a system consisting of an ensemble of N individual electrons spins with magnetic dipole moments ($\boldsymbol{\mu}_i$) it is useful to consider $\mathbf{M}$, where [1]

$$\mathbf{M} = \frac{1}{V}\sum_{i=1}^{N} \boldsymbol{\mu}_i \tag{3-39}$$

$\mathbf{M}$ is known as the *magnetisation* and is the total magnetic moment per unit volume (V) for the spin system. Using Cartesian coordinates, $\mathbf{M}$ can be represented

by M_x, M_y and M_z. $\mathbf{M}$ is a spatially averaged, time-dependent vector. In the absence of a magnetic field the individual magnetic dipoles of a paramagnetic system are randomly oriented and static, resulting in $\mathbf{M} = 0$. However, when a constant homogeneous magnetic field $\mathbf{B}$ is applied ($\mathbf{B} \parallel \mathbf{z}$, where $\mathbf{z}$ is a unit vector along the z-axis) there will be a redistribution over the various orientations to minimise the energy of the system, governed by Boltzmann statistics. If the mean interaction energy is large relative to the thermal energy ($|\mu B| >> |k_B T|$) nearly all dipoles will align parallel to $\mathbf{B}$ since this orientation has the lowest energy. However, usually $|\mu B| << |k_B T|$, so that there is a magnetisation component perpendicular to $\mathbf{B}$ (in the xy-plane). The net magnetisation obeys the classical equation of motion [1]

$$\frac{\mathrm{d}\mathbf{M}}{\mathrm{d}t} = \gamma \mathbf{M} \wedge \mathbf{B} \tag{3-40}$$

where t is time and γ is the gyromagnetic ratio. If there are no relaxation effects the solutions to Eq. 3-40 reveal that $\mathbf{M}$ precesses about $\mathbf{B}$ at the (angular) *Larmor frequency*, $\omega_B = -\gamma B = 2\pi\nu_B$ [1]. For an isotropic material at thermal equilibrium the magnitude of M_z stays constant during the precession, whilst that of M_x and M_y average to zero at any instant in time if averaged over a sufficient number of spins since there is no phase coherence in the xy-plane [3].

3.1.5.2 Magnetisation subjected to B and $\mathbf{B}_1(t)$

Let's consider the case where the system is perturbed by applying an oscillating field $\mathbf{B}_1(t)$ perpendicular to $\mathbf{B}$. $\mathbf{B}_1(t)$ can usually be described by two oppositely rotating fields of equal magnitude [1]:

$$\begin{aligned} \mathbf{B}_1(t) &= \mathbf{B}_1(+) + \mathbf{B}_1(-) \\ &= B_1[\cos(\omega t)\mathbf{x} + \sin(\omega t)\mathbf{y}] + B_1[\cos(\omega t)\mathbf{x} - \sin(\omega t)\mathbf{y}] \end{aligned} \tag{3-41}$$

The effect of the two components can be considered independently. $\mathbf{B}_1(+)$ rotates in the same direction as the Larmor precession induced by $\mathbf{B}$, whilst $\mathbf{B}_1(-)$ rotates in the opposite direction. Hence, the difference $\omega_B - \omega$ will be smaller for $\mathbf{B}_1(+)$ and the effect of $\mathbf{B}_1(-)$ can be ignored. The components of $\mathbf{B}_1(t)$ in the lab frame coordinate system (x, y, z) can thus be expressed as $B_{1x} = B_1 \cos(\omega t)$, $B_{1y} = B_1 \sin(\omega t)$ and $B_{1z} = 0$.

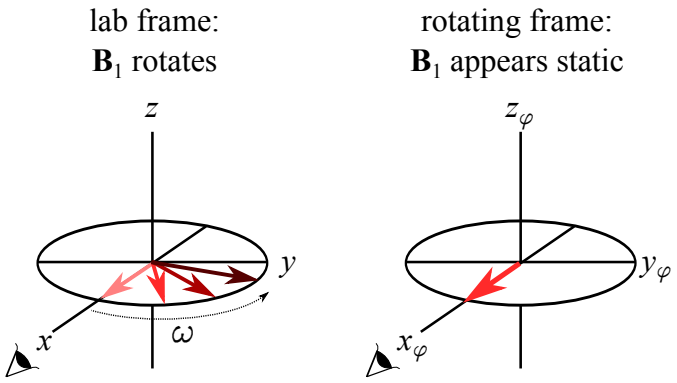

Figure 3-2: In the lab frame of reference (x, y, z) the oscillating magnetic field $\mathbf{B}_1$ can be seen rotating about the z-axis with an angular frequency ω. In the rotating frame of reference (x_φ, y_φ, z_φ) the observer is rotating about the z-axis ($z = z_\varphi$) in the same sense and with the same frequency at ω as $\mathbf{B}_1$ does in the lab frame. Consequently $\mathbf{B}_1$ appears to be static, here aligned parallel to the x_φ-axis.

When the the spin system is subjected to both $\mathbf{B}$ and $\mathbf{B}_1(t)$ the motion of the magnetisation $\mathbf{M}$, as seen in the lab frame, will be a superposition of the simultaneous precessions about $\mathbf{B}$ (natural frequency ν_B) and $\mathbf{B}_1(t)$ (frequency $\nu = \omega/(2\pi)$), consequently changing the angle between $\mathbf{B}$ and $\mathbf{M}$. It is easier to visualise the system by transforming to a coordinate frame that is rotating about the z-axis (azimuthal angle φ) at an angular frequency ω with the same sense as the rotation of $\mathbf{B}_1$. In this new frame, described by the axes x_φ, y_φ and z_φ $\mathbf{B}_1$ appears static. Here the x_φ-axis is chosen so that $\mathbf{B}_1 \parallel \mathbf{x}_\varphi$. Figure 3-2 illustrates $\mathbf{B}_1$ as seen in the lab and rotating frames. In the rotating frame $\mathbf{M}$ is described by $M_{x\varphi}$, $M_{y\varphi}$ and $M_{z\varphi}$, where $M_{z\varphi} = M_z$ since $\mathbf{z} = \mathbf{z}_\varphi$. The motion of the magnetisation can be described by the following *Bloch equations* [1]:

$$\frac{\mathrm{d}M_{x\varphi}}{\mathrm{d}t} = -(\omega_B - \omega)M_{y\varphi} - \frac{M_{x\varphi}}{\tau_2} \tag{3-42}$$

$$\frac{\mathrm{d}M_{y\varphi}}{\mathrm{d}t} = (\omega_B - \omega)M_{x\varphi} + \gamma B_1 M_z - \frac{M_{y\varphi}}{\tau_2} \tag{3-43}$$

$$\frac{\mathrm{d}M_z}{\mathrm{d}t} = -\gamma B_1 M_{y\varphi} - \frac{M_z - M_z^0}{\tau_1} \tag{3-44}$$

where M_z^0 is the magnitude of M_z at the instant before perturbation ($t = 0$). τ_1 and τ_2 are characteristic time constants often written as T_1 and T_2 in literature, respectively; the current nomenclature has been chosen to avoid confusion with temperature T. τ_1 is known as the *longitudinal relaxation time* as it describes the relaxation of the longitudinal component of the magnetisation, M_z. An alternative

name for τ_1 is the *spin-lattice relaxation time* since it is related to the exchange of energy between the spin system and the host lattice [3]. Conversely, τ_2 describes the relaxation of the magnetisation in the $x_\varphi y_\varphi$-plane (and equivalently the xy-plane) and is known both as the *transverse relaxation time* and the *spin-spin relaxation time*. The dipoles within a system interact with each other (spin-spin interactions), producing local magnetic fields. Since $|\mathbf{B}|$ is much larger than these local fields the component of the magnetisation along the direction of the applied field, M_z, will not be affected. However, the transverse components can be affected, so that their relaxation behaviour is based on τ_2. Processes which affect the spin-lattice relaxation time are treated in §3.1.6.4.

In conventional continuous wave (CW) EPR experiments $|\mathbf{B}|$ is changed whilst the frequency of the exciting field, ν, is kept constant. In *slow adiabatic passage* experiments B is swept through resonance slowly compared to τ_1 and τ_2, and $\mathrm{d}M_{x\varphi}/\mathrm{d}t = \mathrm{d}M_{y\varphi}/\mathrm{d}t = \mathrm{d}M_z/\mathrm{d}t = 0$ [3]. Field modulation effects are also ignored. Thus, the steady state solutions for Eq. 3-42 to 3-44 are applicable [1]:

$$M_{x\varphi} = -M_z^0 \frac{\gamma B_1 (\omega_B - \omega)\tau_2^2}{1 + (\omega_B - \omega)^2\tau_2^2 + \gamma^2 B_1^2 \tau_1 \tau_2} \tag{3-45}$$

$$M_{y\varphi} = +M_z^0 \frac{\gamma B_1 \tau_2}{1 + (\omega_B - \omega)^2\tau_2^2 + \gamma^2 B_1^2 \tau_1 \tau_2} \tag{3-46}$$

$$M_{z\varphi} = +M_z^0 \frac{1 + (\omega_B - \omega)^2\tau_2^2}{1 + (\omega_B - \omega)^2\tau_2^2 + \gamma^2 B_1^2 \tau_1 \tau_2} \tag{3-47}$$

$M_{x\varphi}$ and $M_{y\varphi}$ are in phase or 90° out of phase with $\mathbf{B}_1$, respectively. $M_{x\varphi}$ is related to the dispersion and $M_{y\varphi}$ to the absorption.

In CW EPR the signal's absorption *lineshape function* $Y(B)$ is proportional to $M_{y\varphi}$, so that using $\omega = \omega_B = -\gamma B_r$ where $B = B_r$ (resonance condition):

$$Y(B) \propto M_z^0 \frac{\gamma B_1 \tau_2}{1 + (B - B_r)^2 \gamma^2 \tau_2^2 + \gamma^2 B_1^2 \tau_1 \tau_2} \tag{3-48}$$

The term $\gamma^2 B_1^2 \tau_1 \tau_2$ in the denominator (also seen in Eq. 3-45 to 3-47) is related to the *microwave power saturation* behaviour of the system. As the microwave power is increased the spin transitions occur at faster rates. The saturation term can be ignored if $\gamma^2 B_1^2 \tau_1 \tau_2 << 1$ and the microwave power absorbed by the system, P, and the rate at which it is absorbed, $\mathrm{d}P/\mathrm{d}B$, are proportional to B_1^2 [1]. In this regime the amplitude of the resonance line will double if the attenuation of the microwave

source is decreased by -6 dB. Also, the lineshape will be approximately Lorentzian, with a half width at half height $\Gamma = 1/(\gamma\tau_2)$ and an amplitude $Y(B = B_r) \propto M_z^0 B_1$.

3.1.6 Pulsed Electron Paramagnetic Resonance

In continuous wave EPR the "static" magnetic field $\mathbf{B}$ ($\| \mathbf{z}$) is swept while an oscillating magnetic field $\mathbf{B}_1(t)$, with a maximum amplitude which is constant with time (B_1), is applied perpendicular to $\mathbf{B}$. For slow passage, the standard mode employed, $\mathbf{B}$ is swept slowly and the steady state solutions to the Bloch equations can be used to describe bulk magnetisation components (Eq. 3-45 to 3-47). In a pulsed EPR experiment B is not varied, but is chosen so that the resonance condition (§3.1.2) is satisfied for a spin system, i.e. $B = B_r$. A strong $\mathbf{B}_1$ is applied for a time t_p, the pulse duration, after which it is turned off. The behaviour of the magnetisation as it returns to its equilibrium value following this strong perturbation is studied; the steady state solutions of the Bloch equations no longer apply. Several pulse lengths and combinations can be used to monitor changes to the magnetisation, providing information about relaxation effects.

Once again it is useful to consider the behaviour of $\mathbf{M}$ using the rotating coordinate frame of reference ($x_\varphi, y_\varphi, z_\varphi$, where $z_\varphi = z$ and the $x_\varphi y_\varphi$-plane is equivalent to the xy-plane in the lab frame), illustrated in Fig. 3-2. In this frame $\mathbf{B}_1$ appears static ($\mathbf{B}_1 \| \mathbf{x}_\varphi$). Furthermore, in thermal equilibrium under resonance ($\omega = \omega_B$) the Larmor precession of $\mathbf{M}$ cannot be seen and $\mathbf{M}$ is pointing along $\mathbf{z}_\varphi = \mathbf{z}$. The pulse has the effect of rotating the magnetisation about $\mathbf{B}_1$ (i.e rotating in the $y_\varphi z_\varphi$-plane) by an amount proportional to t_p. The angle by which $\mathbf{M}$ is rotated is known as the *flip angle* (or *tip angle*), $\Omega(t_p) = |\gamma_e| B_1 t_p$ [1]. Pulses are generally labelled by their flip angle, and their durations are chosen to be short in comparison to τ_1 or τ_2. When the pulse is switched off the magnetisation will relax back to its equilibrium position. The spectrometer gives a measure of the magnetisation as a function of time, detecting in the plane normal to $\mathbf{B}$. Starting from the instant that $\mathbf{B}_1$ is switched off, the change in the magnetisation observed will be described by a *free induction decay* (FID), where "free" refers to the fact that the magnetisation is no longer subjected to $\mathbf{B}_1$.

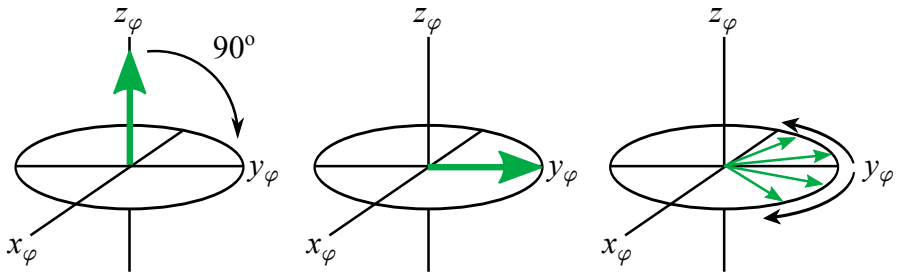

Figure 3-3: Effect of a 90° B_1 pulse on the magnetisation (depicted by the green arrow) of a system with $S = 1/2$, assuming the static field $\mathbf{B}$ is applied along the z-axis and the rotating coordinate system for the excitation field $\mathbf{B}_1$ is taken to lie along the x_φ-axis. The fanning out of the magnetisation produces an exponential decay in the transverse magnetisation. Figure based on a schematic in Ref. [10].

3.1.6.1 The 180°-pulse

If t_p is chosen so that $|\gamma|B_1 t_p = \pi$ the magnetisation will rotate by 180° about $\mathbf{B}_1$ from its initial position, so that it is flipped (e.g. $\mathbf{z} \rightarrow -\mathbf{z}$), retaining its magnitude. This *180°-pulse* has the effect of inverting the electron spin population, so that the higher-energy state is now more populated than the lower-energy state. During the *inversion recovery*, after the pulse has been switched off, the locus of $\mathbf{M}$ will remain longitudinal, but $|\mathbf{M}|$ will shrink along -$\mathbf{z}$, reach zero, and then grow along $\mathbf{z}$ until the initial magnetisation magnitude has been reached. The decay rate of this process is exponential, with a characteristic relaxation time given by the spin-lattice relaxation time τ_1.

3.1.6.2 The 90°-pulse

Another important pulse is the *90°-pulse* where t_p is chosen so that $|\gamma|B_1 t_p = \pi/2$. This pulse has the effect of rotating the magnetisation by 90° about $\mathbf{B}_1$, so that at the end of the pulse it lies in the $x_\varphi y_\varphi$-plane (i.e. $M_z = 0$), parallel to or antiparallel to $\mathbf{y}$ if γ is positive or negative, respectively [3]. The 90°-pulse scenario for a positive γ is illustrated in Fig. 3-3. During this process the magnitude $|\mathbf{M}|$ is unchanged and the spins are coherently dispersed. In this plane ($\perp\mathbf{B}$), the individual magnetic moments which make up the bulk magnetisation are sensitive to local fields created by neighbouring spins or other inhomogeneities. There will hence be two simultaneous relaxation processes occurring once the excitation field is switched off. As for the 180°-pulse M_z, will grow exponentially and return to its

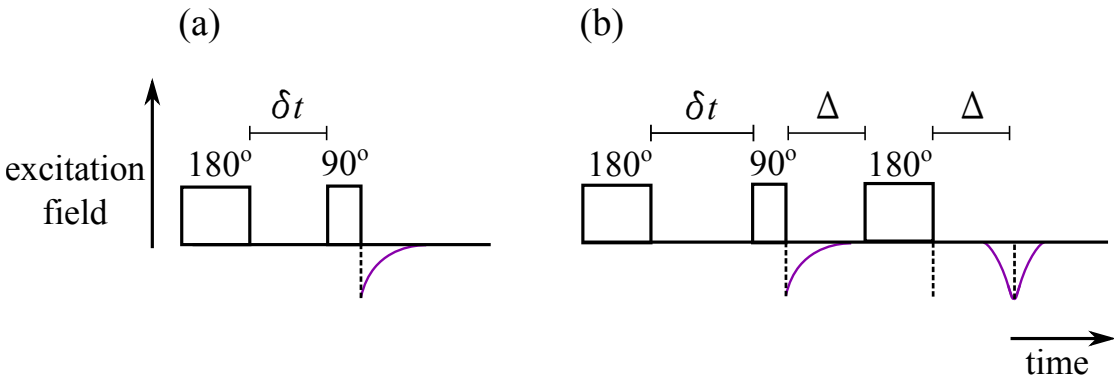

Figure 3-4: The (a) two- and (b) three-pulse inversion recovery sequences used to measure the spin lattice relaxation time τ_1 of a spin system.

equilibrium value with a relaxation time τ_1. The local fields will cause dephasing of the spins and the individual dipoles will "fan out" in the xy-plane, resulting in a decrease in the transverse magnetisation, with a *phase-memory time* τ_m. τ_m is defined as the time, taken from the end of the pulse, needed for the intensity of the transverse magnetisation to fall to $1/e$ (where e is the exponential number) of its maximum value [1]. Note that τ_m is not necessarily equal to τ_2 as the former is affected by inhomogeneities in $\mathbf{B}$.

3.1.6.3 Multiple pulse combinations for the measurement of τ_1

Clever multiple pulse combinations have been designed to determine relaxation parameters of a spin system, often improving the signal to noise ratio and removing some of the complexities associated with single pulse FID experiments. Several pulse sequences, though commonly used, are beyond the scope of this thesis and will not be discussed. However, they are comprehensively dealt with in the books by and Kevan and Schwartz [11] and Kevan and Bowman [12]. Here the two main pulse sequences to determine the spin-lattice relaxation time τ_1 will be considered. τ_1 governs the relaxation after perturbation of the longitudinal magnetisation component, M_z, aligned along the static magnetic field $\mathbf{B}$, as described by Eq. 3-44. However, in pulsed EPR experiments detection usually occurs in the plane perpendicular to $\mathbf{B}$ (the xy-plane). Thus $\mathrm{d}M_z/\mathrm{d}t$ cannot be measured directly using a single pulse such as the 180°-pulse (§3.1.6.1). Instead, the two- or three-pulse inversion recovery sequences can be utilised to make the measurement.

A *two-pulse inversion recovery sequence* is conventionally described by $\pi - \delta t - \pi/2$ and is illustrated in Fig. 3-4(a). The 180°-pulse ($t_p = t_\pi$) is applied to invert the magnetisation ($\mathbf{z} \rightarrow -\mathbf{z}$), which will start to recover with the relaxation rate $\mathrm{d}M_z/\mathrm{d}t$ when the pulse is switched off ($t = t_\pi$). After a duration δt a 90°-pulse ($t_p = t_\pi/2$) is used to place the magnetisation $M_z(t = t_\pi + \delta t)$ in the xy-plane. The evolution of M_y is then recorded ($t > t_\pi + \delta t + t_\pi/2$) as an inverted FID, with a maximum amplitude proportional to $M_z(t = t_\pi + \delta t)$. By stepping δt it is possible to measure changes to M_z as a function of time, and thus extract τ_1 by fitting the exponential decay described by Eq. 3-44.

If τ_1 is short the recovery of M_z is fast and $M_z(t = t_\pi + \delta t)$ will not be appreciable, rendering the two-pulse inversion recovery sequence unsuitable to measure τ_1. Alternatively, the *three-pulse inversion recovery sequence* (also known as the *three-pulse echo detection sequence*) can be employed, $\pi - \delta t - \pi/2 - \Delta - \pi - \Delta - \text{echo}$ (Fig. 3-4(b)). As for the previous sequence, a 180°-pulse is used to invert the magnetisation. However, detection occurs using a $\pi/2 - \Delta - \pi - \Delta - \text{echo}$ sequence, known as a *Hahn echo* [1, 12]. The 90°-pulse brings the magnetisation into the xy-plane (along $\mathbf{y}_\varphi$ in the rotating frame) and during time Δ the spins dephase, fanning out in the plane. The final 180°-pulse flips $M_{y\varphi}$, so the spins that were dephasing move towards equal phasing. Maximum $|M_{y\varphi}|$ occurs at a time Δ after the third pulse, after which it will decay again. Thus, the observer will see an *echo*, consisting of two back-to-back FIDs. The maximum amplitude of the echo can be measured as a function of δt, resulting in a decay with a decay constant τ_1.

3.1.6.4 Processes affecting the spin-lattice relaxation time, τ_1

Experiments to measure spin-lattice relaxation times are presented in this thesis; its key mechanisms will therefore be introduced. τ_1 should be considered in terms of the processes which couple the electron spins to the lattice. The main processes can be divided into three groups, the direct, Raman and higher-order, such as Orbach, processes [3]. Experimentally, it is possible to distinguish between the relaxation processes since they depend on phonon densities, which in turn are determined by the sample temperature T. In the majority of cases the temperature

dependence of the spin-lattice relaxation rate can be given by [3]

$$\frac{1}{\tau_1} = \underbrace{a \coth\left(\frac{h\nu}{2k_BT}\right)}_{\text{direct}} + \underbrace{bT^n}_{\text{Raman}} + \underbrace{\frac{c}{\exp(\Delta/k_BT) - 1}}_{\text{Orbach}} \tag{3-49}$$

where the different terms arise from the processes involved, described individually below, and a, b, c and n are constants.

The first term describes the *direct process*, which is analogous to a direct dipole transition in optical spectroscopy. It can occur when the energy required (released) by a magnetic dipole transition is matched by the creation (annihilation) of a phonon of equal energy, and is thus limited to an extremely small fraction of the total number of phonons available. If $(h\nu/k_BT) \ll 1$, $\frac{1}{2}\coth(h\nu/k_BT) \to (k_BT/h\nu)$, i.e. the rate is proportional to T [3]. If $(h\nu/k_BT) \gg 1$, $\coth(h\nu/k_BT) \to 1$ and the spin-lattice relaxation time becomes independent of temperature [3]. For EPR measurements at $\sim 9\,\text{GHz}$ the direct process will lead to a linear temperature dependence for $T \gtrsim 2\,\text{K}$ [11].

The *Raman process* involves the inelastic scattering of a phonon by a defect, flipping the electron spin. The difference between the initial and final phonon energy is equal to $h\nu$. Alternatively, it can be seen as a process whereby a phonon is absorbed by the centre and another is emitted and is thus also known as a two-phonon process. The temperature dependence of $1/\tau_1$ for a Raman process is T^n, where $n = 9, 7$ or 5, determined by the type of spin levels involved in the transition [3].

An *Orbach process* may occur if there is an excited state at an energy Δ above the ground state [3]. A direct transfer may be induced from one of the spin levels of the ground state into the excited state by the absorption of a phonon. The excited state can then emit a phonon so that a transition occurs into an alternative spin level, indirectly transferring the population from one ground state spin level into another, producing an effective spin-lattice relaxation process. It may be faster than a direct process between the different ground state spin levels as there may be a greater density of phonons with energy Δ than with energy equal to the separation between the spin levels. If an Orbach process dominates $1/\tau_1 \propto (\exp(\Delta/k_BT) - 1)^{-1}$. However, when $\Delta \gg k_BT$, this can be approximated to $1/\tau_1 \propto \exp -\Delta/k_BT$ [3].

3.1.6.5 Off-resonance effects

At resonance, the frequency of the excitation field is exactly equal to that of the Larmor frequency of the precessing magnetisation, i.e $\omega_B = \omega$. However, in CW EPR it has been shown that there are several different values of B for which the resonance condition is met. Hence, during a pulsed EPR experiment, where a specific value of B is chosen, it will not be possible to be at resonance with all allowed transitions simultaneously.

Let's consider what happens after a 90°-pulse is applied to bring the magnetisation into the detection plane (xy-plane). In the rotating frame of reference (rotating at frequency ω, see Fig. 3-3) the magnetisation will tip so that it initially lies parallel to y_φ and perpendicular to $\mathbf{B}_1$. However, since $\omega_B \neq \omega$ the magnetisation will rotate either faster or slower than $\mathbf{B}_1$ so that it will appear to rotate even in the rotating frame. Note, this is a separate effect to the fanning out of the dipoles related to τ_m. The rotation rate will be described by [12]

$$\delta\omega = \omega_B - \omega \tag{3-50}$$

The FID recorded after a 90°-pulse will now oscillate as it decays, encoding the individual frequency components of the EPR spectrum. A spectrum analogous to that of a CW scan (frequency domain) can be extracted by Fourier transforming the FID, thus converting from a time to a frequency domain ($\propto B$). This technique is known as FT-EPR.

When the system is on resonance and at thermal equilibrium the Larmor precession of the magnetisation about the z-axis will not be observed in the rotating frame (only M_z is visible), so that $\mathbf{B}$ seems to have disappeared. If the system is off-resonance the magnetisation is precessing with an angular frequency $\delta\omega$ and the apparent magnetic field along z-axis in the rotating frame is

$$B' = \frac{\delta\omega}{-\gamma} \tag{3-51}$$

Thus the excitation field is no longer simply given by $\mathbf{B}_1$, but by the vector sum of $\mathbf{B}'$ and $\mathbf{B}_1$, $\mathbf{B}_{eff}$; all tipping by pulse application now occurs about $\mathbf{B}_{eff}$. The effect is two-fold: tipping the magnetisation into the xy-plane using a 90°-pulse will not be as efficient as when on resonance since $\mathbf{B}_{eff}$ lies out of this plane, and

the magnitude of the rotation angular frequency about $\mathbf{B}_{eff}$ will be [12]

$$\omega_{eff} = \sqrt{\omega_1^2 + (\delta\omega)^2} \tag{3-52}$$

where ω_1 is the *Rabi* or *nutation frequency* ($\omega_1 = -\gamma B_1$), the angular frequency of tipping when at resonance.

3.2 Symmetry and point groups

Point defects in the diamond lattice can occur in various orientations or symmetry related "sites" which are crystallographically equivalent. The *point group symmetry* of a point defect defines all the different *symmetry operations* under which it is apparently unchanged, where an operation is an action such as a rotation, reflection or inversion. The operations are known as the *elements* of the group, and the point, line or plane with respect to which the operation is carried out is known as a *symmetry element*. Diamond belongs to the tetrahedral point group, which is denoted T_d by the Schönflies system [13]. Consequently a lattice point of an undistorted crystal remains invariant under 24 different symmetry operations. Alternatively, one could say that the operations from the T_d point group would generate 24 "sites." The point group symmetry of any given defect in diamond is limited to being a subgroup of T_d.

3.2.1 The basics of group theory

Group theory is a powerful tool when analysing the physical and electronic structure of a centre (point defect) due to its mathematical rigour, often greatly simplifying the problem at hand by placing restrictions on the centre's spectral properties. The possible symmetry operations and elements encompassed by a point group are summarised in Table 3-2. Atkins and Friedman [13] contains an accessible account on the mathematical theory of symmetry; their work is the basis for this section.

A set of *elements* $R, S, ...$ form a group G if:

- The product of two elements RS, where R is performed on the result of S,

is also an element belonging to G,

$$RS = T, \quad T \in G \tag{3-53}$$

- The multiplication of the elements is associative,

$$(RS)T = R(ST) \tag{3-54}$$

- The identity e is an element of the set,
- The inverse of each element is an element of the set, so that

$$RR^{-1} = R^{-1}R = e \tag{3-55}$$

For the study of the symmetry of crystal structures it is the set of symmetry operations which form the point group.

Point defects with C_{3v} symmetry, such as the single substitutional nitrogen (N_s) or nitrogen-vacancy (N-V) centres in diamond, are often used to explain group theoretical concepts [13]. Here the divacancy centre (V_2), with D_{3d} symmetry, will be considered instead as the results of this analysis will be used in §5.1.1. Figure 3-6 illustrates V_2, which consists of two nearest-neighbour vacant sites in the diamond lattice. The neutral charge state of the centre, V_2^0, is EPR-active (known as both R4 and W6 [14, 15]) and observable by optical absorption (TH5, at 2.3-2.8 eV [16]). The electronic structure for V_2^0 was originally outlined by Coulson and Larkins who calculated the linear combination of the ligand orbitals from the six nearest-neighbour carbon atoms relative to the V_2 unit [17], as will be treated here. The reader is referred to their paper for examples of predictions for spin- and orbitally-allowed transitions for V_2^0 which could be drawn by further analysis of these results.

A defect with symmetry D_{3d} can be described as having a [111] axial distortion with inversion symmetry. There are twelve elements (symmetry operations) to this point group (e, C_3^+, C_3^-, C_2, C_2', C_2'', i, S_6^+, S_6^-, σ_d, σ_d', σ_d'') and it is thus said to have an *order* $h = 12$ [18]. The general definition of the elements are summarised in Table 3-2. Additionally, the "+" and "−" superscripts denote whether the C_n rotation for $n > 2$ is anti-clockwise or clockwise, respectively, whilst the prime ($'$)

Table 3-2: Symmetry operations and their elements [13]. The σ mirror planes are illustrated in Fig. 3-5.

Key Groups & Symbols	Symmetry operations & symmetry elements
e	The identity
C_n	An n-fold rotation by an angle $2\pi/n$ about the principal axis
$C_{n\mathrm{v}}$	Operations of C_n & n vertical reflections
$C_{n\mathrm{h}}$	Operations of C_n & a horizontal reflection $\perp$ to principal axis
D_n	Operations of C_n & n two-fold rotations $\perp$ to n-fold axis
$D_{n\mathrm{h}}$	Operations of D_n & a horizontal reflection $\perp$ to principal axis
$D_{n\mathrm{d}}$	Operations of D_n & n dihedral reflections
σ_v	A reflection in a vertical symmetry plane
σ_h	A reflection in a horizontal symmetry plane
σ_d	A reflection in a dihedral symmetry plane
i	An inversion through a centre of symmetry
S_n	n = even; an n-fold improper rotation, i.e. a C_n rotation followed by a reflection in a plane $\perp$ to n-fold axis

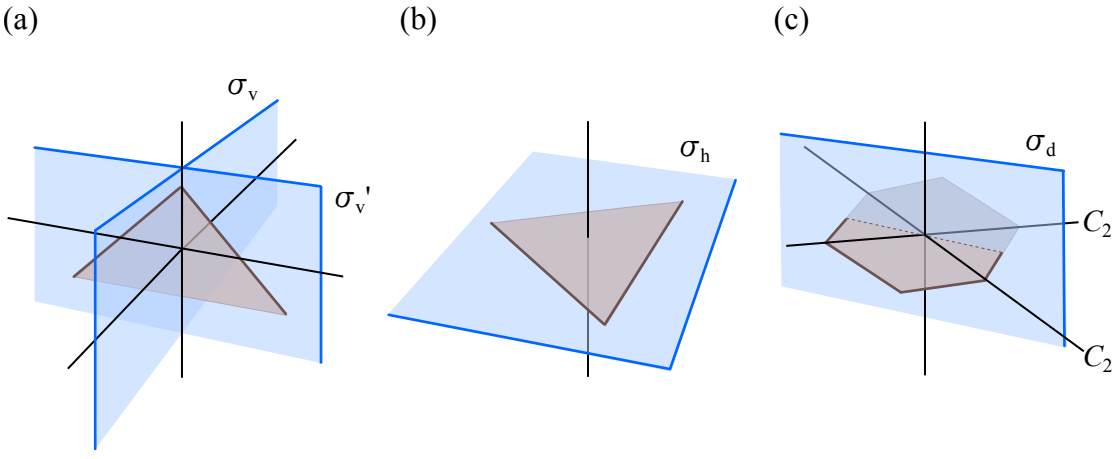

Figure 3-5: (a) Two vertical mirror planes, σ_v, (b) a horizontal mirror plane, σ_h, (c) a dihedral plane σ_d. Based on Ref. [13].

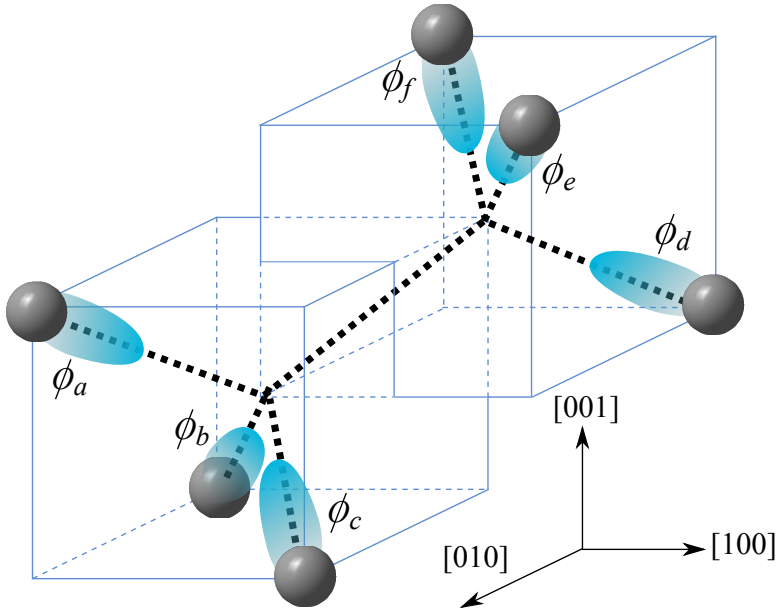

Figure 3-6: The divacancy centre in diamond, V_2. The dangling orbitals for each of the six nearest-neighbour carbon atoms have been labelled.

and double prime ($''$) symbols are used to differentiate between different elements belonging to the same *class* [13]. If two symmetry operations R and R' belong to the same class they are the same type of operation (such as a reflection or rotation) and can be related by a symmetry operation S, so $R' = S^{-1}RS$. R and R' are then known as *conjugates*.

D_{3d} is a *non-Abelian group*, meaning that the outcome of the product of symmetry operations (RS) depends on the order in which they are applied, i.e. RS is not necessarily equivalent to SR. Mathematically, if $RS \neq SR$ the operations are said to be *non-commutative*. It is often useful to express operations by matrices which can be multiplied with the components of a *basis*, a set of functions on which the operations take place. A basis with functions f_i can be represented by a vector $\mathbf{f}$:

$$\mathbf{f} = (f_1, f_2, ..., f_d) \tag{3-56}$$

where d is its *dimension*, which is equal to the number of functions which form the basis. The choice of basis will determine the form of the n-dimensional *representative matrix* $\mathbf{D}^{(n)}(R)$ for an operation R, so that the effect of the operation on the i^{th} component of the basis is given by

$$Rf_i = \sum_j f_j D_{ji}(R) \tag{3-57}$$

Table 3-3: The D_{3d} character table [18].

	e	$2C_3$	$3C_2$	i	$2S_6$	$3\sigma_d$
$\mathbf{A}_{1g}$	1	1	1	1	1	1
$\mathbf{A}_{2g}$	1	1	-1	1	1	-1
$\mathbf{E}_g$	2	-1	0	2	-1	0
$\mathbf{A}_{1u}$	1	1	1	-1	-1	-1
$\mathbf{A}_{2u}$	1	1	-1	-1	-1	1
$\mathbf{E}_u$	2	-1	0	-2	1	0
$g(c)$	1	2	3	1	2	3
$\chi(c)$	6	0	0	0	0	2

where D_{ji} is a matrix element of $\mathbf{D}^{(n)}(R)$. The matrix representatives of the operations in a group multiply together in the same fashion as the operations of the group; if $RS = T$ then $\mathbf{D}^{(n)}(R)\mathbf{D}^{(n)}(S) = \mathbf{D}^{(n)}(T)$. The *character* $\chi(R)$ of a representative matrix is given by the sum of its diagonal elements, which is equivalent to its trace:

$$\chi(R) = \sum_i D_{ii}(R) = \mathrm{Tr}\{\mathbf{D}^{(n)}(R)\} \tag{3-58}$$

A property of the character of an operation is that it remains invariant under a *similarity transformation* of the basis, which transforms the basis into a similar basis with equal angles and spatial dimensions.

A *matrix representation* Γ of a group consists of a set of matrix representatives for the group's operations. Due to its definition the representation is not unique and alternative representations could be created simply by changing the basis. In a given representation all members of the same class will have the same character. Furthermore, different classes may also share the same character. A matrix representation of dimension d can be separated into a set of matrices of a lower dimension d_l if they have a *block-diagonal form* [13], an action which is known as *reduction*. The label l refers to the *symmetry species*. The *irreducible representation* $\Gamma^{(l)}$ of a group Γ is a representation for which there is no similarity transformation (a linear combination of the basis functions) which would simultaneously convert all representatives into a block-diagonal form of lower dimension, removing all redundant information. Each irreducible representation is a symmetry species, yet a chosen basis may not span all the possible symmetry species

for the group. A *character table* gives a complete list of the characters of all the possible irreducible representations for a symmetry group. A comprehensive list of character tables (and product tables, discussed later) has been published by Atkins *et al.* [18] and a set for the most common symmetries can be found in Atkins and Friedman [13]. The latter text also gives an account on how character tables can be constructed using the *Little Orthogonality Theorem* (LOT), which is derived from the *Great Orthogonality Theorem* (GOT). The character table for $D_{3\mathrm{d}}$ is given in Table 3-3.

The symmetry species of the forms **A** and **E** are one- and two-dimensional irreducible representations, respectively ($d_A = 1$ and $d_E = 2$). **A** is known as a *singlet* whilst **E** is a *doublet*. There are two other possible irreducible representations which do not belong to the $D_{3\mathrm{d}}$ group: the singlet **B** and the triplet **T**, with $d_B = 1$ and $d_T = 3$ [13]. The *parity* of the electron wavefunctions of the molecular orbitals for each of the symmetry species of a point defect are indicated by the subscripts g and u. If, under inversion, the wavefunction remains indistinguishable from itself it has *gerade* (g) symmetry, whilst if the sign of the wavefunction changes it is classified as *ungerade* (u) [13]. The two German words mean "even" and "odd," respectively. The g and u notation is only applicable to symmetry species belonging to point groups for which the inversion symmetry operation occurs.

The representation Γ of a group can be written as

$$\Gamma = \sum_l a_l \Gamma^{(l)} \tag{3-59}$$

where a_l is the number of times that the irreducible representation $\Gamma^{(l)}$ appears in the direct sum $\mathbf{D}(R) = \mathbf{D}^{(\Gamma_1)}(R) \oplus \mathbf{D}^{(\Gamma_2)}(R) \oplus \mathbf{D}^{(\Gamma_3)}(R) \oplus ... \oplus \mathbf{D}^{(\Gamma_n)}(R)$. Since the character of an operation $\chi(R)$ is invariant under a similarity transformation, the character of the original representative is the sum of the characters of the irreducible representations into which it is reduced. Hence,

$$\chi(R) = \sum_l a_l \chi^{(l)}(R) \tag{3-60}$$

It can be shown using the LOT that [13]

$$a_l = \frac{1}{h} \sum_R \chi^{(l)}(R)^* \chi(R) = \frac{1}{h} \sum_c g(c) \chi^{(l)}(c)^* \chi(c) \tag{3-61}$$

Table 3-4: The transform table for the basis $\{\phi_a, \phi_b, \phi_c, \phi_d, \phi_e, \phi_f\}$ under the symmetry operations of the $D_{3\mathrm{d}}$ group. The basis is represents the single dangling orbitals from each of the six unpaired carbon atoms in the V_2 unit as illustrated in Fig. 3-6

	ϕ_a	ϕ_b	ϕ_c	ϕ_d	ϕ_e	ϕ_f
e	ϕ_a	ϕ_b	ϕ_c	ϕ_d	ϕ_e	ϕ_f
C_3^+	ϕ_b	ϕ_c	ϕ_a	ϕ_e	ϕ_f	ϕ_d
C_3^-	ϕ_c	ϕ_a	ϕ_b	ϕ_f	ϕ_d	ϕ_e
C_2	ϕ_e	ϕ_d	ϕ_f	ϕ_b	ϕ_a	ϕ_c
C_2'	ϕ_f	ϕ_e	ϕ_d	ϕ_c	ϕ_b	ϕ_a
C_2''	ϕ_d	ϕ_f	ϕ_e	ϕ_a	ϕ_c	ϕ_b
i	ϕ_d	ϕ_e	ϕ_f	ϕ_a	ϕ_b	ϕ_c
S_6^+	ϕ_f	ϕ_d	ϕ_e	ϕ_c	ϕ_a	ϕ_b
S_6^-	ϕ_e	ϕ_f	ϕ_d	ϕ_b	ϕ_c	ϕ_a
σ_d	ϕ_a	ϕ_c	ϕ_b	ϕ_d	ϕ_f	ϕ_e
σ_d'	ϕ_c	ϕ_b	ϕ_a	ϕ_f	ϕ_e	ϕ_d
σ_d''	ϕ_b	ϕ_a	ϕ_c	ϕ_e	ϕ_d	ϕ_f

where h is the order of the group where there are $g(c)$ members in the class c with character $\chi(c)$.

Further explanation will benefit from using the V_2 centre in diamond as an example of a $D_{3\mathrm{d}}$ point defect. For V_2 each of the six nearest-neighbour carbon atoms to the defect are each bonded to three of the next-nearest-neighbour carbon atoms, using three of its four unpaired valence electrons. Hence, for each of the six nearest-neighbour carbon atoms there will remain a single unpaired electron, termed a "vacancy electron" by Coulson and Larkins [17]. In the absence of the defect, these six vacancy electrons would have bonded with the carbon atoms that otherwise occupy the two vacant lattice site positions. It is assumed that the vacancy electrons populate orbitals which are localised on the defect, labelled ϕ_a, ϕ_b, ϕ_c, ϕ_d, ϕ_e and ϕ_f, as illustrated in Fig. 3-6; the basis set $\mathbf{f} = (\phi_a, \phi_b, \phi_c, \phi_d, \phi_e, \phi_f)$ is chosen to represent the group. The effect of the symmetry operations R (e, C_3^+, C_3^-, C_2, C_2', C_2'', i, S_6^+, S_6^-, σ_d, σ_d' and σ_d'') on each member of the basis f_j is given in Table 3-4. From this it can be seen that only some members of the basis set are left unchanged by each operation. After applying the identity operator e all six basis set members are indistinguishable from the original set, whilst only two (different) members remain unchanged after each of the different operations

belonging to the σ_d class of reflections, i.e. $\chi(e) = 6$ and $\chi(\sigma_d) = 2$. All other operations did not result in any of the basis members transforming to themselves. These results are summarised in Table 3-3.

For D_{3d}, using the character table (Table 3-3) and Eq. 3-61 under the basis defined for V_2 it is found that

$$\begin{aligned}
a_{A_{1g}} &= (1/12)[1\cdot1\cdot6 + 2\cdot1\cdot0 + 3\cdot1\cdot0 + 1\cdot1\cdot0 + 2\cdot1\cdot0 + 3\cdot1\cdot2] \\
&= 1 \\
a_{A_{2g}} &= (1/12)[1\cdot1\cdot6 + 2\cdot1\cdot0 + 3\cdot(-1)\cdot0 + 1\cdot1\cdot0 + 2\cdot1\cdot0 + 3\cdot(-1)\cdot2] \\
&= 0 \\
a_{E_g} &= (1/12)[1\cdot2\cdot6 + 2\cdot(-1)\cdot0 + 3\cdot0\cdot0 + 1\cdot2\cdot0 + 2\cdot(-1)\cdot0 + 3\cdot0\cdot3] \\
&= 1 \\
a_{A_{1u}} &= (1/12)[1\cdot1\cdot6 + 2\cdot1\cdot0 + 3\cdot1\cdot0 + 1\cdot(-1)\cdot0 + 2\cdot(-1)\cdot0 + 3\cdot(-1)\cdot2] \\
&= 0 \\
a_{A_{2u}} &= (1/12)[1\cdot1\cdot6 + 2\cdot1\cdot0 + 3\cdot(-1)\cdot0 + 1\cdot(-1)\cdot0 + 2\cdot(-1)\cdot0 + 3\cdot1\cdot2] \\
&= 1 \\
a_{E_g} &= (1/12)[1\cdot2\cdot6 + 2\cdot1\cdot0 + 3\cdot0\cdot0 + 1\cdot - 2\cdot0 + 2\cdot1\cdot0 + 3\cdot0\cdot3] \\
&= 1
\end{aligned} \tag{3-62}$$

Hence this representation of the six orbitals spans $\Gamma = \mathbf{A}_{1g} + \mathbf{E}_g + \mathbf{A}_{2u} + \mathbf{E}_g$.

The basis set which was initially chosen, $\mathbf{f} = (\phi_a,\ \phi_b,\ \phi_c,\ \phi_d,\ \phi_e,\ \phi_f)$, was arbitrary. It is desirable to form a linear combination of the members of the basis set which span an irreducible representation of a given symmetry species. These basis functions are called *symmetry-adapted linear combinations* (*SALCs*) [13]. The concept of a *projection operator* $p^{(l)}$ corresponding to each symmetry species l needs to be considered, where [13]

$$p^{(l)} = \frac{d_l}{h} \sum_R \chi^{(l)}(R)^* R \tag{3-63}$$

and can be constructed from the character tables. $p^{(l)}$ takes its name from the fact that it acts to project the basis functions (f_j) into a SALC ($f_i^{(l)}$) that transforms as the irreducible representation. Thus [13],

$$p^{(l)} f_j = \frac{d_l}{h} \sum_R \chi^{(l)}(R) R f_j = \sum_i f_i^{(l)} \tag{3-64}$$

Rf_j has already been calculated using the original basis set of V_2 (Table 3-4). Each value can then be multiplied by the character of the respective operations

Table 3-5: $\chi^{(l)}(R)^* Rf_j$ for $l = A_{2u}, E_u, E_g$. The values for $\chi^{(A_{1g})}(R)^* Rf_j$ are equal to the Rf_j values in Table 3-4 since $\chi^{(A_{1g})}(R) = 1$.

original:	ϕ_a	ϕ_b	ϕ_c	ϕ_d	ϕ_e	ϕ_f
			A_{2u}			
e	ϕ_a	ϕ_b	ϕ_c	ϕ_d	ϕ_e	ϕ_f
C_3^+	ϕ_b	ϕ_c	ϕ_a	ϕ_e	ϕ_f	ϕ_d
C_3^-	ϕ_c	ϕ_a	ϕ_b	ϕ_f	ϕ_d	ϕ_e
C_2	-ϕ_e	-ϕ_d	-ϕ_f	-ϕ_b	-ϕ_a	-ϕ_c
C_2'	-ϕ_f	-ϕ_e	-ϕ_d	-ϕ_c	-ϕ_b	-ϕ_a
C_2''	-ϕ_d	-ϕ_f	-ϕ_e	-ϕ_a	-ϕ_c	-ϕ_b
i	-ϕ_d	-ϕ_e	-ϕ_f	-ϕ_a	-ϕ_b	-ϕ_c
S_6^+	-ϕ_f	-ϕ_d	-ϕ_e	-ϕ_c	-ϕ_a	-ϕ_b
S_6^-	-ϕ_e	-ϕ_f	-ϕ_d	-ϕ_b	-ϕ_c	-ϕ_a
σ_d	ϕ_a	ϕ_c	ϕ_b	ϕ_d	ϕ_f	ϕ_e
σ_d'	ϕ_c	ϕ_b	ϕ_a	ϕ_f	ϕ_e	ϕ_d
σ_d''	ϕ_b	ϕ_a	ϕ_c	ϕ_e	ϕ_d	ϕ_f
			E_g			
e	$2\phi_a$	$2\phi_b$	$2\phi_c$	$2\phi_d$	$2\phi_e$	$2\phi_f$
C_3^+	-ϕ_b	-ϕ_c	-ϕ_a	-ϕ_e	-ϕ_f	-ϕ_d
C_3^-	-ϕ_c	-ϕ_a	-ϕ_b	-ϕ_f	-ϕ_d	-ϕ_e
i	$2\phi_d$	$2\phi_e$	$2\phi_f$	$2\phi_a$	$2\phi_b$	$2\phi_c$
S_6^+	-ϕ_f	-ϕ_d	-ϕ_e	-ϕ_c	-ϕ_a	-ϕ_b
S_6^-	-ϕ_e	-ϕ_f	-ϕ_d	-ϕ_b	-ϕ_c	-ϕ_a
			E_u			
e	$2\phi_a$	$2\phi_b$	$2\phi_c$	$2\phi_d$	$2\phi_e$	$2\phi_f$
C_3^+	-ϕ_b	-ϕ_c	-ϕ_a	-ϕ_e	-ϕ_f	-ϕ_d
C_3^-	-ϕ_c	-ϕ_a	-ϕ_b	-ϕ_f	-ϕ_d	-ϕ_e
i	-$2\phi_d$	-$2\phi_e$	-$2\phi_f$	-$2\phi_a$	-$2\phi_b$	-$2\phi_c$
S_6^+	ϕ_f	ϕ_d	ϕ_e	ϕ_c	ϕ_a	ϕ_b
S_6^-	ϕ_e	ϕ_f	ϕ_d	ϕ_b	ϕ_c	ϕ_a

for the species. The results for $l = A_{2u}, E_u, E_g$ are shown in Table 3-5. This table does not include $\chi^{(A_{1g})}(R)^* R$ simply because $\chi^{A_{1g}}(R) = 1$; the resulting values are therefore identical to those displayed in Table 3-4. $(d_l/h)\sum_R \chi^{(l)}(R) R f_j$ for each symmetry species l can be found by summing the columns for the relevant sections of Tables 3-4 and 3-5 and multiplying them by (d_l/h).

Thus (excluding any repeated results and results which are identical, but multiplied by a factor of -1) it is found that:

for $\mathbf{A}_{1g}$ $d = 1$ and $h = 12$

$$\tfrac{1}{12}(2\phi_a + 2\phi_b + 2\phi_c + 2\phi_d + 2\phi_e + 2\phi_f) = \tfrac{1}{6}(\phi_a + \phi_b + \phi_c + \phi_d + \phi_e + \phi_f) \quad (3\text{-}65)$$

for $\mathbf{E}_g$ $d = 2$ and $h = 12$

$$\begin{aligned} \tfrac{2}{12}(2\phi_a - \phi_b - \phi_c + 2\phi_d - \phi_e - \phi_f) &= \tfrac{1}{6}(2\phi_a - \phi_b - \phi_c + 2\phi_d - \phi_e - \phi_f) \\ \tfrac{2}{12}(-\phi_a + 2\phi_b - \phi_c - \phi_d + 2\phi_e - \phi_f) &= \tfrac{1}{6}(-\phi_a + 2\phi_b - \phi_c - \phi_d + 2\phi_e - \phi_f) \\ \tfrac{2}{12}(-\phi_a - \phi_b + 2\phi_c - \phi_d - \phi_e + 2\phi_f) &= \tfrac{1}{6}(-\phi_a - \phi_b + 2\phi_c - \phi_d - \phi_e + 2\phi_f) \end{aligned} \quad (3\text{-}66)$$

for $\mathbf{A}_{2u}$ $d = 1$ and $h = 12$

$$\tfrac{1}{12}(2\phi_a + 2\phi_b + 2\phi_c - 2\phi_d - 2\phi_e - 2\phi_f) = \tfrac{1}{6}(\phi_a + \phi_b + \phi_c - \phi_d - \phi_e - \phi_f) \quad (3\text{-}67)$$

for $\mathbf{E}_u$ $d = 2$ and $h = 12$

$$\begin{aligned} \tfrac{2}{12}(-2\phi_a + \phi_b + \phi_c + 2\phi_d - \phi_e - \phi_f) &= \tfrac{1}{6}(-2\phi_a + \phi_b + \phi_c + 2\phi_d - \phi_e - \phi_f) \\ \tfrac{2}{12}(\phi_a - 2\phi_b + \phi_c - \phi_d + 2\phi_e - \phi_f) &= \tfrac{1}{6}(\phi_a - 2\phi_b + \phi_c - \phi_d + 2\phi_e - \phi_f) \\ \tfrac{2}{12}(\phi_a + \phi_b - 2\phi_c - \phi_d - \phi_e + 2\phi_f) &= \tfrac{1}{6}(\phi_a + \phi_b - 2\phi_c - \phi_d - \phi_e + 2\phi_f) \end{aligned} \quad (3\text{-}68)$$

Finally, since the number of SALCs must equal the dimensionality of the irreducible representation d_l, one of the SALCs is arbitrarily chosen and an orthogonal combination is created using the remaining SALCs for the symmetry species. Hence, ignoring the normalisation factors, for the analysis of V_2 (D_{3d} symmetry) the orbital transform for each symmetry species is summarised as

$$\begin{aligned} \mathbf{A}_{1g} &\begin{cases} \phi_1 = \phi_a + \phi_b + \phi_c + \phi_d + \phi_e + \phi_f \end{cases} \\ \mathbf{E}_g &\begin{cases} \phi_2 = -\phi_a - \phi_b + 2\phi_c - \phi_d - \phi_e + 2\phi_f \\ \phi_3 = 3\phi_a - 3\phi_b + 3\phi_d - 3\phi_e \end{cases} \\ \mathbf{A}_{2u} &\begin{cases} \phi_4 = \phi_a + \phi_b + \phi_c - \phi_d - \phi_e - \phi_f \end{cases} \\ \mathbf{E}_u &\begin{cases} \phi_5 = \phi_a\phi_b - 2\phi_c - \phi_d - \phi_e + 2\phi_f \\ \phi_6 = 3\phi_a - 3\phi_b - 3\phi_d + 3\phi_e \end{cases} \end{aligned} \quad (3\text{-}69)$$

Table 3-6: The direct product table for D_{3d} [18].

	A_{1g}	A_{2g}	E_g	A_{1u}	A_{2u}	E_u
A_{1g}	A_{1g}	A_{2g}	E_g	A_{1u}	A_{2u}	E_u
A_{2g}		A_{1g}	E_g	A_{2u}	A_{1u}	E_u
E_g			A_{1g}+[A_{2g}]+E_g	E_u	E_u	A_{1u}+[A_{2u}]+E_u
A_{1u}				A_{1g}	A_{2g}	E_g
A_{2u}					A_{1g}	E_g
E_u						A_{1g}+[A_{2g}]+E_g

3.2.2 Calculation of many electron states

If the linear orbitals and their dimensionality has been determined for a point defect it is possible to calculate the many electron states allowed by its symmetry. Consider the divacancy centre in the neutral state, V_2^0, which has six electrons available to populate the orbitals. According to the Pauli exclusion principle each non-degenerate orbital (a) can accommodate two electrons, while each double-degenerate orbital (e, not to be confused with the identity operation) can be populated by up to four electrons. The 37 possible configurations are of the form $a_{1g}^m a_{2u}^n e_g^r e_u^s$, where the superscripts indicate the population of that orbital state [17]. The orbital states transform as the corresponding species, i.e. a_{1g}, a_{2u}, a_g and e_u transform as $\mathbf{A}_{1g}$, $\mathbf{A}_{2u}$, $\mathbf{E}_g$, and $\mathbf{E}_u$, respectively.

The symmetry of each of the resultant states, termed the *many electron states*, for each configuration can be calculated using the direct product table for the symmetry of the defect investigated. The direct product table for D_{3d} is given in Table 3-6. Since holes transform as electrons it follows that, for instance, e_u^3 transforms like e_u, and e_u^4 like a_{1g} as the e_u orbital is "full" when it contains four electrons. Hence, for each configuration one only needs to consider the orbital states which are not fully occupied by electrons. For example, the calculation for the symmetry of the resultant state for the $a_{1g}^2 a_{2u}^2 e_g^2 e_u^0$ configuration is:

$$\mathbf{E}_{1g} \otimes \mathbf{E}_{1g} = \mathbf{A}_{1g} + [\mathbf{A}_{2g}] + \mathbf{E}_g \tag{3-70}$$

The square brackets indicate that the particular many electron state has the highest spin multiplicity $(2S+1)$ allowed for that state. The multiplicity is expressed as a superscript before the symmetry of the many electron state, and is used to

Table 3-7: Some of the allowed states for the neutral charge state of the divacancy defect in diamond, V_2. Based on a table by Coulson and Larkins [17].

Configuration	Symmetry of resultant states
$a_{1g}^2 a_{2u}^2 e_g^2 e_u^0$	${}^1A_{1g} + {}^3A_{2g} + {}^1E_g$
$a_{1g}^2 a_{2u}^2 e_g^1 e_u^1$	${}^3A_{1u} + {}^1A_{1g} + {}^3A_{2u} + {}^1A_{2u} + {}^3E_u + {}^1E_u$
$a_{1g}^2 a_{2u}^2 e_g^0 e_u^2$	${}^1A_{1g} + {}^3A_{2g} + {}^1E_g$
$a_{1g}^1 a_{2u}^2 e_g^3 e_u^0$	${}^3E_g + {}^1E_g$
$a_{1g}^1 a_{2u}^2 e_g^2 e_u^1$	${}^5E_u + 4{}^3E_u + 3{}^1E_u + {}^3A_{2u} + {}^1A_{2u} + {}^3A_{1u} + {}^1A_{1u}$
$a_{1g}^1 a_{2u}^2 e_g^1 e_u^2$	${}^5E_g + 4{}^3E_g + 3{}^1E_g + {}^3A_{2g} + {}^1A + 2g + {}^3A_{1g} + {}^1A_{1g}$

Table 3-8: The allowed electric dipole transitions with D_{3d} symmetry, provided the spin selection rule is satisfied [17].

Initial state		A_{2g}	A_{2u}	A_{1g}	A_{1u}	E_g	E_u
Final state	z	A_{1u}	A_{1g}	A_{2u}	A_{2g}	E_u	E_g
	x, y	E_u	E_g	E_u	E_g	A_{1u}, A_{2u}, E_u	A_{1g}, A_{2g}, E_g

denote the type of spin state. If $S = 0$ then $(2S + 1) = 1$ and it is a *spin singlet*, whilst if $S = 1$ $(2S + 1) = 3$ and it is known as a *spin triplet*. Hence, the many electron states for $a_{1g}^2 a_{2u}^2 e_g^2 e^0$ are ${}^1A_{1g}$, ${}^3A_{2g}$ and ${}^1E_g$. Coulson and Larkins have tabulated some of the allowed states for V_2^0 [17], as summarised in Table 3-7.

Although group theory is a powerful tool for determining the possible many electron states, it does not provide any information regarding their ordering nor relative energies; further experimental and theoretical work is necessary. The ground state of V_2^0 was determined to be ${}^3A_{2g}$ using EPR by Twitchen *et al.* [14]. Furthermore, Coulson and Larkins calculated the allowed transitions for the divacancy centre (D_{3d} symmetry) and found that the components of the electronic dipole operator, which are proportional to x, y, z, transform as $z \subset A_{2u}$ and $x, y \subset E_u$ [17]. Their results are reproduced in Table 3-8.

3.2.3 Effect of defect symmetry on EPR spectra

To demonstrate the effect of the symmetry of paramagnetic defects in diamond on their EPR spectra the single substitutional nitrogen centre, N_s, will be consid-

Table 3-9: Possible symmetries for distorted tetrahedral point sites. The relative intensities of the lines listed assume that the defect ensemble investigated consists of centres that are randomly distributed in all symmetry-allowed configurations. The original table was produced by Cox [19] and was expanded by Edmonds [20].

Symmetry	Distortion from T_d	G	Line intensities		
			⟨100⟩	⟨111⟩	⟨110⟩
T_d ($43m$)	None	1	1	1	1
D_{2d} ($\bar{4}2m$)	[100] axial distortion	3	2,1	3	2,1
D_{3d} ($\bar{3}m$)	[111] axial distortion with inversion symmetry	4	4	1,3	2,2
C_{3v} ($3m$)	[111] axial distortion without inversion symmetry	4	4	1,3	2,2
D_2 (222)	[100] & [010] axial distortion	6	2,2,2	6	2,2,2
C_{2v} ($mm2$)	(Rotation about [001]) [110] axial distortion	6	4,2	3,3	1,1,4
C_{2v} ($mm2$)	(Rotation about [001]) [110] axial distortion, one axis along [001]	6	4,2	3,3	1,1,4
C_2 (2)	[100] & general non-axial distortion	12	4,4,4	6,6	4,4,2,2
C_{1h} (m)	[111] non-axial distortion, one axis along $[1\bar{1}0]$	12	8,4	6,3,3	4,2,4,2
C_{1h} (m)	[111] non-axial distortion, not along $[1\bar{1}0]$	12	8,4	6,3,3	4,2,4,2
C_1 (1)	[111] non-axial distortion, not along $[1\bar{1}0]$	24	8,8,8	6,6,6,6	4,4,4,4,4,4
C_1 (1)	Axial distortion, not along axes	24	8,8,8	6,6,6,6	4,4,4,4,4,4
C_1 (1)	Non-axial distortion, not along axes	24	8,8,8	6,6,6,6	4,4,4,4,4,4

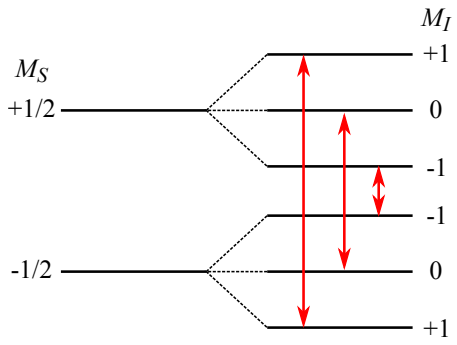

Figure 3-7: Allowed EPR transitions ($\Delta M_S = \pm 1$, $\Delta M_I = 0$) for ^{14}N N_S^0, where $S = 1/2$ and $I = 1$.

ered. This centre consists of a nitrogen atom which has replaced a carbon atom in the crystal lattice. The impurity atom distorts the lattice from its unperturbed T_d symmetry, extending one of the nitrogen-carbon bonds along a $\langle 111 \rangle$ direction and lowering the symmetry to $C_{3\mathrm{v}}$. The defect can therefore have four different symmetry-related configurations, called *sites*, where its principal symmetry axis is aligned parallel to each of the $\langle 111 \rangle$ directions. It is worth noting that the probability for a centre to belong to any one of the sites is usually equal, i.e. the centres are *randomly aligned*. If this is not the case, due to the sample growth method, defect creation technique or treatment, the centres are *preferentially aligned*.

In the neutral charge state, $\mathrm{N_s^0}$, the centre has a single unpaired electron, resulting in a spin $S = 1/2$, making it EPR-active. For ^{14}N, which is nearly 100% abundant (see Table 3-1) $I = 1$. $\mathrm{N_s^0}$ is conventionally known as the P1 paramagnetic centre in diamond [21]. Figure 3-7 illustrates the allowed EPR transitions for $\mathrm{N_s^0}$. In general, during an EPR experiment the principal axis for each of the separate types of sites will make a different angle to the direction of the applied magnetic field $\mathbf{B}$. Each site has three associated allowed transitions which can be detected by EPR. For $\mathrm{N_s^0}$ $\underline{\mathbf{g}}$ is approximately isotropic. Hence the resonance magnetic field (B_r) for the central transition ($|-1/2, 0\rangle \rightarrow |+1/2, 0\rangle$) is approximately constant for each site. However, the hyperfine tensor $\underline{\mathbf{A}}$ is anisotropic. Hence the magnitude of the hyperfine splitting observed, and the values of B which satisfy the resonance condition, can differ for each site. For a single crystal it is simple to investigate the symmetry of a paramagnetic centre by monitoring changes to the relative positions of the resonance lines as the sample is rotated in a static magnetic field, producing

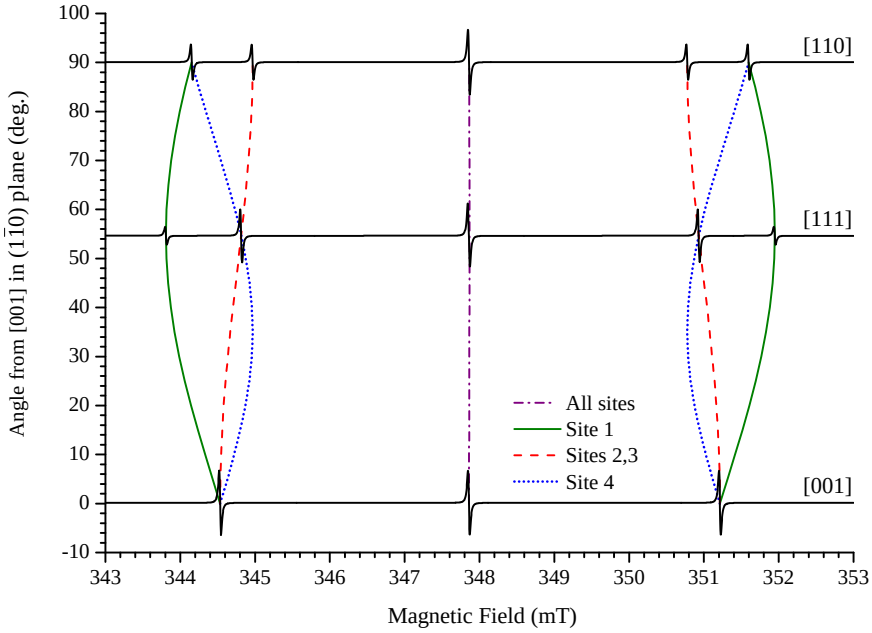

Figure 3-8: Superposition of the roadmap and simulated spectra (assuming a random distribution of sites) for N_s^0 (P1), with ν = 9.75 GHz. The magnetic field was rotated in a $(1\bar{1}0)$ plane.

what is known as a *roadmap* (alternatively the field direction could be changed while the sample orientation is kept constant). Usually it is most useful to choose the axis of rotation to be along a ⟨110⟩ crystallographic direction in the sample, so that **B** can be aligned parallel to each of the principal directions ⟨001⟩, ⟨111⟩ and ⟨110⟩ in a single plane. For these high symmetry directions multiple sites make the same angle with **B** and are thus spectroscopically equivalent. If the plane of rotation is chosen to be $(1\bar{1}0)$, the angles relative to a [001]-direction for $\mathbf{B}\|[001]$, $\mathbf{B}\|[111]$ and $\mathbf{B}\|[110]$ are 0°, 54.74° and 90°, respectively. Figure 3-8 shows a N_s^0 roadmap (ν = 9.75 GHz), where the simulated spectra for the cases where **B** is parallel to each of the principal directions have been been overlayed. EPR spectra can be simulated using the method described by Edmonds [20]. Assuming random alignment of the sites, each site will produce resonance lines with intensities of 1 arbitrary unit. For $\mathbf{B}\|[100]$ all sites are equivalent relative to the field and thus each resulting resonance line has an intensity of 4. For $\mathbf{B}\|[111]$ the hyperfine splitting for site 1 ($\mathbf{B}\|A_\|$) is maximised, whilst sites 2, 3 and 4 become equivalent; a ratio of 1:3 for the outer lines is observed. Finally, for $\mathbf{B}\|[110]$ sites 1 and 4 are equivalent, and the ratio of the lines is 2:2. By constructing a roadmap

and considering the relative intensities of the lines for **B** parallel to the principal directions it is possible to determine the symmetry of the centre investigated using the data in Table 3-9, where the relative intensities assume that the centres are randomly aligned.

Comparison of the integrated intensities for the hyperfine satellites (I_{hf}) of a known element relative to those of the central transition (I_{central}) can be used to determine the number of equivalent positions (N_{eq}) for the nucleus of abundance A:

$$I_{\mathrm{hf}} = N_{\mathrm{eq}} \times \frac{A}{1-A} \times I_{\mathrm{central}} \tag{3-71}$$

Furthermore, this equation can be utilised to determine the relative abundances of the isotopes involved, which can aid in the identification of the elements of which the defect is composed.

3.3 Optical absorption

When an electromagnetic wave passes through a transparent material it is attenuated due to absorption and scattering mechanisms. For smooth plane parallel surfaces scattering only becomes an important attenuation mechanism at high energies such as X-ray or γ-ray energies [22], whist at lower energies absorption dominates. The spectrometers used for optical absorption are generally classified by the spectral range which they cover: commonly they operate in the infra-red (IR), ultraviolet (UV) and visible (Vis) regions. Although luminescence techniques are more sensitive than optical absorption, enabling the detection of certain centres at concentrations less than one in many millions of host atoms, the latter method has the advantage of being quantitative as it is not affected by nonradiative processes [23].

The absorption of a material is quantified by the *absorption coefficient*, α, which is defined as the fraction of the light intensity absorbed in a unit length of the medium. Thus, if surface reflections are ignored, the transmitted light intensity $I_t(E)$ of energy E passing through a sample of thickness t is determined by

$$I_t(E) = I_0(E) e^{-\alpha(E)/t} \tag{3-72}$$

such that

$$\alpha(E) = \frac{1}{t} \ln\left(\frac{I_0(E)}{I_t(E)}\right), \tag{3-73}$$

where $I_0(E)$ is the initial intensity of the incident light [24]. Absorption occurs when the electromagnetic radiation interacts with the electric dipole of a defect or molecule, creating or changing an electric dipole moment. Subject to selection rules, the absorption spectra reflect allowed electronic, vibrational and rotational transitions and combinations thereof. As diamond is a solid material the atoms cannot rotate and rotational transitions will not contribute to the spectra.

3.3.1 Optical absorption in intrinsic diamond

The electrons of a free atom occupy discrete quantised energy levels defined by the solutions (wavefunctions) of the atom's Schrödinger equation. In solids the electron wavefunctions of neighbouring atoms overlap, so that the discrete energy levels are replaced by broad bands where the electron states are delocalised. The wavefunctions of the delocalised states possess the underlying translational symmetry of the crystal [24]. The orbital structure of an insulator or semiconductor consists of two (or more) bands separated by a *band-gap* where orbitals are forbidden as the Schrödinger solutions are non-wavelike. For diamond the valence band, where the wavefunctions of the valence electrons are valid, and the conduction band are separated by an indirect band-gap of energy $E_g \sim 5.47\,\text{eV}$ [25]. Consequently the minimum photon energy required for an across band-gap electronic transition, where an electron is excited from the valence band to the conduction band, is given by E_g, giving rise to an intense absorption continuum for $E > E_g$. For this simple model the electronic absorption spectrum for energies below E_g would be featureless, i.e. transparent, as the homopolar, isotropic, covalent bonding of the diamond lattice results in a homogenous distribution of the electric charge density and an absence of electric dipole moments to interact with the incident electromagnetic radiation [26].

The atoms in the lattice are bound to equilibrium positions by the bonds and can be described as chains of masses connected by springs [24]. When the atoms are displaced relative to their equilibrium position they experience restoring forces which cause them to vibrate at characteristic frequencies. The motion of the atoms

can then be approximated as that of a harmonic oscillator with normal modes of vibrations, the *phonon modes*. Even at low temperatures each atom vibrates about an equilibrium position due to zero-point motion [26, 27]. However, unless a mechanism is provided for the vibration to couple with the electromagnetic wave which simultaneously conserves energy and momentum the incident radiation cannot be absorbed. The phonon modes can be divided into two general categories: *acoustic modes*, where the atoms experience longitudinal vibrations, and *optical modes*, where the two atoms in the primitive unit cell are displaced in opposite directions. If the bonding between the atoms were ionic rather than covalent the asymmetric electron cloud between the atoms creates a dipole which can oscillate, making the acoustic modes directly IR active (Restrahlen absorption) [24, 26]. However, the inversion symmetry of diamond and its covalent bonding prevents the creation of the dipoles necessary for single phonon absorption [28]. Multiple phonon absorption, where two or more phonons simultaneously interact to produce electric dipoles, can be detected in intrinsic diamond from 165 meV across energies which are multiples thereof [26]. The maximum frequency at which a phonon can propagate through the lattice is given by the Raman frequency, where the characteristic Raman frequency for diamond is observed at $1332\,\mathrm{cm}^{-1}$ (165 meV) [28–30]. This corresponds to the maximum energy in the Brillouin zone, which occurs when the transverse and longitudinal optical modes are degenerate and the wave vector is zero.

3.3.2 Point defect induced optical absorption

Defects in the crystal lattice introduce dipole moments which might modify the optical absorption spectrum of intrinsic diamond. The symmetry of the lattice will be lowered at the defect, disturbing the electronic charge distribution and forming electronic states within the band-gap. A *direct electronic transition* may be induced between the defect states by the absorption of a photon with energy equal to the energy separation of the states as long as there is a non-zero rate of change in the dipole moment of the defect during the time taken by the transition to occur [27]. This purely electronic transition does not involve vibrational quanta and produces a sharp spectral line known as the *zero phonon line* (ZPL) whose

energy is characteristic to the specific centre and can therefore be used for defect identification.

If allowed by the centre's symmetry it is possible that the defect-related bond vibrations may create an oscillating dipole, producing a second order dipole moment [27]. Provided that momentum and energy are conserved these vibrations could couple to incident electromagnetic oscillating waves resulting in vibrational absorption. Such absorption is allowed in the otherwise forbidden one-phonon region of the spectrum (§3.3.1) as the periodicity of the diamond lattice has been broken by the defect. It is possible that the natural resonance of a centre is greater than the highest allowed frequency for the lattice, given by the Raman frequency. Consequently in this case the defect-related vibrational mode cannot propagate through the lattice and is instead localised in both frequency and space [23]. These modes are known as *local vibrational modes* (LVMs) and manifest themselves as sharp lines in the absorption spectrum. Usually LVMs occur at impurities lighter than the carbon atoms which comprise the crystal and at strongly bound defects [23].

The electronic states of point defects can couple strongly to the vibrational modes of the crystal lattice via the electron-phonon interaction. The electronic states of the defect are broadened into a continuum of states known as the vibronic band. Note that the vibronic bands are created by the interaction of discrete electronic states with the phonon modes of the solid in contrast to the electronic bands discussed in §3.3.1, where the continuum arises from the overlap between the electron wavefunctions of neighbouring lattice atoms. When bands are formed in solids it is useful to invoke the concept of the *density of states function* $g(E)$ such that the number of states within a given energy range of a band is expressed by $g(E)dE$. The absorption intensity is determined by the quantum mechanical transition rate for exciting an electron between two different energy levels (subject to selection rules), which is proportional to the density of states and the square of the electric dipole matrix element [24]. Thus $g(E)$ needs to be determined in order to calculate the absorption and emission (§3.4) spectra due to band-gap transitions (§3.3.1) and to model the shape of the vibronic bands.

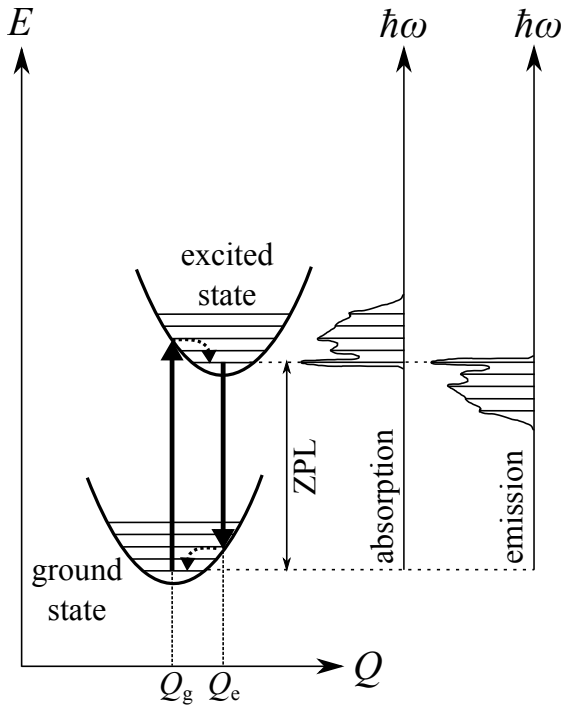

Figure 3-9: Configuration diagram for the ground and excited electronic states of a vibronic centre. Optical transitions are depicted by vertical arrows following the Franck-Condon principle. The dashed arrows indicate the non-radiative transitions that occur in order to bring the system to the equilibrium position from the excited vibrational states. The general shape of the absorption and emission spectra are illustrated on the right hand side of the figure. Figure adapted from Ref. [24].

3.3.3 Vibronic absorption spectra in diamond

According to the *Born-Oppenheimer approximation* the electronic and nuclear motions can be treated as independent since the nuclei are far heavier than the electrons and thus their motion occurs at a substantially slower time scale [24]. The approximation allows us to create configuration diagrams where the electronic energy is plotted as function of a generalised coordinate Q, which has the dimension of length (Fig. 3-9). If the ground and excited electronic states of a system are assumed to be bound each vibronic band will have a minimum energy at some value of Q. The minima occur at the equilibrium position of the optically active centre for each state. In general these minima will not be centred about the same value of Q, with the ground and excited state energy minima occurring at Q_g and Q_e, respectively, and $Q_g < Q_e$ [24]. The energy of the ground electronic state can

be expanded as a Taylor series about Q_g

$$E(Q) = E(Q_g) + \frac{dE}{dQ}(Q - Q_g) + \frac{1}{2}\frac{d^2E}{dQ^2}(Q - Q_g)^2 + ... \tag{3-74}$$

At equilibrium $dE/dQ = 0$ so that $E(Q)$ is approximated by a parabolic function, which to the first order it is equivalent to a harmonic oscillator potential. The same analysis can be extended to the excited states.

The Born-Oppenheimer approximation leads to the *Franck-Condon principle*, which states that the optical transitions occur so rapidly that the nuclei do not move significantly [24]. Consequently the transitions in a configuration diagram are depicted by vertical arrows when the electron moves between states. At 0 K the minimum energy required for an absorption transition is given by the energy separation between the lowest vibrational level of the ground state and that of the excited state, producing a ZPL. An absorption band consists of the ZPL and a series of lines at higher energies created by transitions from the lowest vibrational ground state to the vibronic energy levels of the excited state. However, rather than observing sharp vibronic transitions the spectral vibronic structure is broadened into a continuum by the coupling of the electronic states to the many different phonon modes of the lattice covering a range of frequencies.

Experimental data for optical absorption measurements can be explained by considering the coupling between isolated electronic states and totally symmetric vibrations. As a starting point is it instructive to assume that there is only one dominant mode of vibration. Using the Born-Oppenheimer approximation the total wavefunction ψ for a centre can be separated into an electronic part $\phi(r)$, where r is the electronic coordinate, and a vibrational part $\chi(Q)$. At low temperatures ($kT \ll \hbar\omega$) the defect is initially in its ground state. If the equilibrium point for the ground state is defined to be at $Q = 0$ the total wavefunctions in the ground (g) and excited (e) states can be written as

$$\psi_g(r, Q) = \phi_g(r)\chi_0(Q) \qquad \psi_e(r, Q) = \phi_e(r)\chi_n(Q - Q_e) \tag{3-75}$$

where the zeroth harmonic oscillator state and the nth vibrational state are represented by $\chi_0(Q)$ and $\chi_n(Q - Q_e)$, respectively [23].

Optical transitions between the ground and excited states have a transition

probability which depends on the square of the integral

$$\iint dr dQ \psi_e^* D \psi_g \tag{3-76}$$

and D is the electric-dipolar operator of the light [31]. Applying the *Condon approximation* the integral can be factorised into electronic and vibrational parts which are independent of each other [31]. Therefore, using this approximation and Eq. 3-75 it can be rewritten as

$$\int dr \phi_e^*(r) D \phi_g(r) \int dQ \chi_n^*(Q - Q_e) \chi_0(Q) \tag{3-77}$$

The first integral can be taken as constant whose value depends on the radiative decay time of the transitions. It is then useful to define the second integral as

$$M_{0n} = \int dQ \chi_n^*(Q - Q_e) \chi_0(Q) \tag{3-78}$$

so that

$$|M_{0n}|^2 = \frac{e^{-S} S^n}{n!} \tag{3-79}$$

where S is the *Huang-Rhys factor* [31].

Following the Franck-Condon principle the optical absorption transition of the electron from the ground state to the excited state occurs so rapidly that the position of the nuclei does not change. Since the equilibrium positions of the two electronic states differ the electron will have been promoted to an excited vibrational state as well as an excited electronic state (Fig. 3-9). The excess vibrational energy is lost by non-radiative relaxation processes (heat) and the nuclei move to their new equilibrium position [24]. The dimensionless Huang-Rhys factor is a measure of the relaxation energy in units of the quantum of vibration $\hbar\omega$, i.e. $S = E_R/\hbar\omega$. It is characteristic to centres and values have been tabulated for defects in diamond in Ref. [31]. At $T = 0\,\mathrm{K}$

$$S = \ln\left(\sum_{n=0}^{\infty} \frac{|M_{0n}|^2}{|M_{00}|^2}\right) = \ln\left(\frac{A_{\mathrm{VB}}}{A_{\mathrm{ZPL}}}\right) \tag{3-80}$$

where A_{ZPL} and A_{VB} are the integrated intensities of the ZPL and the vibronic band, respectively. For the single-mode model the absorption and luminescence transitions are very similar, resulting in spectra that are mirror images of each other, reflected about the ZPL, as illustrated in Fig. 3-9.

If the temperature of the system is increased several vibrational levels of the ground state become populated. The population of each phonon mode is given by the *Born-Einstein number* [31],

$$n(\omega) = [\exp(\hbar\omega/kT) - 1]^{-1} \tag{3-81}$$

The ZPL is the sum of transitions between vibrational states with the same quantum numbers, i.e. $\phi_g\chi_0 \rightarrow \phi_e\chi_0$, $\phi_g\chi_1 \rightarrow \phi_e\chi_1$, ... $\phi_g\chi_N \rightarrow \phi_e\chi_N$. The temperature dependence of ZPL can be predicted if S is known and a single-mode model is assumed, using:

$$A_{ZPL} \propto \exp[-S\coth(\hbar\omega/2kT)]J_0[S\mathrm{csch}(\hbar\omega/2kT)] \tag{3-82}$$

where J_0 is a Bessel coefficient [31–33]. In this model the frequency and width of the ZPL are independent of temperature [31].

The vibronic theory can now be expanded to consider the existence of many modes simultaneously. If it is assumed that only linear electron-phonon coupling is allowed and the modes behave independently (harmonic approximation) the coupling will spread out the transitions, modifying the spectral shape. However, the integrated intensity over the entire spectral band for the centre will remain unchanged.

Each mode has a Huang-Rhys factor S_i so that $S_i\hbar\omega_i$ is the relaxation in the ith mode. Hence, the total Huang-Rhys factor is $S = \Sigma_i S_i$.

Summing all independent ways of creating n phonons the total relative intensity is

$$\sum_{n=0}^{\infty} |M_{0n}|^2 = 1 \tag{3-83}$$

It is noteworthy that this condition is independent of temperature; as the temperature changes the relative intensity of the ZPL and the vibronic sideband will change, but the overall spectral integrated intensity will still be unity. The shape of the n-phonon sideband can be determined assuming that the modes are independent and that the combination of phonons occur statistically. To create n phonons which absorb at a frequency ν from the ZPL $(n-1)$ phonons can be created which absorb at $(\nu - \omega)$ and simultaneously create a phonon of frequency ω. Thus, if the intensity of the one-phonon sideband involving phonon frequencies

in the range $\omega \to \omega + d\omega$ is defined as $I_1(\omega)d\omega$ the shape of the the n^{th} band is given by the convolution of the $(n-1)^{\text{th}}$ sideband and the one-phonon sideband:

$$I_n(\nu) = \int_0^{\omega_m} d\omega I_{n-1}(\nu - \omega) I_1(\omega) \tag{3-84}$$

where ω_m is the centre's maximum vibrational frequency.

Finally, it is worth noting that the "bandshapes" referred to in this section ($I_1(\omega)$, $I_n(\omega)$, $I_{n-1}(\omega)$) are transition probabilities. Therefore, they must be multiplied by the photon frequency ν in order to give an absorption spectrum and ν^3 for a luminescence spectrum [31].

3.3.4 Isotope effects

Changing the isotopic abundance of either the lattice atoms or the impurity atoms involved in the centre (if any, as this analysis is also applicable to vacancy defects) has the effect of shifting the ZPL and vibronic band along the energy-axis of the spectrum through a series of mechanisms, grouped into the static and dynamic shifts. Isotopic shifts of optical transitions (both in absorption or luminescence) are an important tool in identifying the centres responsible for the band since isotopic substitution of a suspected elemental component of the defect could result in a measureable shift, unequivocally linking the centre to that specific element. The key points which explain the isotopic shifts of optical bands will be described here, but for a more thorough discussion the reader is directed to the work by Hughes [34].

The *static shift* of the ZPL occurs by the change in the volume created when the isotope is changed. Diamond made with the natural carbon consists of 98.89% ^{12}C and 1.11% ^{13}C [8]. The lattice volume (V) of isotopically pure diamond would change by $\Delta V/V = -4.5 \times 10^{-4}$ if the carbon isotope is changed from ^{12}C to ^{13}C [35, 36]. The response of the centre to the hydrostatic compressive stress from the lattice produces an increase in the zero phonon energy [37, 38]. Isotope shifts for the ZPL of several centres in diamond created by changing the ^{13}C content from 1.1% to 99.9% have been tabulated by Davies in Ref. [37].

The *dynamic shift* is more complicated. An isotopic abundance change results in a change in the nuclear mass of the atomic species, modifying the reduced mass

of the vibrating system. Hence the "mass" of each vibrational mode is altered, leading to a change in the frequency of each mode since $\omega \propto 1/\sqrt{m}$ [23]. The single-mode model discussed in §3.3.3 is based on the linear coupling between the electronic states and harmonic vibrations. The ZPL consists of the sum of the absorption created by transitions between the ground and excited states for vibrational states with the same phonon quanta ($\phi_g\chi_n \rightarrow \phi_e\chi_n$, where $n \geq 0$). According to this model changing the isotope will result in an equal change in the frequency of the ground and excited state modes and consequently no change in the energy difference between the states so that the ZPL will not shift in energy [23].

The dynamic shift for the ZPL can only be understood if high-order electron-phonon coupling and anharmonic potentials are allowed [23]. If the coupling is not limited to being linear the electronic transition will result in a net movement of the electron distribution and a change in the chemical bonding of the centre. Consequently, the equilibrium positions of the atoms will be changed and the vibrational frequencies for the ground and excited states will differ, $\omega_g \neq \omega_e$. For example, let the isotope change from 1 to 2. The effective mass m will produce a change in the mode frequency so that

$$\omega_1/\omega_2 = \sqrt{m_2/m_1} \tag{3-85}$$

At $T = 0\,\mathrm{K}$ only transitions between the zero-point ground and excited states occur, with energies $\hbar\omega_g/2$ and $\hbar\omega_e/2$, respectively.The ZPL shift is then given by [23]

$$\Delta E_{\mathrm{ZPL}} = \frac{1}{2}(1 - \sqrt{m_1/m_2})(\hbar\omega_{e1} - \hbar\omega_{g1}) \tag{3-86}$$

where the frequencies are specifically those for isotope 1. Usually $\omega_e < \omega_g$ so if $m_1 < m_2$ the isotope change will result in an increase in the ZPL energy. Although this is often the case, negative shifts have also been observed [37].

At $T > 0\,\mathrm{K}$ vibrational states with higher phonon quanta will be populated so that the mean quantum state occupied is given by the Bose-Einstein number, given in Eq. 3-81. The temperature dependence of the shift of the mean energy for the ZPL line is then [23]

$$\Delta E_{\mathrm{ZPL}}(T) = n(\hbar\omega_e - \hbar\omega_g) \tag{3-87}$$

When analysing the temperature dependence of E_{ZPL} the contribution from the lattice expansion needs to be taken into account [23, 39].

Finally, the anharmonicity in the vibrational spectrum will affect the ZPL isotope dependence. The anharmonicity of the bond determines the bond length, with the mean position of the vibrating system being centred at a position which is not the minimum of the potential. If the isotope mass is increased the zero-point energy increases and the equilibrium position will move closer to the potential's minimum, i.e. the bond shortens. This introduces a strain which shifts the ZPL to a higher energy [37].

3.3.5 Measuring concentrations

The integrated absorption over the entire optical band for a point defect is proportional to the concentration of the centres in the crystal. The constant of proportionality is known as the calibration constant. For a homogeneous sample the integrated absorption coefficient of the absorption band of a point defect can be related to the concentration N of the centres using *detailed balance* for the optical absorption process, given by

$$N = \frac{g_f}{g_i}\frac{9}{\pi^2}\frac{E^2\tau_{\mathrm{R}}}{\hbar^3 c^2}\frac{n^2}{(n^2+2)^2}\int \mu(E)dE \tag{3-88}$$

where g_i and g_f are the degeneracies of the initial and final states of the optical transition with energy E, $\hbar$ is the reduced Planck constant, c is the speed of light in vacuum, n is the refractive index of the material and τ_{R} is the transition's radiative lifetime (in the absence of nonradiative processes) [23]. This equation is usually accurate to a factor of ~ 2 for centres in diamond [38].

Strictly speaking, the integrated absorption in Eq. 3-88 should cover the ZPL and the vibronic sideband. However, it can be difficult to measure the integrated absorption of the vibronic sideband accurately as it can be distorted by underlying features. Due to the broadness of the band small changes to the baseline can introduce large errors. Therefore, conventionally the calibration constants (in units of $\mathrm{meV\,cm^2}$) for centres in diamond have been determined by integrating the absorption coefficient of the zero phonon line (in $\mathrm{cm^{-1}\,meV}$) at liquid nitrogen temperature (77 K). By keeping the temperature constant the intensity of the ZPL

relative to the vibronic band will be characteristic of the defect and thus applicable for concentration measurements for different samples. If all the parameters in Eq. 3-88 are known the coefficient can be calculated. However, the true radiative decay times are unknown for many point defects in diamond. The calibration constant can be calculated by determining the concentration of the centre using an alternative method, such as electron paramagnetic resonance for paramagnetic defects, and correlating the concentration measurements for a suite of samples to the integrated absorption coefficients. A table of calibration constants for certain point defects in diamond can be found in Ref. [37].

3.4 Photoluminescence

Photoluminescence (PL), where the material re-emits light after absorbing a photon of energy, may occur by excitation with photons with energies less than or greater than the band-gap energy of diamond. PL is more complicated than absorption as it is intimately connected to both radiative and non-radiative energy relaxation mechanisms. Consequently PL is often not considered to be quantitative, although it is very sensitive, allowing the detection of some luminescent centres at concentrations less than one in many millions of carbon atoms [23].

Above band-gap excitation results in the strong absorption of the photons, as explained in §3.3.1. The excitation promotes electrons from the valence band to the conduction band, creating free holes in the valence band. The electrons and the holes may associate, forming excitons [23, 24]. The lifetime of the excitons may be sufficiently long for them to diffuse a significant distance within the lattice, where the electron can be trapped by a centre (bound exciton) [23].

Alternatively, the electron can de-excite and be trapped at a centre. The centre is then left in an excited state with a population of electrons in the excited vibronic band (due to electron-phonon coupling), illustrated in Fig. 3-9. The electrons relax rapidly to the zeroth mode of the excited state by the emission of phonons, conserving both energy and momentum via this non-radiative process. From this state the electrons may drop to the unpopulated vibronic levels of the ground electronic state of the centre, emitting photons. The non-radiative processes will

ultimately reduce the luminescence intensity of the centre, rendering the technique unsuitable for concentration measurements. The luminescence efficiency of the centre will be determined by its radiative (τ_{R}) and non-radiative (τ_{NR}) lifetimes: if $\tau_{\mathrm{R}} \gg \tau_{\mathrm{NR}}$ the centre will be an efficient photon emitter. Furthermore, there may be several different species of centres which can act as traps, competing for the available electrons [23]. Also, note that the luminescence is occurring from centres which may be located a significant distance away from the point of excitation with the incident photons. Therefore, the measured intensity is not necessarily representative of the concentration of point defects at the original point of excitation.

The resulting emission spectrum will reveal the energy separation between the defect states and their vibronic structure, and is unambiguously characteristic of the specific species of optical centre. If the system contains a dominant mode the PL spectrum (measured as a function of energy) will be the mirror image of the absorption spectrum for the point defect, with the ZPL transition as the point of reflection [24, 37]. Figure 3-9 illustrates an example for the formation of both absorption and emission spectra for a centre.

Below band-gap excitation will not be absorbed by the lattice, but may be absorbed by colour centres producing direct excitation if the energy of the exciting light is equal to or greater than the energy separation between the ground and excited vibronic bands of the centres. The upper limit for the excitation energy will be set by the oscillator strength of the centre, which determines the vibronic structure. Hence the luminescence intensity will depend on both the oscillator strength and the concentration of the centres in the material.

References

[1] J. A. Weil and J. R. Bolton, *Electron Paramagentic Resonance: Elementary Theory and Practical Aplications* (John Wiley & Sons, Hoboken, 2007).

[2] B. Odom, D. Hanneke, B. D'Urso, and G. Gabrielse, Physical Review Letters **97** (2006).

[3] A. Abragam and B. Bleaney, *Electron Paramagnetic Resonance of Transition Ions* (Clarendon Press, Oxford, 1970).

[4] D. Hunt, Ph.D. thesis, University of Oxford (1999).

[5] J. R. Morton and K. F. Preston, J. Magn. Reson. **30**, 577 (1978).

[6] J. E. Wertz and J. R. Bolton, *Electron Spin Resonance* (Chapman and Hall, New York, 1986).

[7] J. M. Baker and M. E. Newton, Appl. Magn. Reson. **7**, 209 (1994).

[8] R. C. Weast, ed., *CRC Handbook of Chemistry and Physics* (CRC Press, Cleveland, 1976), 57th ed.

[9] C. P. Slichter, *Principles of Magnetic Resonance* (Springer-Verlag, New York, 1978).

[10] R. T. Weber, *E 580 User's Manual*, Bruker BioSpin Coorporation, Billerica, MA USA, 2nd ed. (2005).

[11] L. Kevan and R. N. Schwartz, eds., *Time Domain Electron Spin Resonance* (John Wiley & Sons, New York, 1979).

[12] L. Kevan and M. K. Bowman, eds., *Modern Pulsed and Continuous-Wave Electron Spin Resonance* (John Wiley & Sons, New York, 1990).

[13] P. Atkins and R. Friedman, *Molecular Quantum Mechanics* (Oxford, Oxford, 2005).

[14] D. J. Twitchen, M. E. Newton, J. M. Baker, T. R. Anthony, and W. F. Banholzer, Phys. Rev. B **59**, 12900 (1999).

[15] M. A. Lea-Wilson, J. N. Lower, and J. A. van Wyk, Philos. Mag. B **72**, 81 (1995).

[16] C. D. Clark, R. W. Ditchburn, and H. B. Dyer, Proc. Soc. London, Ser. A **237**, 75 (1956).

[17] C. A. Coulson and F. P. Larkins, J. Phys. Chem. Solids **30**, 1963 (1969).

[18] P. W. Atkins, M. S. Child, and C. S. G. Phillips, *Tables for Group Theory* (Oxford University Press, Oxford, 1970).

[19] A. Cox, Ph.D. thesis, University of Oxford (1993).

[20] A. M. Edmonds, Ph.D. thesis, University of Warwick (2008).

[21] W. Smith, P. P. Sorokin, I. L. Gelles, and G. J. Lasher, Phys. Rev. **115**, 1546 (1959).

[22] G. F. Knoll, *Radiation Detection and Measurement* (John Wiley & Sons, New York, 1979).

[23] G. Davies, Semiconductors and Semimetals **51(P2)**, 1 (1998).

[24] M. Fox, *Optical Properties of Solids*, Oxford Master Series in Condensed Matter Physics (Oxford University Press, Oxford, 2001).

[25] C. Nebel and J. Ristein, *Thin-Film Diamond I - Semiconductors and Semimetals* (San Diego, 2003), vol. 76, chap. Preface.

[26] D. R. Charles, Ph.D. thesis, King's College London (2008).

[27] H. E. Smith, Ph.D. thesis, King's College London (2004).

[28] M. Lax and E. Burstein, Phys. Rev. **97**, 39 (1955).

[29] C. Ramaswamy, Nature **125**, 704 (1930).

[30] S. A. Solin and A. K. Ramdas, Physical Review B **1**, 1687 (1970).

[31] G. Davies, Reports on Progress in Physics **44**, 787 (1981).

[32] K. Huang and A. Rhys, Proc. R. Soc. A **204**, 406 (1950).
[33] K. K. Rebane, *Impurity Spectra of Solids : Elementary Theory of Vibrational Structure* (Plenum Press, New York, 1970).
[34] A. E. Hughes, Proc. Phys. Soc. **88**, 449 (1966).
[35] H. Holloway, K. C. Hass, M. A. Tamor, T. R. Anthony, and W. F. Banholzer, Phys. Rev. B **44**, 7123 (1991).
[36] H. Holloway, Phys. Rev. B **45**, 6353 (1992).
[37] G. Davies, Physica B **274**, 15 (1999).
[38] G. Davies, I. Kiflawi, G. Sittas, and H. Kanda, J. Phys.- Condens. Mat. **9**, 3871 (1997).
[39] G. A. Slack and S. F. Bartram, Journal of Applied Physics **46**, 89 (1975).

Chapter 4

Experimental Details

4.1 Electron Paramagnetic Resonance

Electron paramagnetic resonance (EPR) measurements provide the backbone of this thesis and were made on a variety of spectrometers at both X-band and Q-band ($\sim 9.75\,\mathrm{GHz}$ and $\sim 35\,\mathrm{GHz}$, respectively). The continuous wave (CW) spectra enabled the determination of paramagnetic impurity concentrations and the chemical and structural identification of point defects. The components of a CW EPR spectrometer (Fig. 4-1) will be discussed, providing the foundation necessary to introduce the specific setups used for the research conducted. This information will then be built upon in order to explain the key specifications of the pulsed EPR spectrometer utilised in the study of the relaxation behaviour of spin systems. For CW EPR measurements the magnitude of the "static" magnetic field ($\mathbf{B}$) is swept, altering the separation between the energy levels of a paramagnetic defect, whilst the frequency and amplitude of the oscillating microwave magnetic field ($\mathbf{B}_1(t)$) are kept constant. When the energy separation is equal to the energy provided by $\mathbf{B}_1(t)$ a magnetic dipole transition can occur, subject to selection rules. Conversely, for a pulsed EPR experiment $\mathbf{B}$ is chosen to fulfill the resonance condition, and the magnitude of $\mathbf{B}_1(t)$ is varied, applying pulses to perturb the spin system.

A series of different EPR spectrometers were utilised. The X-band measurements were made using either the commercially available Bruker EMX or and EMX-E systems, whilst spectra were collected at Q-band using a Clarendon-built[1] spectrometer. Finally, pulsed EPR data were acquired using a Bruker ELEXSYS E580 FT-EPR spectrometer. Details for the experimental setups are summarised

[1]This Q-band spectrometer was built at the Clarendon Laboratory of the University of Oxford. It has been described in detail by Twitchen [1] and Talbot-Ponsonby [2], and has subsequently been modified by Edmonds [3].

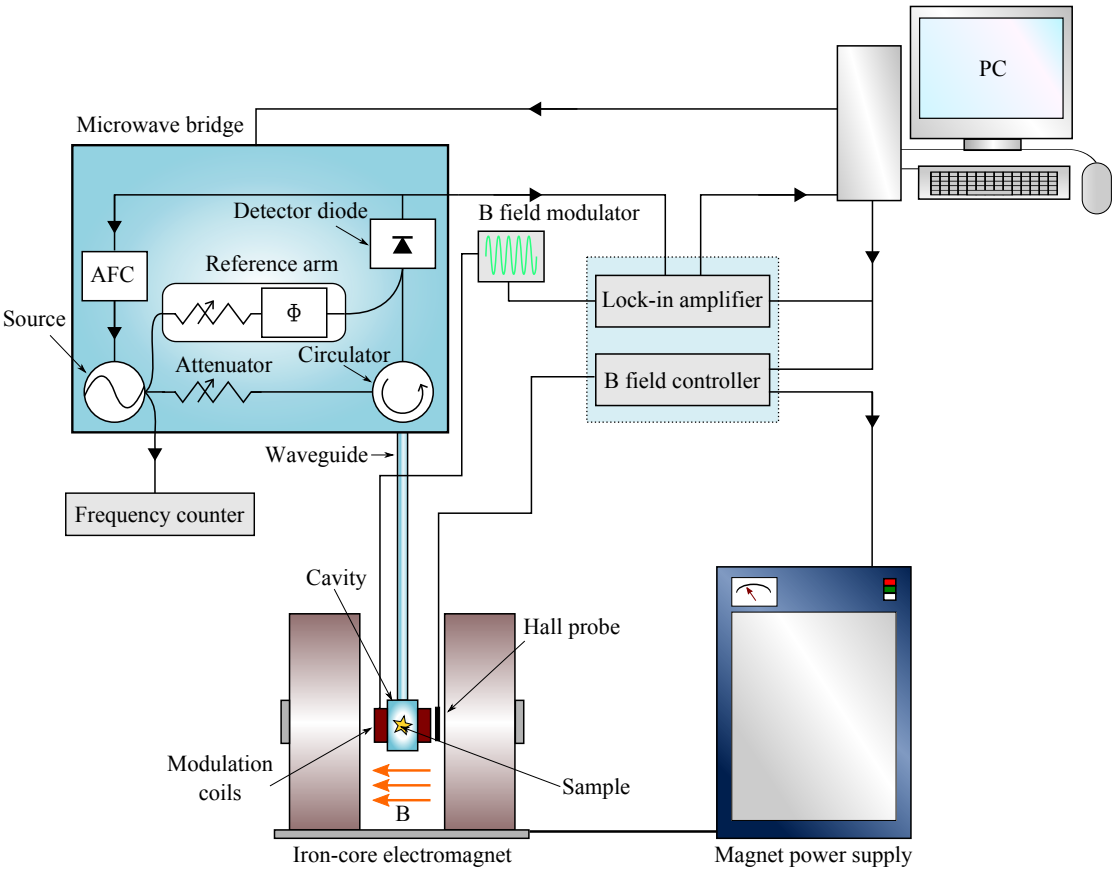

Figure 4-1: Schematic of a standard continuous wave X-band ($\sim 9.5\,\mathrm{GHz}$) electron paramagnetic resonance (EPR) spectrometer.

in Table 4-2.

For a more comprehensive explanation of EPR equipment operation and the individual spectrometer components, the reader is directed to the textbooks by Weil and Bolton [4] and Poole [5].

4.1.1 Magnetic field

The magnetic fields for all the EPR spectrometers used in this study were provided by iron-core electromagnets. For higher fields ($> 2\,\mathrm{T}$) systems can be constructed which utilise superconducting magnets. The main requirements for a magnetic field is that it is both stable and uniform over the sample volume studied. Furthermore, it must be possible to scan the magnetic field reproducibly. Since the relationship between the magnetic field generated by an iron-core electromagnet and the current provided is inherently non-linear it is necessary to incorporate an

Table 4-1: The main characteristics of the frequency bands used for EPR experiments, emphasising the X- and Q-bands since they were used in this work. Details included are the typical frequency of operation ν_{typical}, the magnetic field for the free electron g-factor (§3.1.1) at that frequency $B(g = g_e)$, and the approximate linear dimension for an appropriate cavity [6].

Band	ν_{typical} (GHz)	$B(g = g_e)$ (mT)	Cavity dimensions (cm)
L	1.5	54	20
S	3.0	110	10
C	6.0	220	5
X	9.5	340	3
K	23	820	1.3
Q	34	1300	0.8
W	94	3400	0.3
D	150	5400	0.2
G	250	9000	0.1

active feedback loop to regulate this current. For this purpose, a temperature-stabilised Hall probe, located at a position close to the sample, is connected to a magnetic field controller. The probe is unable to measure absolute field magnitudes, but is sensitive to relative changes. Therefore, the probe is externally calibrated, commonly using a known NMR signal, after which it is able to consistently bring the field to chosen values.

4.1.2 Microwave source and bridge

Microwaves for EPR systems are usually produced by either a Gunn diode or a klystron; the spectrometers used in this work only used the former source. Conventionally, spectrometers are classed according to the range of frequencies over which they operate, referred to as the *band*. Table 4-1 characterises the common frequency bands, emphasising the details for the X- and Q-bands used in this research.

Multifrequency investigations greatly aid in the determination of spin Hamiltonian parameters for an unknown paramagnetic defect, facilitating the differentiation of the contributions from field independent (e.g. hyperfine) and field dependent (e.g. Zeeman) interactions. Higher frequencies can also help resolve overlapping spectra for centres with small Zeeman anisotropy. Furthermore, since

Table 4-2: EPR spectrometers, accessories and resulting regimes employed for the research in this thesis. The frequency bands presented in parentheses can also be produced by the spectrometer, but were not used.

Spectrometer	Type	Frequency band	Bridge	Resonator	Temperature range (K)	Temperature control system	Optical excitation
Bruker EMX-E	CW	X	ER041XG-H	ER4122SHQ (TE_{011})	~300	None	No
Bruker EMX	CW	X (& Q)	ER041XG	ER4105DR (TE_{104})	~300	None	Yes, light via quartz rod
					4 – 300	Oxford Instruments ESR-900	Yes, light via quartz rod
				EX-102 (TE_{011})	300 – 750	Inconel wire heater (WG-836-A & WG-838-A) with K-type thermocouple [3]	No
Clarendon-built	CW	Q	See [1] and [2]	Cylindrical TE_{011} mode cavity in ER5102QT probe head [1, 2]	~ 300	None	No
Bruker ELEXSYS E580	pulsed	X (& Q)	SuperX FT-EPR bridge (with SuperQ-FT multifrequency upgrade)	Flexline Series ER4118X-MD5	4 – 300	Oxford Instruments CF935O	Yes, light via quartz rod or through side window

the absolute spin sensitivity of an EPR spectrometer generally increases with higher frequencies [5], this behaviour may be exploited to improve the signal intensity. However, increasing the frequency also has its limitations. Not only does the cost of the spectrometer increase, but at higher frequencies the sample volume becomes restricted and microwave power saturation (§3.1.5.2 and §4.1.4) may become practically difficult to avoid. These additional factors mean that the theoretical improvement in the signal intensity is often not accomplished.

For the commercial Bruker spectrometers the microwave source is located in the microwave bridge, as illustrated in Fig. 4-1. The output of the microwave source is controlled by a variable attenuator, after which it passes through a circulator and then into the cavity via a waveguide. Since most EPR spectrometers measure changes in the reflected power from the cavity, the circulator is used to separate the incident and reflected microwaves. The reflected microwave power is directed to a Schottky diode which is biased by $\sim 1\,\mathrm{mW}$ power from a reference arm, converting the microwave power to a current. A phase shifter is used to match the phase of the reference arm to that of the reflected microwaves. The applied bias ensures that the diode output falls within the linear range of the detector. The detector system is further explained in §4.1.4.

Several different bridges were used with the various EPR spectrometers. They are often interchangeable, enabling the user to customise the cavity/bridge configuration which best suits the investigation. For the Bruker EMX and EMX-E systems a Bruker ER041XG and ER041XG-H were used, respectively. The former system has a maximum attenuation of $60\,\mathrm{dB}$ ($2 \times 10^{-4}\,\mathrm{mW}$) whilst the latter was used for measurements where attenuations up to $90\,\mathrm{dB}$ ($2 \times 10^{-7}\,\mathrm{mW}$) were necessary.

The Bruker ELEXSYS E580 pulsed system can operate at both *X*- and *Q*-band using a SuperX FT-EPR bridge, with a SuperQ-FT conversion accessory. In addition to creating microwaves and detecting reflected signals in its continuous wave mode, it is also able to detect free induction decay signals (FIDs) and echoes, defined in §3.1.6. This system is discussed separately in §4.1.5.

4.1.3 Resonators and sample mounting

The sample is placed in a resonator, whose purpose is to increase the energy density at the sample and consequently amplify the signal intensity. There are several different designs commercially available, depending on the sample characteristics, the frequency and temperature range to be investigated. Typically, the resonator will be a cavity, such as those used with the EMX and EMX-E spectrometers, but alternatively dielectric ring resonators may be used, as was the case for the pulsed spectrometer (Table 4-2). The cavities can be classified according to the type of mode that they can support: transverse electric (TE) or transverse magnetic (TM). These labels are commonly followed by a subscript which denotes the number of half wave-lengths along the three dimensions.

The cavity is said to be *critically coupled* when the frequency of the loaded resonator (the resonator with the sample) is the same as that of the incident microwaves, occurring when the impedance of the waveguide and loaded resonator are matched. Under these conditions, reflected power reaches the detector when EPR transitions are driven. The *Q-factor* is the ratio of the energy stored in the cavity to the energy dissipated per microwave cycle, and the higher the value, the better the sensitivity (all other things equal). The system can be coupled by adjusting the size of an iris which is located at the interface between the waveguide and the resonator. An automatic frequency controller (AFC) is used to keep the system on resonance by adjusting the frequency. Furthermore, there is the option to let the spectrometer automatically adjust the coupling by modifying the iris.

For reproducible (i.e. quantitative) data it is crucial that the sample is positioned at the optimum position in the resonator, and that the user is able to repeatedly return samples to the same location. The samples were placed in the resonator using two different types of sample rods which were held within either an Oxford instruments manual goniometer or a Bruker automatic goniometer, allowing rotation in the plane parallel to the magnetic field. The greatest range of sample rotational motion was achieved using a purpose-built German silver (an alloy with approximately 60% Cu, 20% Ni and 20% Zn) and brass rod with a dual-axis attachment [3, 7], where the sample was placed in a wheel of a Rexalite end-piece. Alternatively, a the end of a rod (usually quartz) could be polished

to various angles so that, once attached (using vacuum grease), the sample could rotate in a specific plane. For optical excitation experiments the samples were fastened to the end of a quartz rod whose ends had been polished to an optical finish. The quartz rod could be used as a lightguide, bringing the light from the top of the resonator to the sample, as described in §4.1.7.

4.1.4 Detection and analysis of CW EPR spectra

When EPR transitions occur, the reflected microwaves return to the microwave bridge, where their power is converted to a current by a Schottky diode (§4.1.2). The signal-to-noise ratio is improved by employing a phase sensitive detection scheme using a lock-in amplifier. This system is based on the magnetic field being modulated sinusoidally with an amplitude B_{m} and a frequency ν_{m} (typically $\sim 100\,\mathrm{kHz}$) simultaneously as it is swept. Thus the microwave detector output will have a component which is oscillating at a frequency ν_{m} and is proportional to the slope of the resonance line at that field. This latter point means that modulation transfer only occurs when the spectrometer is scanning over a resonance line.

If the modulation field is less than the intrinsic linewidth of the resonance line the resulting lineshape can be approximated by the first derivative of the original line. As the modulation field is further increased the lineshape will broaden. This may be favourably exploited if the signal suffers from microwave power saturation, as it detects the same number of spins across a wider region of magnetic field (hence less spins per magnetic field unit). However, if the modulation field is increased too much the lineshape will be distorted and resolution will be lost.

In the absence of microwave power saturation, explained in §3.1.5.2, the EPR signal intensity is proportional to the number of spins present. Quantitative analysis of concentrations may therefore be conducted by comparing the number of spins of the defect considered with that of a known reference sample [ref]. The signal intensity is also influenced by a number other factors, expressed in the following equation used to determine the concentration of a paramagnetic species [C] [4]:

$$[\mathrm{C}] = [\mathrm{ref}]\frac{I_{\mathrm{C}}}{I_{\mathrm{ref}}}\sqrt{\frac{(P_{\mu\mathrm{W}})_{\mathrm{ref}}}{(P_{\mu\mathrm{W}})_{\mathrm{C}}}}\frac{M_{\mathrm{ref}}}{M_{\mathrm{C}}}\frac{(B_{\mathrm{m}})_{\mathrm{ref}}}{(B_{\mathrm{m}})_{\mathrm{C}}}\frac{g_{\mathrm{ref}}^2}{g_{\mathrm{C}}^2}\frac{[S(S+1)]_{\mathrm{ref}}}{[S(S+1)]_{\mathrm{C}}}\frac{(t_a)_{\mathrm{ref}}}{(t_a)_{\mathrm{C}}}\frac{G_{\mathrm{ref}}}{G_{\mathrm{C}}}\frac{N_{\mathrm{ref}}}{N_{\mathrm{C}}} \qquad (4\text{-}1)$$

where it is assumed that the filling and Q factors are the same for both samples. I is the integrated intensity of the signal, $P_{\mu\mathrm{W}}$ is the microwave power, M is the sample mass, S is the effective spin, t_a is the acquisition time, G is the detector gain, and N is the number of scans collected for the spectrum. The terms are denoted by "ref" or "C" subscripts, which ascribe the terms to either the reference or the examined sample, respectively. The reference sample used in this study is a small, single growth sector of a HPHT synthetic type Ib diamond containing 270 ± 20 ppm atoms of single substitutional nitrogen, N_s^0. For quantitative work it is crucial that the environmental factors are identical for both samples, such as the spectrometer combination used, frequency, and sample temperature and position.

The integrated intensity of the EPR spectra was determined by fitting a simulated spectrum using software developed by Edmonds [3], known as EPR-Wizard. This enabled the simultaneous fitting of multiple overlapping spectra from different paramagnetic defects, facilitating their deconvolution. Since the EPR linshapes are usually not well produced by Lorentzian or Gaussian functions, a Tsallis function was employed instead [3]. EPR-Wizard relies on the user inputting the calculated line positions of a spectrum under certain experimental conditions (the frequency and magnetic field alignment relative to a crystallographic orientation).

These line positions can be output by EPR-NMR (using the EPR-Sim graphical user interface designed by Edmonds [3]), once the spin Hamiltonian parameters for the centre have been determined. EPR-NMR is a free program written by Michael Mombourguette and John Wiel, available online[2], which can be used to calculate spin Hamiltonian parameters from experimentally measured resonance line positions as a function of magnetic field orientation (i.e. a *roadmap*, as described in §3.2.3), or to simulate spectra. For more details regarding the simulation of the spectra and the different pieces of software used for their analysis the reader is referred to the thesis by Edmonds [3].

In the absence of microwave power saturation, decreasing the attenuation by 6 dB steps (i.e. increasing the power) results in the signal intensity increasing by a factor of two. When microwave power saturation (§3.1.5.2) is a problem, its effect

[2]http://www.chem.queensu.ca/eprnmr/

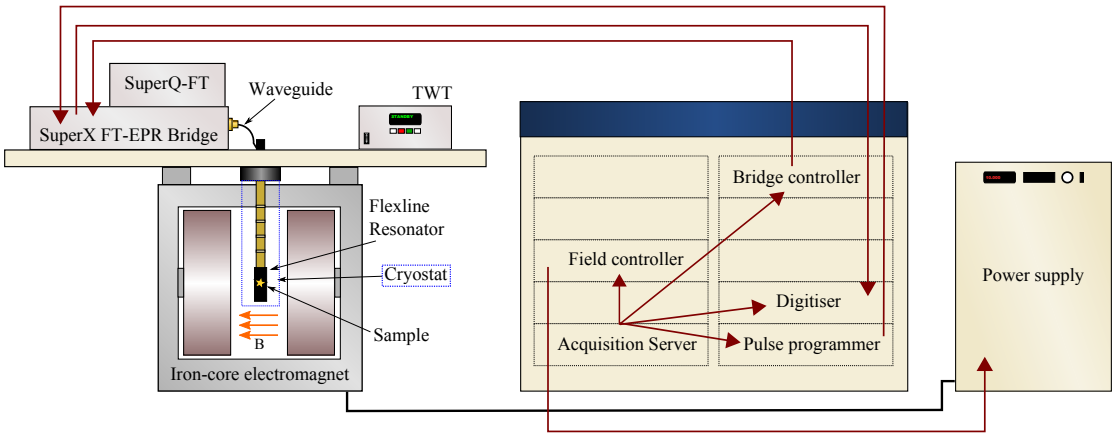

Figure 4-2: Schematic of a the Bruker ELEXSYS E580 pulsed EPR spectrometer. Adapted from a figure in [9, 10].

can be modelled using the following equation [8]:

$$I = \frac{\alpha\sqrt{P_{\mu\mathrm{W}}}}{\left(1 + \frac{P_{\mu\mathrm{W}}}{\beta}\right)^{\frac{1}{2}}} \tag{4-2}$$

where α and β are constants. As long as sufficient points are taken within the unsaturated region of powers, it is possible to fit the equation to the data and extract values for α and β. The unsaturated integrated intensity can then be determined.

4.1.5 Detection and analysis of pulsed EPR spectra

A schematic of a pulsed EPR system is illustrated in Fig. 4-2. Detailed information for the Bruker ELEXYS E580 pulsed spectrometer can be found in the operating manual [9, 10]; only the key components will be outlined here.

A SPFU (stripline pulse formation unit) housed in the microwave bridge, produces low power pulses by switching PIN (p-type, intrinsic, n-type) diodes on and off. The pulses are then amplified by a TWT (travelling wave tube, by Applied Systems Engineering, Inc., Fort Worth, Texas) which can produce 1 kW pulses. The amplitudes of the TWT pulses are controlled by an attenuator, enabling the modification of $B_1(t)$, which is proportional to $\sqrt{P_{\mu\mathrm{W}}}$. The PatternJet II and Xepr programs provided by Bruker allow the operator to orchestrate the pulse sequences. The pulses are directed to the resonator via a waveguide, with the reflected microwave power encoding FID and echo data. Due their weakness, it is

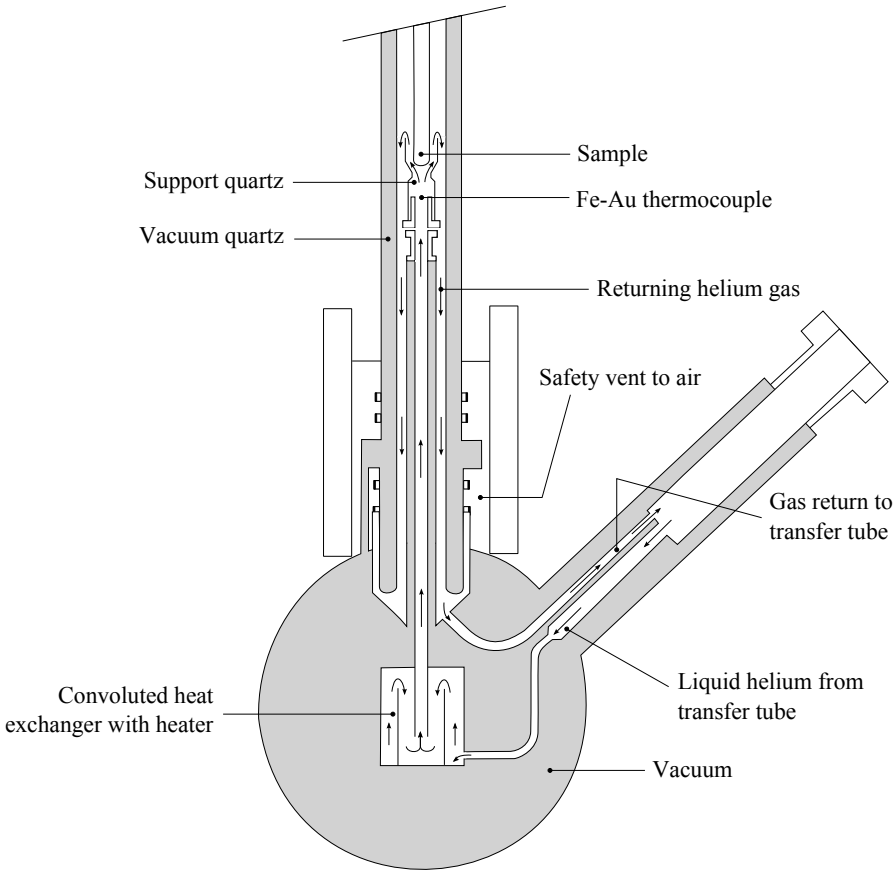

Figure 4-3: The Oxford Instruments EST-900 continuous flow cryostat used for low temperature continuous wave EPR measurements. Figure taken from the Oxford Instruments product guide [11].

necessary to amplify the signal. The amplifier is protected from the high power pulses using a defence pulse, which forces the system to wait (producing *dead time*) for the high power microwaves to dissipate before turning off the defence pulse, amplifying the signal and sending it to a quadrature detector. This detector is able to measure both the transverse magnetisation components in the rotating frame, extracting the amplitude and phase information necessary to transform the signal into a frequency representation. The output from the bridge is transferred to the SpecJet II console, which captures, averages and digitises the free induction decay (FID) and echo signals. The digitised data can then be analysed using the theory relevant to the chosen pulse sequence, as presented in §3.1.6.

4.1.6 Variable temperature EPR

EPR measurements in both CW and pulsed modes were performed at temperatures ranging from 4 to 300 K using cryogenic systems commercially available from Oxford Instruments. The CW spectra were collected using the Bruker EMX spectrometer equipped with an ESR-900 continuous flow helium cryostat with a Bruker ER4105DR rectangular cavity (Fig. 4-10). Meanwhile, pulsed measurements on the ELEXSYS E580 FT-EPR spectrometer employed an ER4118X-MD5 resonator in conjunction with an Oxford Instruments CF935O cryostat (Fig. 4-4). For this setup, both the resonator and the sample are immersed in the helium flow. The cryostat has a set of radial windows with a clear diameter of 5 mm to allow the user to illuminate the sample through the side of the cryostat, as discussed in §4.1.7.

The helium flow for both systems was provided by a dewar through an evacuated Oxford Instruments GFS300 flexline transfer tube. The gas flow was controlled using the transfer tube's needle valve, a small pump and an Oxford Instruments VC30 or VC31 controller. Temperatures were monitored by an Oxford Instruments ITC503 temperature controller, which was also connected to a heater located in the cryostat.

X-band CW EPR measurements spanning 300−750 K were taken on the Bruker EMX system furnished with a EX-102 high temperature cavity. Sample heating was accomplished by exposing it to a steady flow of nitrogen gas, which had been heated by passing by an Inconel wire heater. The temperature of the sample was read using a K-type thermocouple, and it was controlled by either changing the power to the heater power supply or by passing cold water within the cavity walls.

For further detail regarding the operation of the cryogenic and high temperature equipment, the reader is directed to the thesis by Edmonds [3].

4.1.7 Optically excited EPR setup

Optically excited EPR measurements were taken in both CW and pulsed modes. Broadband excitation was produced by a 1 kW Oriel Research HgXe Arc-lamp (model 55021), whilst 532 nm excitation was provided by a 532 nm Q-switched

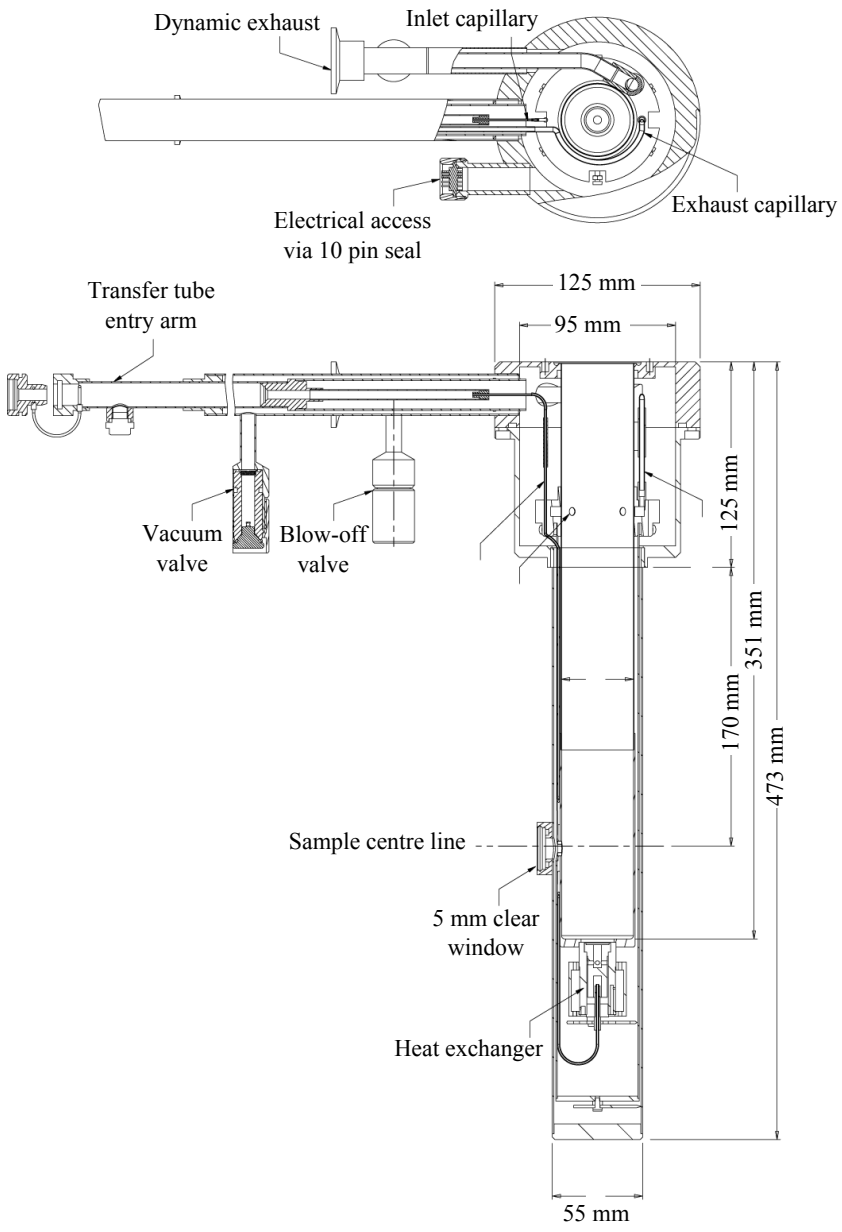

Figure 4-4: The Oxford Instruments CF935O immersion cryostat, with an optical access window, used for pulsed EPR experiments. The schematic has been adapted from the original presented in the Oxford Instruments product guide [11].

laser (MPL532-20μJ-5) with a 100 W peak power.

The HgXe arc-lamp is powered by an Oriel Universal Power Supply (model 68820), which allows the user to vary the output power in the range 400 – 1000 W. For safety purposes, the arc-lamp was run in conjunction with an Oriel Ozone Eater 66087, which efficiently filters ozone from the lamp's cooling air, converting it back into oxygen. The arc-lamp setup for EPR measurements has previously been described in detail by Edmonds [3]; only the main components will be outlined here. The output of the HgXe arc-lamp bulb (Oriel 1000 W HgXe, model 6293) was first collimated by a lens which is built into the lamp housing. The emission spectrum of the bulb is presented in Fig. 4-5. The infrared portion of the output (wavelengths $\lambda > 950$ nm) was removed by passing the light through a liquid filter containing distilled water, see Fig. 4-6. This was necessary in order to reduce the heat from the source, which may damage optical components. A focussing lens was employed to direct the light onto a lightguide, which brought the light to the top of a quartz sample rod whose ends had been polished to an optical finish. The sample, centred in a resonator, was mounted at the opposite end of the quartz rod by applying Araldite epoxy to the sample edges, thus ensuring that the adhesive did not interfere with the light transmission to the sample. Two different Lumatec liquid lightguides were used, the Series 300 ($300 < \lambda < 700$ nm) and Series 2000 ($420 < \lambda < 1500$ nm, protected by a Comar 420GY50 420 nm long-pass filter) models. Their transmission spectra are shown in Fig. 4-7.

Although the power rating for the arc-lamp is 1 kW, the optical components attenuate the power, ultimately reducing the power of the light incident on the sample. Tucker made measurements on a comparable experimental setup with a 100 W Hg arc-lamp, determining that only 200 mW of light arrived at the sample [15]. It is therefore reasonable to assume that the samples in this investigation only experienced broadband optical excitation with a maximum power of ~ 2 W, further depending on the lightguide utilised for the experiment. The energy cut-off of the light could be varied by inserting glass-long pass filters (supplied by Comar) in the unfocused light-path, simultaneously directing a steady flow of nitrogen gas onto the filters in order to cool them. This arc-lamp setup was employed on both the Bruker EMX CW EPR spectrometer equipped with the ER4105DR

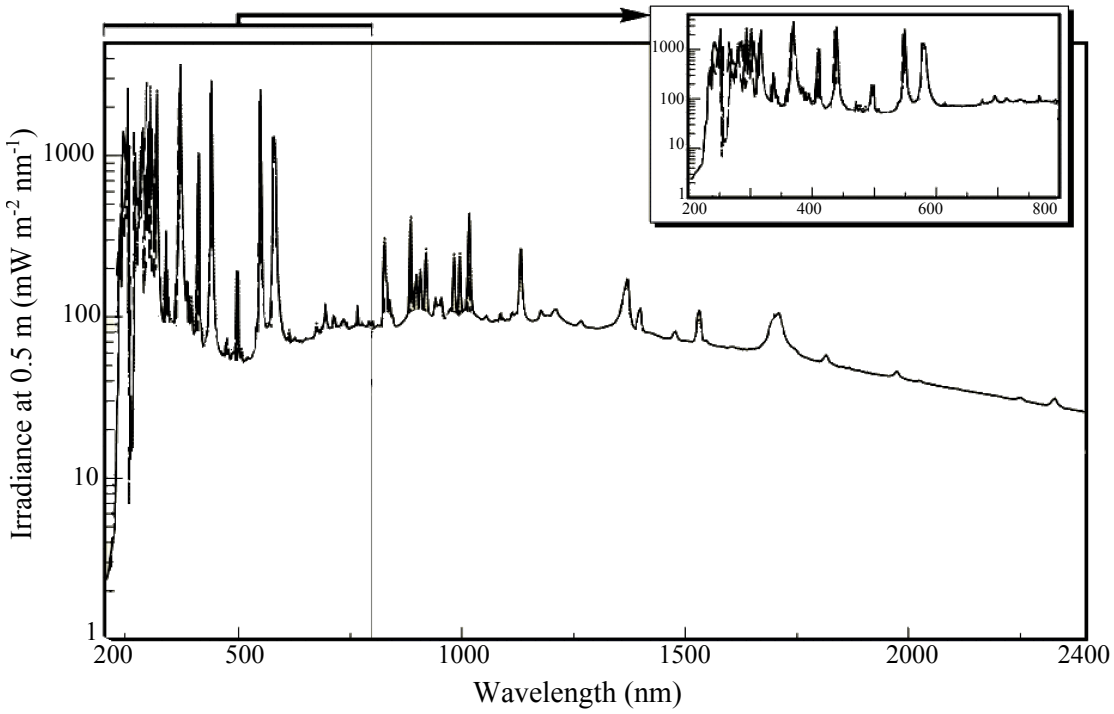

Figure 4-5: Light output from the 1000 W HgXe 6293 bulb used with the Oriel Research Arc-lamp (model 66021). The figure has been adapted from Ref. [12].

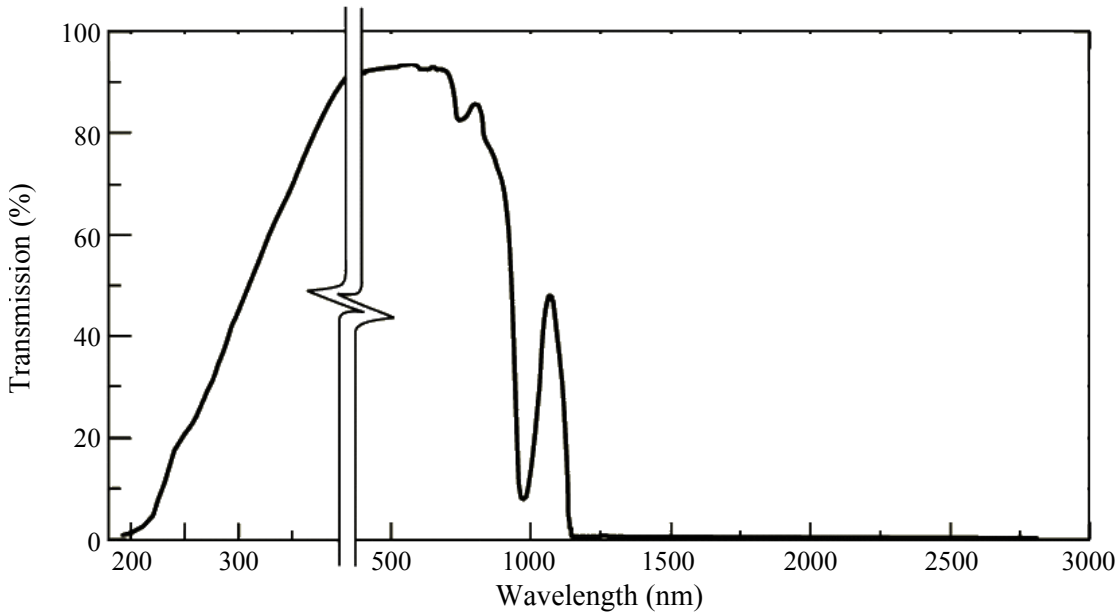

Figure 4-6: Transmission spectrum for a standard liquid filter containing distilled water, which is used to absorb light of wavelengths greater than ~950 nm. The figure was originally presented in Ref. [13].

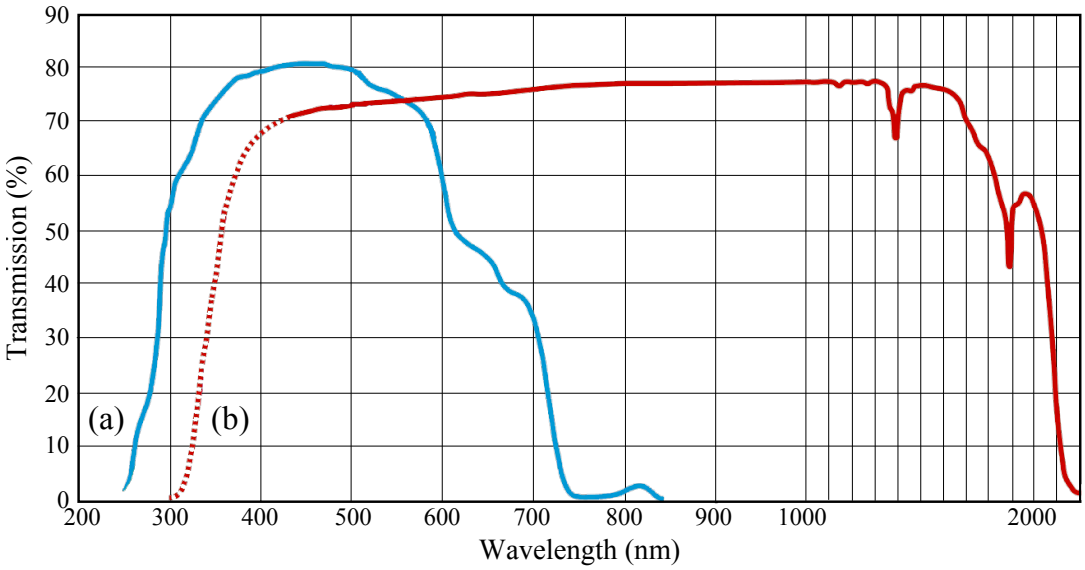

Figure 4-7: Transmission spectra for the two Lumatec liquid lightguides used in this thesis: (a) Series 300 and (b) Series 2000. The figure has been adapted from that provided by the manufacturer [14].

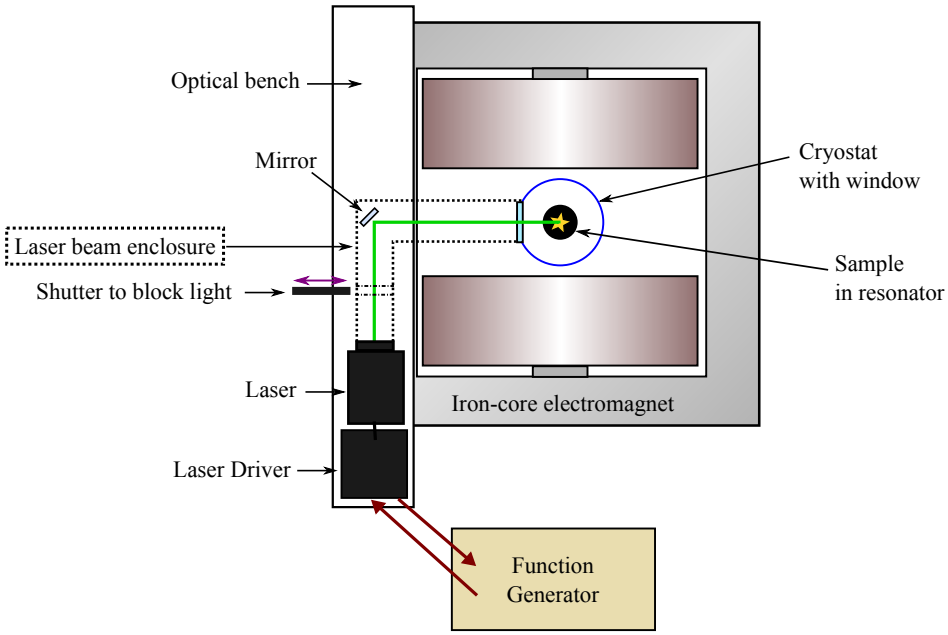

Figure 4-8: Schematic of the setup (as seen from above) used for optically excited pulsed EPR, where a laser illuminates the sample through a window on the side of the Oxford Instruments CF935O cryostat. As a safety precaution, when directed towards the cryostat, the laser beam is confined within a purpose-built enclosure. The user is able to to block the light with a shutter.

cavity and Oxford Instruments ERS-900 cryostat, and the ELEXSYS E580 pulsed EPR system with the ER4118X-MD5 resonator and Oxford Instruments CF935O cryostat.

Alternatively, optical excitation during pulsed EPR measurements (only) could be provided by the 532 nm Q-switched laser (MPL532-20μJ-5), operating at a frequency of 4 MHz and an effective peak power of ~ 100 W. The system was driven using the accompanying DPSSL Driver, connected to a Tektronix AFG3022B Dual Channel Arbitrary/Function Generator. The side window in the cryostat and resonator meant that the sample illumination access was not restricted to the quartz rod setup used with the arc-lamp. Instead, an optical bench was mounted to the side of the magnet and the laser was directed to the sample through the side window, as illustrated in Fig. 4-8, minimising attenuation and reflection losses.

4.2 Optical Absorption

Optical absorption measurements were conducted using a PerkinElmer Lambda 1050 spectrophotometer, illustrated in Fig 4-9, which automatically compares the absorption of a beam of light passing through the sample and a second beam which does not, known as the reference beam, making the measurement insensitive to drifts, for example, in the light output, for timescales greater than the chopping period. The system is equipped with a 3-detector module employing photomultiplier tube (PMT), Peltier-cooled indium gallium arsenide (InGaAs) and Peltier-cooled lead sulphide (PbS) detectors, enabling spectral acquisition over the entire UV (ultraviolet), visible and NIR (near infrared) range of 175 – 3300 nm. High resolution scans could be taken, since the resolving power of the apparatus is 0.05 nm and 0.2 nm in the UV/visible and NIR regions, respectively. The light is provided by either focussed deuterium ($175 < \lambda < 319.2$ nm) or tungsten halogen ($319.2 < \lambda < 3300$ nm) lamps. A common beam depolariser was used to correct for any inherent instrument polarisation. This setting is optional, and could have been removed in order to conduct polarisation studies by inserting suitable polarisers into the Pol/Depol Drive Unit, which can be controlled via the software. Additional features are the common beam mask, which can be used to adjust

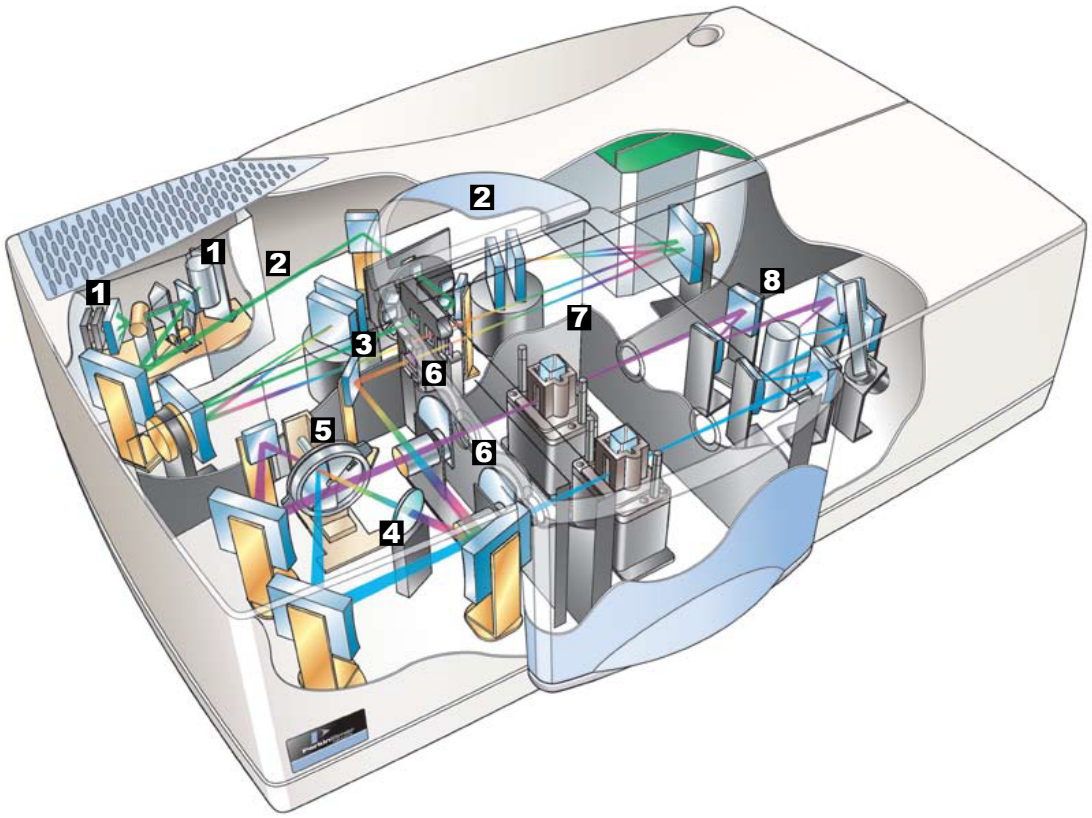

Figure 4-9: Schematic representation of the PerkinElmer Lambda 1050 spectrophotometer used for UV/visible/NIR absorption spectroscopy, highlighting some of the key elements. (1) The deuterium and tungsten halogen light sources; (2) the double holographic grating monochromators; (3) the common beam mask; (4) the common beam depolariser; (5) the chopper, which switches between the reference and sample beams; (6) the reference and sample beam attenuators; (7) the sample compartment; (8) the PMT, InGaAs and PbS detectors. Diagram taken from Ref. [16].

the beam height, and the sample and reference beam attenuators, which aid in improving the sensitivity of data for highly absorbing or small samples.

The spectra acquired in this research were taken at temperatures ranging from 4 – 300 K by using an Oxford Instruments Optistat helium continuous flow cryostat. The sample was mounted into an aperture using packed indium, which was attached to the end of a rod provided with the cryostat, placing the sample in the beam path. This mounting method maximised the light throughput and ensured that the whole sample was being investigated. A silicon diode thermocouple was used to regulate the temperature with an Oxford Instruments ITC5035 unit. The sample chamber was purged with helium gas to remove moisture and reduce the likelihood of condensation forming.

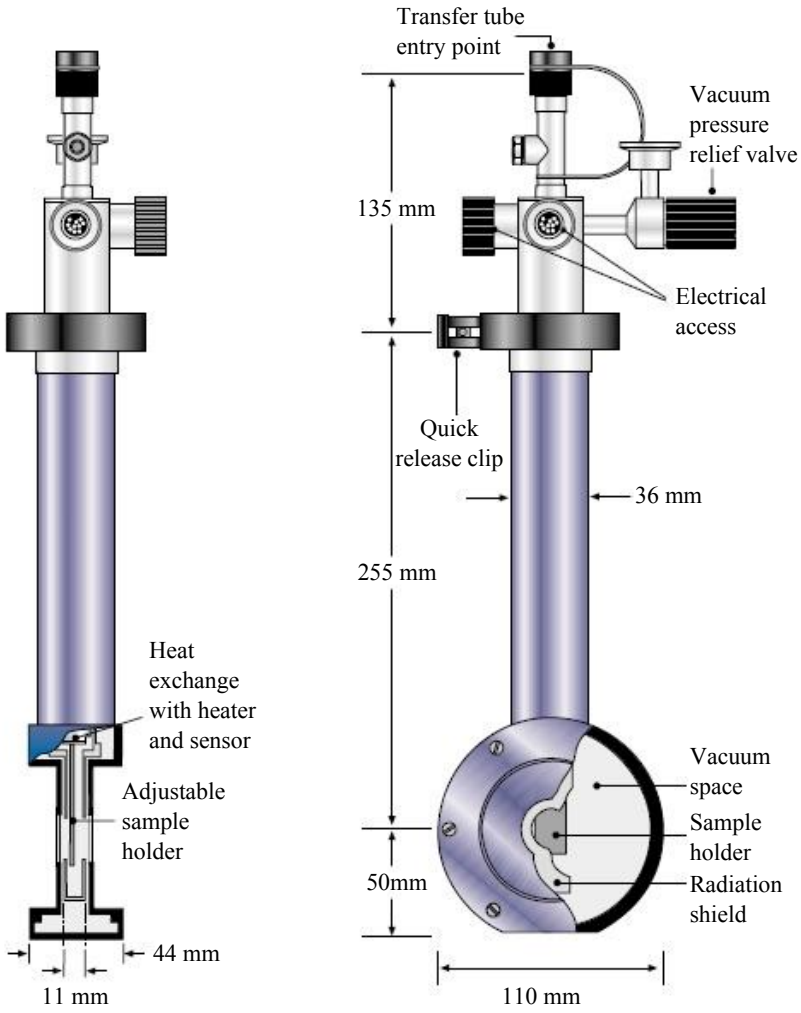

Figure 4-10: The Oxford Instruments continuous flow LHe Microstat utilised for variable temperature photoluminescence measurements. Figure reproduced from Ref. [11].

4.3 Photoluminescence

Variable temperature photoluminescence (PL) measurements were made using a dispersive Renishaw Raman InVia Microscope spectrometer equipped with an Oxford Instruments continuous flow LHe Microstat (see Fig. 4-10). A heat shield was installed around the sample arm to reflect incident radiation and maintain low temperatures with minimal helium flow. The samples were attached to copper sample mounts using silver-paint in order to ensure good thermal contact between the sample, internal heater and the Rh-Fe thermocouple. This system enabled the sampling of temperatures ranging from 5 to 300 K, controlled by striking a balance between the liquid helium flow (using an Oxford Instruments VC30 Gas

Flow Controller) and the heating regulated by an Oxford Instruments Intelligent Temperature Controller ITC4.

Optical excitation was provided by either a 514.5 nm argon-ion laser or a 785 nm solid-state laser. The light was focussed onto the sample using a series of internal mirrors and a confocal microscope. The reflected and emitted light from the sample was collected by a Leica N Plan L 50× objective (0.5 numerical aperture and 8.2 mm working distance), collimated, and directed through a notch or edge filter. This filter removes the reflected light from the laser. The output was then focussed on a RenCam CCD detector. The optics of the system conserves the polarisation of the laser light source. Hence, measurements of the polarisation dependence of the emission may be investigated using polarisers/waveplates which are appropriate for the excitation and emission wavelengths.

For analysis of the spectroscopic features, the integrated intensities of the optical transitions were normalised relative to the integrated intensity of the diamond Raman line (§3.3.1). Cruddace has demonstrated that the Raman signal varies linearly with the laser power employed [17].

4.4 Annealing treatments

Moderate annealing treatments, with temperatures less than 600 °C were conducted at atmospheric pressure, in air, using a Carbolite MTF (mini tube furnace). The system consists of a quartz tube, enveloped by a heating element, which can produce temperatures up to 1000 °C. Once the desired temperature was reached, as measured by a thermocouple, the sample was pushed to the centre of the tube using a quartz rod. The ends of the tube were stopped using rubber bungs. As anneals were conducted at temperatures only up to 600 °C there was no need to exclude oxygen. After completing the treatment, the sample was rapidly removed from the furnace and immersed into distilled water at room temperature, halting any changes to the defect concentrations.

4.5 Sample preparation

Poor quality material could be removed, and surface finishes improved, by laser cutting and polishing samples. Sections of the samples could be cut using an Oxford Lasers class 4 diode-pumped solid state Nd:YAG laser ($\lambda = 355\,\text{nm}$) housed in a class 1 laser enclosure. Surfaces could be polished using a conventional cast iron scaife consisting of a rotating disc in which diamond grit had been embedded. The sample was mounted in a tang and the face to be polished was pressed into the rotating disc, resulting in the mechanical removal of diamond (and non-diamond) surface material. The polishing rate could be varied by changing the pressure, the disc rotation speed and the sample orientation relative to the polishing direction. The orientation of sample edges could be confirmed by analysing diffraction patterns collected with a Laue X-ray back-reflection camera. The polishing system is described in greater detail by Barbu [18].

Diamond samples were cleaned by heating to a temperature of $\sim 250\,^{\circ}\text{C}$ in sulphuric acid which was supersaturated with potassium nitrate for periods of ~ 30 minutes. Once cooled, they were placed in fresh sulphuric acid (only) and reheated for ~ 15 minutes in order to dissolve any potassium nitrate crystal residue from the original cleaning solution. After cooling to room temperature, the samples were rinsed multiple times in de-ionised water and left to air dry. To maintain clean sample surfaces, they were stored between pieces of lint-free paper or cloth in membrane boxes. When possible, sample handling was restricted to using clean tweezers.

References

[1] D. Twitchen, Ph.D. thesis, University of Oxford (1997).

[2] D. Talbot-Ponsonby, Ph.D. thesis, University of Oxford (1997).

[3] A. M. Edmonds, Ph.D. thesis, University of Warwick (2008).

[4] J. A. Weil and J. R. Bolton, *Electron Paramagentic Resonance: Elementary Theory and Practical Aplications* (John Wiley & Sons, Hoboken, 2007).

[5] C. P. Poole Jr., *Electron Spin Resonance: A Comprehensive Treatise on Experimental Techniques* (Dover, New York, 1996), second edition ed.

[6] B. L. Cann, Ph.D. thesis, University of Warwick (2009).

[7] D. Hunt, Ph.D. thesis, University of Oxford (1999).

[8] C. Glover, Ph.D. thesis, University of Warwick (2003).

[9] R. T. Weber, *E 580 User's Manual*, Bruker BioSpin Coorporation, Billerica, MA USA, 2nd ed. (2005).

[10] *Pulsed EPR Practice* (Bruker website, 2010), http://www.bruker-biospin.com/pulsepractice.html.

[11] *Microstat He short working distance liquid helium optical cryostat* (Oxford Instruments website, 2010), http://www.oxinst.com/products/low-temperature/opticaland-spectroscopy/microstathe/Pages/microstathe.aspx.

[12] *1000 Watt Hg(Xe) Lamp, Model: 6293* (Newport website, 2010), http : //search.newport.com/?x2 = sku&q2 = 6293.

[13] *Liquid Filters for Light Sources* (Newport website, 2010), http://www.newport.com/Liquid-Filters-for-Light-Sources/378141/1033/catalog.aspx.

[14] *Lumatec Liquid Lightguides* (Lumatec website, 2010), http://www.lumatec.de/e_lightguides/e_lightguides.htm.

[15] O. D. Tucker, Ph.D. thesis, University of Oxford (1995).

[16] *Lambda UV/Vis and UV/Vis/NIR Spectrophotometers Brochure* (PerkinElmer website, 2010), http://las.perkinelmer.com/Catalog/ProductInfoPage.htm?ProductID=L1050.

[17] R. Cruddace, Ph.D. thesis, University of Warwick (2007).

[18] B. Barbu, Ph.D. thesis, University of Warwick (2009).

Chapter 5

Optical properties of the neutral silicon split-vacancy centre in diamond, (Si-V)^0

5.1 Background and motivation

The presence of silicon in diamond has been routinely verified by the detection of the 1.68 eV (737 nm) zero phonon line (ZPL) in luminescence or absorption, which has been attributed to the negatively charged silicon split-vacancy centre, (Si-V)$^-$ [1, 2]. Unless preventative measures are taken, Si impurities may be introduced into CVD diamond as a consequence of chemical [3] and plasma [3, 4] etching of Si-containing reactor components. Intentional Si-doping has been achieved for both CVD and HPHT diamond during synthesis [5, 6]. Controlled doping of CVD diamond is possible by introducing silicon-containing gases to the source gases, which can, under certain conditions, improve the colour of the diamond [5].

There has recently been renewed interest in the (Si-V)$^-$ centre due to its potential use as a single photon source, which could conceivably be exploited for quantum-information techniques such as quantum computation, cryptography and optics. Wang *et al.* [7] and Neu *et al.* [8] have detected single photon emission from (Si-V)$^-$, with the latter report measuring count rates up to 4.8×10^6 counts/s at saturation. This count rate is an order of magnitude greater than that for the negative charge state of the nitrogen-vacancy centre ((N-V)$^-$), currently the leading candidate for these types of applications. Further properties that render the 1.68 eV band noteworthy are its very sharp ZPL [8] and weak vibronic band (due to a relatively small Huang-Rhys factor, with a reported value of ~ 0.24 [8, 9])

as well as its very short photoluminescence lifetime of 1-4 ns [7, 10] ((N-V)$^-$ has a lifetime of 7.8-12 ns [11]). Theoretical calculations of the radiative lifetime predict a value of 3 ns, in agreement with the experimental data [2]. However, the development of quantum-information applications using the (Si-V)$^-$ centre have been hampered by the fact that to-date the centre has not been unambiguously identified using EPR, despite the prediction that it has a paramagnetic ground state with $S = \frac{1}{2}$ [2, 12].

The occurrence of (Si-V)$^-$ in natural diamond is rare, with only approximately 10 gem-quality specimens reported to contain the centre [13]. Therefore, observation of (Si-V)$^-$ is frequently used to help distinguish between natural, CVD synthetic or treated diamond. This work will show that the (Si-V)$^-$ signal can be bleached by ultraviolet illumination and recovered by moderate annealing. This result emphasises the importance of determining optical analogues of alternative Si-related defects for the positive identification of Si in diamond. EPR and computational studies have shown the existence of the neutral charge state of the silicon split-vacancy centre, (Si-V)^0 [2, 14, 15]. Although the centre has been identified, its optical spectrum had not hitherto been unambiguously determined.

The ZPL at 1.31 eV (946 nm), observed in silicon-containing diamond, has previously been attributed to (Si-V)^0 [13, 16, 17]. In this chapter the optical properties of the 1.31 eV band are investigated in detail and data are presented which support the assignment of this ZPL to the (Si-V)^0 centre in diamond.

5.1.1 The silicon split-vacancy centre in diamond

Spin-polarised local density-functional-cluster theory was employed by Goss *et al.* to predict that an impurity complex consisting of a substitutional silicon atom next to a vacant lattice site in diamond is unstable [2]. The system spontaneously relaxes into a split-vacancy configuration, with the silicon atom lying in a bond-centred site between two vacancies, with D_{3d} symmetry (Figure 5-1(a)). This configuration is also known as a paired or double semivacancy [18] and is consistent with the structure assumed by complexes in diamond which contain vacancies and large dopants, such as cobalt or nickel [19–23].

A simple molecular orbital, similar to that used for a tin atom at the centre of

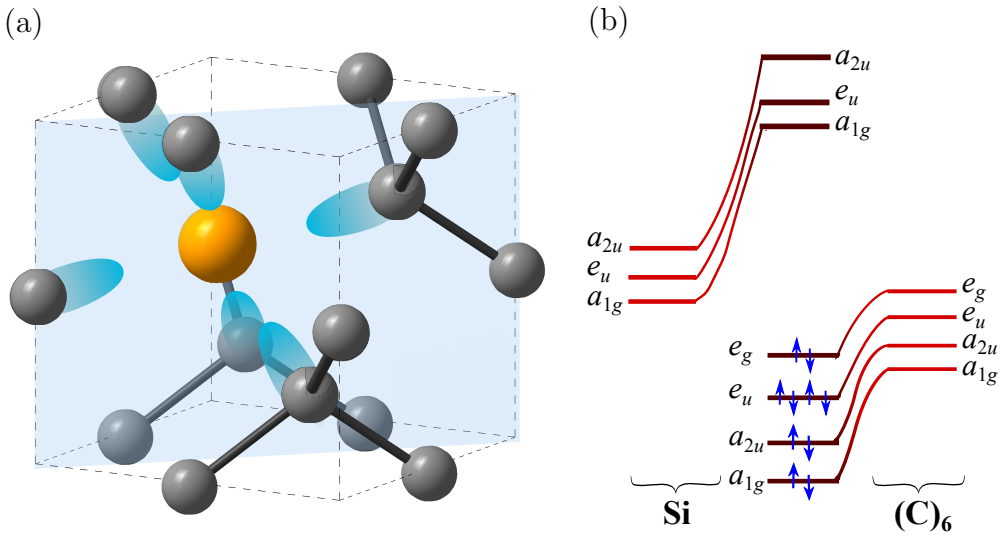

Figure 5-1: (a) Schematic of the silicon split-vacancy defect in diamond, (Si-V), with the {110} mirror plane highlighted. The silicon atom is illustrated as a large yellow sphere lying halfway between two vacant lattice sites; all other atoms are carbon, with the dangling orbitals emphasised in blue. The silicon atom is equidistant from six nearest-neighbour carbon atoms. (b) Simple molecular-orbital model for (Si-V): the central silicon atom and ligand orbitals interact, resulting in the molecular orbitals illustrated. The arrows indicate the ten unpaired electrons available to fill the energy levels for (Si-V)^0.

a divacancy in silicon [24], can be used to interpret the electronic structure of the (Si-V) defect in diamond. The central silicon atom's $3s$ and $3p$ orbitals interact with the ligand orbitals which are made up as a linear combination of a single dangling orbital from each of the six carbon atoms (§3.2). In D_{3d} symmetry the linear combination of carbon dangling orbitals transform as a_{1g}, a_{2u}, e_u and e_g, while those for the silicon $3s$ and $3p$ transform as a_{1g}, and a_{2u} and e_u, respectively. Figure 5-1(b) shows that in this model the populated electronic orbitals derive primarily from the "divacancy" ligand orbitals of the six carbon atoms [25], which have been lowered in energy by the presence of the silicon atom. Only a small admixture of silicon character is expected.

For (Si-V)^0 ten electrons are accommodated in these orbitals. the lowest energy configuration is $a_{1g}^2 a_{2u}^2 e_u^4 e_g^2$ (assuming the order of the orbital energy levels shown in Fig. 5-1(b)). This one electron configuration gives rise to $^3A_{2g}$, ^1E_g and $^1A_{1g}$ many electron states. The spin triplet $^3A_{2g}$ state has been assigned to the observed $S = 1$ ground state of (Si-V)^0, where S is the effective spin [14]. Promotion of an electron from e_u to e_g results in the configuration $a_{1g}^2 a_{2u}^2 e_u^3 e_g^3$, giving rise to the many

electron states $^3A_{1u}$, $^1A_{1u}$, $^3A_{2u}$, $^1A_{2u}$, ^3E_u and ^1E_u. Another electron promotion results in an $a_{1g}^2 a_{2u}^2 e_u^2 e_g^4$ configuration and gives rise to $^3A_{2g}$, ^1E_g and $^1A_{1g}$ many electron states. We would expect other configurations to be significantly higher in energy. Determining the order of the many electron states from even the three configurations considered above is a taxing theoretical problem, and this is not attempted here, though possible electron dipole transitions from the $^3A_{2g}$ ground state are considered. For the divacancy system of $D_{3\mathrm{d}}$ symmetry the components of the electronic dipole operator, which are proportional to x, y, z, transform as follows: $z \subset A_{2u}$; $x, y \subset E_u$. Therefore, the allowed electron dipole transitions from the ground state are $^3A_{2g} \rightarrow {}^3A_{1u}$ and $^3A_{2g} \rightarrow {}^3E_u$ (see Table 3-8 and Ref. [25]). It is interesting to note that the $^3A_{2g} \rightarrow {}^3A_{1u}$ and $^3A_{2g} \rightarrow {}^3E_u$ transitions have different polarisation behaviour, and this is discussed further in §5.4.2.

In the negative charge state, (Si-V)$^-$, there are eleven electrons to accommodate, giving rise to the lowest energy configuration $a_{1g}^2 a_{2u}^2 e_u^4 e_g^3$. A ^2E_g ground state is expected, and since the promotion of one electron from e_u to e_g gives rise to the ^2E_u state the 1.68 eV optical transition associated with (Si-V)$^-$ has been assigned to the $^2E_g \rightarrow {}^2E_u$ transition [1, 2]. The band was shown to consist of a 12-line fine structure by Clark *et al.* [1], where the twelve lines were divided into three groups of four equally intense lines, whose relative intensities reflected the relative abundance of the silicon isotopes (^{28}Si, ^{29}Si and ^{30}Si). The multiplicity of the lines was consistent with a transition from an orbitally two-fold degenerate ground state, split by 0.20 meV, to a doublet state split by 1.07 meV.[1] The splitting of the doublets has been attributed to a (dynamic) Jahn-Teller effect [2]. Despite the prediction that (Si-V)$^-$ has a paramagnetic ground state with $S = \frac{1}{2}$ [2, 12], it has not yet been unambiguously observed using EPR.

5.2 Experimental details

A suite of single crystal samples (Element Six, Ltd.) grown homoepitaxially by microwave-assisted CVD on {110}, {001} and {113}-oriented single crystal substrates (samples A, B and C, respectively) were studied. All samples were intentionally doped with silicon by adding silane to the CVD growth gases; samples

A and B were grown with 90% ^{29}Si-enriched silane (Voltaix, Inc., USA), whereas samples C and D were grown using silane containing the natural abundance of Si-isotopes (^{28}Si:^{29}Si:^{30}Si = 92.3:4.7:3.0). Sample D was grown on a {001}-oriented substrate and during growth the concentration of silicon in the gas phase was adjusted to produce a sample with six layers with progressively higher silicon doping. For samples A, B and C the substrates were removed to leave free-standing plates, which were cut and polished to eliminate poor quality material from the edges. A cross-sectional piece of sample D was prepared, allowing the study of the different layers. Sample B was investigated in its as-grown state, while the other samples were treated by irradiation (samples C and D) and annealing (samples A, C and D). The treatment histories of these samples are summarised in Table 5-1. Anneals at temperatures of 1600 °C or below were carried out in forming gas (96% argon and 4% hydrogen) at atmospheric pressure and the anneal at 2000 °C occurred under a stabilising pressure of 6 GPa (HPHT carried out by Element Six, Ltd.). The concentration of silicon-split vacancy complexes was increased in samples C and D by treatments consisting of irradiation with 1.5 MeV electrons followed by annealing for 4 hours at 900 °C. The electron irradiation introduced vacancies into the lattice. Vacancies become mobile at ~ 600 °C and they could therefore combine with the substitutional silicon atoms present upon annealing [26], producing additional (Si-V) centres. The relative concentration of (Si-V)^0 and (Si-V)$^-$ depends on the concentration of donors (such as the neutral single substitutional nitrogen, N_s^0) and other traps. Before and after each treatment the samples were cleaned in boiling sulphuric acid supersaturated with potassium nitrate. EPR, PL and UV/visible/NIR absorption spectroscopy studies were performed.

The commercial Bruker 9.7 GHz (X-band) EMX-E spectrometer described in §4.1 was equipped with a Super-High Q (ER4122SHQ) cavity and used for room temperature EPR measurements. The average concentrations of (Si-V)^0 were determined by EPR, using the method outlined in §4.1.4. Microwave power saturation, which occurs when the spin lattice relaxation rate is not sufficiently high to maintain equilibrium population distribution whilst stimulated transitions are excited by microwaves (§3.1.5.2), needs to be considered if EPR is to be used in a quantitative manner. Spectra were collected at several different powers to

Table 5-1: Summary of sample histories for samples A, C and D. For the samples that were irradiated, each irradiation treatment was followed by annealing according to the tabulated details.

	Sample A	Sample C	Sample D
Substrate	{110}	{113}	{001}
^{29}Si-abundance	90%	4.7%	4.7%
1st treatment	N/A	1×10^{18} 1.5 MeV e$^-$/cm^2 + 4 h anneal at 900 °C	1×10^{17} 1.5 MeV e$^-$/cm^2 + 4 h anneal at 900 °C
2nd treatment	N/A	N/A	5×10^{17} 1.5 MeV e$^-$/cm^2 + 4 h anneal at 900 °C
1st anneal	1 h at 1200 °C	N/A	N/A
2nd anneal	1 h at 1400 °C	N/A	N/A
3rd anneal	1 h at 1600 °C	N/A	N/A
4th anneal	2 h at 2000 °C	N/A	N/A

verify that microwave power saturation was not occurring. The defect concentrations were calculated by comparing the EPR signal intensity to that of a reference sample of known concentration (the methodology is outlined in §4.1.4).

PL measurements were obtained on a Renishaw Raman InVia microscope system equipped with an Oxford Instruments LHe Microstat cryostat for low temperature experiments, as described in §4.3. Measurements were made using 514 nm (2.410 eV) and 785 nm (1.579 eV) excitations, provided by an argon-ion laser and a solid-state laser, respectively. A PerkinElmer Lambda 1050 spectrophotometer furnished with an Oxford Instruments Optistat continuous flow helium cryostat was utilised to acquire UV/visible/NIR absorption spectra at temperatures between 4 K and room temperature (§4.2).

The average total silicon concentration in each ~200 μm thick layer of sample D was determined by secondary ion mass spectrometry (SIMS). The experiments were carried out in a Cameca IMS 3F using $^{18}O_2^+$ bombardment and positive secondary ion detection to optimise the sensitivity to silicon. In order to minimise sample charging effects the sample was coated with a thin layer of gold, which was subsequently sputtered away in the region of interest by rastering over an area nominally 200 μm across. The raster was then collapsed to a spot and measurements were taken every 50 μm. Five of the six layers were found to be relatively homogeneous, to within the uncertainty of the measurement (±10%). However, the

final growth layer, which contained the highest silicon concentration (~ 1.4 ppm), was inhomogeneously doped.

Thermochromic and photochromic changes in the charge states of defects were investigated. The samples were illuminated at room temperature for ~ 2 minutes with 224 nm (5.45 eV) light from a Photon Systems AgHe laser with an effective continuous wave power of 1 mW (the indirect band gap of diamond [27] is 5.48 eV). Sample heating was conducted at 577 °C for 20 minutes in a Carbolite tube furnace in the dark, after which the sample was quenched. After this treatment further sample handling was conducted in the dark and care was taken to avoid exposure to UV excitation. Before and after each treatment the average concentrations of (Si-V)^0 and N_s^0 were measured using EPR. Additionally, visible/NIR absorption spectra were collected to monitor any changes to the optical spectra.

5.3 Results

5.3.1 Optical absorption and PL

Both the 1.31 eV and 1.68 eV ((Si-V)$^-$) bands were detected in all samples using PL and optical absorption. A typical absorption spectrum at 77 K is illustrated in Fig. 5-2(a). The features observed at 1.447 ± 0.001 eV and 1.493 ± 0.002 eV have previously been reported in silicon-containing diamond [16]. The intensities of these features were found to correlate with the intensity of the 1.31 eV peak by Allers and Collins [16]. The result was explained by attributing the peaks to transitions to excited states of the same defect giving rise to the photoconductivity threshold at 1.5 eV [16]. The photoconductivity results in a rise in the absorption, possibly obscuring the vibronic band of the 1.31 eV feature during optical absorption. At 77 K the 1.310 ± 0.001 eV and 1.684 ± 0.001 eV peaks dominated the optical absorption spectra up to the band edge energy. Additional ZPLs at 1.272 ± 0.001 eV, 1.3028 ± 0.0003 eV and 1.3044 ± 0.0003 eV were only observed in PL.

Figure 5-3 shows the Raman normalised PL spectra (785 nm excitation, 5 K) for sample A, in its as-grown state (Fig. 5-3(a)) and after annealing at 2000 °C (Fig. 5-3(b)). The intensities of the 1.304 eV and 1.31 eV bands do not correlate

(a)

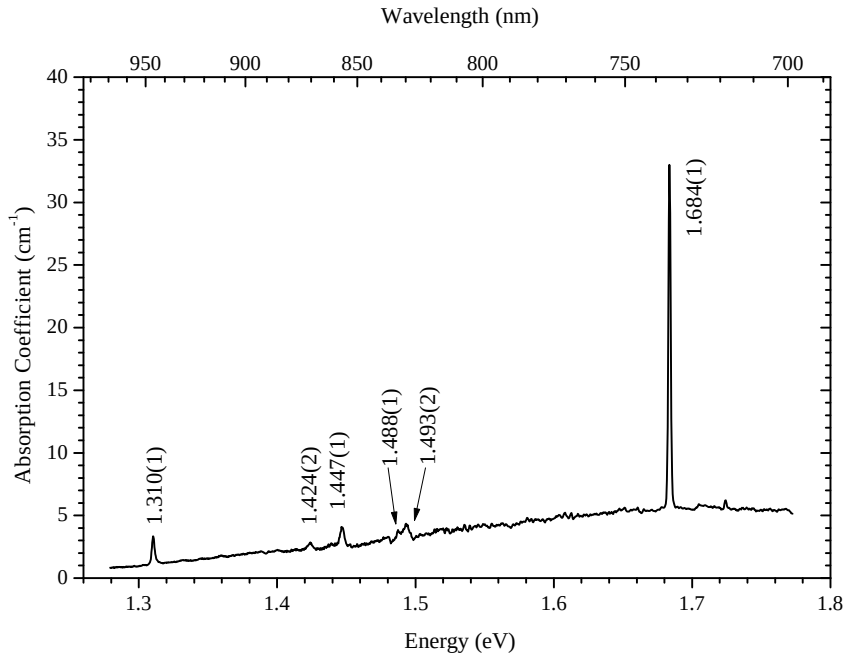

(b)

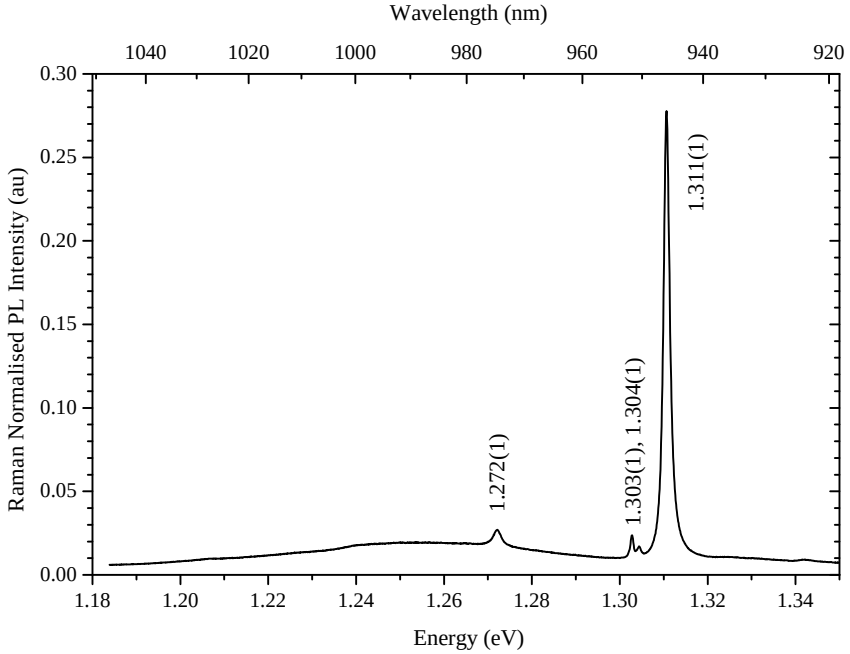

Figure 5-2: (a) NIR absorption and (b) PL spectra of sample A (after annealing at 2000 °C), taken at 77 K. In the absorption spectrum the peaks at 1.447 ± 0.001 eV and 1.493 ± 0.002 eV related to the photoconductivity threshold at 1.5 eV are visible [16]. The photoconductivity produces a rise in absorption which partially obscures the vibronic band of the 1.310 ± 0.001 eV feature. Vibronic structure can be resolved in the PL spectrum, though it is noteworthy that the data has not been corrected for the detector response, which decreases with decreasing energy; the actual band will therefore be stronger than apparent.

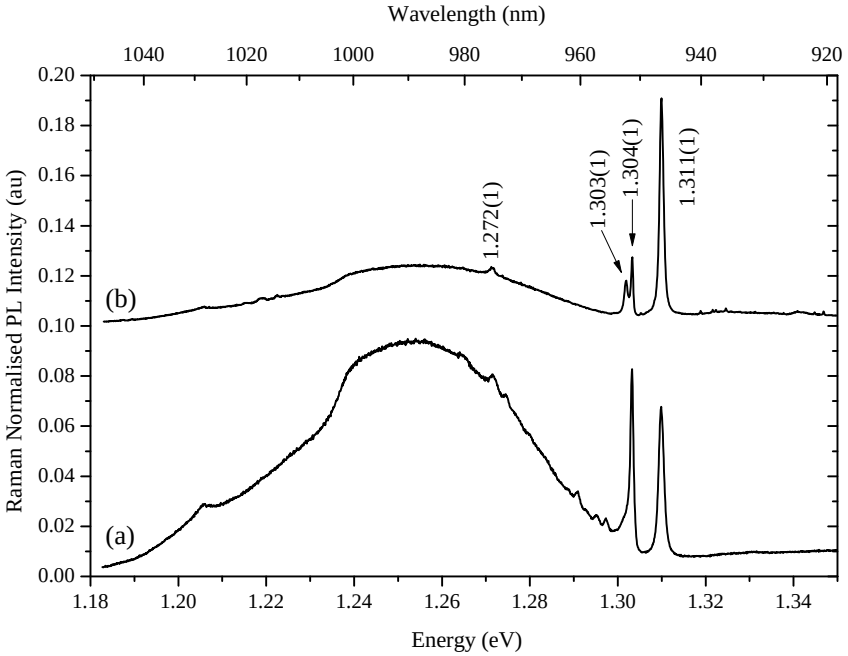

Figure 5-3: Raman normalised PL spectra measured at 5 K of sample A when it was (a) as-grown and (b) annealed at 2000 °C. The 1.311 ±0.001 eV feature was visible in both absorption and PL, all other labelled features were not detected in absorption.

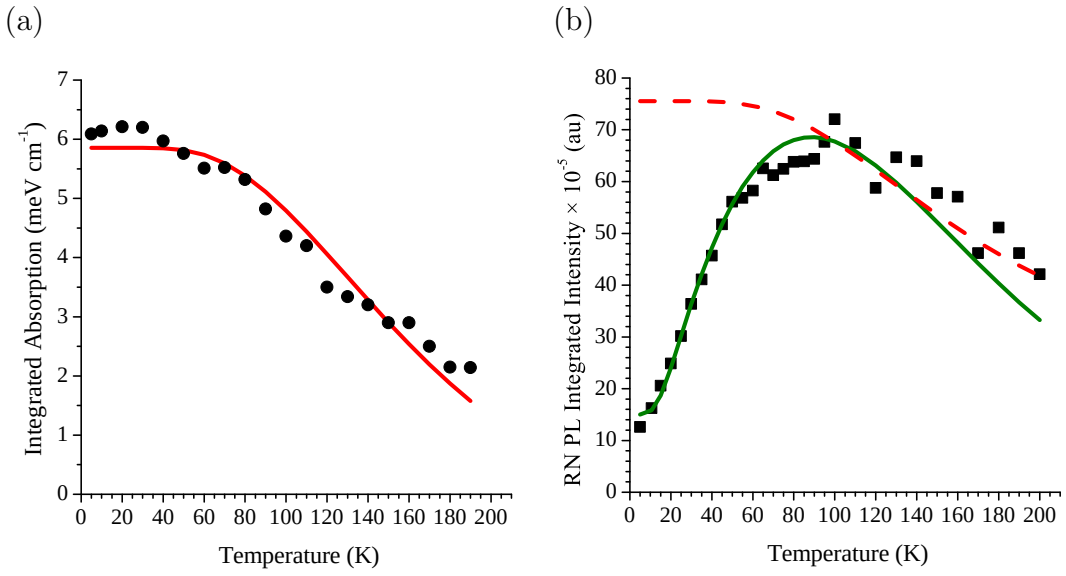

Figure 5-4: (a) Integrated absorption coefficient of the 1.31 eV zero phonon line as a function of the sample temperature. The solid curve is the best fit to the data using Eq. 5-1. (b) Temperature variation of the 1.31 eV zero phonon line Raman normalised PL integrated intensity. The broken curve shows the variation in the absorption and is for comparison only. The solid line is the best fit of the data to Eq. 5-2. These measurements were made on sample A after it had been annealed at 2000 °C.

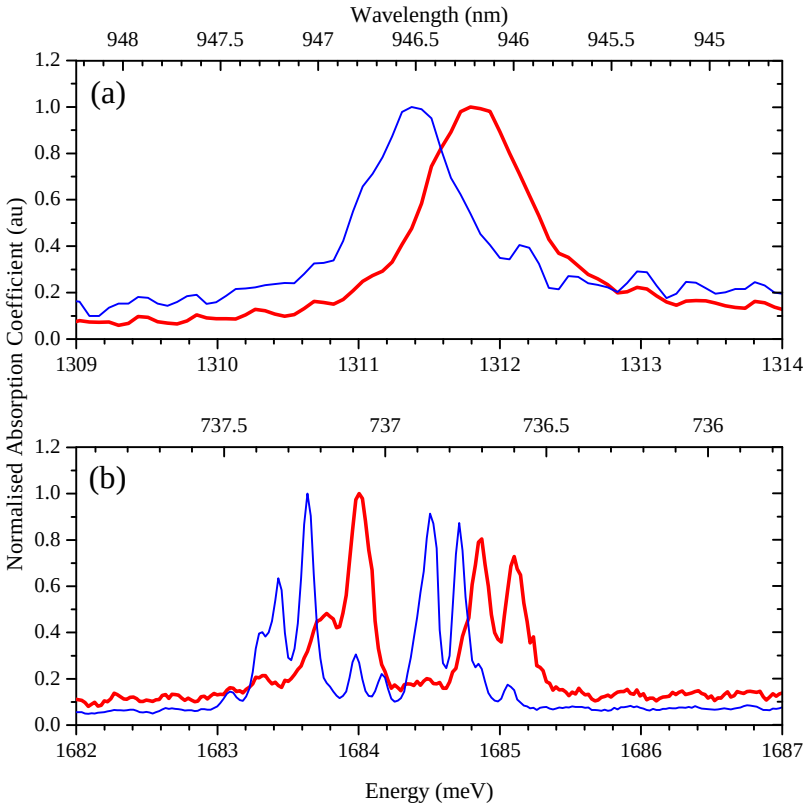

Figure 5-5: UV/visible/NIR absorption spectra obtained at 4 K for samples B (thin, blue curve) and C (thick, red curve), which have ^{29}Si isotopic-abundances of 90% and 4.7%, respectively. The spectral intensities have been normalised to the maximum height of the each band to facilitate comparison. The (a) 1.31 eV and (b) 1.68 eV bands shift to a lower energy by 0.4 ± 0.1 meV when the ^{29}Si abundance was increased.

in different samples and so these features cannot originate from the same defect. The broad emission band centred on ~1.25 eV appears to correlate with the ZPL at 1.304 eV and is thus associated with its vibronic band. The vibronic coupling in the 1.304 eV system is strong, and overlaps with the vibronic band of the 1.31 eV system, making measurement of this band very difficult.

To investigate the vibronic coupling of the 1.31 eV system the temperature variation of the integrated intensity of its ZPL was measured in absorption and PL for sample A (after annealing at 2000 °C); the resulting data are shown in Fig. 5-4. The experimental data are shown by points and the lines were calculated as described in §5.4.1.

The defect associated with the 1.31 eV ZPL was unambiguously confirmed to be silicon-related by comparing the peak positions in absorption of the 1.31 eV

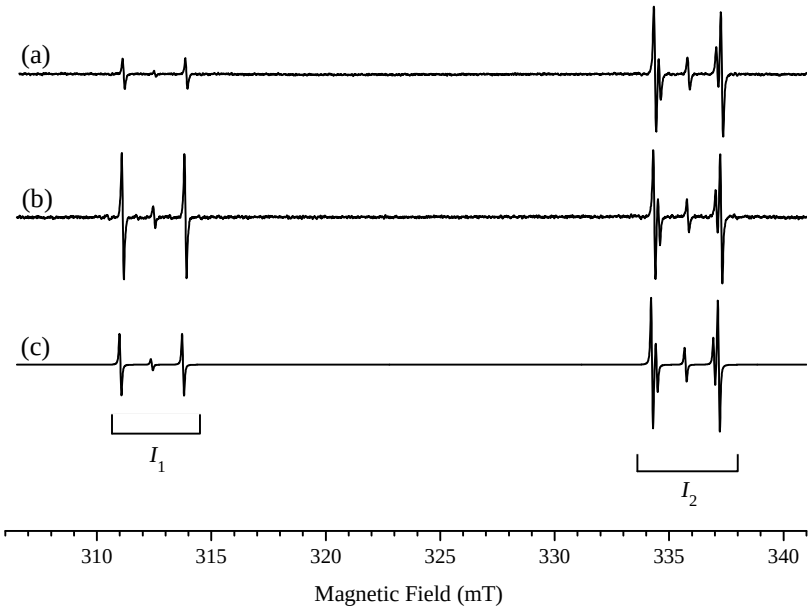

Figure 5-6: EPR spectra of (Si-V)^0 at X-band frequencies for the as-grown sample A with the magnetic field aligned parallel to the (a) $[\bar{1}1\bar{1}]$ or (b) [111] directions, where the growth plane is assumed to be (110). The former direction lies in the growth plane while the other lies out of the growth plane. The difference in the relative resonance line intensities of the spectra is attributed to the preferential alignment of the centres in this sample. If the centres were statistically aligned along each crystallographically equivalent direction the resulting spectra would look like the simulated spectrum (c). These spectra have previously been reported by Edmonds [28].

and 1.68 eV bands in samples containing ^{29}Si-isotopic abundances of either 4.7% (sample C) or 90% (samples A and B). Both ZPLs were found to decrease in energy by on average 0.4 ± 0.1 meV when the dominant silicon isotope changed from ^{28}Si to ^{29}Si (Fig. 5-5).

5.3.2 EPR

(Si-V)^0 concentration measurements were made using EPR, where it was noted that for sample A (as-grown) the relative intensities of the resonance lines changed depending on whether the magnetic field, **B**, was aligned parallel to a crystallographically equivalent direction lying in or out of the {110} growth plane. The EPR spectra acquired for the as-grown sample A with $\mathbf{B} \parallel \langle 111 \rangle$ are shown in Fig. 5-6. If the (Si-V)^0 centres in a sample were statistically aligned with their

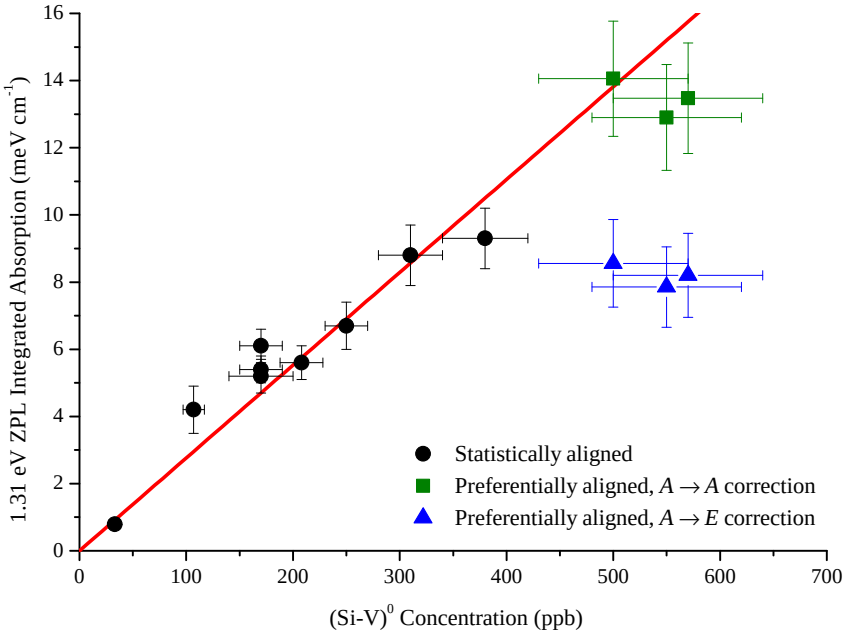

Figure 5-7: Correlation between the integrated absorption coefficient of the 1.31 eV ZPL (recorded at 77 K) and the concentration of (Si-V)^0 as determined by EPR. The black circles represent data for samples where the (Si-V)^0 centres are statistically aligned. The remaining data points were recorded for samples where the (Si-V)^0 centres exhibited a degree of preferential alignment, which could be quantified using EPR. The effect of preferential alignment on the absorption measurements has been corrected assuming that the 1.31 eV band is produced by either an $A \rightarrow A$ transition (green squares) or an $A \rightarrow E$ transition (blue triangles).

⟨111⟩-symmetry axes along all crystallographically equivalent directions the resulting spectrum would look like the simulated spectrum (spectrum (c) in Fig. 5-6). The spectrum was simulated using the Hamiltonian parameters published by Edmonds *et al.* [14]. The preferential alignment of (Si-V)^0, as detected by EPR, has previously been reported for this sample [28].

The integrated absorption of the 1.31 eV ZPL was correlated with the (Si-V)^0 concentration in the samples, as measured using EPR. To ensure that charge transfer between (Si-V)^0 and (Si-V)$^-$ was not induced during the experiments the samples were not exposed to UV light during the EPR measurements. Subsequently, sample handling was carried out in the dark and optical absorption spectra were recorded using monochromatic light, starting at low (< 1.29 eV) energies and finishing at ~ 1.7 eV. Fig. 5-7 shows the integrated absorption of the 1.31 eV ZPL plotted against the integrated absorption of (Si-V)^0 measured by EPR in a variety

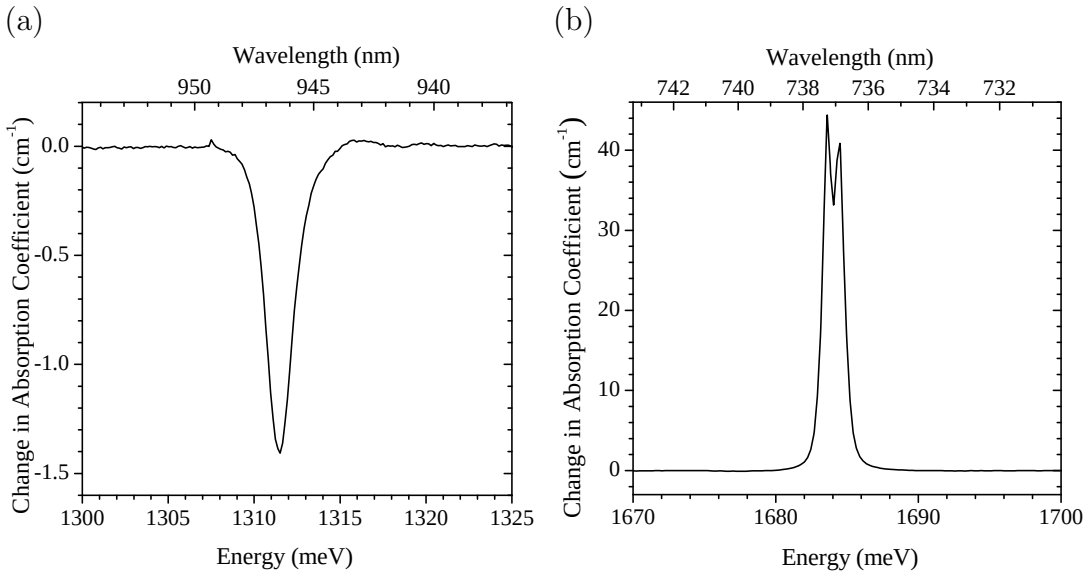

Figure 5-8: Difference of the absorption coefficient for the 1.31 eV and 1.68 eV ZPLs between the cases where sample A (after annealing at 2000 °C) was heated or illuminated. Heating was done in the dark for 20 minutes at 577 °C, while the illumination treatment was carried out by exposing the sample for ~ 2 minutes to a 224 nm laser. Under these conditions the heating led to a decrease in the intensity of the 1.31 eV band an increase in that of the 1.68 eV band. The opposite effect was induced by illumination. The data were recorded at 77 K.

of samples. Some of the data points are from samples treated (UV photoexcitation or heating in the dark) to change the relative concentration of (Si-V)^0 and (Si-V)$^-$ (explained below). The graph also includes data from samples where EPR measurements indicated that the (Si-V)^0 defects were not randomly oriented over the available sites. The analysis required to correct for the preferential alignment is discussed in §5.4.2.

A few minutes of UV excitation (1.54 eV) at room temperature increased the intensity of the 1.31 eV band whilst decreasing that of the 1.68 eV band. Conversely, heating the samples in the dark for 20 minutes at 577 °C decreased the intensity of the 1.31 eV band and increased that of the 1.68 eV band. An example of the change in the intensities of the 1.31 eV and 1.68 eV bands which could be induced by these treatments is illustrated in Fig. 5-8. The concentration of substitutional nitrogen donor centres and other acceptors and defects influenced the magnitude of the change induced by charge transfer. However, the changes in integrated absorption for the 1.31 eV ZPL matched the changes observed in the

(Si-V)^0 concentration within experimental error.

5.3.3 Irradiation and annealing studies

In order to confirm that the centre responsible for the 1.31 eV band involved both a vacancy and a silicon atom the layered sample (D) was irradiated with 1.5 MeV electrons to a dose of 1×10^{17} cm^{-2} and annealed at 900 °C for 4 hours. The PL intensities of both the 1.31 eV and 1.68 eV features were observed to increase in each layer of the sample as seen in Fig. 5-9. The sample was subjected to a second irradiation and annealing treatment, with the irradiation dose increased to 5×10^{17} 1.5 MeV electrons cm^{-2}. The 1.31 eV peak was seen to further increase after this treatment in the layers with higher silicon concentrations, as measured by SIMS. The intensity of the ZPL for the neutral nitrogen-vacancy centre, (N-V)^0 (2.156 eV), was always measured to be 2 or 3 orders of magnitude greater than that for the negative charge state, (N-V)$^-$ (1.945 eV), indicating that the sample layers contained low concentrations of nitrogen donors, N_s^0 [29–31].

The irradiation and photoluminescence measurements were performed by D. Evans and Dr. Philip Martineau from the DTC Research Centre; all data analysis was carried out by the author of this thesis.

5.4 Discussion

5.4.1 Vibronic structure of the 1.31 eV band

According to theory (§3.3.3), the transition probability, and thus total integrated intensity, of a vibronic absorption band is temperature (T) independent for two energetically isolated electronic states [32, 33]. However, the fraction of the transition probability in the ZPL decreases as the temperature is increased. Since the vibronic bandshapes are uncertain in both PL and optical absorption, the temperature dependence of the ZPL will be parameterised using the well-known single, effective mode model [32–35]. The integrated absorption of the ZPL, A_{ZPL}, is thus given by

$$\begin{aligned} A_{\mathrm{ZPL}}(T) \quad \propto \quad & \exp[-S_{\mathrm{HR}} \cdot \coth(\hbar\omega / 2k_B T)] \\ & \cdot J_0[S_{\mathrm{HR}} \cdot \mathrm{csch}(\hbar\omega / 2k_B T)] \end{aligned} \tag{5-1}$$

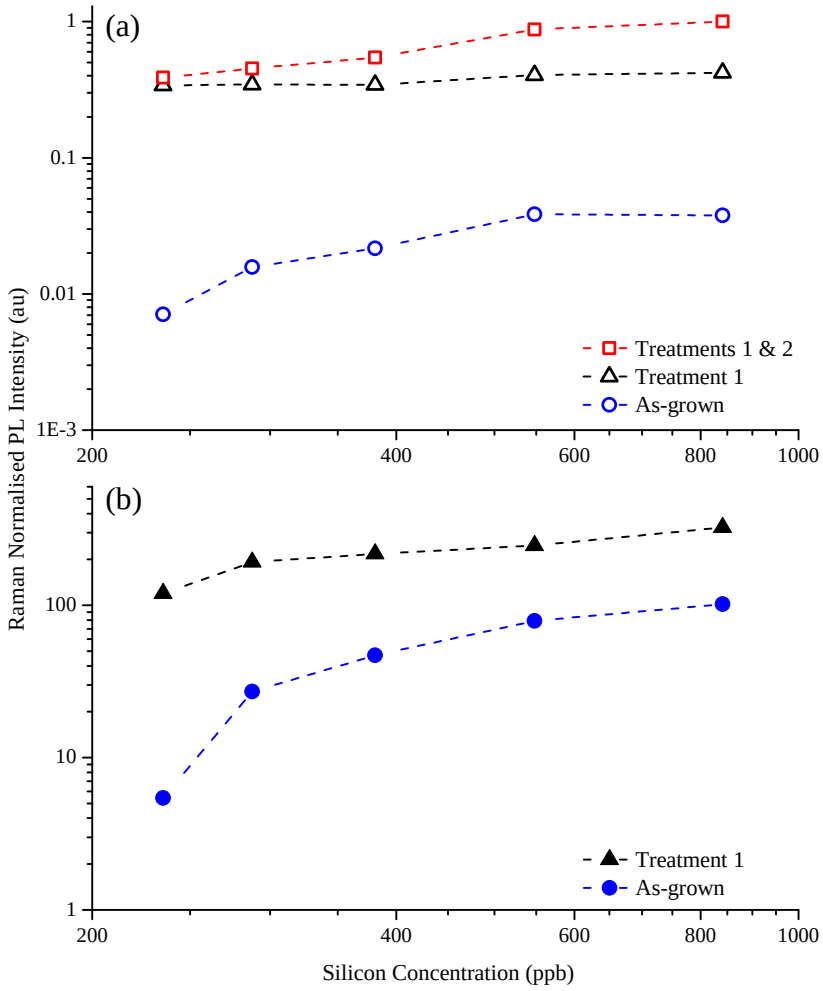

Figure 5-9: Raman normalised PL intensity of the (a) 1.31 eV and (b) 1.68 eV zero phonon lines as a function of silicon concentration in a sample (D) consisting of layers with different Si-doping levels. The sample has been electron irradiated and annealed twice in order to produce vacancy complexes. Please refer to text for treatment details. The data for the 1.31 eV band (open symbols) were acquired at 100 K while the 1.68 eV data (solid symbols) were measured at 77 K. The dashed lines are included to guide the eye of the reader.

(a)

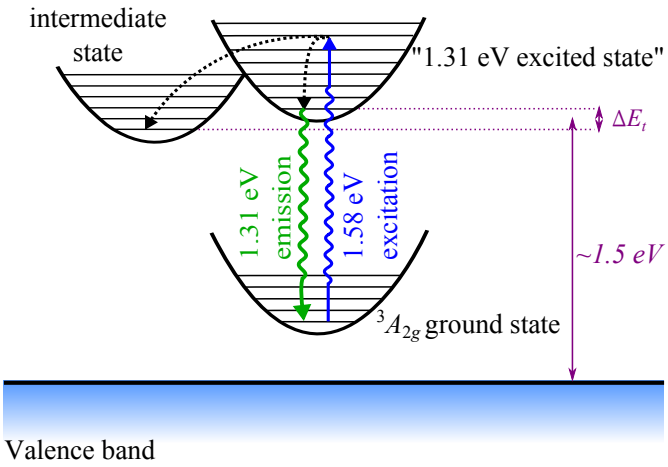

(b)

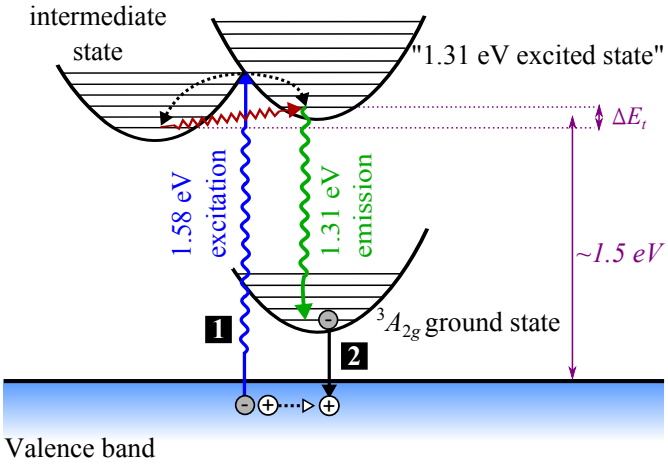

Figure 5-10: Schematic representation of the energy levels of $(Si\text{-}V)^0$ involved in the production of the 1.31 eV band visible in absorption and luminescence (not to scale). The characteristic emission requires the de-excitation of an electron from the 1.31 eV excited state into the $^3A_{2g}$ ground state. There are several possible methods to populate the 1.31 eV excited state when using 1.58 eV (785 nm) laser excitation. (a) The laser excites an electron directly from the $^3A_{2g}$ ground state into the vibronic band of the 1.31 eV state. The excited electron can then relax to the bottom of the 1.31 eV excited state and de-excite back into the $^3A_{2g}$ ground state. A nonradiative transition into an intermediate level, lying ΔE_t below the 1.31 eV state, is also possible. (b) Excitation of an electron from the valence band by the laser may also ultimately result in 1.31 eV emission, as long as two conditions are met. Firstly, the excited electron needs to reach the bottom of the 1.31 eV excited state. It may have originally been excited from the valence band into the 1.31 eV state's vibronic band, followed by relaxation, or it may have been excited into the intermediate state. An electron in the intermediate state cannot contribute to the 1.31 eV luminescence unless it is thermally excited into the 1.31 eV band. The second condition is that the $^3A_{2g}$ state cannot be full; recombination between an electron from the $^3A_{2g}$ state and a hole in the valence band fulfills this condition.

where J_0 is a Bessel function, $\hbar$ is the reduced Planck's constant, and k_B is the Boltzmann constant [33–35]. The least-squares fit to the data, illustrated in Fig. 5-4, estimated that $S_{\mathrm{HR}} \sim 1.5$ and $\hbar\omega \sim 28\,\mathrm{meV}$ for the 1.31 eV optical band.

In Fig. 5-4 the fit to the temperature variation of the ZPL in absorption is superimposed on the PL data. For a simple two level system the ZPL in PL and absorption is expected to have the same temperature dependence. Rather than decreasing in intensity as the temperature increased, the PL ZPL intensity showed a steady increase up to $T \sim 100\,\mathrm{K}$. This increase could be explained by including a nonradiative intermediate state between the ground and 1.31 eV excited states, which competes to trap the excited electrons [33]. A possible energy level diagram is shown in Fig. 5-10, presenting some of the processes which may contribute to the 1.31 eV emission observed during 1.58 eV (785 nm) laser excitation. Allers and Collins detected photoconductivity of the centre responsible for the 1.31 eV transition, explaining their results by placing the defect's active level ~ 1.5 eV away from a band edge. The photoconductivity and temperature dependence of the PL data can be explained using Fig. 5-10. In Fig. 5-10(a) direct optical excitation of an electron from the $^3A_{2g}$ ground state to the 1.31 eV excited state, followed by relaxation and de-excitation back to the $^3A_{2g}$ state, results in emission of light with an energy of 1.31 eV. In Fig. 5-10(b) excitation of an electron from the valence band (producing a hole) to the excited states (the 1.31 eV state or the intermediate state, lying ΔE_t below the 1.31 eV state) is considered. As the temperature is increased the intermediate state may thermally populate the 1.31 eV state. Recombination between a hole from the valence band and an electron from the $^3A_{2g}$ ground state enables the de-excitation of the electron from the 1.31 eV state and the characteristic emission. The results presented in Fig. 5-4 suggest that the excited electrons are preferentially trapped by the nonradiative intermediate level with a higher probability than the 1.31 eV excited state. Assuming this model, the PL ZPL intensity is given by

$$\begin{aligned} I_{\mathrm{ZPL}}(T) &= C + [I(0)/(1 + g\cdot\exp(\Delta E_t/k_B T)] \\ &\quad \cdot\exp[-S_{\mathrm{HR}}\cdot\coth(\hbar\omega/2k_B T)] \\ &\quad \cdot J_0[S_{\mathrm{HR}}\cdot\mathrm{csch}(\hbar\omega/2k_B T)] \end{aligned} \tag{5-2}$$

where $I(0)$ is the intensity at $T = 0\,\mathrm{K}$, C is a constant to account for the possibility

of direct excitation to the 1.31 eV level, g is the ratio of degeneracies of the trap and the 1.31 eV excited level, and ΔE_t is the energy separation between those states. Fitting the data to Eq. 5-2 using S_{HR} and $\hbar\omega$ determined from the absorption data gives $\Delta E_t \sim 5$ meV, $1 \leq g \leq 3$ and $C/I(0) \sim 10^{-2}$. The fraction of the excitation leading to direct excitation of the 1.31 eV level is then $C/[C + I(0)/(1+g)] \approx 0.02$ to 0.04. The trap state cannot be ^3E_u since the electronic dipole transition $^3A_{2g} \leftrightarrow {}^3E_u$ is allowed. However, candidate states include ^1E_g ($g = 1.5$) and $^1A_{1g}$ ($g = 3$) from the configuration $a_{1g}^2 a_{2u}^2 e_u^4 e_g^2$, but other states cannot be ruled out. It is noteworthy that Allers and Collins observed a photoconductivity peak at 1.493 eV [16], which is also present in Fig. 5-2. This may be associated with the intermediate state in Fig. 5-10. Nevertheless, from these results it is suggested that the filled $^3A_{2g}$ ground state lies ~ 0.2 eV above the valence band.

5.4.2 Preferential alignment of (Si-V)^0

The preferential alignment of (Si-V)^0 in single crystal CVD diamond grown on {110}-oriented samples has previously been reported by Edmonds [28] (published Ref. [36]). The (Si-V) centre in diamond has $D_{3\mathrm{d}}$ symmetry. Therefore, the principal symmetry axis of the centre can be aligned along four different directions: [111], [$\bar{1}\bar{1}1$], [$1\bar{1}\bar{1}$] and [$\bar{1}1\bar{1}$]. Consequently, if the (Si-V)^0 defects are randomly oriented over the four ⟨111⟩ directions then the EPR spectrum produced by applying the magnetic field (**B**) along any ⟨111⟩ direction would consist of four groups (n = 1, 2, 3, 4) of hyperfine (^{29}Si, ^{13}C) split lines. If the total integrated intensity of the n^{th} group is I_n, then the relative integrated intensities I_1:I_2:I_3:I_4 would be 1:3:3:1, simply representing the fact that 1/4 of the defects have their symmetry axis parallel to the applied field, and for 3/4 the angle between the applied magnetic field and this axis is arccos(1/3). Figure 5-6(c) shows the low field half of the EPR spectrum, simulated using the published values for randomly oriented (Si-V)^0 centres and $R_{\langle 111\rangle} = I_2/I_1 = 3$, where the subscript on R indicates the direction of the magnetic field [14]. For a CVD diamond sample grown on a [110]-oriented substrate (i.e. growth on a (110) plane) two of the four ⟨111⟩ directions lie in the (110) plane ([$1\bar{1}\bar{1}$] and [$\bar{1}1\bar{1}$]) and two out of the (110) plane ([111] and [$\bar{1}\bar{1}1$]), as illustrated in Fig. 5-11 [28, 36].

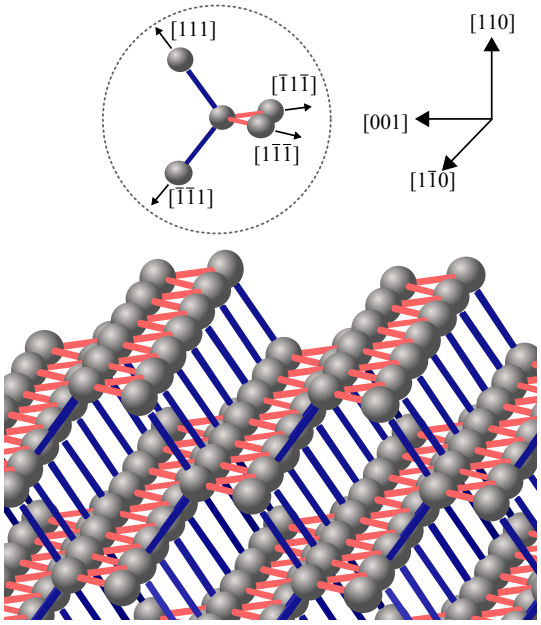

Figure 5-11: Cartoon of a view along a (110) growth plane, displaying the atomic scale roughness of the surface. Bonds that lie in the growth plane ([$\bar{1}1\bar{1}$] and [$1\bar{1}\bar{1}$]) are shown in red and those that are out of the growth plane ([111] and [$\bar{1}\bar{1}1$]) are indicated by blue bonds. Adapted from Fig. 7-3 in Ref. [28].

Edmonds [28, 36] parameterised the possible preferential orientation of (Si-V)^0 centres either "out of" or "in" the (110) plane by defining the probability that a (Si-V)^0 defect is aligned along [111] as $p_{[111]} = \frac{p}{4}$, where $0 \leq p \leq 2$. Since the [$\bar{1}\bar{1}1$] direction is also "out of" the plane $p_{[\bar{1}\bar{1}1]} = \frac{p}{4}$. Then $p_{[\bar{1}1\bar{1}]} = p_{[1\bar{1}\bar{1}]} = \frac{2-p}{4}$. If $p = 1$, the (Si-V)^0 defects are randomly oriented over the four possible ⟨111⟩ directions. Thus, when **B** is along [111] or [$\bar{1}\bar{1}1$]

$$R_{[111]} = R_{[\bar{1}\bar{1}1]} = \frac{4-p}{p} \left(= \frac{I_2}{I_1} \right) \tag{5-3}$$

and for **B** along [$\bar{1}1\bar{1}$] or [$1\bar{1}\bar{1}$]

$$R_{[\bar{1}1\bar{1}]} = R_{[1\bar{1}\bar{1}]} = \frac{2+p}{2-p} \left(= \frac{I_2}{I_1} \right) \tag{5-4}$$

where the subscripts indicate the direction of **B** [28, 36].

A study of the as-grown sample A (grown on a {110} substrate, here designated as (110)) by Edmonds [28, 36] found that $R_{[\bar{1}1\bar{1}]} = 7.3 \pm 0.1$ and $R_{[111]} = 1.6 \pm 0.1$ (see Figs. 5-6(a) and 5-6(b), respectively). These yield a value of $p = 1.51 \pm 0.01$, showing that ~80% of the (Si-V)^0 defects were oriented out of the growth plane (i.e. with the D_{3d} axis along [111] or [$\bar{1}\bar{1}1$]). A degree of preferential alignment of the (Si-V)^0

centres in sample A was retained until it was annealed at 2000 °C, whereupon the (Si-V)^0 concentration was halved and the centres were observed to be statistically aligned. Reorientation of the (Si-V)^0 unit is not possible without dissociation, and so it can be inferred that the HPHT anneal resulted in dissociation of (Si-V)^0 centres and formation of (Si-V)^0, with the former process dominating.

An incorporation process during CVD synthesis which could account for the preferential alignment of (Si-V)^0 in samples grown on {110}-oriented diamond substrates can be postulated. First, a silicon atom is incorporated in a substitutional site on the uppermost diamond layer. The presence of the silicon atom may reduce the probability of incorporating a carbon atom in the nearest-neighbouring site in the next layer, producing a vacant site. The subsequent layer might overgrow the centre. The substitutional silicon atom will then relax into the split-vacancy configuration, with the D_{3d} symmetry axis pointing out of the growth plane. Similarly, other trigonal silicon-vacancy-type defects would be expected to show preferential alignment in diamonds grown on {110}-oriented substrates. This behaviour has been reported for both the neutral silicon split-vacancy complex decorated by a hydrogen atom, (Si-V:H)^0 [28], and for the (Si-V$_2$:H)^0 complex (Chapter 7 and [37]), which were detected in sample A and observed to be preferentially aligned. A consequence of this process is that all the (Si-V)^0 centres are expected to be preferentially oriented. The fact that only ~ 80% of the (Si-V)^0 centres were preferentially oriented out of the growth plane is probably due to the sample studied containing material that was not only the result of growth on a flat {110} surface. Roughening of the surface during growth [28], producing differently oriented micro-facets, and material grown on the edge of the sample on different crystal faces would result in the reduced preferential orientation measured.

Sample B, which was grown on a {100}-oriented substrate, did not show any preferential alignment. This is understandable since the ⟨111⟩ directions all make the same angle relative to the direction perpendicular to the growth plane and are thus indistinguishable during growth.

The incorporation efficiency of (Si-V) centres appears to be significantly lower in samples grown on {001}- rather than {110}-oriented substrates. Samples A and B were grown simultaneously, yet the (Si-V) concentration (the sum of (Si-V)^0

Table 5-2: Effective relative excitation rates for transitions for differently oriented trigonal defects, where α is the angle between the linearly polarised **E**-field and [001], and $\phi = \arccos\left(1/\sqrt{3}\right)$.

Defect Symmetry Axis	$A_{2g} \leftrightarrow A_{1u}\,(D_{3d})$ $A \leftrightarrow A\,(C_{3v})$	$A_{2g} \leftrightarrow E_u\,(D_{3d})$ $A \leftrightarrow E\,(C_{3v})$
[111]	$\frac{1}{3}\cos^2(\alpha)$	$\left[\sin(\alpha) + \sqrt{\frac{2}{3}}\cos(\alpha)\right]^2$
$[\bar{1}\bar{1}1]$	$\frac{1}{3}\cos^2(\alpha)$	$\left[\sin(\alpha) + \sqrt{\frac{2}{3}}\cos(\alpha)\right]^2$
$[\bar{1}1\bar{1}]$	$\cos^2(\phi - \alpha)$	$\sin^2(\alpha - \phi)$
$[1\bar{1}\bar{1}]$	$\cos^2(\phi + \alpha)$	$\sin^2(\alpha + \phi)$

and (Si-V)$^-$, where the concentrations were determined from EPR and optical absorption, respectively, using Eq. 5-6) was 6 ± 1 times greater in sample A than in B.

Preferential orientation of defects can also influence the measured absorption and emission. For an individual trigonal defect the dipole moment of the allowed optical transition is either parallel ($A \rightarrow A$ transition) or perpendicular ($A \rightarrow E$ transition) to the trigonal axis. In an $A \rightarrow E$ transition, the x and y polarisations must have equal dipole moments, by symmetry. In an experiment where the optical excitation is incident along the [110] crystallographic direction, and the angle between the linearly polarised electric (**E**) field vector of the light and [001] is α, then the effective relative excitation rates for $A \rightarrow A$ and $A \rightarrow E$ transitions for the differently oriented trigonal defects are given in Table 5-2, and plotted out in Fig. 5-12.

It is clear that for an optical absorption measurement on an ensemble of defects, randomly oriented over the possible $\langle 111 \rangle$ directions, the optical excitation, and hence absorption, is independent of the polarisation of the electric field vector of the light. However, if all the defects are oriented out of the plane (i.e. [111] and $[\bar{1}\bar{1}1]$), for an $A \rightarrow A$ ($A \rightarrow E$) transition the optical absorption will be weaker (stronger) than for the same number of defects randomly oriented over the possible orientations. For the three samples indicated in Fig. 5-7, the optical absorption measurements were made with the light incident along [110], and from EPR it was known that the (Si-V)^0 defects were preferentially oriented along [111] and $[\bar{1}\bar{1}1]$.

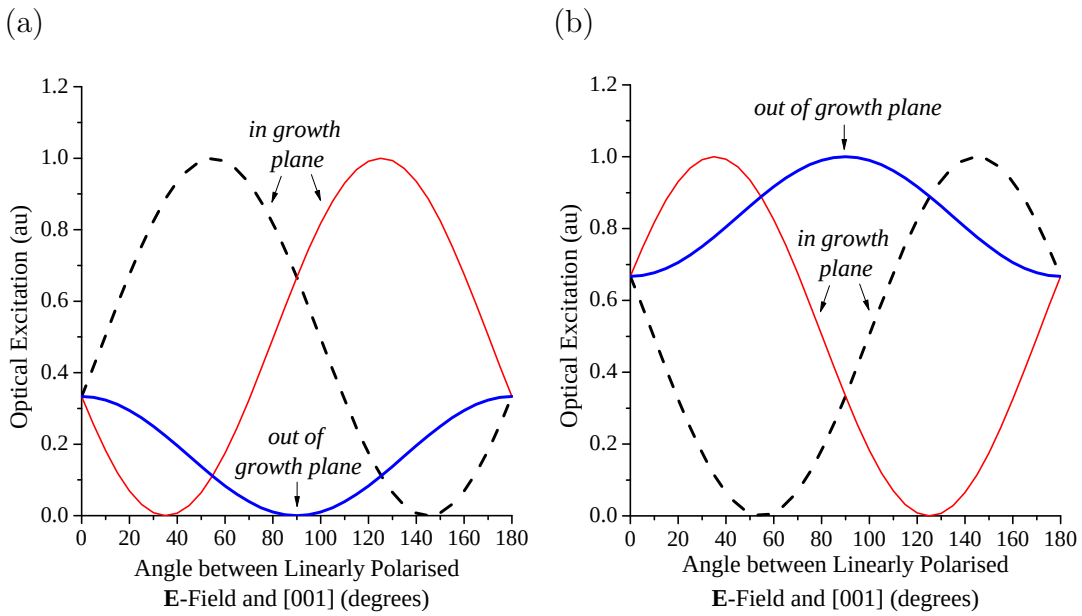

Figure 5-12: Theoretical polarisation dependence of the optical excitation for trigonal defects with their symmetry axes aligned parallel to ⟨111⟩ directions lying in (dashed (black) and thin solid (red) curves) and out of (thick solid (blue) curve) the growth plane for CVD diamond grown on a {110}-oriented substrate for (a) an $A \rightarrow A$ transition and (b) an $A \rightarrow E$ transition.

Assuming that 80% of the (Si-V)^0 were oriented along [111] and [$\bar{1}\bar{1}$1], and that the incident light was unpolarised or circularly polarised, the optical absorption can be corrected to account for the preferential orientation. If the 1.31 eV (Si-V)^0 transition is either $^3A_{2g} \rightarrow {}^3A_{1u}$ or $^3A_{2g} \rightarrow {}^3E_u$ it is apparent that these data points are only consistent with the correlation between the concentration of (Si-V)^0 and the integrated intensity of the 1.31 eV optical absorption if the transition is between a $^3A_{2g}$ ground state and a $^3A_{1u}$ excited state.

The PL spectrum in Fig. 5-3(a) is from an as-grown sample for which EPR measurements showed that the (Si-V)^0 centres were preferentially oriented, at a concentration of 500 ± 70 ppb (1 ppb = 1 part per billion carbon atoms). After annealing at 2000 °C, the concentration decreased to 250 ± 20 ppb, with equally distributed orientations, and with little change to the Raman normalised PL from the 1.31 eV line (Fig. 5-3(b)). Correcting the intensities to allow for the effect of the anisotropic distribution on the excitation efficiency and on the luminescence, it is found that the intensity of the PL is approximately proportional to the (Si-V)^0 concentration.

5.4.3 Charge transfer between 1.31 eV and 1.68 eV bands

The simultaneous presence of different charge states of the same defect in diamond is not uncommon. The relative concentrations of the charge states is determined by (a) the concentrations of other impurities which can act as acceptors or donors and (b) the treatment history such as illumination or moderate heating (here defined as < 800 °C). An example of the first effect is given by the neutral single substitutional nitrogen (N_s^0) centre, which often acts as a donor. Therefore, the concentration of the more negative charge states of centres increases with increasing N_s^0 concentration. This outcome has been explained by the impurities affecting the Fermi level in diamond [38]. This assumption has been drawn from the model of the Fermi level position in semiconductors such as silicon and germanium, where the donors and acceptors are fully ionised at room temperature. However, Collins has noted that this model is not applicable to diamond, where the nitrogen donors are scarcely ionised [29]. The material should be treated as an insulator, where the charge state of a centre depends on the local environment and the ability of an electron to tunnel from a donor to an acceptor. This also accounts for the co-existence of multiple charge states of a centre in a single sample, an observation which is incompatible with the former model. Charge transfer may be induced in defects via sample heating at moderate temperatures or photoexcitation. Using this method, the neutral and negative charge states of several defects in diamond have been studied, such as those of the vacancy ($V^{0/-}$, known as GR1 and ND1) [39, 40], the di-nitrogen vacancy ((N-V-N)$^{0/-}$, known as H3 and H2) [38], the nitrogen-vacancy-hydrogen ((N-V-H)$^{0/-}$) [41, 42], and the nitrogen-vacancy ((N-V)$^{0/-}$) centres [43].

For the charge transfer experiments reported in this investigation the concentrations of the centres were monitored using EPR ((Si-V)^0 and N_s^0) and optical absorption ((Si-V)^0 and (Si-V)$^-$ via the intensities of the 1.31 eV and 1.68 eV ZPLs, respectively). Figure 5-8 illustrates the effect of charge transfer between (Si-V)^0 and (Si-V)$^-$ for sample A after annealing at 2000 °C. Heating in the dark resulted in an increase in the intensity of the 1.68 eV band and a decrease in that of the 1.31 eV band. This treatment also induced a decrease in the N_s^0 and (Si-V)^0 concentrations as measured by EPR. The opposite effect could be generated by sample

(a)

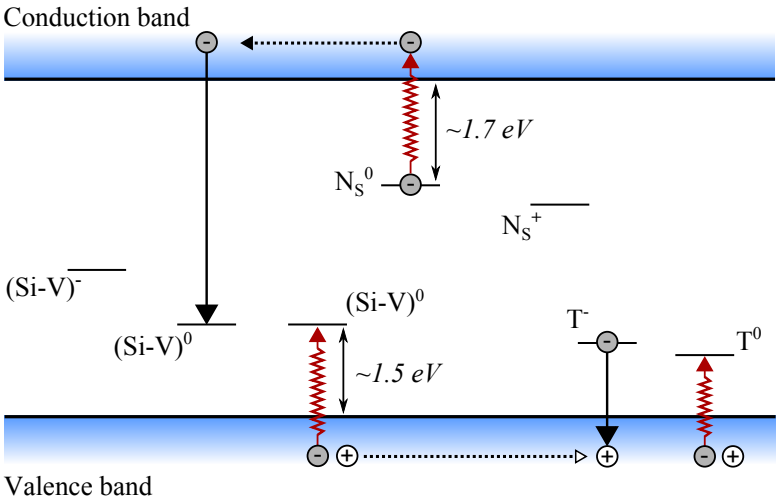

(b)

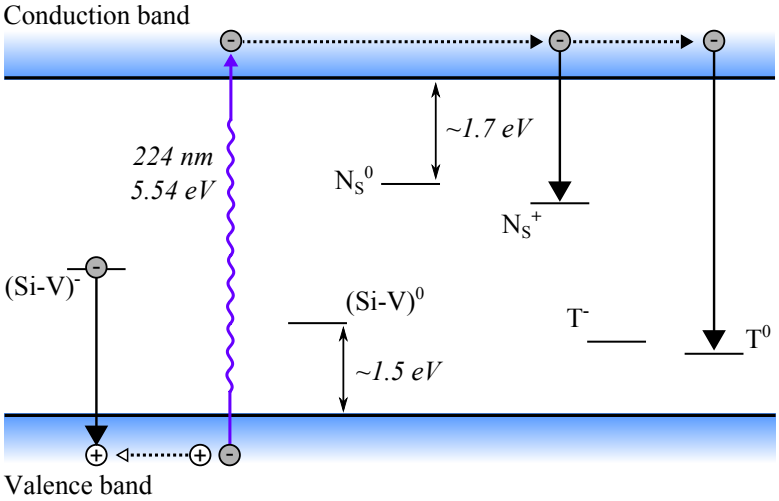

Figure 5-13: Schematic of the main phenomena occurring during the charge transfer process involving (Si-V)^0, (Si-V)$^-$, N_s^0, N_s^+ and the neutral and negative charge states of an unknown trap T. (a) When samples are heated for 20 minutes at 850 K (Si-V)^0 centres are converted to (Si-V)$^-$ centres by two processes: electrons are thermally released from the valence band to the (Si-V)^0 acceptor levels, converting them into (Si-V)$^-$ centres. Electrons are also thermally excited from the N_s^0 levels into the conduction band, from which they can de-excite into the (Si-V)^0 level. Simultaneously, recombination between T$^-$ and the holes in the valence band occurs. (b) Illuminating the sample with 5.54 eV (224 nm) energy excites electrons from the valence band into the conduction band. The electrons can then diffuse and de-excite into the N_s^+ and T^0 levels. The holes which were consequently produced in the valence band trap electrons from the (Si-V)$^-$ centres, increasing the (Si-V)^0 concentration.

illumination with light of energy greater than the band gap. The 1.68 eV band has previously been ascribed to either the (Si-V)$^-$ or (Si-V)^0 centres [1, 2, 44], these results unambiguously show that the 1.68 eV band cannot be (Si-V)^0 as the change in intensity of the ZPL is opposite to that observed for the (Si-V)^0 concentration measured by EPR. Instead, the relative change in the intensity of the 1.31 eV band after the treatments matched the changes to the EPR concentration of (Si-V)^0. These results can be explained by assuming that the 1.31 eV and 1.68 eV bands arise from chemically indistinguishable sites, so that the 1.31 eV band is attributed to a transition from the ground state to an excited state at the (Si-V)^0 centre. This is further supported by the correlation between the average (Si-V)^0 concentration measured by EPR and the integrated intensity of the 1.31 eV illustrated in Fig. 5-7 and discussed in §5.4.2.

Using this information it is possible to envisage a simplified model for the processes induced by the treatments. The positions of the ground states of the N_s^0 and (Si-V)^0 centres relative to the conduction and valence bands of diamond have been published. The donor level for N_s^0 lies ~ 1.7 eV below the conduction band of diamond [45]. For the proposed band diagram in Fig. 5-13 the (Si-V)^0 acceptor level is positioned ~ 1.5 eV above the valence band, as discussed in §5.4.1. When the samples are heated it is suggested that some of the charge from the N_s^0 impurities was transferred to the (Si-V)^0 centres, creating (Si-V)$^-$. However, the change in the (Si-V)^0 concentration was greater than that of the N_s^0 ($|\Delta[\text{(Si-V)}^0]| = 100 \pm 20$ ppb while $|\Delta[N_s^0]| = 19 \pm 1$ ppb) for sample A (after the 2000 °C anneal), implying that electrons were also thermally excited directly into the (Si-V)^0 levels and/or the involvement of other traps. Comparison of the energy separation between the (Si-V)^0 and N_s^0 levels to their closest carrier bands suggest that this is an acceptable proposition. However, this requires that the resulting holes in the valence band were then filled by the loss of an electron from at least one other defect, here denoted T. Conversely, illuminating the samples excited electrons from the valence band into the conduction band, simultaneously creating holes in the former band, which could have stimulated transitions to and from gap states. Free holes could diffuse to (Si-V)$^-$ defects, converting (Si-V)$^-$ centres to (Si-V)^0 centres. Meanwhile, the electrons in the conduction band could be trapped by N_s^+

and T^0. This picture is highly simplified, as several of the capture processes will occur simultaneously for both treatments. However, their relative probabilities will be different for each treatment, such that the processes outlined for each case in Fig. 5-13 would dominate.

Unknown traps such as T have previously been invoked to explain charge transfer processes in CVD diamond, for instance in the investigation of $(N\text{-}V\text{-}H)^{0/-}$ by Khan, *et al.* [42]. Interestingly, even for sample A, which was HPHT annealed, the existence of T was required in order to balance the charge transfer processes. An EPR or absorption feature which could be ascribed to T was not observed in the samples studied. However, this is unsurprising as the maximum concentration of T necessary to explain these results would be of the order of 100 ppb, which may be below our detection limit for this particular defect.

Optical absorption, like EPR, is a quantitative technique and the integrated intensity of a ZPL (in $\mathrm{meV\,cm^{-1}}$) is often used to calculate the concentration of the centre attributed to it (in $\mathrm{cm^{-3}}$) using published calibration constants (in $\mathrm{meV\,cm^2}$) [46]. For diamond, it is standard to do the absorption measurements for defect concentration calculations at 77 K since cooling to this temperature is experimentally common and features are generally sharp, facilitating detection. From the linear correlation between the $(Si\text{-}V)^0$ concentration and the integrated intensity of the absorption coefficient for the 1.31 eV band (Fig. 5-7) a calibration constant could be calculated, giving:

$$A_{1.31} = \left(1.57(\pm 0.06) \times 10^{-16}\right) \times \left[(Si\text{-}V)^0\right] \tag{5-5}$$

Furthermore, by equating the change in the $(Si\text{-}V)^0$ concentration to that of the $(Si\text{-}V)^-$ centres during charge transfer and linking that to the change in the 1.68 eV ZPL integrated intensity a calibration equation for $(Si\text{-}V)^-$ could also be determined:

$$A_{1.68} = \left(3.6(\pm 0.3) \times 10^{-15}\right) \times \left[(Si\text{-}V)^-\right] \tag{5-6}$$

The calibration constant for $(Si\text{-}V)^0$ is similar to that for the $(N\text{-}V)^-$ and V^0 (GR1) centres, which are $1.40(\pm 0.35) \times 10^{-16}\,\mathrm{meV\,cm^2}$ [46] and $1.2(\pm 0.3) \times 10^{-16}\,\mathrm{meV\,cm^2}$ [26], respectively. Comparing equations 5-5 and 5-6 suggests that the oscillator strength (which is proportional to the calibration constant) for $(Si\text{-}V)^-$ is approximately 23 times larger than that for $(Si\text{-}V)^0$. The factor of 23 could be partly

accounted for by the difference in vibronic coupling. Taking the Huang-Rhys factor for the 1.68 eV band as 0.24 [8, 9], and the 1.31 eV band as 1.5 (§5.4.1) it is possible to account for a factor of ~4. It is possible that a difference in radiative lifetime could also partially account for the difference.

5.4.4 Electron irradiation and annealing studies

At room temperature vacancies are immobile in diamond. Upon annealing at temperatures $\gtrsim 600\,^{\circ}$C the vacancies diffuse through the lattice [26]. In type IIa diamond the annealing of isolated vacancies (V) typically is described by mixed first and second order kinetics, $\mathrm{d[V]}/\mathrm{d}t = -r_1[\mathrm{V}] - r_2[\mathrm{V}]^2$, where [V] is the concentration of the vacancies, t is the time and r_1 and r_2 are the rate constants at a specific annealing temperature. The first term represents the loss of vacancies to non-saturable traps (e.g. surfaces and dislocations) and the second term accounts for the formation of divacancies, which are stable to ~ 800 °C [47].

Substitutional nitrogen centres are known to be effective traps for vacancies in diamond [48]. The relative intensities of the ZPLs for the neutral (2.156 eV) and negative (1.945 eV) charge states of the nitrogen-vacancy centres suggest that sample D contained a low concentration of $\mathrm{N_s^0}$ donors and (N-V) centres [29]. It is thus reasonable to assume that silicon, which is the dominant dopant, and its complexes will be the principal traps for the vacancies created and mobilised during the irradiation and annealing treatments, respectively. The divacancy was ignored in the modelling of irradiation damage and annealing, given that the divacancy anneals out at the annealing temperature used and the significant concentration of traps for isolated vacancies present. Isolated self-interstitials [49] anneal out at temperatures ~ 550 °C and although a variety of interstitial complexes have been identified in type IIa diamond [50, 51] there is no evidence for the interaction of self-interstitials with silicon. Thus, for this analysis self-interstitials were also ignored. Furthermore, due to the low substitutional nitrogen concentration, the treatments will primarily produce silicon-vacancy complexes in the neutral charge state. In as-grown material comparison of the EPR determined concentration of (Si-V)^0, plus the optically determined concentration of (Si-V)$^-$ (§5.4.3), and SIMS measurements of the total silicon concentration indicate that typically only

a fraction ($\lesssim 15\%$) of the silicon is accounted for in (Si-V) defects. The bulk of the silicon is presumed to be incorporated as substitutional silicon impurities (Si_S). Both (Si-V) and silicon divacancy, (Si-V_2), centres are expected to form according to $Si_S + V \rightarrow$(Si-V) and (Si-V) + V$\rightarrow$(Si-V_2) [12]. The kinetics of the system during isothermal annealing may therefore be described by

$$\frac{d[V]}{dt} = -r_1[V] - r_2[Si_S][V] - r_3[(Si\text{-}V)][V] \tag{5-7}$$

$$\frac{d[Si_S]}{dt} = -r_2[Si_S][V] \tag{5-8}$$

$$\frac{d[(Si\text{-}V)]}{dt} = r_2[Si_S][V] - r_3[(Si\text{-}V)][V] \tag{5-9}$$

$$\frac{d[(Si\text{-}V_2)]}{dt} = r_3[(Si\text{-}V)][V] \tag{5-10}$$

Twitchen *et al.* [47] determined that the vacancy production rate for irradiation of diamond with 1.9 MeV electrons at nominally room temperature was $\sim 0.5\,cm^{-1}$. Lawson *et al.* [52] derived a value of $0.6\,cm^{-1}$ for 2 MeV electrons and Collins and Dahwich [53] $0.7\,cm^{-1}$ for 3 MeV electrons for diamond with low concentrations of nitrogen. The fit in Fig. 5-14(a) assumes a vacancy production rate of $\sim 0.44\,cm^{-1}$ for 1.5 MeV electrons at room temperature, a value that is not out of line with other results.

The intensity of the 1.31 eV and 1.68 eV bands across all layers of sample D increased dramatically after the first treatment, and the resulting (Si-V)^0 concentration was approximately constant. For the subsequent treatment the electron irradiation dose was increased five-fold and the intensity of the 1.31 eV ZPL was observed to further increase in the layers containing high concentrations of silicon. However, the strength of the ZPL did not change (within error) in the layers containing low concentrations of silicon (~ 250 ppb). It was assumed that all the available substitutional silicon impurities had formed silicon-vacancy complexes after the first treatment, i.e. ~ 250 ppb, and that the Raman normalised 1.31 eV ZPL PL intensity is proportional to the (Si-V)^0 concentration. It was thus possible to estimate the (Si-V)^0 concentration from the PL data, as illustrated in Fig. 5-14(a). This calibration is consistent with the PL measurements of other silicon-doped samples containing known concentrations of (Si-V)^0 defects.

Using these assumptions it was possible to model the system upon annealing at 900 °C by numerically solving the coupled differential equations 5-7 to 5-10. The

(a)

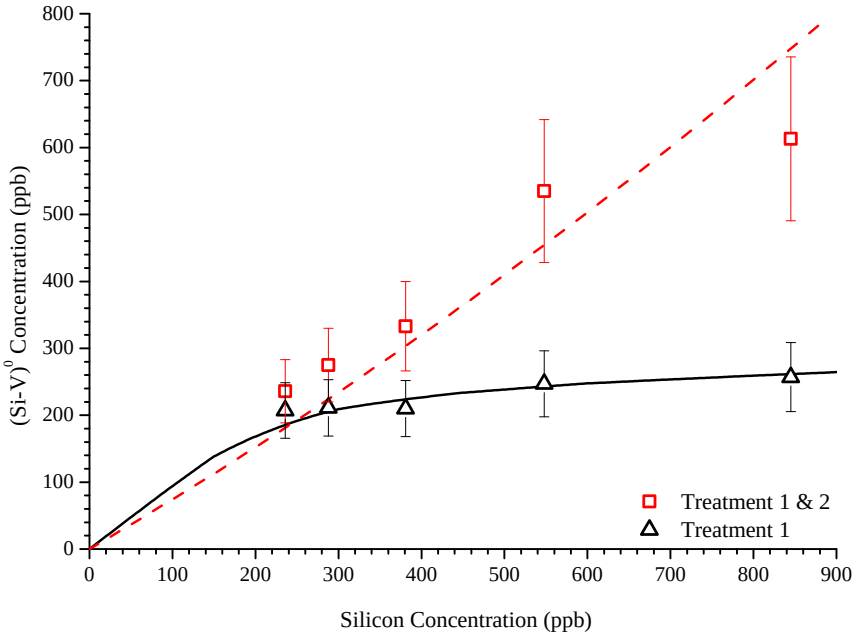

(b)

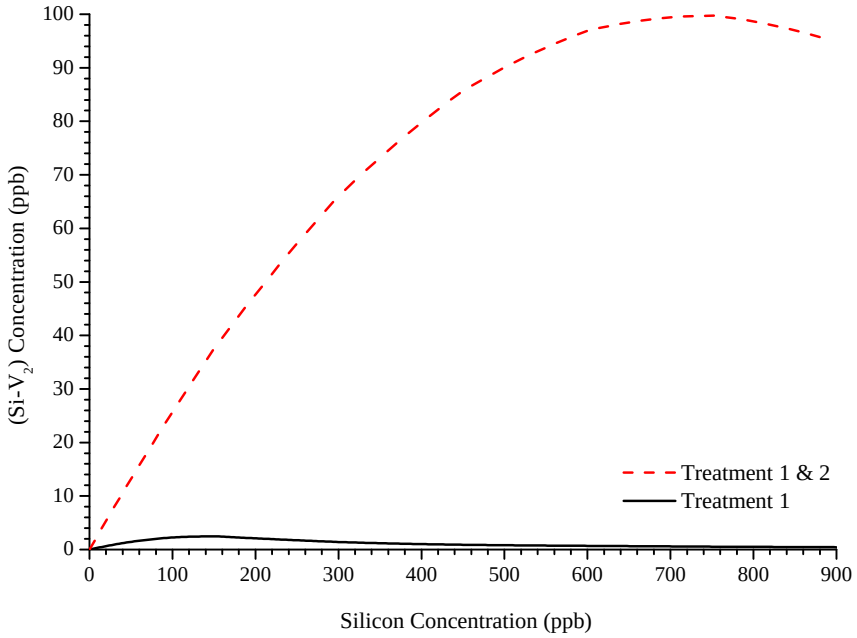

Figure 5-14: (a) (Si-V)^0 concentration in the different layers of sample D after electron irradiation and annealing treatments 1 and 2 (Table 5-1). The lines indicate the simulated behaviour when the system is modelled to include the loss of vacancies to dislocations and the formation (and destruction) of (Si-V) and (Si-V$_2$) centres via the reactions Si + V → (Si-V) and (Si-V) + V → (Si-V$_2$). (b) The resulting simulated data for the (Si-V$_2$) concentration in the layers after each treatment, assuming that there were no (Si-V$_2$) centres in the untreated sample.

rate constant for the first order loss of vacancies was determined from the data of Davies *et al.* in type IIa diamond and not varied [26]. The only variable parameters were r_2 and r_3. The best fits to the data, shown by the lines in Fig. 5-14(a), were achieved with r_1 = 4.40 h^{-1}, r_2 = 0.11 ppb^{-1}h^{-1} and r_3 = 10^{-3} ppb^{-1}h^{-1}. The value of r_2, and the data in Fig. 5-14(a) indicated that Si_S is an excellent trap for vacancies. (Si-V_2) is predicted to be stable at the annealing temperatures [12], but the production is vacancy limited. Figure 5-14(b) presents the simulated data for the concentrations of (Si-V_2) produced after each irradiation and annealing treatment, assuming that there were no (Si-V_2) centres in the untreated material. The analysis predicts that further irradiation and annealing could produce substantial quantities of (Si-V_2).

5.5 Conclusions and further work

The 1.31 eV system is identified with the (Si-V)^0 centre in diamond. The 1.31 eV ZPL shifts in energy when the silicon isotope is changed, conclusively identifying the centre as silicon-related. The electronic structure and vibronic coupling in the 1.31 eV system has been studied. The Huang-Rhys factor is ~1.5 and a trapping level or shelving state has been identified ~5 meV below the excited state involved in the 1.31 eV ZPL. The (Si-V)^0 concentration determined by EPR has been shown to correlate with the integrated absorption of the 1.31 eV ZPL. This, combined with the analysis of charge transfer between (Si-V)$^-$ (1.68 eV system) and (Si-V)^0 has enabled the calculation of calibration constants relating the integrated absorption of the 1.68 eV and 1.31 eV ZPLs with the (Si-V)$^-$ and (Si-V)^0 defect concentrations, respectively.

(Si-V)^0 defects have been shown to predominantly grow into CVD diamond as complete units, rather than being produced by the migration of vacancies which are trapped at substitutional silicon impurities. This results in the preferential alignment of the (Si-V)^0 centres for homoepitaxial CVD on {110}-oriented substrates, with the D_{3d} symmetry axis pointing out of the growth plane. The reduction of the number of possible orientations of this defect from four to two could be useful in applications where their optical emission is coupled out of the diamond. It is

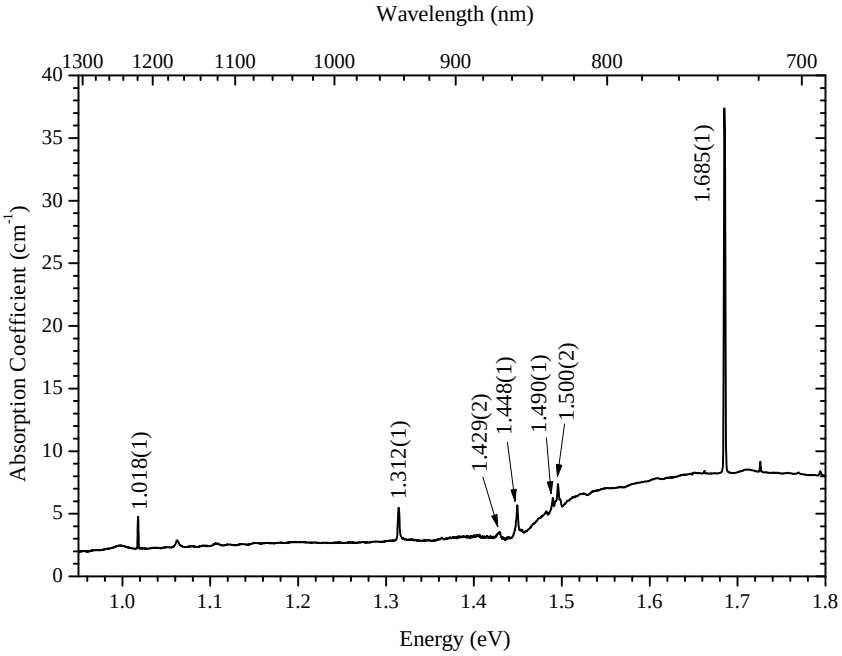

Figure 5-15: Optical absorption spectrum at 4 K of sample A (after annealing at 2000 °C), showing an unidentified, possibly silicon-related, ZPL at 1.018 ±0.001 eV.

important to correct for the preferential alignment of (Si-V)^0 in the quantitative analysis of EPR and optical spectroscopic measurements. The preferential orientation has been utilised in polarised spectroscopic studies to identify the 1.31 eV ZPL as a transition between the $^3A_{2g}$ ground state and $^3A_{1u}$ excited states of (Si-V)^0. A uniaxial-stress study of the 1.31 eV band would enable the determination of the defect symmetry and verify the nature of the transition. These experiments could be conducted in absorption or PL, though the latter technique would provide the investigator with a higher level of sensitivity.

No evidence for quenching of the 1.31 eV band in PL has been detected, even though a variety of previously unreported, probably silicon-related, optical centres have been observed, allowing semi-quantitative analysis of PL data. SIMS measurements show that only a fraction of the incorporated silicon impurities in as-grown CVD diamond is in the form of (Si-V) defects, the majority being substitutional silicon atoms. Irradiation and annealing at temperatures where vacancies are mobile dramatically increases the concentration of (Si-V) defects; substitutional silicon appears to be a very effective trap for vacancies. Modelling of the experimental data on the production of (Si-V) in irradiated silicon-doped diamond

suggests that substantial quantities of (Si-V_2) can be produced if sufficient concentrations of vacancies are introduced. Future experiments are planned to maximise the (Si-V_2) concentration in silicon-doped CVD diamond via the introduction of a high concentration of vacancies by either electron or neutron irradiation, followed by annealing at 900 °C. The negative charge state, (Si-V_2)$^-$, should be EPR active with $S = \frac{1}{2}$ [12]. Furthermore, (Si-V_2) has been proposed to be optically active, with a transition energy in the 1.0-1.5 eV range and one close to the band-gap energy tentatively predicted [12]. It is noteworthy that a previously unreported ZPL at 1.018 ± 0.001 eV (1219.5 ± 0.1 nm) has been observed in absorption only in silicon-containing material, as shown in Fig. 5-15. This line has not yet been investigated in any detail, and it has not yet been established whether it was present in the layered sample (if visible in PL). Therefore, it would be of interest to carry out a systematic study of this peak, including $^{28}\text{Si} \rightarrow {}^{29}\text{Si}$ isotopic shift, photochromic, thermochromic, and irradiation and annealing experiments in a similar manner to those conducted on the 1.31 eV band.

The temperature dependence of the 1.31 eV ZPL in PL suggests that less that 5% of the 785 nm excitation led to direct excitation to this state. Thus the signal-to-noise intensity of the luminescence could potentially improve by a factor ~ 20 if an appropriate laser excitation is chosen such that the valence band and the intermediate state (illustrated in Fig. 5-10), were no longer involved in the excitation process of the 1.31 eV band. Additionally, resonant excitation into the 1.31 eV state could be investigated using a 946 nm Nd:YAG laser. Reports of single photon detection of the (Si-V)$^-$ centre can be found in the literature [7, 8]; it would be of interest to attempt these types of experiments on the 1.31 eV band as well.

The highest concentration of (Si-V)$^-$ recorded for the samples studied (including treated samples) was of the order of 100 ppb, as determined by the optical absorption spectrum and equation 5-6. The centre is predicted to be EPR-active, with a spin $S = \frac{1}{2}$ [2, 12]. However, the EPR spectra acquired did not contain any unaccounted resonance lines. The ground state of (Si-V)$^-$ is split by a dynamic Jahn-Teller coupling [2], which may result in an averaging between the different possible configurations at a time scale that is fast relative to that of EPR measurements. Consequently, the centre's EPR lines may broaden, becoming difficult

to detect. (Si-V)$^-$ could be investigated by applying uniaxial-stress during EPR experiments, which may lift the degeneracy and sharpen the line. Preparations to commence these experiments are underway.

References

[1] C. D. Clark, H. Kanda, I. Kiflawi, and G. Sittas, Phys. Rev. B **51**, 16681 (1995).

[2] J. P. Goss, R. Jones, S. J. Breuer, P. R. Briddon, and S. Öberg, Phys. Rev. Lett. **77**, 3041 (1996).

[3] J. Barjon, E. Rzepka, F. Jomard, J. M. Laroche, D. Ballutaud, T. Kociniewski, and J. Chevallier, Phys. Status Solidi A **202**, 2177 (2005).

[4] L. H. Robins, L. P. Cook, E. N. Farabaugh, and A. Feldman, Phys. Rev. B **39**, 13367 (1989).

[5] S. D. Williams, D. J. Twitchen, P. M. Martineau, G. A. Scarsbrook, and I. Friel, *High colour diamond*, UK Patent GB2428690 B (2010).

[6] H. Kanda and T. Sekine, in *Properties and Growth of Diamond*, edited by G. Davies (INSPEC, London, 1994), no. 9 in EMIS Datareview Series, chap. 12, pp. 405 – 408, 1st ed.

[7] C. L. Wang, C. Kurtsiefer, H. Weinfurter, and B. Burchard, J. Phys. B-At. Mol. Opt. **39**, 37 (2006).

[8] E. Neu, D. Steinmetz, J. Riedrich-Möller, S. Gsell, M. Fischer, M. Schreck, and C. Becher, New J. Phys. **13**, 025012 (2011).

[9] A. T. Collins, L. Allers, C. J. Wort, and G. A. Scarsbrook, Diam. Relat. Mater. **3**, 932 (1994).

[10] H. Sternschulte, K. Thonke, R. Sauer, P. C. Munzinger, and P. Michler, Phys. Rev. B **50**, 14554 (1994).

[11] A. Batalov, C. Zierl, T. Gaebel, P. Neumann, I. Y. Chan, G. Balasubramanian, P. R. Hemmer, F. Jelezko, and J. Wrachtrup, Phys. Rev. Lett. **100**, 077401 (2008).

[12] J. P. Goss, P. R. Briddon, and M. J. Shaw, Phys. Rev. B **76**, 075204 (2007).

[13] C. M. Breeding and W. Wang, Diam. Relat. Mater. **17**, 1335 (2008).

[14] A. M. Edmonds, M. E. Newton, P. M. Martineau, D. J. Twitchen, and S. D. Williams, Phys. Rev. B **77**, 245205 (2008).

[15] K. Iakoubovskii, A. Stesmans, B. Nouwen, and G. J. Adriaenssens, Phys. Rev. B **62**, 16587 (2000).

[16] L. Allers and A. T. Collins, J. Appl. Phys. **77**, 3879 (1995).

[17] D. J. F. Evans, C. F. Kelly, P. Leno, P. M. Martineau, and A. J. Taylor, in *The 57th Diamond Conference* (2006), p. 38.

[18] B. J. Masters, Solid State Comm. **9**, 283 (1971).

[19] V. A. Nadolinny, A. P. Yelisseyev, O. P. Yuryeva, and B. N. Feygelson, Appl. Magn. Reson. **12**, 543 (1997).

[20] J. P. Goss, P. R. Briddon, R. Jones, and S. Sque, Diam. Relat. Mater. **13**, 684 (2004).

[21] A. Nadolinny, V. amd Yelisseyev, J. Struct. Chem. **35**, 133 (1994).

[22] R. Larico, J. Justo, W. Machado, and L. Assali, Physica B **376-377**, 292 (2006).

[23] L. Assali, W. Machado, R. Larico, and J. Justo, Diam. Relat. Mater. **16**, 819 (2007).

[24] G. D. Watkins, Phys. Rev. B **12**, 4383 (1975).

[25] C. A. Coulson and F. P. Larkins, J. Phys. Chem. Solids **30**, 1963 (1969).

[26] G. Davies, S. C. Lawson, A. T. Collins, A. Mainwood, and S. J. Sharp, Phys. Rev. B **46**, 13157 (1992).

[27] C. D. Clark, J. Phys. Chem. Solids **8**, 481 (1959).

[28] A. M. Edmonds, Ph.D. thesis, University of Warwick (2008).

[29] A. T. Collins, J. Phys.-Condens. Mat. **14**, 3743 (2002).

[30] G. Davies and M. F. Hamer, Proc. R. Soc. Lond. A **348**, 285 (1976).

[31] G. Davies, J. Phys. C: Solid State **12**, 2551 (1979).
[32] G. Davies, Semiconductors and Semimetals **51(P2)**, 1 (1998).
[33] G. Davies, Reports on Progress in Physics **44**, 787 (1981).
[34] K. Huang and A. Rhys, Proc. R. Soc. A **204**, 406 (1950).
[35] K. K. Rebane, *Impurity Spectra of Solids : Elementary Theory of Vibrational Structure* (Plenum Press, New York, 1970).
[36] U. F. S. D'Haenens-Johansson, A. M. Edmonds, B. L. Green, M. E. Newton, G. Davies, P. M. Martineau, R. U. A. Khan, and D. J. Twitchen, Phys. Rev. B p. (submitted) (2011).
[37] U. F. S. D'Haenens-Johansson, A. M. Edmonds, M. E. Newton, J. P. Goss, P. Briddon, J. M. Baker, P. M. Martineau, R. U. A. Khan, D. J. Twitchen, and S. D. Williams, Phys. Rev. B **82**, 155205 (2010).
[38] Y. Mita, Y. Nisida, K. Suito, A. Onodera, and S. Yazu, J. Phys.- Condens. Mat. **2**, 8567 (1990).
[39] H. B. Dyer and L. D. du Preez, J. Chem. Phys. **42**, 1898 (1965).
[40] A. T. Collins and S. Rafique, Proc. R. Soc. A **367**, 81 (1979).
[41] R. U. A. Khan, P. M. Martineau, B. L. Cann, M. E. Newton, H. K. Dhillon, and D. J. Twitchen, Gems. Gemol. **46**, 18 (2010).
[42] R. U. A. Khan, P. M. Martineau, B. L. Cann, M. E. Newton, and D. J. Twitchen, J. Phys.- Condens. Mat. **21**, 6171 (2009).
[43] N. Manson and J. Harrison, Diam. Relat. Mater. **14**, 1705 (2005).
[44] K. Iakoubovskii, G. J. Adriaenssens, and M. Nésladek, J. Phys.-Condens. Mat. **12**, 189 (2000).
[45] R. G. Farrer, Solid State Commun. **7**, 685 (1969).
[46] G. Davies, Physica B **274**, 15 (1999).
[47] D. J. Twitchen, M. E. Newton, J. M. Baker, T. R. Anthony, and W. F. Banholzer, Phys. Rev. B **59**, 12900 (1999).
[48] A. T. Collins, J. Phys. C: Solid State **13**, 2641 (1980).
[49] D. C. Hunt, D. J. Twitchen, M. E. Newton, J. M. Baker, J. K. Kirui, J. A. van Wyk, T. R. Anthony, and W. F. Banholzer, Phys. Rev. B **62**, 6587 (2000).
[50] D. C. Hunt, D. J. Twitchen, M. E. Newton, J. M. Baker, T. R. Anthony, W. F. Banholzer, and S. S. Vagarali, Phys. Rev. B **61**, 3863 (2000).
[51] D. J. Twitchen, M. E. Newton, J. M. Baker, O. D. Tucker, T. R. Anthony, and W. F. Banholzer, Phys. Rev. B **54**, 6988 (1996).
[52] S. C. Lawson, D. Fisher, D. C. Hunt, and M. E. Newton, J. Phys.- Condens. Mat. **10**, 6171 (1998).
[53] A. T. Collins and A. Dahwich, J. Phys.- Condens. Mat. **15**, L591 (2003).

Chapter 6

Optical spin polarisation of the neutral silicon split-vacancy centre

6.1 Background and motivation

There has been a great deal of research conducted on colour centres in diamond in order to find viable candidates which could be utilised as qubits for solid-state quantum computation [1–3] or nanoscale magnetic sensing [4–6], or as single-photon sources for quantum communication [7, 8]. Single photon detection from the following centres in diamond has been reported: the negatively charged nitrogen-vacancy ($(\text{N-V})^-$) centre [7, 8], the NE8 nickel-nitrogen complex [9, 10], a silicon-nitrogen complex [11], a possibly chromium-related defect [12], and the negatively charged silicon split-vacancy ($(\text{Si-V})^-$) centre [13, 14], with zero phonon lines (ZPLs) at 1.945 eV (637 nm), 1.565 eV (793 nm), 1.616 eV (768 nm), 1.642 eV (756 nm), and 1.685 eV (737 nm), respectively.

Most research has focussed on $(\text{N-V})^-$ due to its long spin-spin relaxation time τ_2 (§3.1.5.2), which is approximately the time available to perform any operations on the spin, and the relative ease of fabrication [15]. In order for a centre to be a viable qubit it has to have a value of τ_2 which is several orders of magnitude greater than the spin manipulation time. $(\text{N-V})^-$ has a long spin-lattice relaxation time τ_1 (§3.1.5.2 and §3.1.6.4) which is expected to be of the order of seconds at room temperature in the best quality material [15, 16]. This is significant since $\tau_2 \leq 2\tau_1$ [17]. The centre has a ${}^3A_2$ spin triplet ground state (effective spin $S = 1$) which can be optically spin polarised [18–20] via a non-spin conserving intersystem crossing

mechanism, leading to the preferential population of the $M_S = 0$ ground state spin level (explained in the following section, §6.1.1). The populations of the spin levels of the ground state manifold can be manipulated by inducing optical spin polarisation and applying strong microwave pulses to invert the populations of the levels. The ZPL at 1.945 eV arises from a transition between the $^3A_2$ ground state and the ^3E excited state [21, 22]. The populations of the ground state spin levels can be read out by exploiting the difference in the brightness of the fluorescence between the bright singlet ($M_S = 0$) and the relatively dark doublet ($M_S = \pm 1$) levels [23, 24]. However, the broad emission band of (N-V)$^-$ at room temperature is a disadvantage as it prevents efficient filtering of the background signals [8].

Room temperature single photon emission has been observed from (Si-V)$^-$ centres in ion implanted type IIa bulk diamond [13] and more recently with a much greater quantum efficiency in Si-doped CVD nano-diamonds by Neu *et al.* [14]. There are several properties that render (Si-V)$^-$ noteworthy for quantum-information applications. (Si-V)$^-$ has a remarkably sharp ZPL, with a width of ~ 0.7 nm reported at room temperature (to date, the most narrow for a colour centre in diamond) [14], and a weak vibronic sideband characterised by a small Huang-Rhys factor of $S \sim 0.24$ [14, 25]. Furthermore, the centres emit light in a wavelength region where there is low background fluorescence from diamond [14]. Recent reports of single photon count rates up to 4.8×10^6 counts/s at saturation for (Si-V)$^-$ are significantly higher than those for (N-V)$^-$ ($\sim 10^5$ counts/s) and even "chromium" colour centres (3.2×10^6 counts/s) [8, 12, 14]. However, the development of applications based on this system will be (presently) hampered by the fact that the centre has not yet been identified using EPR, despite predictions that it has a spin $S = 1/2$ and is thus paramagnetic [26, 27].

The first observation of the $^3A_{2g}$ ground state [26] of the neutral silicon split-vacancy centre ((Si-V)^0) using EPR was achieved by Iakoubovskii *et al.* [28–30], who named the paramagnetic centre KUL1. The multifrequency EPR studies on intentionally silicon-doped CVD single crystal diamond by Edmonds *et al.* [31] in conjunction with the theoretical work by Goss *et al.* [26] confirmed the assignment of KUL1 to (Si-V)^0. In Chapter 5 a ZPL at 1.311 eV (946 nm), visible in absorption and luminescence, has been attributed to the $^3A_{2g} \leftrightarrow {}^3A_{1u}$ transition.

In this chapter EPR under optical illumination is used to investigate the optically induced spin polarisation of the ${}^3A_{2g}$ ground state of (Si-V)^0. The change in the signal intensity is investigated as a function of excitation energy and temperature and two possible mechanisms for the optical spin polarisation will be considered. Furthermore, the effect of the illumination on τ_1 values for both (Si-V)^0 and (N-V)$^-$ will be examined to elucidate the reason for the difference in the degree of optical spin polarisation achieved for the two centres.

6.1.1 Optical spin polarisation of (N-V)$^-$

The nitrogen-vacancy defect in diamond consists of a substitutional nitrogen atom located next to a vacant lattice site, resulting in a centre with C_{3v} symmetry, with the principal axis lying along the $\langle 111 \rangle$ axis which connects the impurity and the vacancy. A linear combination of the dangling orbitals (§3.2.1-§3.2.2) from the three carbon atoms surrounding the vacancy (labelled ϕ_a, ϕ_b and ϕ_c) with that from the neighbouring nitrogen atom (ϕ_N) produces two non-degenerate orbital states (singlets, a) and a doubly degenerate orbital (doublet, e), according to:

$$\begin{aligned} a_{1N} &\left\{ \begin{array}{l} \phi_1 = \phi_N \end{array} \right. \\ a_{1C} &\left\{ \begin{array}{l} \phi_2 = \phi_a + \phi_b + \phi_c \end{array} \right. \\ e &\left\{ \begin{array}{l} \phi_3 = \phi_b - \phi_c \\ \phi_4 = 2\phi_a - \phi_b - \phi_c \end{array} \right. \end{aligned} \qquad (6\text{-}1)$$

Assuming that the levels lie in the following order, $a_{1N} < a_{1C} < e$, the many electron states for different charge states of the nitrogen vacancy can be calculated by populating the levels with the available unpaired electrons, obeying the Pauli exclusion principal, and applying group theoretical arguments (§3.2.2). For (N-V)$^-$ there are six electrons available to occupy the levels; the lowest energy configuration $a_{1N}^2 a_{1C}^2 e^2$ gives rise to ${}^1A_1$, ${}^3A_2$ and ${}^1E$ many electron states. If an electron is promoted from the a_{1C} level to the e level (which can accept up to four electrons) ${}^1E$ and ${}^3E$ many electron states are produced.

Uniaxial stress experiments of a ZPL at 1.945 eV, coupled with annealing studies of type Ib electron irradiated diamond, were conducted by Davies and Hamer [21], who attributed the line to a transition between the A_1 (ground) and E (ex-

cited) states of (N-V)$^-$. Loubser and van Wyk [32] used EPR to investigate material for which the 1.945 eV ZPL had been observed, but were unable to detect a spectrum for (N-V)$^-$ in the dark. However, upon illumination they revealed a spectrum of a centre with $S = 1$, a nearly isotropic g factor and a zero-field splitting of magnitude $|\mathbf{D}| = D = 2.878 \pm 0.006$ GHz (where $\mathbf{D}$ is parallel to $\langle 111 \rangle$). These results were taken to mean that the EPR spectrum detected arose from a "metastable" spin triplet state rather than the ground state, which was thought to be $^1A_1$. Subsequently, holeburning [33], EPR [22] and optically detected magnetic resonance (ODMR) [34] studies have demonstrated that the $^3A_2$ state observed by Loubser and van Wyk was actually the ground state of (N-V)$^-$ and that the 1.945 eV ZPL originates from the $^3A_2 \leftrightarrow {}^3E$ transition. The ordering of the other possible many electron states, in particular the spin singlets $^1A_1$ and ^1E, is still controversial [18, 26, 35–37].

The spin triplet $^3A_2$ ground state of (N-V)$^-$ consists of a singlet ($M_S = 0$, with A_1 symmetry) and a doublet ($M_S = \pm 1$, with E symmetry) which are separated at zero field by $D = 2.878 \pm 0.006$ GHz [32] due to a spin-spin and spin-orbit coupling, where the latter interaction dominates. If the static magnetic field of a CW EPR experiment is aligned parallel to a $\langle 111 \rangle$ axis the resonance lines with the highest splitting arise from the trigonal centres which have their symmetry axes along the field. The intensities of these lines are proportional to the difference in the populations of the $M_S = 0$ and $M_S = \pm 1$ spin levels, which in the absence of optical pumping are dictated by Boltzmann statistics. The sign of D, and thus the ordering of the ground state singlet and doublet, was determined to be positive by Harrison *et al.* by comparison of the intensities of the low and high field resonance lines at 2 K [18]. An illustration of the ground state spin levels under EPR conditions for (N-V)$^-$ in the dark are shown in Fig. 6-1(a). Under optical illumination Loubser and van Wyk [32] noted that the low-field line was seen in enhanced absorption while that at high field was in emission (seen as an inverted characteristic line shape), a result which has been reproduced by Harrison [18, 19], Edmonds [31], Rogers [38] and their collaborators. This effect is known as *optical spin polarisation*, often shortened to "spin polarisation," and producess a non-Boltzmann population of the ground state spin levels. If D is positive the

(a)

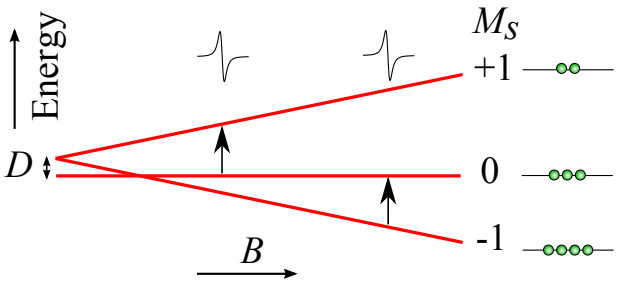

(b)

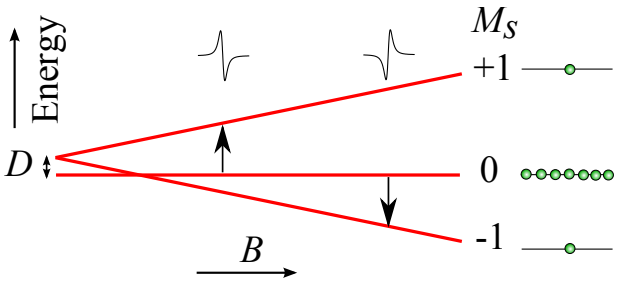

(c)

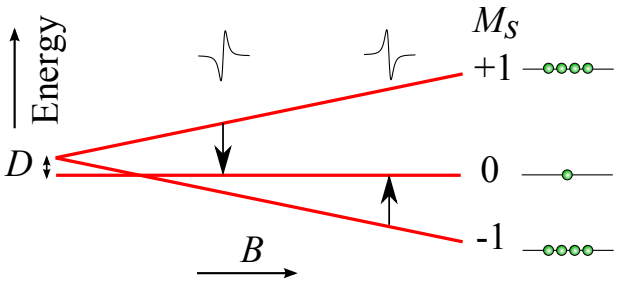

Figure 6-1: Schematic of the splitting of the triplet ground state spin levels, with $M_s = 0$ and ± 1, under an increasing magnetic field B and a positive zero-field splitting of magnitude D. (a) In the dark the population of the levels is governed by Boltzmann statistics and the resulting resonance lines will be detected in absorption. During illumination of sufficient energy the ground state may be optically spin polarised (if a mechanism exists), resulting in the preferential population of the (b) $M_S = 0$ or (c) $M_S = \pm 1$ spin levels and an EPR spectrum with differently ordered resonance lines in (enhanced) absorption and emission.

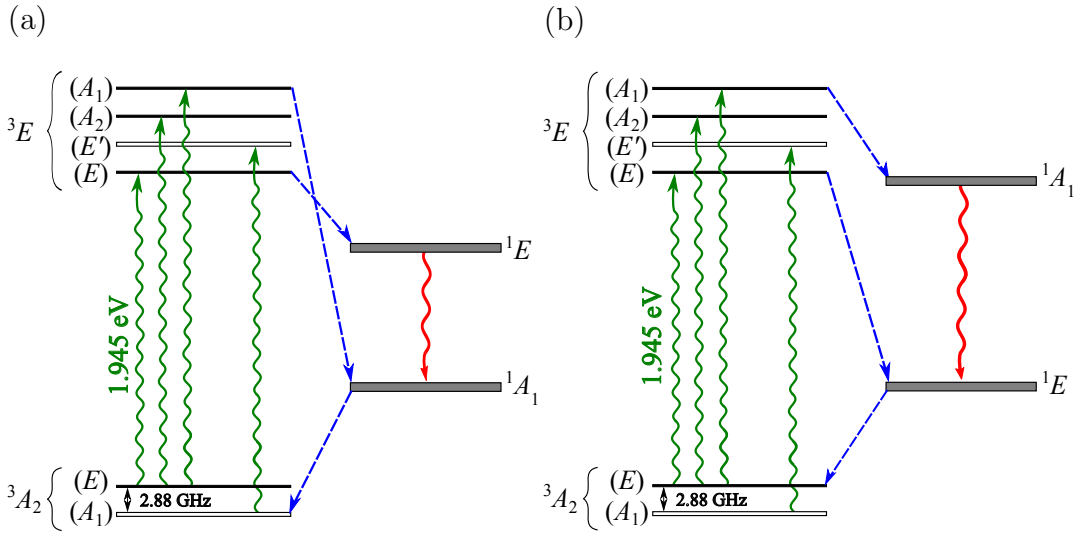

Figure 6-2: Two competing models for the energy structure of the (N-V)$^-$ centre in the absence of strain. A spin-spin and spin-orbit interaction splits the triplet ground state $^3A_2$ into a singlet (A_1) with $M_S = 0$ and a doublet (E) with $M_S = \pm 1$. The separation between the singlet and doublet for $\mathbf{B} = 0$ is given by $D = 2.88$ GHz. The ^3E excited state, which lies 1.945 eV above the ground state, is split due to spin-orbit and spin-spin interactions into levels with A_1, A_2, E and E' symmetries. The allowed spin and symmetry conserving transitions between $^3A_2 \leftrightarrow {}^3E$ and $^1E \leftrightarrow {}^1A_1$ are indicated by wavy arrows in green or red, respectively. The spin-orbit interaction can mix the triplet and singlet many electron states, so that nonspin conserving transitions (blue dashed arrows) become allowed. If light of energy equal to or greater than 1.945 eV is incident on the centre the intersystem crossing may preferentially populate either the singlet or doublet levels of the ground state, a phenomenon known as optical spin polarisation. (a) In the model proposed by Manson and his colleagues [35, 36] the $^1A_1$ state lies below the ^1E state and the intersystem crossing results in a preferential population of singlet level of the ground state, in agreement with experimental data. (b) However, density functional theory (DFT) calculations predict that the $^1A_1$ state lies above the ^1E state, in which case the intersystem crossing would produce a preferential population of the doublet level of the ground state. Delaney *et al.* predict the separation between the $^1A_1$ and ^1E states to be ~ 1.42 eV, in reasonable agreement with the 1.187 eV ZPL attributed to the transition by Rogers *et al.* [38].

data indicate that the M_S = 0 level was preferentially populated during optical pumping (see Fig. 6-1(b)). Conversely, if the M_S = ±1 levels had been preferentially populated the low and high field lines would have been in emission and absorption, respectively [18], contrary to observations.

The mechanism for the optical spin polarisation of the (N-V)$^-$ centre is currently under debate. The model proposed by Manson and his colleagues [18, 35, 36, 38] is based on a nonspin conserving intersystem crossing from the triplet ^3E excited state to the singlet $^1A_1$ or/and ^1E states. The axial spin-orbit interaction $(\lambda_{\mathrm{SO}})_z \hat{L}_z \hat{S}_z$ (§3.1.3.1) splits the ^3E excited state into three twofold degenerate levels, labelled (E), (E') and (A_1, A_2) according to the irreducible representation of $C_{3\mathrm{v}}$ symmetry [35, 36, 38, 39]. The transverse spin-orbit coupling $(\lambda_{\mathrm{SO}})_{x,y}$ term is weak [40] and can be neglected. Spin-spin (also known as dipole-dipole) interactions displace the (A_1, A_2) levels by the energy $D(\hat{S}_z^2 - 2/3)$ [39]. For a more detailed explanation on the determination of the symmetry adapted wave-functions related to the different levels the reader is directed to Refs. [35, 36, 39]. A cartoon of the electronic structure based on that presented by Manson is displayed in Fig. 6-2(a). The only symmetry allowed, spin conserving ($\Delta M_S = 0$) transitions are $^3A_2(A_1) \leftrightarrow {}^3E(E')$, $^3A_2(E) \leftrightarrow {}^3E(E)$, $^3A_2(E) \leftrightarrow {}^3E(A_1)$ and $^3A_2(E) \leftrightarrow {}^3E(A_2)$. Spin polarisation cannot be induced by the optical cycling of the allowed electronic dipole transitions since they do not result in a transfer of electrons between the ground state spin levels. However, the spin-orbit interaction can mix the spin triplet and spin singlet many electron states so that nonspin conserving relaxation pathways between the two systems become weakly allowed. Intersystem crossing, which is a nonradiative process, can only occur between states which transform according to the same irreducible representation. Group theory does not provide information regarding the ordering of the $^1A_1$ and ^1E states relative to the $^3A_2$ and ^3E states. If the intersystem crossing only involved the $^1A_1$ singlet it would be restricted to states that transform as A_1 irreducible representations. Hence, the process could be $^3A_2(E) \rightarrow {}^3E(A_1) \Rightarrow {}^1A_1 \Rightarrow {}^3A_2(A_1)$, where intersystem crossing transitions are indicated by $\Rightarrow$. This would lead to the preferential population of the M_S = 0 level of the ground state ($^3A_2(A_1)$) after a number of cycles. If, instead, the nonradiative relaxation involved only the ^1E state the end result would

be the preferential population of the $M_S = \pm 1$ ground levels, which is inconsistent with the experimental data [18, 19, 31, 32].

If both the $^1A_1$ and ^1E states are involved it is their relative ordering which becomes significant: if $^1A_1 > {}^1E$ (the energy of $^1A_1$ is greater than that of ^1E) the $M_S = \pm 1$ levels would become preferentially populated, whilst if $^1E > {}^1A_1$ the $M_S = 0$ level would be preferentially populated instead [18, 35, 36]. The radiative $^1A_1 \leftrightarrow {}^1E$ (for either ordering) transition has been assigned to a ZPL at 1.187 eV (1046 nm) [38]. Due to the agreement between Manson's model and the experimental data the scheme in Fig. 6-2(a) has been widely used by experimentalists. Nevertheless, the ordering of the $^1A_1$ and ^1E levels is not supported by three [26, 37] out of four separate density functional theory (DFT) calculations of the system published to date, who find $^1A_1 > {}^1E$ (Fig. 6-2(b)). Only the calculations by Gali predict $^1E > {}^1A_1$ [41, 42]. If the conventional intersystem crossing model is assumed, the conclusions of the majority of the DFT results would produce optical spin polarisation behaviour which conflicts with that observed. This implies that an unknown mechanism may be responsible for the optical spin polarisation behaviour of $(\text{N-V})^-$.

6.2 Experimental details

Three synthetic single-crystal diamonds were used in this study, labelled A, C and E. Additional investigations using samples A and C are reported in this thesis; in Chapter 5 both are studied, while sample A is also used in Chapter 7. The samples were grown using plasma-assisted CVD on {110}- and {113}-oriented single crystal substrates and were intentionally doped with silicon [43]. Silane was introduced to the growth gases with either a (C) natural abundance of the silicon isotopes (^{28}Si:^{29}Si:^{30}Si = 92.3:4.7:3.0) or (A) ^{29}Si-enriched to 90% (supplied by Voltaix, Inc., USA), such that the resulting silicon-related defects exhibit the corresponding isotopic abundances. Sample A was annealed for 2 hours at 2000 °C under a 6 GPa stabilising pressure (HPHT technology at Element Six, Ltd.). Sample C was treated in order to increase the concentration of (Si-V) centres. First, vacancies were introduced into the lattice by irradiating the sample with 1.5 MeV electrons

to a dose of approximately $10^{18}\,\mathrm{cm}^{-2}$. It was then annealed for 4 hours at 900 °C, mobilising the vacancies [44] which were then trapped by substitutional silicon atoms present in the sample. The substrates were removed, leaving freestanding plates which were polished to eliminate polycrystalline and graphitic material from the edges. Despite the different treatment histories the samples contained similar $(\text{Si-V})^0$ concentrations of 250 ± 20 ppb and 170 ± 20 ppb, respectively (as measured by EPR, prior to any of the charge transfer inducing treatments described in Chapter 5 had been applied). After these treatments, preferential alignment of the $(\text{Si-V})^0$ centres (discussed in [45] and §5.4.2) was not observed in either sample.

Sample E was manufactured by HPHT synthesis using a cobalt-containing solvent-catalyst and titanium as a "nitrogen getter" (§2.1.1). The remaining nitrogen in the specimen consisted of its natural isotopic abundances, with 99.6% ^{14}N. The sample was cut predominantly from the cube growth sector, although small volumes of alternative sectors were also included. Infrared (IR) absorption measurements revealed that the as-grown sample contained 9 ± 1 ppm N_s^0. In order to maximise the concentration of nitrogen-vacancy centres the sample was irradiated with 1.9 MeV electrons to a dose of $3 \times 10^{18}\,\mathrm{cm}^{-2}$, forming approximately 20 ppm vacancies [46]. Subsequent annealing at ~ 850 °C in a non-oxidising environment resulted in the migration of vacancies to nitrogen centres and the formation of nitrogen-vacancy complexes. Consequently the average concentration of N_s^0 was reduced to 1.2 ± 0.1 ppm and a $(\text{N-V})^-$ concentration of 1.0 ± 0.1 ppm was observed.

The samples were cleaned by boiling in sulphuric acid supersaturated with potassium nitrate prior to each investigation (§4.5).

The continuous wave (CW) EPR measurements conducted for temperatures ranging 5 – 295 K were made using a Bruker EMX (X-band) spectrometer operating at ~ 9.6 GHz equipped with a Bruker ER4105DR rectangular cavity and an Oxford Instruments ESR-900 continuous flow cryostat (§4.1.6). This enabled the sampling of temperatures ranging 5 – 295 K. Diamond specimens were fixed with Araldite epoxy to the end of quartz rods whose ends were polished to a mirror finish, allowing single-axis rotation of the samples (§4.1.3 and §4.1.6). The samples were oriented so that the magnetic field $\mathbf{B}$ was aligned parallel to a $\langle 111 \rangle$

direction. To avoid microwave power saturation of the EPR transitions a low microwave power of 0.5 μW was used for quantitative work. Microwave power saturation occurs when the microwave power is sufficiently high to induce transitions at a faster rate than the spin lattice-relaxation rate ($1/\tau_1$) (§3.1.5.2 and §4.1.4). Nevertheless, despite using a low microwave power, saturation was inevitable in the absence of optical pumping at temperatures below 100 K. However, microwave power saturation was not observed for the temperature range investigated when the samples were illuminated at full power. Optical illumination was provided by a 1 kW HgXe arc-lamp whose light was focussed onto one of two lightguides. Figure 4-5 shows the spectrum from the lamp output, before the broadband light passes through a liquid filter (transmission spectrum shown in Fig. 4-6) utilised to absorb light with $\lambda > 950$ nm, where λ is the wavelength. The Lumatec Series 300 lightguide transmits light for $300 < \lambda < 700$ nm, while the Series 2000 lightguide transmits between $420 < \lambda < 1500$ nm (protected by a 420 nm long-pass filter). Their transmission spectra can be seen in Fig. 4-7. The opposite end (emitting) of the chosen lightguide was placed flush against the top of the the quartz rod, which led the light to the sample in the cavity (§4.1.7). Although the power rating for the arc-lamp is 1 kW, the optical components attenuate the power, ultimately reducing the maximum power of the light incident on the sample to ~ 2 W (§4.1.7). This will also further decrease depending on the lightguide utilised for the experiment. Long-pass filters (280 – 780 nm) were employed to vary the energy cut-off of the excitation light.

EPR measurements were made on sample C in the dark for the temperature range 290-500 K. The same CW system was used for these studies, but the low temperature cavity and cryostat setup was replaced by an EX-102 high-temperature cavity, as described in §4.1.6.

A Bruker ELEXSYS E580 FT-EPR spectrometer with a ER4118X-MD5 *X*-band dielectic module was employed to conduct pulsed EPR measurements (§4.1). The cavity was placed in an Oxford Instruments CF935O continuous flow cryostat so that the sample temperature could be varied from 5 – 295 K. The samples were oriented so that the static magnetic field **B** was aligned parallel to a $\langle 111 \rangle$ direction. The $(\text{Si-V})^0$ and $(\text{N-V})^-$ concentrations of the samples studied were too

low to enable the measurement of the spin-lattice relaxation times (τ_1) in the dark using conventional pulsed EPR methods. To maximise the signal strength the samples were illuminated using either the HgXe arc-lamp or a 532 nm Q-switched pulsed laser (MPLH532-20μJ-5) operating at 4 MHz and an effective peak power of ~ 100 W. Arc-lamp illumination was conducted using the same setup as that used for the CW EPR measurements (with the Lumatec Series 2000 lightguide). When using the laser it was possible to illuminate the sample through a quartz window on the side of the cavity, bypassing the the quartz rod and lightguide setup, as described in §4.1.7. The spin-lattice relaxation time, τ_1, was investigated under continuous optical illumination using either a two-pulse ($180^\circ - \delta t - 90^\circ$) or three-pulse ($180^\circ$ – δt – 90° – Δ – 180° – Δ – echo) inversion recovery pulse sequence (introduced in §3.1.6 and illustrated in Fig. 3-4). The integrated intensity of the high amplitude section of the FID (free induction decay) or echo was measured as a function of the time interval δt. The duration of the microwave pulses was 16 ns and 32 ns for the 90°- and 180°-pulses, respectively.

6.3 Results

6.3.1 CW EPR studies on the optical spin polarisation of (Si-V)^0

6.3.1.1 Degree of optical spin polarisation for (Si-V)^0 and its temperature dependence

To study the optical spin polarisation of (Si-V)^0, EPR spectra for the full field ($\Delta M_S = \pm 1$) transitions were recorded with the magnetic field $\mathbf{B}$ applied approximately parallel to a $\langle 111 \rangle$ orientation in the dark and under illumination. The symmetry axis of a (Si-V)^0 defect can be aligned along four different $\langle 111 \rangle$ directions. Thus, for $\mathbf{B} \| \langle 111 \rangle$ the EPR spectrum for (Si-V)^0 consists of four groups of lines, where each group contains the contribution from the $I = 0$ (^{28}Si and ^{30}Si) "parent" transitions and the $I = 1/2$ (^{29}Si) "satellite" transitions. The two outer groups in the spectra arise from resonance transitions for the centres with their symmetry axes aligned parallel to $\mathbf{B}$. The symmetry axes of the remaining three

orientations make equal angles to **B** and form the inner pair of groups. The resulting integrated intensities of the groups are therefore 1:3:3:1 (§3.2.3 and Refs. [31, 45]). In this investigation only the lines which correspond to the centres oriented parallel to the field were considered, referred to as the "low" and "high" field lines.

Figure 6-3 shows the (Si-V)^0 EPR spectra of samples A and C under optical excitation at 5 K. The (Si-V)^0 centres in both samples were optically spin polarised by the light, with the the low and high field lines detected in absorption and emission, respectively. Analysis of the ^{13}C hyperfine satellites of (Si-V)^0 by Edmonds revealed that the zero field splitting $D > 0$ [31, 45]. The splitting of the triplet ground state $^3A_{2g}$ can thus be represented by the illustrations in Fig. 6-1, and it is immediately obvious that the optical spin polarisation results are consistent with the preferential population of the $M_S = 0$ spin level. Consequently, for $\mathbf{B} \| \langle 111 \rangle$ the low and high field lines arise from $M_S = 0 \rightarrow +1$ and $M_S = -1 \leftarrow 0$ transitions, respectively. If a transition is described by a forward arrow ($\rightarrow$) the resonance line observed is in absorption, whilst if a backwards arrow ($\leftarrow$) is appropriate the line is in emission.

When analysing the optical spin polarisation of the $^3A_{2g}$ triplet ground state it is necessary to examine the spin occupation probabilities of the $M_S = -1, 0$ and $+1$ spin levels, labelled p_{-1}, p_0 and p_{+1}, respectively. By this definition

$$p_{-1} + p_0 + p_{+1} = 1 \tag{6-2}$$

At the high field limit, where EPR experiments are conducted, the energies of the levels are ordered according to $E_{-1} < E_0 < E_{+1}$, where the subscripts denote the spin levels. The energy separations (Δ) between the spin levels are thus given by $\epsilon_{0,+1} = E_{+1} - E_0$ and $\epsilon_{-1,0} = E_0 - E_{-1}$, and will depend on the magnetic field. In the dark (superscript d), the occupation probabilities of the spin levels are governed by Boltzmann statistics, so that

$$p_{-1}^d = \frac{1}{Z} \tag{6-3}$$

$$p_0^d = \frac{e^{-\epsilon_{-1,0}/k_B T}}{Z} \tag{6-4}$$

$$p_{+1}^d = \frac{e^{-\epsilon_{0,+1}/k_B T}}{Z} \tag{6-5}$$

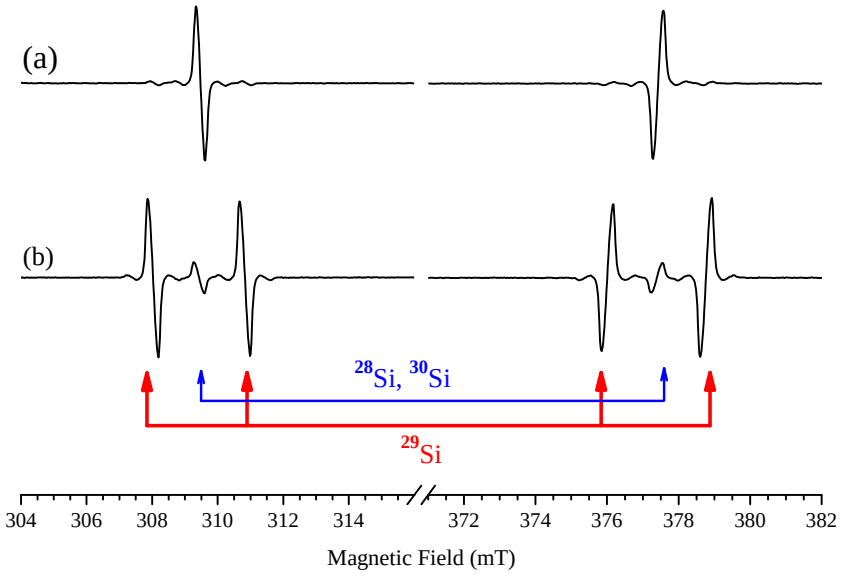

Figure 6-3: Selected regions of the optically excited (1 kW power, $420 < \lambda < 1500$ nm) EPR spectra at 5 K of $(\text{Si-V})^0$ for (a) sample C (4.7% ^{29}Si) and (b) sample A (90% ^{29}Si) when $\mathbf{B} \| \langle 111 \rangle$. The two groups of resonance lines displayed are the $\Delta M_S = \pm 1$ transitions for the sites which are oriented with their $\langle 111 \rangle$ principal axes parallel to the magnetic field. The nuclear spin zero (^{28}Si and ^{30}Si) lines are referred to as either the "low" or "high" field lines. $(\text{Si-V})^0$ is optically spin polarised in both samples, with the low and high field lines in absorption and emission, respectively.

where k_B is the Boltzmann factor and T is the temperature. Z is the partition function, given by

$$Z = 1 + \exp\left(\frac{-\epsilon_{-1,0}}{k_\text{B}T}\right) + \exp\left(\frac{-(\epsilon_{-1,0} + \epsilon_{0,+1})}{k_\text{B}T}\right) \tag{6-6}$$

The signal intensity of a $\Delta M_S = \pm 1$ EPR transition is proportional to the difference in the occupation probabilities of the two spin levels, η, where

$$\eta_{+1,0} = p_0 - p_{+1} \tag{6-7}$$

$$\eta_{0,-1} = p_{-1} - p_0 \tag{6-8}$$

Once the sample is illuminated the occupation probabilities of the spin levels are no longer governed by Boltzmann statistics (Eq. 6-3 to 6-6). However, it is possible to calculate the difference in the occupation probabilities under illumination by considering the experimentally determined intensities of the low and high

field resonance lines using the following relationship:

$$\eta^l = \eta^d \frac{I^l}{I^d}. \tag{6-9}$$

where l refers to the sample being exposed to light. I was considered to be positive if the transition was in absorption and negative if the transition was in emission. However, Eq. 6-9 only applies to cases where the intensities are not microwave power saturated. For this investigation it was noted that microwave power saturation of the (Si-V)^0 spectrum in the dark occurred at low temperatures. The unsaturated value for I^d_T (I^d at temperature T) was instead calculated using the following relationship, based on the experimental value for I^d_{RT} (I^d at room temperature) and the theoretical occupation probability difference between the spin levels at the different temperatures in the dark:

$$I^d_T = I^d_{RT} \frac{\eta^d_T}{\eta^d_{RT}}. \tag{6-10}$$

Solving for the occupation probabilities of the M_S = +1, 0 and -1 spin levels under optical illumination one finds

$$p^l_{+1} = \frac{1}{3}\left[1 - 2\left(\eta^d_{RT}\frac{I^l_T}{I^d_{RT}}\right)_{+1,0} - \left(\eta^d_{RT}\frac{I^l_T}{I^d_{RT}}\right)_{0,-1}\right] \tag{6-11}$$

$$p^l_0 = \frac{1}{3}\left[1 + \left(\eta^d_{RT}\frac{I^l_T}{I^d_{RT}}\right)_{+1,0} - \left(\eta^d_{RT}\frac{I^l_T}{I^d_{RT}}\right)_{0,-1}\right] \tag{6-12}$$

$$p^l_{-1} = \frac{1}{3}\left[1 + \left(\eta^d_{RT}\frac{I^l_T}{I^d_{RT}}\right)_{+1,0} + 2\left(\eta^d_{RT}\frac{I^l_T}{I^d_{RT}}\right)_{0,-1}\right] \tag{6-13}$$

The results presented in Fig. 6-3, combined with the knowledge that D is positive [31, 45], indicate that the $M_S = 0$ spin level is preferentially populated. It is then useful to define the *degree of optical spin polarisation* ξ as

$$\xi = \frac{p^l_0 - p^d_0}{p^d_{+1} + p^d_{-1}} \times 100\% \tag{6-14}$$

Thus, ξ = 100% occurs when all the spins are in the M_S = 0 spin level and $p^l_0 = p^d_{+1} + p^d_0 + p^d_{-1}$. At the other extreme, when p^l_0 = p^d_0 the system is not optically spin polarised and ξ = 0%. It is worth noting that Edmonds [45], Felton [20], Harrison [19] *et al.* have chosen to define the optical spin polarisation as the population in the M_S = 0 spin state (%), i.e. $p^l_0 \times 100\%$ [19, 20, 45]. A disadvantage with their definition is that it makes it difficult to compare how effectively

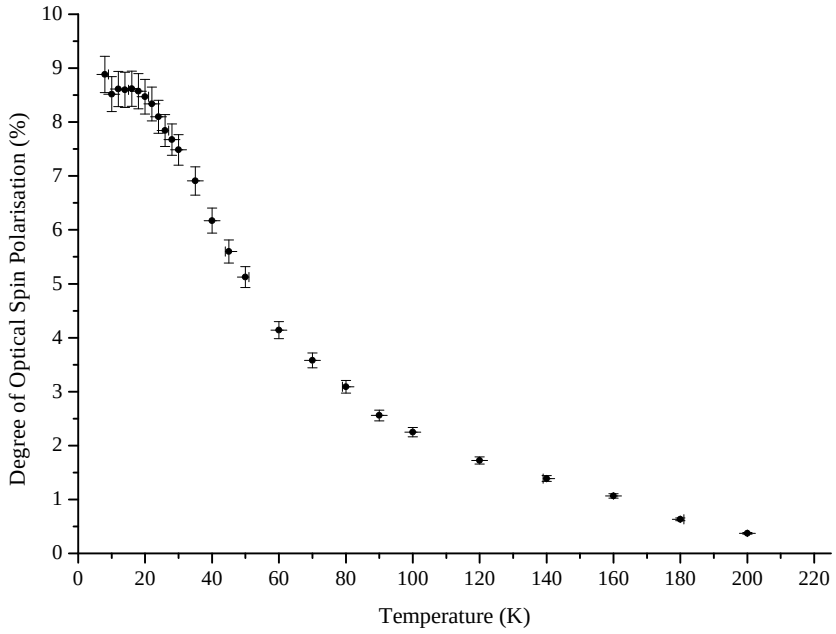

Figure 6-4: The temperature dependence of the degree of optical spin polarisation (defined in text) of $(\text{Si-V})^0$ for sample C under illumination from the arc-lamp (full output power, $300 < \lambda < 700\,\text{nm}$).

the $M_S = 0$ level is being preferentially populated at different temperatures since the population of the level in the dark, which is temperature dependent, is not considered.

At room temperature $\xi = 0.04 \pm 0.01\%$ was measured for sample C, which at first appears to be very small. However, this degree of optical spin polarisation was sufficient to double the intensity of the low field ($M_S = 0 \rightarrow +1$) resonance line when compared to the dark spectrum. Meanwhile, the optical spin polarisation resulted in the intensity of the high field line ($M_S = 0 \rightarrow -1$) dropping to below the noise level of the spectrum. When the temperature was reduced during optical pumping the intensities of the low field resonance lines ($\propto \eta_{+1,0}$) increased while the high field lines became more negative ($\propto \eta_{0,-1}$). In the dark, in the absence of microwave power saturation, $\eta_{+1,0}$ and $\eta_{0,-1}$ (and thus the intensities) also change, following Boltzmann statistics. Therefore, plotting the intensities of the resonance lines under illumination as a function of temperature would not be particularly informative. Instead, the temperature dependance of the degree of optical spin polarisation was calculated from the data; the results are presented in Fig. 6-4. The maximum spin polarisation was achieved at $T = 8 \pm 1\,\text{K}$, with $\xi = 8.9 \pm 0.4\%$

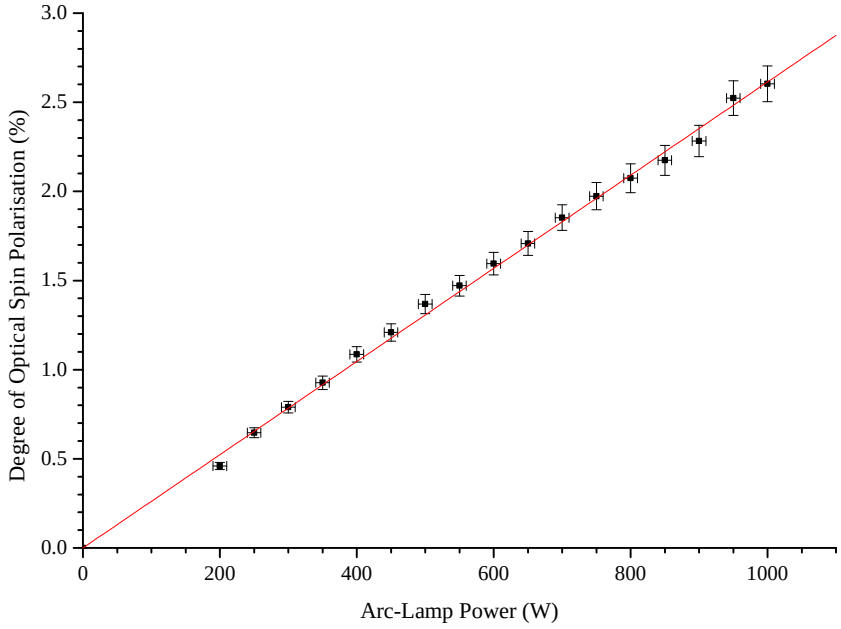

Figure 6-5: The degree of optical spin polarisation of (Si-V)^0 at 100 K as a function of the electrical arc-lamp power with $300 < \lambda < 700$ nm for sample C. The line of best fit has a gradient $0.00261 \pm 0.00002\,\% \text{ W}^{-1}$.

and p_0^l = 0.393 ± 0.002= 39.3 ±0.2% for sample C. The maximum degree of optical spin polarisation measured for sample A was consistent with these values.

6.3.1.2 Degree of optical spin polarisation as a function of excitation power

The degree of optical spin polarisation of sample C was investigated as a function of the electrical power to the arc-lamp. The measurements were taken at 100 ± 1 K in order to ensure that microwave power saturation would not occur at the lower optical excitation powers. Figure 6-5 shows that for the range of light intensities at the sample achievable with the arc-lamp the degree of optical spin polarisation was proportional to the the intensity. This indicates that the degree of optical spin polarisation observed was limited by the available excitation power.

6.3.1.3 Degree of optical spin polarisation as a function of excitation energy

Attempts were made to determine the minimum energy of the optical excitation necessary to drive the spin polarisation of the (Si-V)^0 centres. Long-pass

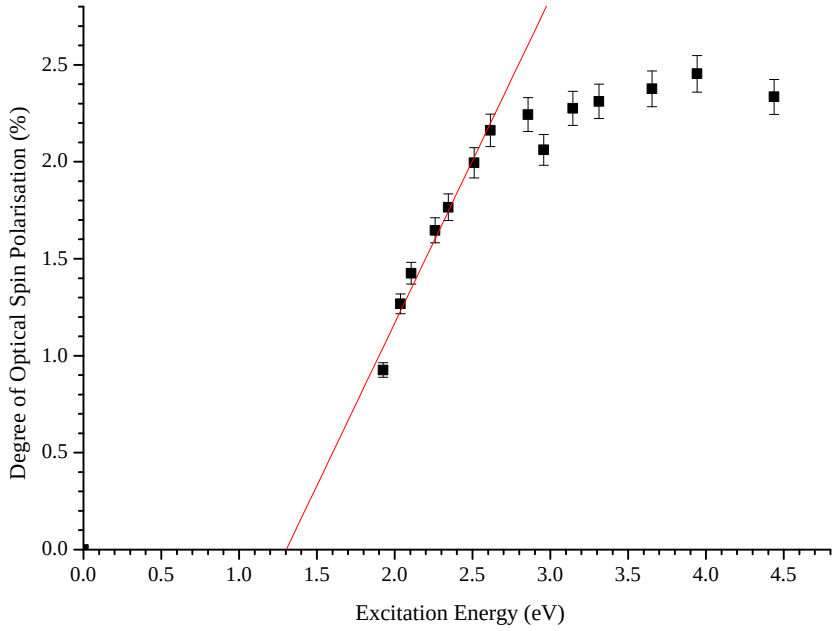

Figure 6-6: The degree of optical spin polarisation of (Si-V)^0 as a function of the excitation energy at 100 K, where long pass filters were used to vary the energy cut-off of the arc-lamp source (with the full output power). These measurements were made on sample C, with the Series 300 lightguide (transmission spectrum in Fig. 4-7).

filters ranging from 280 nm (4.44 eV) to 645 nm (1.93 eV) were placed in front of the arc-lamp to remove light components with lower wavelengths (higher energies). For this setup the Series 300 lightguide, which transmits light in the range $300 < \lambda < 700$ nm (see Fig. 4-7), was used and measurements were made at 100 ± 1 K. Figure 6-6 presents this data.

6.3.2 High-temperature CW EPR

The intensity of the EPR signal of (Si-V)^0 was observed to reduce at high temperatures. Figure 6-7(a) presents spectra for the low field line ($\mathbf{B} \| \langle 111 \rangle$) at room temperature and at $T \sim 490$ K, where the loss in intensity is attributed to the broadening of the line. The linewidth of the line was monitored as a function of temperature for $290 \lesssim T \lesssim 490$ K (Figure 6-7(b)), during which the symmetry of the centre was not observed to change. These data were taken by A. M. Edmonds.

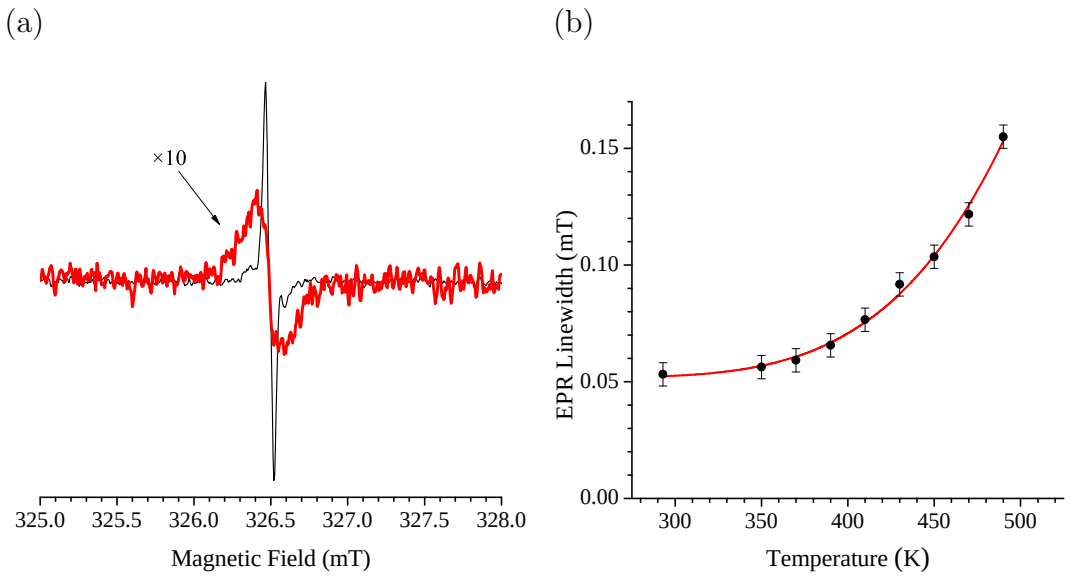

Figure 6-7: (a) The low field $(\text{Si-V})^0$ EPR resonance line ($\Delta M_S = \pm 1$) with $\mathbf{B} \| \langle 110 \rangle$ for temperatures of $\sim 290\,\text{K}$ (thin,black curve) and $\sim 490\,\text{K}$ (thick, red curve), with the linewidth broadening from $0.053 \pm 0.005\,\text{mT}$ to $0.155 \pm 0.005\,\text{mT}$. The intensity of the original data for $T \sim 490\,\text{K}$ has been multiplied by a factor of 10 here. (b) Temperature variation of the EPR linewidth of $(\text{Si-V})^0$. The fitted exponential curve is explained in §6.4.1. These data were taken by A. M. Edmonds.

6.3.3 Pulsed EPR studies on $(\text{Si-V})^0$ and $(\text{N-V})^-$

The spin-lattice relaxation rates $1/\tau_1$ of the ensemble of $(\text{Si-V})^0$ and $(\text{N-V})^-$ centres were studied for sample A and E, respectively. The data for the $(\text{N-V})^-$ centres were taken by S. Liggins, but the analysis was conducted by the author of this thesis. The static magnetic field $\mathbf{B}$ was aligned parallel to a $\langle 111 \rangle$ crystallographic direction and its magnitude was chosen so that the resonance condition was fulfilled for the $M_S = 0 \rightarrow +1$ transition of the defects oriented with their $\langle 111 \rangle$ symmetry axes parallel to magnetic field. τ_1 is a measure of the time taken for the spins to revert to their Boltzmann distribution across the available spin levels via spin-lattice relaxation mechanisms following a perturbation. Measurements of τ_1, using the two- and three-pulse inversion recovery sequences described in §3.1.6.3, should be conducted in the absence of optical excitation. The illumination may enable mechanisms which can modify the occupation probabilities of the spin levels, resulting in a measured relaxation time which is not the true τ_1 value, but is instead an "effective spin-lattice relaxation time," τ_{eff}. The concentrations of the centres in these samples were too low to enable the detection of the FIDs or echoes

(a)

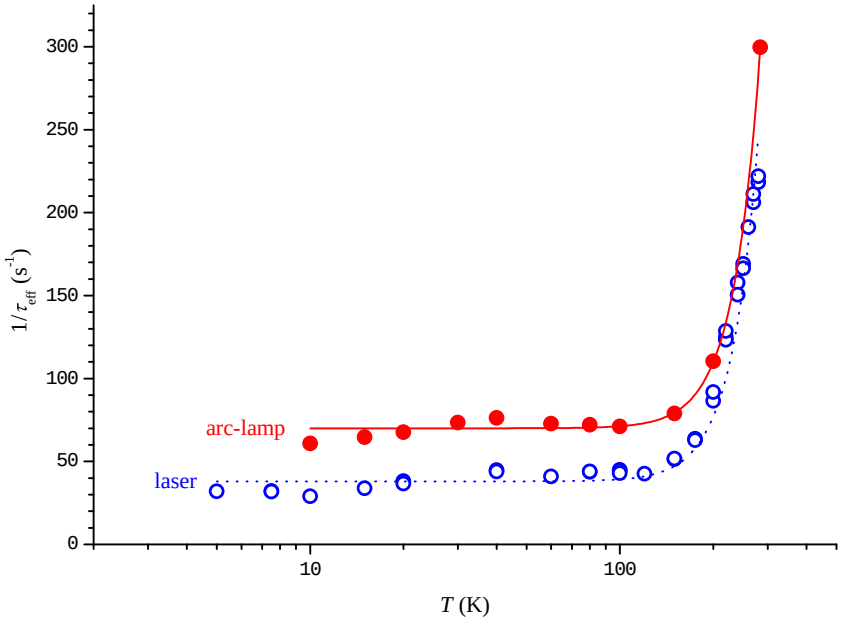

(b)

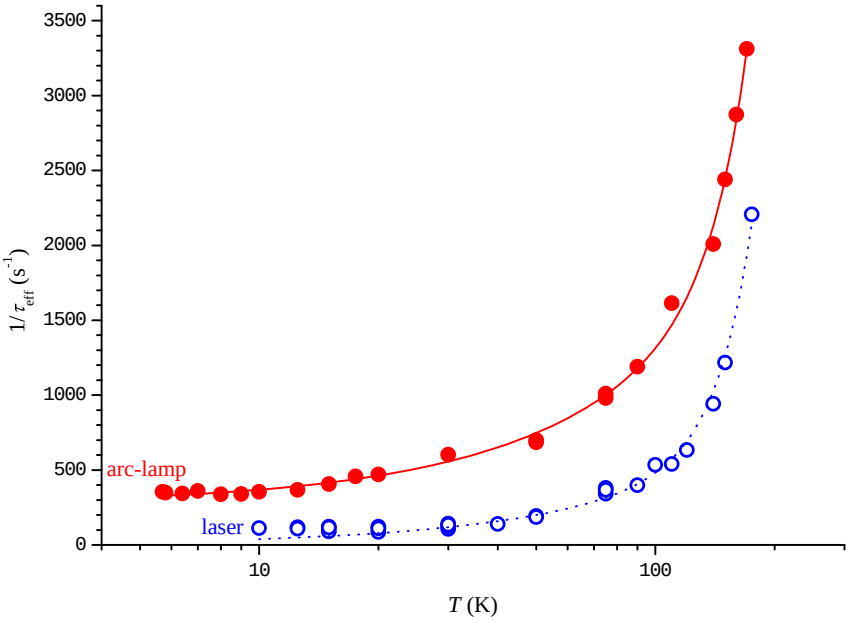

Figure 6-8: Temperature variation of the effective relaxation rate $1/\tau_{\text{eff}}$ for (a) $(\text{N-V})^-$ and (b) $(\text{Si-V})^0$ under excitation from an arc-lamp and a 532 nm laser. The curves fitted to the data are explained in §6.4.3. The experimental data for $(\text{N-V})^-$ were measured by S. Liggins.

resulting from the pulse sequences in the dark. The signal-to-noise was greatly improved by illuminating the samples and spin polarising the $(\text{Si-V})^0$ and $(\text{N-V})^-$ centres. Consequently, the "effective spin-lattice relaxation rate" $1/\tau_{\text{eff}}$ measured was not the characteristic $1/\tau_1$, but also included a component related to the time taken to establish the optical spin polarisation.

τ_{eff} for $(\text{N-V})^-$ and $(\text{Si-V})^0$ was investigated for $5 < T < 280\,\text{K}$. The optical spin polarisation was induced using either the arc-lamp (full power) or a 532 nm (2.33 eV) laser. The emission of the arc-lamp (Fig. 4-5) passed through a liquid filter (Fig. 4-6), and the Series 2000 lightguide (Fig. 4-7). Figure 6-8 presents the resulting $1/\tau_{\text{eff}}$ as a function of temperature for $(\text{N-V})^-$ and $(\text{Si-V})^0$.

6.4 Discussion

6.4.1 Optical spin polarisation mechanism for $(\text{Si-V})^0$

Two possible mechanisms for the observed optical spin polarisation of $(\text{Si-V})^0$ will be considered: an intersystem crossing process analogous to that proposed for $(\text{N-V})^-$ [18, 35, 36, 38], and the photoionisation of $(\text{Si-V})^-$ centres, which might result in a non-Boltzmann population of the $(\text{Si-V})^0$ ground state.

The spin-orbit interaction will mix the spin triplet and spin singlet states, providing an intersystem crossing pathway. These transitions are nonradiative and occur by vibrational decay. For $(\text{Si-V})^0$ there are a variety of many electron states possible, as determined in §5.1.1. The configuration $a_{1g}^2 a_{2u}^2 e_u^4 e_g^2$ gives rise to ${}^3A_{2g}$, ${}^1E_g$, and ${}^1A_{1g}$, whilst $a_{1g}^2 a_{2u}^2 e_u^3 e_g^3$ produces ${}^3A_{1u}$, ${}^1A_{1u}$, ${}^3A_{2u}$, ${}^1A_{2u}$, ${}^3E_u$ and ${}^1E_u$ many electron states. In §5.4.2 the 1.31 eV zero phonon line was attributed to an electronic dipole transition between the ${}^3A_{2g}$ ground and ${}^3A_{1u}$ excited states of $(\text{Si-V})^0$. The ordering of the other states is not known. The spin-orbit interaction splits the ${}^3A_{2g}$ ground and ${}^3A_{1u}$ excited states. The operator of the interaction has components which transform as rotations [47, 48]; in the $D_{3\text{d}}$ group these are A_{2g} and E_g. Hence, the spin-orbit coupling results in levels spanning $\mathbf{A}_{2g}\otimes\mathbf{A}_{2g} = \mathbf{A}_{1g}$ and $\mathbf{A}_{2g}\otimes\mathbf{E}_g = \mathbf{E}_g$, using the direct product table for the $D_{3\text{d}}$ point group (Table 3-6 and Ref. [49]). Similar treatment of the ${}^3A_{1u}$ excited many electron state results in a splitting by the spin-orbit interaction into a singlet A_{2u} ($\mathbf{A}_{1u}\otimes\mathbf{A}_{2g} =$

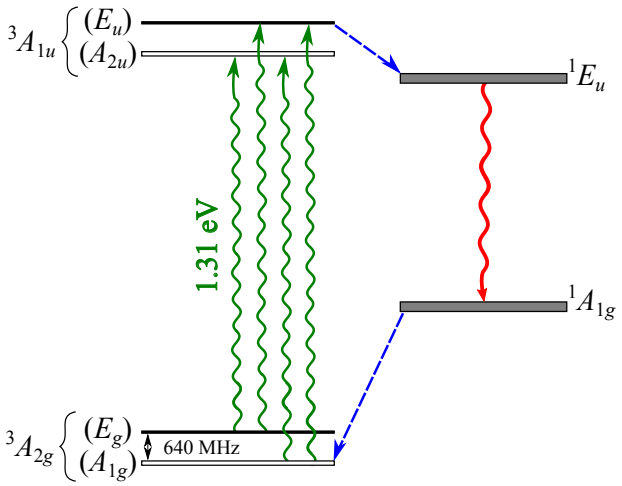

Figure 6-9: Schematic of a possible nonspin conserving intersystem crossing model resulting in the optical spin polarisation of the spin triplet ground state of (Si-V)^0 during optical illumination with light $\lambda \gtrsim 1.31\,\text{eV}$. The wavy arrows represent spin- and symmetry-allowed radiative transitions, while the dashed arrows indicate nonradiative symmetry-allowed transitions which do not conserve spin. Only the dominant transitions are illustrated. The ordering of the spin singlet states is not known, but this scenario is consistent with experimental observations, where the $M_S = 0$ ground state spin level becomes preferentially populated.

$\mathbf{A}_{2u}$) and a doublet E_u ($\mathbf{A}_{1u} \otimes \mathbf{E}_g = \mathbf{E}_u$). The $^3A_{2g}(A_{1g})$, $^3A_{2g}(E_g)$, $^3A_{1u}(A_{2u})$ and $^3A_{1u}(E_u)$ levels are illustrated in Fig. 6-9. Spin-spin interactions have been ignored. Furthermore, spin singlet many electron states cannot be subjected to spin-orbit coupling as they posses no spin, $S = 0$.

An energy level structure which can explain the observed optical spin polarisation of (Si-V)^0 is shown in Fig. 6-9. An intersystem crossing to the ^1E_u state can occur only from the $^3A_{1u}(E_u)$ level. $^1E_u \rightarrow {}^1A_{1g}$ is an allowed electric dipole transition [50], and intersystem crossing to the $^3A_{2g}(A_{1g})$ level can occur from the $^1A_{1g}$ state. These processes would give rise to preferential population of the $M_S = 0$ level of the ground state. At least two states between the $^3A_{2g}$ and $^3A_{1u}$ states are necessary to achieve the observed spin polarisation. It is not unreasonable that the $^1A_{1g}$ and ^1E_u states are low lying [50]. However, it is unwise to speculate further given the information available. This investigation could be furthered by searching for the $^1E_u \rightarrow {}^1A_{1g}$ transition in the near infrared optical region.

Photoionisation of a centre has previously been used as a possible explanation for the optical spin polarisation of spin triplet [51] and spin pentuplet ($S = 2$) [52] excited states of different centres. Here the discussion will be limited to the

creation of a spin triplet excited state. Watkins [51] noted that if a particular excited state of the centre is produced by the capture of a hole or an electron from the conduction or valence bands during illumination, rather than by a localised excitation, a Boltzmann distribution of the electron population in the spin levels of the state would be expected. This would not produce the preferential population distribution necessary for spin polarisation. However, if there is a lower lying singlet state, intersystem crossing might be possible, which would selectively depopulate the triplet excited state, producing the observed effect.

In §5.4.3 it was demonstrated that charge transfer could be induced between $(\text{Si-V})^0$ and $(\text{Si-V})^-$. Illumination with a 224 nm (5.45 eV) laser ionised the $(\text{Si-V})^-$ centres and produced an increase in the $(\text{Si-V})^0$ concentration. If photoionisation of $(\text{Si-V})^-$ results in the creation of the ${}^3A_{2g}$ ground state of $(\text{Si-V})^0$ Watkins's model cannot account for the optical spin polarisation. If, on the other hand, the $(\text{Si-V})^-$ centres converted to the $(\text{Si-V})^0$ centres in one of the excited states, the intersystem crossing model illustrated in Fig. 6-9 might still apply, but with the cycle starting at an excited state rather than the ground state.

The linear decrease in the degree of optical spin polarisation as the electrical power of the arc-lamp, and thus the light intensity, was reduced indicates that the degree of spin polarisation has not saturated (Fig. 6-5). A more intense light source would improve the degree of optical spin polarisation. The effect of varying the cut-off energy of the arc-lamp (using long pass filters) on the degree of spin polarisation was also investigated; the resulting data is shown in Fig. 6-6. A linear drop is observed for energies less than approximately 2.3 eV (i.e. $\gtrapprox 540$ nm). This coincides with a decrease in the transmission of the Series 300 lightguide utilised (Fig. 4-7). Furthermore, the transmission of the liquid filter used to protect the optical components falls by nearly an order of magnitude from ~ 1.7 eV (~ 750 nm) to ~ 1.3 eV (~ 950 nm), as shown in Fig. 4-6. Therefore, the change in the degree of optical spin polarisation may be explained by a loss in intensity of the light arriving at the sample. A linear fit to the slope of the data in the range 1.8 – 2.6 eV suggests that the minimum excitation energy necessary to optically spin polarise $(\text{Si-V})^0$ is 1.3 ± 0.2 eV, in good agreement with the energy of the ${}^3A_{2g} \rightarrow {}^3A_{1u}$ transition. This result does not rule out the involvement of a possible indirect excitation process

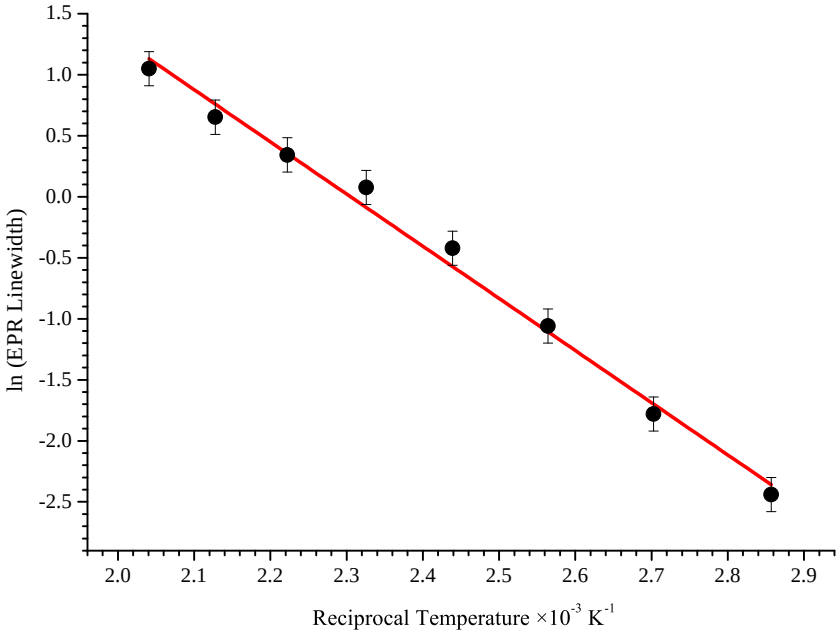

Figure 6-10: Natural logarithm of the linewidth of EPR transitions for $(\text{Si-V})^0$, measured in units of MHz, as a function of reciprocal temperature. The line of best fit was used to calculate an activation energy $E_\text{A} = 0.4 \pm 0.1\,\text{eV}$.

(e.g. photoionisation). It would be of interest to investigate whether $(\text{Si-V})^0$ can be optically spin polarised by resonant pumping, using for example a 946 nm Nd:YAG laser or other suitable excitation source.

For temperatures above 300 K the linewidth of the EPR signal of the $M_S = 0 \rightarrow +1$ transition ($\mathbf{B} \| \langle 110 \rangle$) was observed to broaden significantly in the dark. As the ground state is an orbital singlet ($^3A_{2g}$) a dynamic Jahn-Teller effect cannot account for the broadening. However, it may be a manifestation of lifetime broadening, with a low lying state being thermally populated from the ground state. The linewidth will then be proportional to $\exp(-E_A/k_BT)$, where E_A is the energy separation between the low lying excited state and the ground state. The fit to the data, shown in Fig. 6-10, gives $E_A = 0.4 \pm 0.1\,\text{eV}$. It is possible that this state is the $^1A_{1g}$ state illustrated in Fig. 6-9.

6.4.2 Comparison between the degree of optical spin polarisation achieved for (Si-V)^0 and (N-V)$^-$

Regardless of the mechanism responsible for the preferential population of the M_S = 0 ground state level, the ultimate degree of optical spin polarisation observed for (Si-V)^0 was poor, only reaching $\xi = 8.9 \pm 0.4\%$ and $p_0^l = 0.40 \pm 0.02$ at $T = 8 \pm 1$ K. Usually it is the population of the M_S = 0 level during optical spin polarisation (p_0^l) which is reported in literature for (N-V)$^-$ [19, 20]. This value gives no direct indication of how efficiently the population from the $M_S = \pm 1$ levels was lost to the singlet. To facilitate comparison between optical spin polarisation behaviour of the two centres ξ will be calculated for the (N-V)$^-$ data presented by Harrison [19] and Felton [20] *et al.*

Harrison reported a maximum $p_0^l \sim 0.80$ at ~ 2 K [19]. Given that at this temperature the population of the $M_s = 0$ state in the dark is 0.27 at 35 GHz, the frequency at which the data were recorded, using equations 6-2, 6-12 and 6-14 it is found that $\xi \sim 73\%$. This is significantly greater than the maximum achieved for (Si-V)^0 in this study. Meanwhile, Felton's investigation of (N-V)$^-$ achieved only $\xi \sim 47\%$ ($p_0^l \sim 0.65$) at 10 K [20]. It was suggested that the difference in their values might be due to the different light sources used by the two groups. Harrison utilised 600 nm excitation produced by a coherent ring-dye laser with a power which was sufficiently high that a decrease of an order of magnitude in laser power did not affect the EPR signal. The power density at the sample using their setup was likely substantially higher than that achievable using the 200 W Hg arc-lamp by Felton due to power loss by optical components (lightguide and quartz sample rod) of the latter setup. Similarly, the highest possible optical spin polarisation for (Si-V)^0 has not been obtained, as evidenced by the linear relationship between the degree of optical spin polarisation and the arc-lamp power shown in Fig. 6-5. Thus, ξ for (Si-V)^0 may potentially be improved by optimising the power.

Another factor which might cause the relative difference in ξ between the two centres might be the difference in the spin-lattice relaxation time τ_1. The ability to maintain the preferential population of the singlet level during illumination depends on both the spin polarisation rate R_{SP} and the competing spin-lattice relaxation rate. If $R_{\mathrm{SP}} \gg 1/\tau_1$ the system will be able maintain a high degree of

spin polarisation. However, if $1/\tau_1$ is large, the ultimate degree of spin polarisation attainable will be limited. The spin-lattice relaxation rates for $(\text{Si-V})^0$ and $(\text{N-V})^-$ during optical pumping will be discussed in the following section.

6.4.3 Effective spin-lattice relaxation rates for illuminated $(\text{N-V})^-$ and $(\text{Si-V})^0$ centres

The spin-lattice relaxation rates $1/\tau_1$ were investigated for $(\text{Si-V})^0$ (sample A) and $(\text{N-V})^-$ (sample E) using pulsed EPR methods. Due to the low concentration of these defects it was not possible to detect an FID or echo for either centre in the dark. To improve the signal-to-noise the samples were illuminated using either a 532 nm laser or an arc-lamp (utilising the liquid filter and Series 2000 lightguide, see Figs. 4-5, 4-6 and 4-7), resulting in the optical spin polarisation of the spin triplet ground states. The optical pumping produced a steady state non-Boltzmann spin population distribution amongst the $M_S = 0$ and $M_S = \pm 1$ levels, influencing the effective spin-lattice relaxation rate ($1/\tau_{\text{eff}}$) measured by the pulse sequences. Hence,

$$\frac{1}{\tau_{\text{eff}}(T)} = \frac{1}{\tau_1(T)} + \frac{1}{\tau_{\text{p}}} \tag{6-15}$$

where the temperature-independent rate $1/\tau_{\text{p}}$ is the contribution from the optical pumping. Figure 6-11 illustrates the (exaggerated) effect of applying a 180°-pulse on the populations of the spin levels of a triplet ground state for which $\xi = 0\%$ (dark) and $\xi = 100\%$ (illuminated).

The $(\text{N-V})^-$ data for the temperature dependence of the effective spin-lattice relaxation rate presented in Fig. 6-8(a) were successfully fit using a Raman process (§3.1.6.4) and an additional temperature independent term, i.e.

$$\frac{1}{\tau_{\text{eff}}} = BT^5 + \frac{1}{\tau_{\text{p}}} \tag{6-16}$$

where B is a constant parameter. The parameters used to fit the data are presented in Table 6-1. The same value of B, $B = 1.2(\pm 0.1) \times 10^{-10}\,\text{K}^{-5}\text{s}^{-1}$, was found to fit the data for both illumination sources, whilst $1/\tau_p$ was greater when using the arc-lamp rather than laser excitation. This implies that the spin polarisation was established faster with the arc-lamp. Takahashi *et al.* noted that the behaviour of $1/\tau_1$ for unilluminated $(\text{N-V})^-$ centres was reasonably fit using $1/\tau_1 = AT + BT^5$,

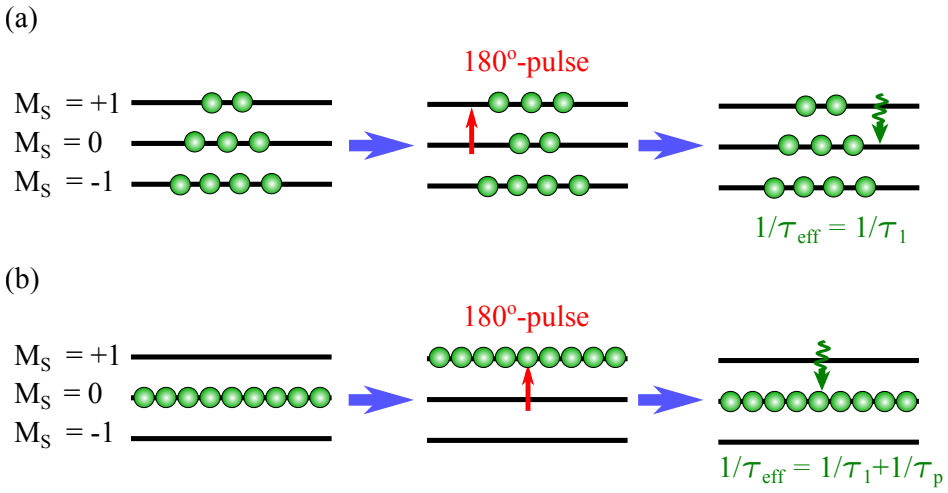

Figure 6-11: Cartoon of the effect of optical spin polarisation on the effective spin-lattice relaxation rate $1/\tau_{\text{eff}}$. When at resonance with the $M_S = 0 \rightarrow +1$ transition, the application of a 180°-pulse inverts the populations of the levels. (a) In the dark the unperturbed equilibrium population of the levels is governed by Boltzmann statistics. Following the pulse the electrons relax back into the original distribution with a rate $1/\tau_1$. (b) During optical pumping the $M_S = 0$ level is preferentially populated; here the situation for $\xi = 100\%$ is illustrated. The pulse excites all of the spins into the $M_S = +1$ level, relaxing back to the steady state with a rate $1/\tau_{\text{eff}} = 1/\tau_1 + 1/\tau_{\text{p}}$.

where $A = 8.0\times10^{-3}\,\text{s}^{-1}$ and $B = 3.5\times10^{-10}\,\text{K}^{-5}\text{s}^{-1}$ [16]. It is not possible to measure A using the data from this study since $1/\tau_{\text{p}}$ dominates over $1/\tau_1$ in the temperature region investigated. However, it is encouraging that the B parameters for both studies are the same order of magnitude. Since spin singlet excited states are predicted to exist between the $^3A_2$ and ^3E states, it is possible that an Orbach process may also occur (§3.1.6.4). Redman *et al.* attributed the temperature dependence of $1/\tau_1$ for $(\text{N-V})^-$ to a combination of Raman ($\propto T^5$) and Orbach processes, where a low lying state was $\Delta = 62.2 \pm 0.1\,\text{meV}$ above the ground state [22]. The data collected here do not cover a sufficiently large range of temperatures to allow meaningful fits with an Orbach model. Nevertheless, it is noteworthy that the data from Takahashi, for which measurements were made up to $T \sim 300\,\text{K}$, did not fit well to an Orbach process [16].

The data in Fig. 6-8(a) show that $1/\tau_{\text{eff}}$ for $(\text{N-V})^-$ was dominated by the temperature-independent term $1/\tau_{\text{p}}$ for $T \lesssim 100\,\text{K}$, i.e. the spin polarisation rate is sufficient to compete with the rate at which the ground state spin level occupation probabilities are relaxing back to their Boltzmann distribution values. Above this

Table 6-1: Parameters used to fit the data for the temperature dependence of the effective spin-lattice relaxation rates for $(\text{N-V})^-$ and $(\text{Si-V})^0$ during optical illumination, presented in Fig. 6-8. The equation used for the fits was $(1/\tau_{\text{eff}}) = AT + BT^5 + (1/\tau_{\text{p}})$, based on Eq. 3-49 and a temperature-independent contribution from the optical pumping (τ_{p}).

Centre	Excitation Source	$\frac{1}{\tau_p}$ (s^{-1})	A (s^{-1})	B ($\text{K}^{-5}\text{s}^{-1}$)
$(\text{N-V})^-$	532 nm laser	32 ± 2	-	$1.2(\pm 0.1) \times 10^{-10}$
$(\text{N-V})^-$	arc-lamp	70 ± 2	-	$1.2(\pm 0.1) \times 10^{-10}$
$(\text{Si-V})^0$	532 nm laser	54 ± 10	3.1 ± 0.2	$96(\pm 3) \times 10^{-10}$
$(\text{Si-V})^0$	arc-lamp	270 ± 20	9.4 ± 0.4	$101(\pm 5) \times 10^{-10}$

temperature $1/\tau_1$ increased. This behaviour agrees with the observations reported by Felton *et al.* [20], who noted that between 10 and 100 K the population of the $M_S = 0$ level did not change significantly ($\sim 3\%$) for optically spin polarised centres. Raising the temperature above 100 K to room temperature led to a large decrease in p_0^l ($0.65 \rightarrow 0.38$, equivalent to $\xi(100\,\text{K}) \sim 43\% \rightarrow \xi(300\,\text{K}) \sim 7\%$). This overall behaviour was seen by Felton in three different samples.

The $1/\tau_{\text{eff}}$ variation with temperature data for $(\text{Si-V})^0$ under illuminations was fit by (§3.1.6.4)

$$\frac{1}{\tau_{\text{eff}}} = AT + BT^5 + \frac{1}{\tau_{\text{p}}} \tag{6-17}$$

which contains contributions from direct and Raman processes (see Fig. 6-8(b)). Table 6-1 summarises the parameters used for the two light sources. Similar to $(\text{N-V})^-$, $1/\tau_{\text{p}}$ was not the same for the two excitations. The most noteworthy difference between the two centres is that the spin polarisation rate $1/\tau_p$ for $(\text{Si-V})^0$ is significantly larger than that for $(\text{N-V})^-$ using the arc-lamp excitation. This means that the $(\text{Si-V})^0$ system is much faster at establishing spin polarisation. However, the value for B is an order of magnitude greater for $(\text{Si-V})^0$ relative to $(\text{N-V})^-$. Thus, the competing spin-lattice relaxation processes limits the preferential population of the $M_S = 0$ spin level at high temperatures.

Overall, the arc-lamp produced a higher spin polarisation rate than the laser, indicating that the laser energy was not ideal for the optical pumping for both the $(\text{N-V})^-$ and $(\text{Si-V})^0$ centres. Felton *et al.* were able to saturate the degree of spin polarisation for the $(\text{N-V})^-$ centre using a a similar setup, but a lower

power (and thus intensity) arc-lamp [20]. Hence, it should also be saturated for $(\text{N-V})^-$ in this investigation at low temperatures. However, this is not the case for $(\text{Si-V})^0$, where in §6.3.1.2 it was shown that the degree of spin polarisation was proportional to the arc-lamp intensity ($\propto$ the electrical power to the arc-lamp). Hence, increasing the intensity would improve the degree of spin polarisation. Furthermore, the combination of the filters and lightguides used for the excitation resulted in poor transmission of the arc-lamp output to the sample, in particular in the region of 1.31 eV. This leaves room for further optimisation by changing the optical excitation setup.

6.5 Conclusions and further work

The optical spin polarisation of the ${}^3A_{2g}$ ground state of $(\text{Si-V})^0$ has been observed for the first time. A mathematical formulism for the degree of optical spin polarisation, ξ, has been defined, taking into account the Boltzmann population of the spin levels in the dark. A maximum degree of optical spin polarisation of $\xi = 8.9 \pm 0.4\%$, with a population of the $M_S = 0$ level of $p_0^l = 0.40$, was observed at 8 ± 1 K. This is dramatically lower than that induced in $(\text{N-V})^-$, where values of $\xi \sim 73\%$ [19] (2 K) and $\xi \sim 47\%$ [20] (10 K) can be calculated from published p_0^l data.

Two different mechanisms for the optical spin polarisation of $(\text{Si-V})^0$ have been discussed, an intersystem crossing cycle analogous to that proposed for $(\text{N-V})^-$, and the photoionisation of $(\text{Si-V})^-$, which indirectly also involves selective intersystem crossing. In the standard intersystem crossing scheme the selection rules necessitate the presence of multiple low lying spin singlet states. A possible electronic arrangement which is consistent with the observed optical spin polarisation has been given, illustrated in Fig. 6-9. Evidence for a low lying state approximately 0.4 eV above the ground state was detected, resulting in lifetime broadening of the EPR linewidth. If this model of the electronic structure is correct it might be possible to detect a ZPL arising from an allowed electric dipole transition between the intermediate spin singlet states. An electronic structure which would result in optical spin polarisation via an indirect excitation process cannot be predicted

using the data available, it depends on specifically which excited state the (Si-V)^0 centres are in after indirect excitation.

The ability to spin polarise these centres is affected by a number of factors and can be sample dependent. The two (Si-V)^0-containing CVD samples studied here showed the same optical spin polarisation behaviour, but their properties, such as the presence of other defects, may not have been ideal for these type of measurements. Furthermore, it is apparent that the degree of spin polarisation is limited by the light intensity available. Experiments where the excitation energy is varied utilising powerful monochromatic light sources may reveal the energy necessary for optical spin polarisation and provide information regarding the mechanism which produces the optical spin polarisation. Resonant pumping with a suitable light source (e.g. a 946 nm Nd:YAG laser) will be the most effective at stimulating the $^3A_{2g} \rightarrow {}^3A_{1u}$ transition. If the intersystem crossing model illustrated in Fig. 6-9 is the correct model resonant optical pumping should improve the degree of spin polarisation. However, if the spin polarisation originated from an indirect excitation process the energy dependence of the degree of spin polarisation will be more complex. It will be necessary to carefully select optical components which will transmit well in the spectral region of interest.

Pulsed EPR sequences during continuous illumination indicate that the spin lattice relaxation rate of (Si-V)^0 is significantly greater ($\gtrsim 3$ times) than that of (N-V)$^-$. However, in addition to being poorly excited by the light source available, the degree of optical spin polarisation achieved was further limited by a large spin-lattice relaxation rate. This latter factor will be particularly problematic for maintaining a high level of preferential population of the $M_S = 0$ level at higher temperatures, as $1/\tau_1 \sim T^5$.

The temperature dependence of the data for (N-V)$^-$ was successfully fit for two different light sources using a Raman spin-lattice relaxation process ($1/\tau_1 \propto T^5$), in agreement with published work by Takahashi *et al.* [16], while the data for (Si-V)^0 required an additional linear T-dependent term, indicating the involvement of a direct process. To verify that these fits and are not simply fortuitous, but are actually representative of physical processes, it is necessary to confirm these trends by measuring τ_1 in the dark using samples with greater concentrations of (N-V)$^-$

and (Si-V)^0. Alternatively, optical excitation may be used to spin polarise the centres and a pulse sequence could be triggered to commence the instant that the light is switched off. This technique will benefit from having a large signal-to-noise, yet the spin-lattice relaxation rate is measured in the dark.

In order to evaluate whether the (Si-V)^0 centre would be viable for quantum information applications several key bits of information need to be determined. τ_1 has been shown to be sample dependent for (N-V)$^-$. It would be interesting to synthesise high purity and low strain material with low concentrations of (Si-V)^0 to increase τ_1 and investigate whether single photon detection is possible. The 1.31 eV ZPL appears weak, yet it has a lower Huang-Rhys factor ($\sim$ 1.5, see Chapter 5) than that of (N-V)$^-$ ($\sim$ 3.73 [21, 53]), so that less of its intensity lies in the vibronic band. This, in conjunction with the low background fluorescence about the transition, renders (Si-V)^0 a potential qubit candidate worthy of further research for the optimisation of its properties. Optically detected magnetic resonance (ODMR) investigations should be conducted on ensembles of (Si-V)^0 centres. In an ODMR experiment microwave-induced repopulation of spin levels of a paramagnetic multiplet state is indirectly detected by a change in some property of the light, which is either emitted or absorbed by the centre [54]. This technique allows the study of the excited state multiplet and can improve the EPR sensitivity dramatically, from 10^{10} Hz to 10^{15} Hz. If ensemble ODMR is successful it should be applied to single centres, which will ultimately reveal whether the (Si-V)^0 can be used as a qubit for quantum information processing devices.

References

[1] M. V. Gurudev Dutt, L. Childress, L. Jiang, E. Togan, J. Maze, F. Jelezko, A. S. Zibrov, P. R. Hemmer, and M. D. Lukin, Science **316**, 1312 (2007).

[2] R. Hanson, Nat. Mater. **8**, 368 (2009).

[3] J. Wrachtrup and F. Jelezko, J. Phys.- Condens. Mat. p. S807 (2006).

[4] V. M. Acosta, E. Bauch, M. P. Ldbetter, C. Santori, K.-M. C. Fu, P. e. Barclay, R. G. Beausoleil, H. Linget, J. F. Roch, F. Treussart, et al., Phys. Rev. B **80**, 115202 (2009).

[5] G. Balasubramanian, I. Y. Chan, R. Kolesov, M. Al-Hmoud, C. Shin, C. Kim, A. Wojcik, P. R. Hemmer, A. Kreuger, T. Hanke, et al., Nature **455**, 648 (2008).

[6] J. R. Maze, P. L. Stanwix, J. S. Hodges, S. Hong, J. M. Taylor, P. Cappellaro, L. Jiang, M. V. Gurudev Dutt, E. Togan, A. S. Zibrov, et al., Nature **455**, 644 (2008).

[7] A. Beveratos, S. Kühn, R. Brouri, T. Gacoin, J.-P. Poizat, and P. Grangier, Eur. Phys. J. D **18**, 191 (2002).

[8] F. Jelezko and J. Wrachtrup, Phys. Status Solidi a **203**, 3207 (2006).

[9] T. Gaebel, I. Popa, A. Gruber, M. Domhan, F. Jelezko, and J. Wrachtrup, New J. Phys. **6**, 98 (2004).

[10] E. Wu, J. R. Rabeau, G. Roger, F. Treussart, H. Zeng, P. Grangier, S. Prawer, and J.-F. Roch, New J. Phys. **9**, 434 (2007).

[11] I. Aharonovich, C. Zhou, A. Stacey, J. Orwa, S. Catelletto, S. D., A. D. Greentree, F. Treussart, J.-F. Roch, and Prawer, Phys. Rev. B **79**, 235316 (2009).

[12] I. Aharonovich, S. Castelletto, D. A. Simpson, A. D. Greentree, and S. Prawer, Phys. Rev. A **81**, 043813 (2010).

[13] C. L. Wang, C. Kurtsiefer, H. Weinfurter, and B. Burchard, J. Phys. B-At. Mol. Opt. **39**, 37 (2006).

[14] E. Neu, D. Steinmetz, J. Riedrich-Möller, S. Gsell, M. Fischer, M. Schreck, and C. Becher, New J. Phys. **13**, 025012 (2011).

[15] G. Balasubramanian, P. Neumann, D. Twitchen, M. Markham, R. Kolesov, N. Mizuochi, J. Isoya, J. Achard, J. Beck, J. Tissler, et al., Nat. Mater. **8**, 383 (2009).

[16] S. Takahashi, R. Hanson, J. van Tol, M. S. Sherwin, and D. D. Awschalom, Phys. Rev. Lett. **101**, 047601 (pages 4) (2008).

[17] C. P. Slichter, *Principles of Magnetic Resonance* (Springer-Verlag, New York, 1978).

[18] J. Harrison, M. J. Sellars, and N. B. Manson, J. Lumin. **107**, 245 (2004).

[19] J. Harrison, M. J. Sellars, and N. B. Manson, Diam. Relat. Mater. **15**, 586 (2006).

[20] S. Felton, A. M. Edmonds, M. E. Newton, P. M. Martineau, D. Fisher, D. J. Twitchen, and J. M. Baker, Phys. Rev. B **79** (2009).

[21] G. Davies and M. F. Hamer, Proc. R. Soc. Lond. A **348**, 285 (1976).

[22] D. A. Redman, S. Brown, R. H. Sands, and S. C. Rand, Phys. Rev. Lett. **67**, 3420 (1991).

[23] F. T. Charnock and T. A. Kennedy, Phys. Rev. B **64**, 041201 (2001).

[24] T. Kennedy, F. Charnock, J. Colton, J. Butler, R. Linares, and P. Doering, Phys. Status Solidi b **233**, 416 (2002).

[25] A. T. Collins, L. Allers, C. J. Wort, and G. A. Scarsbrook, Diam. Relat. Mater. **3**, 932 (1994).

[26] J. P. Goss, R. Jones, S. J. Breuer, P. R. Briddon, and S. Öberg, Phys. Rev. Lett.

77, 3041 (1996).
[27] J. P. Goss, P. R. Briddon, and M. J. Shaw, Phys. Rev. B **76**, 075204 (2007).
[28] K. Iakoubovskii and A. Stesmans, Phys. Rev. B **66**, 195207 (2002).
[29] K. Iakoubovskii and A. Stesmans, Phys. Status Solidi a **186**, 199 (2001).
[30] K. Iakoubovskii and G. J. Adriaenssens, Phys. Rev. B **61**, 10174 (2000).
[31] A. M. Edmonds, M. E. Newton, P. M. Martineau, D. J. Twitchen, and S. D. Williams, Phys. Rev. B **77**, 245205 (2008).
[32] J. H. N. Loubser and J. A. van Wyk, Diamond Research **11**, 11 (1977).
[33] N. R. S. Reddy, N. B. Manson, and E. R. Krausz, J. Lumin. **38**, 46 (1987).
[34] E. van Oort, N. B. Manson, and M. Glasbeek, J. Phys. C Solid State **21**, 4385 (1988).
[35] N. B. Manson, J. P. Harrison, and M. J. Sellars, Phys. Rev. B **74**, 104303 (2006).
[36] N. B. Manson and R. L. McMurtrie, J. Lumin. **127**, 98 (2007).
[37] P. Delaney, J. C. Greer, and J. A. Larsson, Nano Lett. **10**, 610 (2010).
[38] L. J. Rogers, S. Armstrong, M. J. Sellars, and N. B. Manson, New J. Phys. **10**, 103024 (2008).
[39] A. Batalov, V. Jacques, F. Kaiser, P. Siyushev, P. Neumann, L. J. Rogers, R. L. McMurtrie, N. B. Manson, F. Jelezko, and J. Wrachtrup, Phys. Rev. Lett. **102**, 195506 (2009).
[40] P. Tamarat, N. B. Manson, J. P. Harrison, R. L. McMurtrie, A. Nizovtsev, C. Santori, R. G. Beausoleil, P. Neumann, T. Gaebel, F. Jelezko, et al., New J. Phys. **10**, 045004 (2008).
[41] A. Gali, M. Fyta, and E. Kaxiras, Phys. Rev. B **77**, 155206 (2008).
[42] A. Gali, M. Fyta, and E. Kaxiras, Phys. Rev. B **78**, 239902 (2008).
[43] S. D. Williams, D. J. Twitchen, P. M. Martineau, G. A. Scarsbrook, and I. Friel, *High colour diamond*, UK Patent GB2428690 B (2010).
[44] G. Davies, S. C. Lawson, A. T. Collins, A. Mainwood, and S. J. Sharp, Phys. Rev. B **46**, 13157 (1992).
[45] A. M. Edmonds, Ph.D. thesis, University of Warwick (2008).
[46] D. C. Hunt, D. J. Twitchen, M. E. Newton, J. M. Baker, T. R. Anthony, W. F. Banholzer, and S. S. Vagarali, Phys. Rev. B **61**, 3863 (2000).
[47] P. W. Atkins and G. T. Evans, Molecular Physics **1974**, 1633 (27).
[48] M. S. de Groot, I. A. M. Hesselmann, and J. H. van der Waals, Molecular Physics **12**, 259 (1967).
[49] P. W. Atkins, M. S. Child, and C. S. G. Phillips, *Tables for Group Theory* (Oxford University Press, Oxford, 1970).
[50] C. A. Coulson and F. P. Larkins, J. Phys. Chem. Solids **30**, 1963 (1969).
[51] G. D. Watkins, Phys. Rev. **155**, 802 (1967).
[52] J. A. van Wyk, O. D. Tucker, M. E. Newton, J. M. Baker, G. S. Woods, and P. Spear, Phys. Rev. B **52**, 12657 (1995).
[53] G. Davies, Reports on Progress in Physics **44**, 787 (1981).
[54] J.-M. Spaeth, J. R. Niklas, and R. H. Bartam, *Structural Analysis of Point Defects in Solids - An introduction to multiple magnetic resonance spectroscopy*, vol. 42 of *Solid-State Sciences* (Springer, New York, 1992).

Chapter 7

WAR3: The neutral silicon-divacancy-hydrogen centre, (Si-V_2:H)^0

7.1 Background and motivation

Four EPR-active centres detected in diamond have previously been ascribed to silicon-related complexes: KUL1, KUL8, KUL3 and KUL4 [1–4]. The silicon split-vacancy centre in diamond, (Si-V), consists of a silicon atom located in the centre of a nearest-neighbour divacancy [5, 6], resulting in a defect with D_{3d} symmetry. The electronic structure and its model has been described in Chapter 5 and it is illustrated in Fig. 5-1.

KUL1 [1–4], which has an effective spin $S = 1$, was unequivocally identified as the neutral silicon split-vacancy centre, (Si-V)^0, by Edmonds *et al.* The ^{29}Si and ^{13}C hyperfine parameters determined experimentally for KUL1 [3] agreed with those calculated by Goss *et al.* for the (Si-V)^0 centre using density functional theory [6]. The symmetry of the tensors $\underline{\mathbf{g}}$ and $\underline{\mathbf{D}}$ for KUL1 were also consistent with the (Si-V)^0 model proposed [3, 6]. KUL1 has an approximately isotropic ^{29}Si hyperfine interaction and nearly 100% of its unpaired electron density was localised on the six nearest-neighbour carbon atoms surrounding the silicon atom [3]. The optical properties of this centre have been investigated in Chapter 5 and the spin polarisation of its $^3A_{2g}$ ground state has been demonstrated in Chapter 6.

KUL8 has been detected in CVD polycrystalline diamond deposited on silicon substrates by Iakoubovskii *et al.* [2, 7], who suggested that the axially symmetric $S = \frac{1}{2}$ defect is the (Si-V)$^-$ centre. The concentration of the KUL8 centre increased

in regions close to the substrate, taken to mean that it was silicon-related. KUL8 was linked to the (Si-V)$^-$ centre since charge transfer was observed between the KUL1 and KUL8 centres, induced by photoexcitation with a 457.9 nm laser [2]. However, the involvement of silicon could not be confirmed as the centre's hyperfine structure was not resolved. Furthermore, they did not find a correlation between the intensities of the ZPL at 1.682 eV (attributed to the (Si-V)$^-$ centre [5, 8] and here referred to as the 1.68 eV ZPL) and the intensities of the KUL8 resonance lines [2]. The KUL8 defect is often not detected in CVD diamond for which the 1.68 eV band has been observed [3], including the samples investigated in Chapters 5 and 6, weakening the argument for the assignment of the KUL8 centre to (Si-V)$^-$.

The only other conclusively identified EPR-active silicon-related defect is KUL3, a monoclinic-I (C_{1h}) centre with $S = \frac{1}{2}$ [1, 3, 4]. It was apparent that KUL3 involved an $I = \frac{1}{2}$ nucleus with 100% abundance due to the presence of weak satellites on the principal lines [1]. These satellites were explained to be electron-nuclear double spin-flip transitions, attributed to the involvement of hydrogen in the KUL3 complex. Decoration of the (Si-V) unit by a hydrogen atom has been predicted by Goss *et al.* [6]. First principle calculations suggest that the complex is electrically active, forming an acceptor level at $E_v + 1.1$ eV and is EPR-active in its neutral charge state, with $S = \frac{1}{2}$. KUL3 was ultimately unambiguously confirmed as the (Si-V:H)^0 centre by the agreement between experimental [3] and calculated [6] ^{29}Si and ^{1}H hyperfine parameters.

Another $S = \frac{1}{2}$ centre, referred to as KUL4, was observed in CVD polycrystalline diamond grown on silicon substrates after annealing at 1400 °C [1]. Iakoubovskii *et al.* suggested that KUL4 was silicon-related, though the involvement of silicon in KUL4 could not be verified since ^{29}Si hyperfine data was not reported. However, the centre's ^{1}H hyperfine structure was resolved, indicating that it contains at least one hydrogen atom. The appearance of KUL4 occurred as the KUL3 centre annealed out, which Iakoubovskii *et al.* took to mean that KUL4 was formed from KUL3 [1]. Spectra were not presented in their paper [1], but a note was made that the signal intensity of KUL4 was weak, possibly due to the small size of the sample studied. Thus, their results do not rule out that KUL4 was

present before annealing, but may have been obscured by the combined factors of low signal-to-noise and an overlap with the stronger KUL3 spectrum.

Finally, there is the possibility of forming the silicon divacancy complex, (Si-V_2) [6]. It is predicted that (Si-V_2) may be found in implanted (leading to the introduction of a high concentration of vacancies) and annealed material, forming by (Si-V) + V→(Si-V_2), a reaction which releases 2.9 eV [6]. The dissociation energy for the complex is estimated to be 5.2 eV, rendering it stable to high temperatures [6]. The dangling orbitals produce several gap states and the formation of at least one acceptor level in the bottom half of the band gap is predicted [6]. This suggests that the centre may be optically active. A transition energy in the 1.0 – 1.5 eV range and one close to the band gap energy have been tentatively predicted [6]. Furthermore, the negative charge state of (Si-V_2) should be EPR-active, with $S = \frac{1}{2}$. Nevertheless, (Si-V_2) has not yet been conclusively identified in silicon-doped material.

In this chapter, data obtained from multifrequency EPR studies on silicon-doped CVD diamond and theoretical modelling of defect structures are presented. The theoretical work was conducted by J. P. Goss and P. R. Briddon at the University of Newcastle (published in Ref. [9]). Through this combined approach, we have identified a silicon divacancy complex which is decorated by a hydrogen atom, (Si-V_2:H)^0, which is preferentially oriented with respect to the growth direction for samples grown on {110}-oriented substrates.

7.2 Experimental and computational details

7.2.1 Experimental method

Sample A, previously described in Chapters 5 and 6, was further studied to obtain the results presented in this chapter. This single crystal CVD diamond was grown on a {110}-oriented substrate. It was intentionally doped with silicon by the addition of 90% ^{29}Si-enriched silane (supplied by Voltaix, Inc., USA) to the source gases. The sample was prepared for analysis by removing the substrate and polishing away poor quality material from the edges. In this work sample A was investigated after it was annealed for 1 hour at 1200, 1400 and 1600 °C in forming

gas (96% argon and 4% hydrogen) at atmospheric pressure and for 2 hours at 2000 °C under a stabilising pressure of 6 GPa. After each anneal the diamond was cleaned in boiling sulphuric acid supersaturated with potassium nitrate. EPR, low temperature ultraviolet, visible, and near-infrared (UV/visible/NIR) absorption spectroscopy and photoluminescence (PL) studies were performed.

EPR measurements were conducted at room temperature using a commercial Bruker 9.7 GHz (X-band) spectrometer equipped with a Super-High Q cavity (ER4122SHQ) and a home-built 35 GHz (Q-band) spectrometer operating with a TE_{011} mode cylindrical cavity; both setups are described in §4.1. The systems were set up so that it was possible to rotate the sample in two perpendicular planes. This enabled the tracking of the resonance line positions as a function of the orientation of the Zeeman field in a crystallographic plane and the generation of roadmaps from which the values for the spin Hamiltonian parameters could be extracted (§3.2.3). The orientation of the sample's crystallographic directions relative to the magnetic field **B** was identified using the positions of the resonance lines of (Si-V)^0 (KUL1) and N_s^0 (P1), whose roadmaps can be simulated using published Hamiltonian parameters [3, 10]. By employing multifrequency EPR, it was easier to distinguish between the different spin Hamiltonian interactions (e.g. the Zeeman interaction is frequency-dependent whilst to first order the hyperfine splitting is not). The concentrations of EPR-active defects were determined using the X-band EPR system by applying the method described in §4.1.4, including the collection of spectra at various powers to account for the effect of microwave power saturation.

PL measurements were obtained using either a Horiba Jobin Yvon Labram HR grating spectrometer or a Renishaw Raman InVia microscope system, both equipped with an Oxford Instruments Microstat cryostat for low temperature measurements. Sample A was mounted in indium to maintain good thermal contact with the cooled mount. A range of laser excitations were employed: 325 nm (HeCd), 458 nm, 488 nm, 514 nm (Ar^+), 660 nm (solid state) and 785 nm (solid state). A grating of 1200 lines/mm was used for the 325 nm excitation, whilst 600 lines/mm were used for all other excitations.

UV/visible/NIR absorption measurements were made at ~77 K using one of

two systems: a PerkinElmer Lambda 19 spectrometer with a liquid nitrogen cryostat, or a PerkinElmer Lambda 1050 spectrometer furnished with an Oxford Instruments Optistat continuous flow helium cryostat.

7.2.2 Computational method

Calculations were carried out by J. P. Goss and P. R. Briddon using the spin-density-functional technique within the practice-based evidence (PBE) generalised gradient approximation [11] implemented using the AIMPRO [12, 13] (*ab initio* modelling program) code. This quantum mechanical method can be used to investigate the electronic properties and geometrical structures of point defects in diamond by considering the electron density distribution which minimises the total energy of the system. The reader is referred to the review by Jones and Briddon [12] for a detailed explanation of this scheme.

The defects were simulated in 216-atom cubic supercells of sidelength $3a_0$. The cluster size is chosen to ensure that the local environment of the simulated defect resembles that of the bulk crystal. For periodic materials such as diamond it is necessary to take into account the dispersion in the electronic eigenstates in reciprocal space (k-space), i.e. the band structure of the material [14]. Rather than calculating the total energy in a primitive cell of diamond by integrating over all k-space, the Brillouin-zone was sampled using the Monkhorst-Pack scheme [15]. This scheme effectively obtains the integral by only considering selected k-points, where the special k-points are arranged in a uniform mesh. A 10×10×10 mesh needs to be considered for a diamond primitive cell, which has 48 symmetry operations associated with it [14]. The number of points in the mesh can be reduced depending on the symmetry of the system investigated [14]. In this case a mesh made up of 2×2×2 special k-points was utilised.

The all-electron potentials which represent the interaction between the nuclei and the electrons were replaced by norm-conserving pseudo-potentials. The pseudo-potentials only explicitly consider the valence electrons and ignore the presence of core electrons, and benefit from being both simpler and smoother functions to approximate than all-electron wavefunctions [12]. By choosing to use pseudo-potentials it is implied that the atomic charge density of the pseudo-potentials

beyond the core radius is exactly the same as that of the all-electron potential [16]. This approximation can be justified by the fact that the highly localised core wavefunction does not take part in the formation of bonds between atoms [12].

For highly localised systems, such as point defects in a crystal, it is appropriate to expand the wavefunctions in a basis of localised orbitals [14]. The wavefunction basis sets for all atoms were based on independent s-, and p-Gaussians [17] with four widths. One further set of d-Gaussians was included to account for polarisation for carbon, whereas for silicon two sets of d-Gaussians were added. Three sets of s- and p-Gaussians were centred on the hydrogen atom. It is advantageous to use Gaussian orbitals since the integrals produced can be evaluated analytically, improving the computational efficiency of the calculations.

The charge density was Fourier transformed using plane-waves with a cut-off of 300 Ry[1], so that the total energies converged to ~ 1 meV. The lattice constant and bulk modulus were within $\sim 1\%$ and 5% of experimentally determined values, respectively. The direct and indirect band-gaps of 5.68 eV and 4.26 eV, respectively, were close to previously published plane-wave values [18]. It is common that the band-gaps predicted using the spin-density-functional technique computational method are smaller than those measured experimentally [12].

The formation energy E^f is the energy required to create a defect from its constituent parts, such as (in this case) vacancies, hydrogen and silicon atoms. The formation energy of X in charge-state q is calculated using [19]

$$E^f(X,q) = E(X,q) - \sum \mu_i + q(E_v^X + \mu_e) + \chi(X,q) \tag{7-1}$$

where E is the total energy, μ_i and μ_e are the chemical potentials of the atoms and electrons, respectively. E_v^X is the position of the valence band maximum (E_v) of the defect supercell, which corresponds to the reference energy level for the electron chemical potential. χ is the correction for periodic boundary conditions, for which only the Madelung term was included [20]; for cubic supercells of side length $2a_0$ and $3a_0$ this is around $0.35q^2$ eV. The form of the correction due to periodic boundary conditions is controversial [21–26], and care must be taken when applying any *post hoc* term to the total energy. By convention the binding

[1] A Rydberg is an energy unit equal to $m_e e^4/2\hbar^2 \approx 13.6$ eV

energy was defined by

$$E^b(XY) = E^f(Y) + E^f(X) - E^f(XY). \tag{7-2}$$

Hyperfine interactions were modelled as outlined by Shaw *et al.* [27]. The hyperfine tensor $\underline{\mathbf{A}}$ (§3.1.3.3) depends on the Fermi and dipolar interactions, which depend on the electronic wavefunction within the ion core region. The pseudopotentials were combined with reconstructed all-electron wavefunctions for isolated atoms within this region [28, 29]. Reconstruction of the ion cores allows the calculation of the hyperfine tensor elements within a frozen-core all-electron wavefunction approximation, without the computational difficulties associated with a full all-electron calculation [27].

7.3 Results

7.3.1 Experimental data

A series of unidentified EPR resonance lines which overlapped with those of the (Si-V:H)^0 (KUL3) defect [3] were observed in the as-grown sample A. The (Si-V:H)^0 defect annealed out after 1 hour at 1200 °C, simplifying the study of the unknown defect, denoted WAR3. Figure 7-1 displays an X-band spectrum recorded with the magnetic field $\mathbf{B}$ applied parallel to the [111] crystallographic direction (assuming a (110)-oriented growth plane). Each resonance line has a pair of strong hyperfine satellites. The relative intensities of the central and outer lines demonstrate that the defect involves an element comprised of both low abundance $I = 0$ nuclei and high abundance $I = \frac{1}{2}$ nuclei. A defect containing a single silicon atom would exhibit a central set of lines attributed to ^{28}Si and ^{30}Si, in addition to ^{29}Si-satellites, with a ratio indicative of the isotopic abundance. The ratio of the total summed intensity of both outer lines to the central lines is ~9:1, in agreement with the quoted isotopic enrichment of silane, confirming that WAR3 involves silicon. Each group is composed of three resonance lines which are further split into two equally intense lines, arising from an $I = \frac{1}{2}$ isotope with 100% natural abundance. This hyperfine splitting is ascribed to hydrogen as the element is ubiquitous in CVD diamond synthesis.

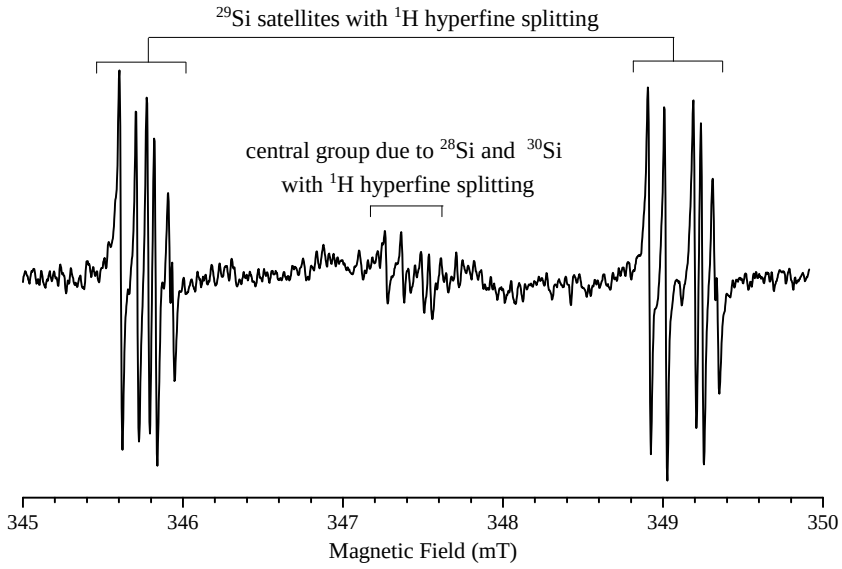

Figure 7-1: X-band ($\upsilon \sim 9.75\,\mathrm{GHz}$) WAR3 EPR spectrum recorded at room temperature with $\mathbf{B}\|[111]$ for sample A after annealing at 1200 °C. The ^{29}Si hyperfine splitting is apparent, where the group of lines arising from ^{28}Si and ^{30}Si lies between the ^{29}Si (90% relative abundance) satellite groups. Each group consists of three resonance lines, which are further split into two due to a hyperfine interaction with a ^{1}H atom.

Table 7-1: Concentrations of N_s^0, (Si-V:H)^0, WAR3 and (Si-V)^0 determined by EPR for sample A. Anneals at temperatures ≤ 1600 °C were carried out at atmospheric pressure in forming gas. The anneal at 2000 °C was performed under a stabilising pressure of 6 GPa. The concentration of (Si-V)$^-$ was determined from the integrated intensity of the 1.68 eV (737 nm) optical absorption band using a calibration factor of $3.6(3) \times 10^{-15}\,\mathrm{meVcm}^2$, determined in §5.4.3.

Treatment	$[N_s^0]_{EPR}$ (ppb)	$[(\text{Si-V:H})^0]_{EPR}$ (ppb)	$[\text{WAR3}]_{EPR}$ (ppb)	$[(\text{Si-V})^0]_{EPR}$ (ppb)	$[(\text{Si-V})^-]_{OA}$ (ppb)
as-grown	23(10)	6(3)	20(5)	500(70)	50(10)
1 hr @ 1200 °C	15(10)	< 1	20(5)	570(70)	80(10)
1 hr @ 1400 °C	50(25)	< 1	32(5)	550(70)	90(10)
1 hr @ 1600 °C	30(15)	< 1	< 5	570(70)	90(10)
2 hrs @ 2000 °C	20(10)	< 1	< 5	250(20)	90(10)

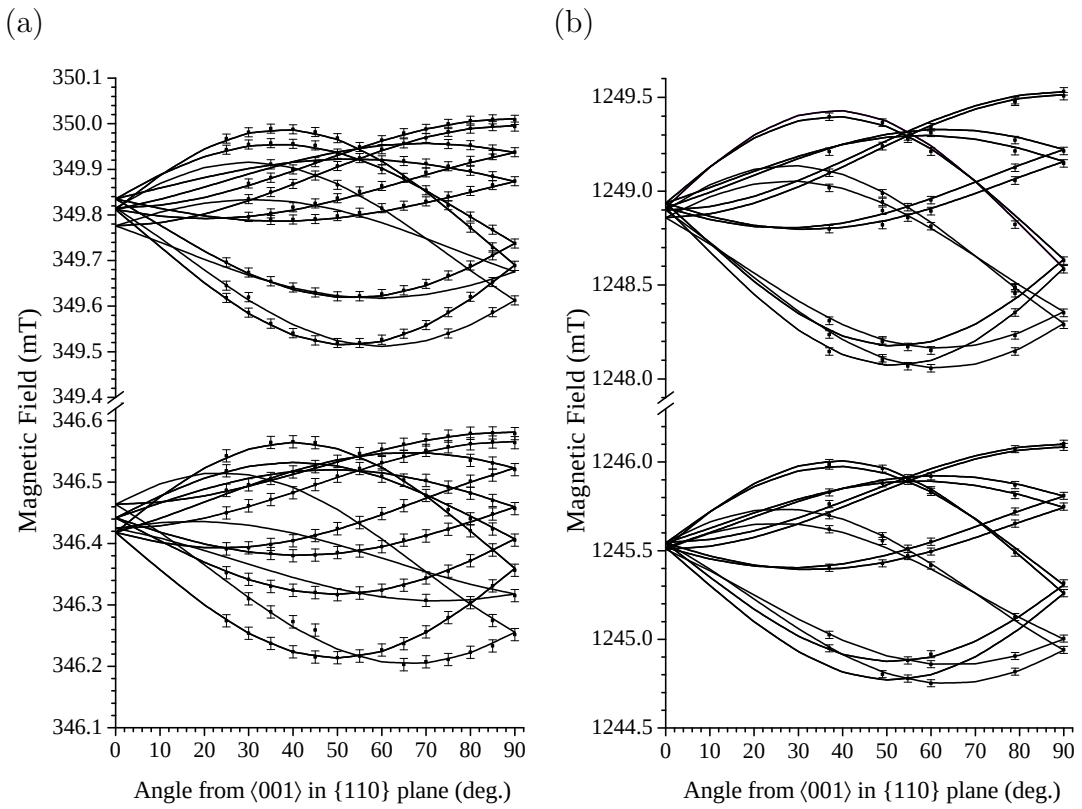

Figure 7-2: Roadmaps showing the positions of the ^{29}Si hyperfine EPR lines for WAR3, as a function of angle in a {110} plane at (a) X-band and (b) Q-band frequencies. The solid curves show the best fits to the experimental data and were obtained using the determined spin Hamiltonian parameters summarised in Table 7-2.

To investigate the orientation dependence of the ^{29}Si satellites and to determine the number of equivalent positions for the ^{29}Si and ^{1}H atoms in WAR3, spectra at both X- and Q-band frequencies were obtained with **B** applied parallel to different orientations in a {110} plane. The positions of the observed resonance lines as a function of the angle from ⟨001⟩ at both X- and Q-band are illustrated in Fig. 7-2. The concentration of WAR3 is significantly smaller than that of (Si-V)^0; the resonance lines of the latter overlap and obscure the WAR3 spectra for magnetic field directions close to ⟨001⟩. The EPR linewidth did not show an angular dependance.

Defects are usually oriented such that there is an equal probability for the symmetry axis of the defect to lie along each of the crystallographically equivalent directions. It was noted that the relative intensities of the WAR3 resonance lines changed drastically when **B** was aligned along different crystallographically equiv-

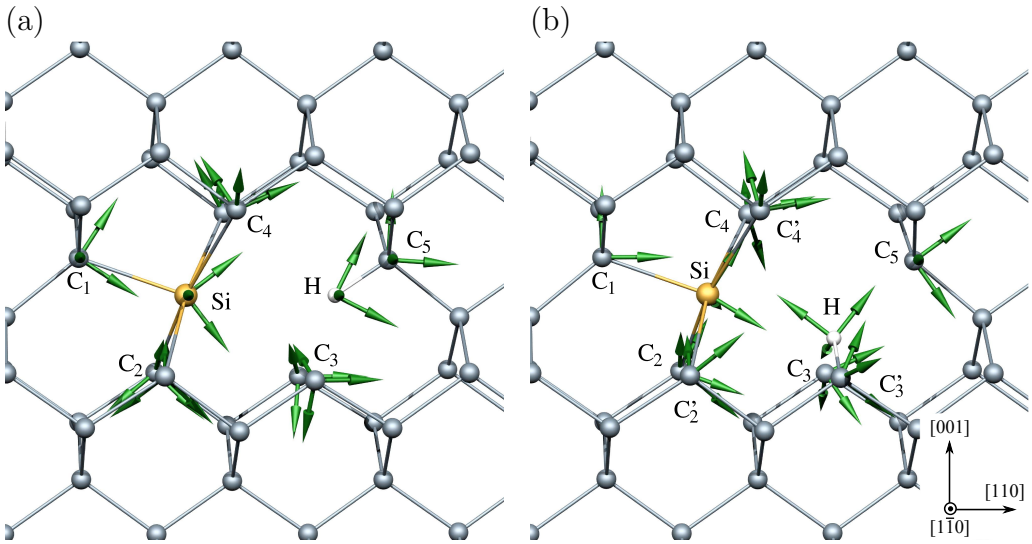

Figure 7-3: Schematics of (a) planar and (b) non-planar (Si-V_2:H) complexes showing the ^{13}C sites for which hyperfine terms are quoted in Table 7-2 and Table 7-3. The arrows showing the directions of the theoretical hyperfine tensor elements listed.

alent directions. This indicates that the defect showed preferential alignment, i.e. there was a non-equal distribution over equivalent directions. To explore this phenomenon spectra were collected with **B** parallel to [111], [110], [$\bar{1}1\bar{1}$] and [$\bar{1}$10], where the latter two orientations lay within the growth plane (assumed to be (110)).

The thermal stability of WAR3 was studied by monitoring its concentration (see Table 7-1) and degree of preferential alignment after each annealing treatment. The relative intensities of the WAR3 peaks did not increase after annealing at 1200 °C, suggesting that (Si-V:H)^0 did not evolve into this new defect and that the degree of preferential alignment of WAR3 remained unchanged.

7.3.2 Theoretical model for (Si-V_2:H)

A complex made from a silicon impurity, two lattice vacancies and a hydrogen atom may in principle adopt a wide range of geometries and charge states. The density functional simulations conducted by Goss and Briddon suggest that the most stable structure for (Si-V_2) consists of a structure based upon the split-vacancy (Si-V) unit [6], but where one of the six nearset-neighbour carbon atoms is replaced by a vacancy. This structure has a {110} plane of symmetry. An

Table 7-2: Predicted hyperfine $\underline{\mathbf{A}}$ tensors for ^{29}Si and ^{1}H for two configurations of (Si-V_2:H) and the experimentally derived $\underline{\mathbf{g}}$ and $\underline{\mathbf{A}}$ tensors for WAR3. The components of the hyperfine tensors $A_n\|[\theta,\phi]$ are quoted in units of MHz. θ is the angle from [001], whilst ϕ is the angle from [100] in a (001) plane. Published experimental [3] and theoretical [6] Hamiltonian parameters for (Si-V:H)^0 are included for comparison.

Parameters	(Si-V_2:H)$_{\text{th.}}$ (C_{1h})	(Si-V_2:H)$_{\text{th.}}$ (C_1)	WAR3$_{\text{expt.}}$	(Si-V:H)$^0{}_{\text{th.}}$[6]	(Si-V:H)$^0{}_{\text{expt.}}$[3]
g_1			2.0036(2)‖[63.14(7),45]		2.0048(2)‖[0,45]
g_2			2.0034(2)‖[153.14(7),45]		2.0054(2)‖[90,45]
g_3			2.0027(2)‖[90,315]		2.0030‖[90,315]
A_1 (^{29}Si)	100‖[53,45]	74‖[33,50]	±92.4(3)‖[43.1(3),45]	88‖[55(3),45]	±76.1(2)‖[53(1),45]
A_2 (^{29}Si)	101‖[143,45]	74‖[120,20]	±95.7(3)‖[133.2(3),45]	86‖[145(3),45]	±81.1(2)‖[143(1),45]
A_3 (^{29}Si)	103‖[90,315]	76‖[103,119]	±96.1(4)‖[90,315]	89‖[90,315]	±79.1(2)‖[90,315]
A_1 (^{1}H)	-1‖[27,45]	-24‖[108,140]	∓2.9(2)‖[61.4(1),45]	-7‖[133(2),45]	∓7.9(1)‖[130(1),45]
A_2 (^{1}H)	2‖[117,45]	3‖[53,-144]	±2.3(4)‖[151.4(1),45]	3‖[43(2),45]	±4.7(1)‖[40(1),45]
A_3 (^{1}H)	1‖[90,315]	34‖[43,71]	±0.4(4)‖[90,315]	6‖[90,315]	±7.3(1)‖90,315]

Table 7-3: Calculated hyperfine tensors (MHz) for the ^{13}C sites identified in Fig. 7-3. n indicates the number of equivalent sites. θ is the angle from [001], whilst ϕ is the angle from [100] in a (001) plane.

Site	n	$A_1\|[\theta,\phi]$	$A_2\|[\theta,\phi]$	$A_3\|[\theta,\phi]$
		(Si-V_2:H)(C_{1h})		
C_1	1	-2‖[33,45]	-1‖[123,45]	-1‖[90,315]
C_2	2	53‖[132,70]	50‖[125,-162]	103‖[61,130]
C_3	2	24‖[151,149]	24‖[90,60]	37‖[61,150]
C_4	2	63‖[42,178]	64‖[67,60]	121‖[57,-49]
C_5	1	-2‖[90,135]	-2‖[4,45]	-1‖[94,45]
		(Si-V_2:H)(C_1)		
C_1	1	-1‖[0,82]	-1‖[89,123]	-1‖[90,33]
C_2	1	23‖[110,28]	26‖[41,94]	63‖[55,-48]
C'_2	1	28‖[127,73]	29‖[54,16]	60‖[57,134]
C_3	1	-236‖[125,134]	-107‖[137,-3]	-107‖[67,61]
C'_3	1	0‖[73,-16]	3‖[124,63]	11‖[39,96]
C_4	1	61‖[144,104]	63‖[76,35]	121‖[58,135]
C'_4	1	65‖[34,155]	67‖[80,50]	124‖[58,-46]
C_5	1	143‖[89,-45]	144‖[144,44]	315‖[54,46]

alternative complex consisting of a substitutional silicon atom with two nearest-neighbour vacant lattice sites is predicted to be around 1.4 eV higher in energy.

The relatively large number of carbon dangling bonds produced in the (Si-V_2) complex are predicted to lead to three bands in the lower part of the band gap, two of which are fully occupied in the neutral charge state. There is hence a range of possible charge and spin states. The defect is predicted to have an acceptor level around $E_v + 2.5$ eV and possibly a second acceptor level close to E_c. There is no evidence for a deep donor level for this complex. In the neutral charge state, a spin-triplet electronic configuration is predicted to lie around 0.3 eV above the spin-singlet ground state.

The carbon dangling bonds are possible traps for hydrogen. Hydrogen may be trapped by the (Si-V_2) centre *in-situ* during its formation when the sample is synthesised. In this case, the (Si-V_2:H) centre has been created as a unit. Additionally, post-growth treatments may mobilise hydrogen, which can diffuse to (Si-V_2) defects already present in the crystal. Of the potential sites to decorate with a single H atom, that with a {110} plane of symmetry (Fig. 7-3(a)) has marginally lower calculated energy, with the non-planar low-energy form (Fig. 7-

3(b)) around 0.1 eV higher in energy. Other geometries investigated include those where the second vacancy is separated from the (Si-V) split-vacancy structure by one host-site. However, the resulting structures are higher in energy by 2.8 eV or more.

The stability of the (Si-V_2:H) complex was also considered. The formation energy of the lattice vacancy is strongly influenced by many-body effects and cannot be easily obtained using density functional techniques. However, Quantum Monte Carlo methods have predicted that the formation energy is very close to 6 eV [30]. There are three key energetic quantities in this study: the binding energies of (Si-V), (Si-V_2) and (Si-V_2:H) with respect to substitutional silicon, Si_s, the vacancy, V, and interstitial hydrogen, H_i. The reactions $Si_s + V \rightarrow$ (Si-V), (Si-V) + V $\rightarrow$ (Si-V_2) and (Si-V_2) + $H_i \rightarrow$ (Si-V_2:H) are all exothermic, releasing 4.8, 3.1 and 5.7 eV, respectively. These thermodynamic formation energies do not provide information about the growth kinetics; the defects may be introduced as complete units into the lattice during diamond synthesis.

The neutral charge state of the complex, (Si-V_2:H)^0, is EPR-active with a predicted $S = \frac{1}{2}$. The calculated hyperfine tensors for both the planar and the non-planar structures are listed in Table 7-2 and Table 7-3, with the directions illustrated in Fig. 7-3. The unpaired electrons are localised primarily upon the remaining carbon dangling bonds (as indicated by the relatively higher A magnitudes), with only a small localisation on the silicon or hydrogen atoms.

7.4 Discussion

7.4.1 Experimentally determined Hamiltonian parameters

The WAR3 EPR spectrum consists of a set of resonance lines with small splittings around $g = 2$, indicating the absence of a zero field interaction and consequently a spin $S = \frac{1}{2}$. The orientation dependence demonstrates that the defect has C_{1h} (monoclinic-I) symmetry. The spectra reveal a splitting due to one hydrogen atom and one silicon atom.

The roadmaps measured at X- and Q-band frequencies were fitted using the following spin Hamiltonian (§3.1.3):

$$\mathscr{H} = \mu_B \hat{\mathbf{S}} \cdot \underline{\mathbf{g}} \cdot \mathbf{B} + \sum_j [\hat{\mathbf{S}} \cdot \underline{\mathbf{A}}_j \cdot \hat{\mathbf{I}}_j - \mu_n g_{n_j} \hat{\mathbf{I}}_j \cdot \mathbf{B}] \tag{7-3}$$

where μ_B is the Bohr magneton, $\underline{\mathbf{g}}$ is the electronic Zeeman tensor, $\underline{\mathbf{A}}$ is the hyperfine tensor, μ_n is the nuclear magneton and g_n is the nuclear g-factor for nuclei j. The Zeeman and hyperfine (^{29}Si and ^{1}H) parameters were determined by least squares fitting to the data in Fig. 7-2 to Equation 7-3. The $\underline{\mathbf{g}}$-parameters were determined relative to g for N_s^0, which is taken to be $g = 2.0024$ [10]. $\underline{\mathbf{A}}$ for ^{29}Si was found to be approximately axially symmetric, with A_1 tilted $\sim 11°$ away from $\langle 111 \rangle$ (toward a $\langle 001 \rangle$) in a $\{110\}$ plane. Constraining $\underline{\mathbf{A}}$ to be axial along a $\langle 111 \rangle$ direction resulted in a statistically significant deterioration in the fit quality. The experimentally obtained parameters are summarised in Table 7-2. The absolute sign of the hyperfine parameters for ^{29}Si and ^{1}H has not been determined. Comparison between the experimental hyperfine parameters with those predicted by theory confirms that WAR3 is a silicon divacancy decorated by a hydrogen atom in a planar configuration, with the spin state indicating that it is in the neutral charge state, (Si-V_2:H)^0. There is no experimental evidence for the presence of the non-planar (Si-V_2:H)^0 structure, suggesting the difference in the formation energies between the two structures to be greater than that calculated in §7.3.2.

The hyperfine interaction can be split into isotropic A_s and anisotropic A_p components (§3.1.3.3), where $A_s = \frac{1}{3}(A_\parallel + 2A_\perp)$ and $A_p = \frac{1}{3}(A_\parallel - A_\perp)$. Hence, the localisation of the unpaired electron can be estimated in the usual manner [31, 32]. The theoretical modelling overestimates the magnitude of the isotropic A_s by $\sim 6\%$. The experimentally determined ^{29}Si value for $A_\parallel$ ($= A_1$) is less than $A_\perp$ ($\approx (A_2 + A_3)/2$), showing that A_s and A_p have opposite signs. Thus, the ^{29}Si hyperfine interaction cannot originate simply from an unpaired electron probability density localised on the silicon; the isotropic component of the ^{29}Si hyperfine interaction can be explained by indirect spin polarisation [33]. Only 2% $3s$ unpaired electron probability density is required to produce the ^{29}Si hyperfine interaction observed; far less for spin polarisation of the $2s$ shell. The small anisotropic contribution to the ^{29}Si hyperfine interaction could be easily accounted for by dipolar coupling

between the ^{29}Si and the unpaired electron probability density localised on the neighbouring atoms. The concentration (and hence EPR signal-to-noise ratio) was too low for measurement of the ^{13}C hyperfine satellites.

The predicted ^{1}H hyperfine interaction for the co-planar structure (Fig. 7-3(a)) is very small as is found experimentally. As expected for the structure, the experimental values are consistent with a distant dipolar interaction with the unpaired electron probability density. The uncertainties in the calculated magnitudes and directions of the ^{1}H hyperfine interaction are large, but nevertheless the non-planar model is definitely ruled out.

The anisotropy in the Zeeman interaction for both (Si-V:H)^0 and (Si-V_2:H)^0 is as one would expect for complexes with the unpaired electron probability density located on carbon dangling orbitals [3]. It is noted that defect labelled KUL4 [1], but not characterised in detail, may have been (Si-V:H)^0.

7.4.2 Preferential alignment and thermal stability

Work by Edmonds demonstrated that the silicon-split vacancy defect in diamond is preferentially aligned in CVD diamond grown on {110}-oriented substrates [3]; this phenomenon was further investigated in §5.4.2. The preferential alignment of WAR3, which results in a change in the relative intensities of resonance peaks when applying the magnetic field parallel to different crystallographically equivalent directions, is illustrated in Fig. 7-4. This shows that WAR3, like (Si-V), grows in as a unit during the CVD growth process, and was not formed by the diffusion and aggregation of its constituents during growth. There are 12 unique orientations (sites) for the {110} mirror plane of the C_{1h} symmetry of the centre relative to the (110) growth plane. The degree of preferential alignment can be quantified by simulating spectra for a single site belonging to each of the three groups of sites whose mirror planes make angles of 90° (s_α), 45° (s_β) or 0° (s_γ) relative to the growth plane, and fitting a weighted combination to the experimental spectra, e.g.

$$\text{spectrum intensity} = N(\alpha s_\alpha + \beta s_\beta + \gamma s_\gamma) \tag{7-4}$$

where N is a scaling factor and α, β and γ are the probabilities of the centre's mirror plane making angles of 90°, 45° and 0° relative to (110), respectively. By

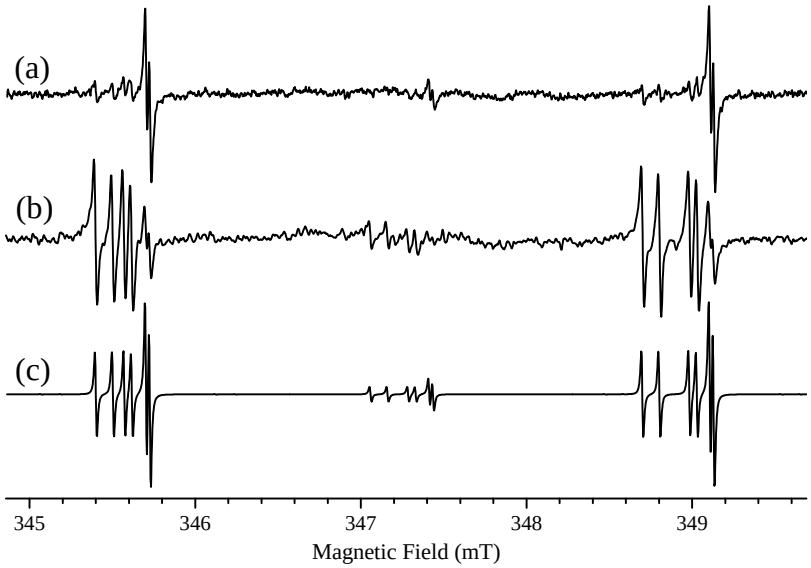

Figure 7-4: WAR3 EPR lines observed around $g = 2$ at X-band frequencies for sample A with (a) $\mathbf{B}\|[\bar{1}1\bar{1}]$ and (b) $\mathbf{B}\|[111]$, where a (110) growth plane is assumed. Consequently, the former direction lies *in* the growth plane, whilst the latter lies *out* of the growth plane. The difference in the relative intensities of the peaks is attributed to the preferential alignment of the defect. (c) displays the simulated spectrum for WAR3 if it was statistically oriented. The spectra were collected after annealing the sample for 1 hour at 1200 °C.

constraining $\alpha + \beta + \gamma = 1$ and varying N, α and β, a best fit to the experimental data was obtained by minimising the sum of the squares of the residual between experimental and simulated spectra. Data for spectra where the magnetic field was aligned parallel to three different crystallographic orientations were used. If the WAR3 centres were statistically aligned the probabilities would be $\alpha = 0.1\dot{6}$, $\beta = 0.6\dot{6}$ and $\gamma = 0.1\dot{6}$.

After annealing sample A at 1200 °C to remove (Si-V:H)^0, the preferential orientation of (Si-V_2:H)^0 was characterised by $\alpha = 0.67(7)$, $\beta = 0.29(3)$ and $\gamma = 0.04(1)$. Thus approximately four times as many WAR3 centres were aligned with their mirror planes lying perpendicular to the growth plane, compared to a statistical distribution, as illustrated in Fig. 7-5. This behaviour is similar to that displayed by (Si-V)^0, where it was calculated that for this sample the D_{3d} symmetry axis of the centre was approximately three times more likely to be aligned along a $\langle 111 \rangle$ direction lying out of the growth plane (§5.4.2).

In §5.4.2 a model for the incorporation of (Si-V) as a unit during CVD growth on a {110}-oriented diamond substrate was proposed. The scenario can be easily extended to account for the production of preferentially aligned WAR3 centres. First, the silicon is incorporated on a substitutional site, reducing the probability for incorporation of a carbon atom in the next layer, thus forming (Si_S-V). Overgrowth and relaxation would lead to the (Si-V) structure. Another vacancy (and a hydrogen) could be favoured in the subsequent overgrowth layer, producing preferentially oriented WAR3. This model predicts that 100% of the WAR3 centres would be preferentially aligned, with $\alpha = 1$. Similarly, the (Si-V) centres would also be produced with 100% of the defects aligned with their D_{3d} axes pointing out of the growth plane. The same sample (A) was used for the investigation of the preferential alignment of (Si-V) and WAR3, and in both cases the centres displayed a reduced degree of preferential alignment. This is possibly due to the sample containing material which was not solely grown on a flat {110} surface, but also includes deposition on alternative facets that evolved during growth.

WAR3 was not observed in the samples B and C, previously studied in Chapter 5, which were synthesised by CVD growth on {001}- and {113}-oriented diamond substrates, respectively. This does not rule out that the centre is present, albeit in concentrations below the current detection limit (< 5 ppb). Samples A and B were synthesised simultaneously (§5.2). The (Si-V) concentration in A was 6 ± 1 times greater than in B (§5.4.2), indicating that the incorporation efficiency of (Si-V) during CVD growth on {110}-oriented substrates is significantly higher than on {001} oriented substrates. It is reasonable to assume that this may also be the case with WAR3. Sample C was synthesised in a separate growth run using silane with different silicon isotope abundances. Thus the growth chemistry is expected to differ from that for the other samples, such that conclusions about the incorporation efficiency of (Si-V) during growth on {113}-oriented substrates cannot be drawn by comparison of the defect concentrations. If the ratio between the (Si-V) and WAR3 concentrations is assumed to be constant among the different samples the WAR3 concentration in samples B and C would be below our EPR detection limit.

Upon annealing sample A at 1400 °C the WAR3 concentration increased by

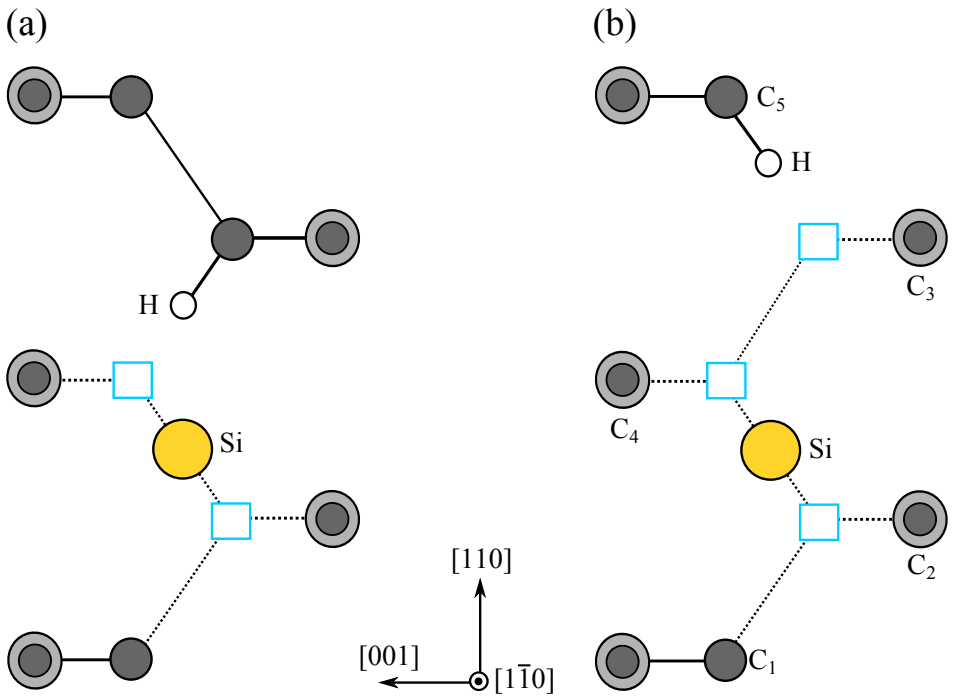

Figure 7-5: Cross-sectional view of the $(1\bar{1}0)$ mirror plane of (a) (Si-V:H) and (b) WAR3. Vacancies are illustrated as squares. The carbon atoms above and below the $(1\bar{1}0)$ plane are shown as larger and smaller circles, respectively. The numbered carbon atoms for the WAR3 defect refer to those given in Table 7-3 and Fig. 7-3(a).

~50%. Furthermore, a simulation for the spectra of statistically aligned WAR3 fits with the EPR spectra after the 1400 °C anneal. The centres created during the anneal may have been formed by the diffusion of several different centres to silicon-related defects: (Si-V) + V + H → (Si-V_2:H), (Si-V_2) + H → (Si-V_2:H), Si_s + (V_2-H) → (Si-V_2:H). The EPR and absorption data suggest that the concentration of (Si-V)$^-$ increased whilst that of (Si-V)^0 remained constant after annealing. Since their concentrations were significantly larger than the change in concentration of WAR3, it cannot be ruled out that either defect was involved in the process which created WAR3. It has been reported that the silicon content in silicon-doped CVD samples is substantially higher than that which can currently be accounted for using EPR and optical spectroscopic techniques [3, 34]. Silicon-containing diamond is expected to have substitutional silicon (Si_s) (§2.2.4.2 and §5.4.4), a centre which is unfortunately EPR-inactive and invisible to electronic-optical spectroscopy [6]. Furthermore, theoretical work by Goss *et al.* (Ref. [6] and §7.3.2) has predicted the existence of (Si-V_2), though this EPR-active de-

fect has not yet been identified by experiment. Positron annihilation studies have shown that vacancy clusters can be produced in as-grown CVD diamond [35]. It is likely that such structures are decorated with hydrogen [36]. In brown CVD diamond samples positron annihilation investigations indicate that the concentration of larger clusters increases at the expense of smaller clusters for annealing at 1400 °C [35]. Assuming vacancy clusters are present in the silicon-doped sample, there is a ready source of vacancies and hydrogen available for post-growth WAR3 formation under these annealing conditions.

The reduction in overall preferential alignment after the 1400 °C anneal cannot be explained by the formation of new WAR3 centres solely via the reactions which utilise (Si-V) and (Si-V_2), since the as-grown (Si-V) (and presumably (Si-V_2)) units were also preferentially oriented (§5.4.2). Conversely, the reaction Si_s + (V_2-H) → (Si-V_2:H) would produce defects oriented along each of the allowed sites. This observation does not rule out the alternative formation processes, but suggests that the as-grown and newly created WAR3 centres may have reoriented. It is possible that at 1400 °C an equilibrium is reached between the formation and dissociation of the WAR3 centres, thus destroying the preferential alignment. WAR3 anneals out for annealing temperatures above 1600 °C.

7.5 Conclusions and further work

Multifrequency EPR studies in conjunction with theoretical modelling have been employed to identify a silicon-related defect in CVD diamond, WAR3. WAR3 has a spin $S = \frac{1}{2}$ and C_{1h} symmetry. The excellent agreement between the experimental and computationally derived spin Hamiltonian parameters confirms that WAR3 is a planar silicon divacancy complex decorated by a single hydrogen atom, (Si-V_2:H)^0. The presence of silicon was verified by ^{29}Si enrichment, whilst hydrogen was the only plausible candidate for the small hyperfine interaction resulting from the inclusion of an $I = \frac{1}{2}$ element with 100% natural abundance.

WAR3 showed preferential alignment relative to the growth direction, indicating that the complex grows in as a unit when the sample is grown on a {110}-oriented substrate. The degree of preferential alignment can only change if the

defect reorients during a treatment or additional WAR3 is created. The preferential orientation of defects in as-grown CVD diamond could provide a fingerprint of the growth direction and could thus potentially elucidate the processes occurring on the growth surface. Furthermore, any changes in the degree of preferential orientation may provide evidence for post-growth processing and/or insight into defect migration mechanisms.

References

[1] K. Iakoubovskii and A. Stesmans, Phys. Status Solidi a **186**, 199 (2001).

[2] K. Iakoubovskii and A. Stesmans, Phys. Rev. B **66**, 195207 (2002).

[3] A. M. Edmonds, M. E. Newton, P. M. Martineau, D. J. Twitchen, and S. D. Williams, Phys. Rev. B **77**, 245205 (2008).

[4] K. Iakoubovskii, A. Stesmans, K. Suzuki, J. Kuwabara, and A. Sawabe, Diam. Relat. Mater. **12**, 511 (2003).

[5] J. P. Goss, R. Jones, S. J. Breuer, P. R. Briddon, and S. Öberg, Phys. Rev. Lett. **77**, 3041 (1996).

[6] J. P. Goss, P. R. Briddon, and M. J. Shaw, Phys. Rev. B **76**, 075204 (2007).

[7] K. Iakoubovskii, A. Stesmans, M. Nésladek, and G. Knuyt, Phys. Status Solidi A **193**, 448 (2002).

[8] C. D. Clark, H. Kanda, I. Kiflawi, and G. Sittas, Phys. Rev. B **51**, 16681 (1995).

[9] U. F. S. D'Haenens-Johansson, A. M. Edmonds, M. E. Newton, J. P. Goss, P. Briddon, J. M. Baker, P. M. Martineau, R. U. A. Khan, D. J. Twitchen, and S. D. Williams, Phys. Rev. B **82**, 155205 (2010).

[10] W. Smith, P. P. Sorokin, I. L. Gelles, and G. J. Lasher, Phys. Rev. **115**, 1546 (1959).

[11] J. P. Perdew, K. Burke, and M. Ernzerhof, Phys. Rev. Lett. **77**, 3865 (1996).

[12] R. Jones and P. R. Briddon, in *Identification of Defects in Semiconductors*, edited by M. Stavola (Academic Press, Boston, 1998), vol. 51A of *Semiconductors and Semimetals*, chap. 6.

[13] M. Rayson and P. Briddon, Comput. Phys. Comm. **178**, 128 (2008).

[14] J. P. Goss, J. Phys.-Condens. Mat. **15**, R551 (2003).

[15] H. J. Monkhorst and J. D. Pack, Phys. Rev. B **13**, 5188 (1976).

[16] C. Hartwigsen, S. Goedecker, and J. Hutter, Phys. Rev. B **58**, 3641 (1998).

[17] J. P. Goss, M. J. Shaw, and P. R. Briddon, in *Theory of Defects in Semiconductors*, edited by D. A. Drabold and S. K. Estreicher (Springer, Berlin/Heidelberg, 2007), vol. 104 of *Topics in Applied Physics*, pp. 69–94.

[18] D. A. Liberman, Phys. Rev. B **62**, 6851 (2000).

[19] S. B. Zhang and J. E. Northrup, Phys. Rev. Lett. **67**, 2339 (1991).

[20] G. Makov and M. C. Payne, Phys. Rev. B **51**, 4014 (1995).

[21] H. Nozaki and S. Itoh, Phys. Rev. E **62**, 1390 (2000).

[22] U. Gerstmann, P. Deák, R. Rurali, B. Aradi, T. Frauenheim, and H. Overhof, Physica B **340-342**, 190 (2003).

[23] J. Shim, E.-K. Lee, Y. J. Lee, and R. M. Nieminen, Phys. Rev. B **71**, 035206 (2005).

[24] C. W. M. Castleton, A. Höglund, and S. Mirbt, Phys. Rev. B **73**, 035215 (2006).

[25] P. Erhart, K. Albe, and A. Klein, Phys. Rev. B **73**, 205203 (2006).

[26] C. W. M. Castleton and S. Mirbt, Phys. Rev. B **70**, 195202 (2004).

[27] M. J. Shaw, P. R. Briddon, J. P. Goss, M. J. Rayson, A. Kerridge, A. H. Harker, and A. M. Stoneham, Phys. Rev. Lett. **95**, 105502 (2005).

[28] P. E. Blöchl, Phys. Rev. B **50**, 17953 (1994).

[29] B. Hetényi, F. De Angelis, P. Giannozzi, and R. Car, J. Chem. Phys. **115**, 5791 (2001).

[30] R. Q. Hood, P. R. C. Kent, R. J. Needs, and P. R. Briddon, Phys. Rev. Lett. **91**, 076403 (2003).

[31] J. R. Morton and K. F. Preston, J. Magn. Reson. **30**, 577 (1978).

[32] G. D. Watkins, Phys. Rev. **155**, 802 (1967).

[33] G. D. Watkins, Phys. Rev. B **12**, 4383 (1975).
[34] A. M. Edmonds, Ph.D. thesis, University of Warwick (2008).
[35] J. M. Mäki, F. Tuomisto, C. Kelly, D. Fisher, and P. Martineau, Physica B **401**, 613 (2007).
[36] L. S. Hounsome, R. Jones, P. M. Martineau, D. Fisher, M. J. Shaw, P. R. Briddon, and S. Oberg, Phys. Rev. B **73**, 125203 (2006).

Chapter 8

Summary

8.1 Motivation

The majority of the research conducted for this thesis has focussed on the identification and characterisation of silicon-related complexes in CVD diamond. The silicon split-vacancy centre, (Si-V) has garnered the interest of the scientific community due to its frequent unintentional presence in CVD diamond. Furthermore, it has been shown to grow in as a unit when the diamond is synthesised homoepitaxially on a {110}-oriented substrate, resulting in its preferential orientation [1]. These properties making it an ideal centre to investigate the incorporation of defects in diamond and the processes occurring at the growing surface. Moreover, recently it has been demonstrated that its negative charge state, $(\text{Si-V})^-$, can be used as a single photon source [2, 3]. This, combined with other attractive properties such as a sharp ZPL (with a Huang-Rhys factor of ~ 0.24 [3, 4]) located in a spectral region with low background fluorescence and a currently unrivalled single photon count rate, underscore its potential use in quantum information processing technologies. However, the EPR spectrum for the ground state of $(\text{Si-V})^-$ ($S = \frac{1}{2}$) has not yet been identified, possibly due to a Jahn Teller broadening of the signal [5]. In the future, uniaxial stress may be able to lift the degeneracy and enable the detection of $(\text{Si-V})^-$ by EPR methods.

The neutral charge state, $(\text{Si-V})^0$, has been investigated in greater detail. The EPR spectrum for this centre, labelled KUL1, has already previously been conclusively identified [1, 6, 7]. Further study of the centre has been carried out for this thesis using optical absorption, photoluminescence, and EPR spectroscopy, exploiting their specific areas of distinction, ultimately resulting in the identification and characterisation of its optical analogue.

The currently identified silicon-related defects in diamond cannot account for

the total silicon content in doped material, as measured by secondary ion mass spectrometry (SIMS) [5]. It is therefore of interest to try to establish spectroscopic features for silicon-related complexes and determine their structure. A previously unreported EPR-active centre, named WAR3, has been characterised extensively and identified as the silicon divacancy unit decorated by a hydrogen atom.

The following sections will summarise the key results from the various investigations presented in this thesis.

8.2 Identification and characterisation of the optical spectrum for (Si-V)^0

The 1.31 eV (946 nm) band visible in optical absorption and luminescence has been identified as the (Si-V)^0 centre using an approach which combined EPR and optical spectroscopy. $^{28}\text{Si} \rightarrow {}^{29}\text{Si}$ isotopic substitution experiments demonstrated that the 1.31 eV zero phonon line (ZPL), like the 1.68 eV (737 nm) ZPL attributed to (Si-V)$^-$ [8–10], shifts to a lower energy by 0.4 ± 0.1 meV at ~ 4 K, conclusively attributing the line to a silicon-related defect. The 1.31 eV band correlates in intensity with the (Si-V)^0 concentration determined by EPR. Furthermore, reversible charge transfer can be induced between (Si-V)^0 and (Si-V)$^-$ by illumination with a 5.45 eV (224 nm) laser light source or moderate (~580 °C) heating in the dark. The former treatment led to an increase in the (Si-V)^0 concentration and a decrease in that of the (Si-V)$^-$ centres, whilst the opposite effect was observed when heating in the dark. By utilising the EPR data and the photochromic and thermochromic relationship between the (Si-V)^0 and (Si-V)$^-$ centres calibration factors which can be used to calculate the defect concentrations based on the 1.31 eV and 1.68 eV ZPL integrated intensities, respectively, were determined.

The electronic structure and vibronic coupling of the 1.31 eV band was investigated by considering its integrated intensity in absorption and photoluminescence as a function of temperature. The results estimate a Huang-Rhys factor of ~ 1.5 and suggest the presence of a trapping level or shelving state located approximately 5 meV below the 1.31 eV excited state.

The (Si-V)^0 defects have been shown to grow in as units in CVD material

grown on {110}-oriented diamond substrates [5]. The centres display preferential orientation, whereby there is a non-equal probability for the centres to form with their D_{3d} symmetry axes aligned along each of four crystallographically equivalent ⟨111⟩ directions in the lattice. The majority of centres (~ 80%) were oriented with their symmetry axes along the ⟨111⟩ directions which lie out of the {110}-oriented growth plane. The preferential orientation of the centres is attributed to the layer-by-layer growth sequence of CVD, with a silicon impurity atom incorporating into the surface, modifying the chemistry of the nearest-neighbouring site above it, leading to a higher probability of a vacant site. HPHT annealing at 2000 °C led to a decrease of 50% of the (Si-V)^0 concentration, and the loss of preferential alignment, indicating that the centres were breaking apart and reforming during the treatment.

The integrated absorption intensity is proportional to the defect concentration as long as the centres are oriented statistically amongst all of the crystallographically equivalent allowed directions. However, this is not the case when the centres are preferentially aligned. The effect of preferential orientation of trigonal defects on their absorption spectra has been modelled. If the degree of preferential orientation is known from alternative techniques, such as EPR, it is possible to correct the experimentally measured absorption spectra. Both $^3A_{2g} \leftrightarrow {}^3A_{1u}$ and $^3A_{2g} \leftrightarrow {}^3E_u$ are allowed electric dipole transitions which may have been assigned to the 1.31 eV ZPL. Analysis of the spectra for samples with preferentially oriented (Si-V)^0 defects revealed that the 1.31 eV band arises from a $^3A_{2g} \leftrightarrow {}^3A_{1u}$ transition. This result could be confirmed by conducting uniaxial-stress experiments on the 1.31 eV vband, which would provide information regarding the symmetry of the centre responsible for the line and the nature of the ground and excited states.

Preferential orientation would be expected for other impurity-vacancy complexes which are based on a unit where the vacancy (which might be "split") and impurity lie along the same ⟨111⟩ direction. However, these types of defects will not exhibit preferential orientation if the CVD material is grown homoepitaxially on a {100}-oriented substrate. Vacancy impurity defects with other symmetries may be preferentially aligned in CVD diamond when using differently aligned substrates.

The production of silicon-vacancy complexes by irradiation and annealing of silicon-containing diamond has been modelled using a set of coupled differential equations describing the vacancy migration to silicon-related traps, including single substitutional silicon, and the formation and destruction of (Si-V) and silicon divacancy (Si-V_2) centres. The existence of the latter defect has been predicted by density functional theory calculations by Goss *et al.* ([11] and §7.3.2). The negative state, (Si-V_2)$^-$, has a spin predicted to be $S = \frac{1}{2}$ and is thus EPR active [11]. Furthermore, (Si-V_2) is predicted to produce an optical absorption feature in the 1.0 – 1.5 eV range, with another closer to the band edge [11]. However, the centre has not yet been identified spectroscopically. The model devised indicates that persistent irradiation and annealing treatments will eventually convert the majority of substitutional silicon and (Si-V) centres to (Si-V_2). It would be of interest to investigate a sample which has been subjected to such treatments in order to try to identify the spectrum of (Si-V_2) using EPR, optical absorption or PL spectroscopy. Unidentified optical features have been observed in silicon-containing samples, such as the 1.018 ±0.001 eV ZPL seen in absorption and PL (Fig. 5-15). A systematic study, including isotopic substitution, illumination and moderate heating treatments, should be conducted on these features to elucidate their origin.

8.3 Optical spin polarisation of (Si-V)^0

The optical spin polarisation of the $^3A_{2g}$ ground state of the (Si-V)^0 centre has been demonstrated for the first time. Illumination with a Hg-Xe arc-lamp or a 532 nm laser can be used to preferentially populate the $M_S = 0$ level of the ground state multiplet. A mathematical definition for the degree of spin polarisation, ξ, which takes into account the Boltzmann distribution of spin level occupation, has been proposed, enabling the direct meaningful comparison of data for different experiments and defects. The nitrogen-vacancy centre in the negative charge state, (N-V)$^-$, is currently the most promising colour centre in diamond for quantum information processing or applications which require a single photon source [12–19]. One of its key traits is that its ground state can be spin polarised, allowing

the manipulation of the population of the spin levels. The maximum ξ achieved for $(\text{Si-V})^0$ in this investigation ($\sim 9\%$ at 8 K) is significantly smaller than that reported by Felton *et al.* for $(\text{N-V})^-$ using a similar setup ($\sim 49\%$, at 10 K) [20]; it is even worse compared to the maximum value for $(\text{N-V})^-$ found in the literature [21], $\xi \sim 73\%$, measured at ~ 2 K.

Two possible mechanisms for the optical spin polarisation of $(\text{Si-V})^0$ have been considered. Both rely on at least one intersystem crossing pathway to produce the observed preferential population of the $M_S = 0$ ground state level. The first model is based on an intersystem crossing cycle similar to the one proposed for $(\text{N-V})^-$ [22, 23], where the spin-orbit interaction mixes states which are characterised by a different spin, but which transform according to the same irreducible representations. Analysis of the splittings produced by the spin-orbit interaction for the ${}^3A_{2g}$ ground and ${}^3A_{1u}$ excited level (lying 1.31 eV above the ground state) reveal that this model requires the presence of two low lying spin singlet states. There are various candidate states available for $(\text{Si-V})^0$. A possible electronic arrangement which would be consistent with the experimental results situates the ${}^1E_u$ and ${}^1A_{1g}$ states between the ${}^3A_{2g}$ and ${}^3A_{1u}$ states, with the ${}^1E_u$ state above the ${}^1A_{1g}$ state.

The second possible mechanism is the photoionisation of $(\text{Si-V})^-$, forming $(\text{Si-V})^0$ in one of its excited states, from which it de-excites, eventually preferentially populating the $M_S = 0$ level of the ground state. However, to achieve this result the de-excitation process must involve intersystem crossing as well. There is insufficient data to rule out any of the models and further experimentation is necessary. The nature of the mechanism might be unravelled by using different energies for the excitation source. If the standard intersystem crossing cycle is the correct model resonant pumping into the ${}^3A_{1u}$ state using a 1.31 eV excitation source would result in a significant improvement in the degree of optical spin polarisation achieved.

It has been shown that the optical excitation setup employed for the study of $(\text{Si-V})^0$ is not ideal, and there are several factors which could be modified to improve the degree of spin polarisation. Firstly, the degree of spin polarisation was proportional to the intensity of the Hg-Xe arc-lamp excitation, indicating that increasing its power would also lead to an increase in ξ. Additionally, the

liquid filter and lightguides utilised were poor at transmitting light in the region of 1.31 eV. Further experiments should be conducted to optimise the energy of the excitation and ensure that it is efficiently reaching the sample. From the temperature variation of the 1.31 eV band in photoluminescence it is known that there are other bands and states lying close to the 1.31 eV excited state. The energy chosen for excitation should ensure that the electrons are efficiently excited into a state which is involved in the process producing optical spin polarisation, and avoid their trapping by alternative bands or states.

Analysis of the spin-lattice relaxation rate and spin polarisation rate for $(\text{N-V})^-$ and $(\text{Si-V})^0$ during continuous excitation has revealed that at liquid helium temperatures the spin polarisation rate is $\gtrsim 3$ greater for the latter defect using broad band excitation, i.e. the maximum degree of spin polarisation achievable for a set of experimental conditions is reached significantly faster for $(\text{Si-V})^0$ than $(\text{N-V})^-$. However, for $(\text{Si-V})^0$ at room temperature the large spin-lattice relaxation rate (short spin-lattice relaxation time), which is competing to revert the population of the spin levels back to the Boltzmann distribution, reduces the effectiveness of the optical spin polarisation. This means that $(\text{Si-V})^0$ will not (potentially) rival $(\text{N-V})^-$ for quantum information applications at room temperature, but may still be useful at cryogenic temperatures. Therefore, efforts should be made to further investigate the potential of the $(\text{Si-V})^0$ centre. For instance, single photon detection has already been achieved for the negative charge state of the centre [2, 3]. Is this possible with $(\text{Si-V})^0$ as well?

8.4 Identification of the EPR spectrum for the $(\text{Si-V}_2\text{:H})^0$ complex

Multifrequency EPR studies on an intentionally silicon-doped (90% ^{29}Si) CVD sample have revealed the presence of a previously unreported defect with $C_{1\text{h}}$ symmetry and a spin $S = \frac{1}{2}$, labelled WAR3. Analysis of ^{29}Si and ^{1}H hyperfine structure indicated that it contained a single silicon atom and hydrogen. Comparison between the experimental data and hyperfine parameters computed for silicon-divacancy-hydrogen structures modelled using density functional theory by J. P.

Goss and P. R. Briddon (reviewed in Chapter 7 and published in Ref. [24]) unambiguously confirm that WAR3 is the neutral charge state of a silicon-divacancy decorated by a hydrogen atom with a {110} plane of symmetry, (Si-V_2:H)^0.

Like (Si-V)^0, (Si-V_2:H)^0 was found to be preferentially oriented in CVD material grown on a {110}-oriented diamond substrate, indicating that the (Si-V_2) structure can grow into diamond as a unit. The growth model suggested for (Si-V)^0 can be extended to produce this complex, resulting in the preferential formation of (Si-V_2:H)^0 centres with their {110} oriented symmetry plane lying out of the growth plane. Approximately four times as many (Si-V_2:H)^0 centres were aligned in this manner, compared to the distribution over all crystallographically identical configurations in the absence of preferential orientation. The incorporation of (Si-V_2:H)^0 as a unit requires more steps that that of (Si-V)^0, therefore it is understandable that its concentration is only $\sim 4\%$ that of (Si-V)^0.

The thermal stability of (Si-V_2:H)^0 was investigated, revealing that its concentration can be increased by annealing at $\sim 1400\,^{\circ}$C. This coincided with a loss of the preferential orientation of the centres, explained by the formation of new defects and the dissociation and reformation of the original centres present. This illustrates that treatments can be used to modify the preferential orientation of centres, providing scientists with another tool to identify post-growth treatments. The centre starts to anneal out at $1600\,^{\circ}$C.

An optical analogue for (Si-V_2:H)^0 has not yet been identified. However, the maximum concentration of the centre in the sample investigated was only 32 ± 5 ppb. It may be possible to observe this centre, in addition to other silicon-related defects, in a sample which has been doped more heavily with silicon. Furthermore, reversible treatments such as moderate heating or illumination might be able to increase the concentration of specific charge states, facilitating their detection.

References

[1] A. M. Edmonds, M. E. Newton, P. M. Martineau, D. J. Twitchen, and S. D. Williams, Phys. Rev. B **77**, 245205 (2008).

[2] C. L. Wang, C. Kurtsiefer, H. Weinfurter, and B. Burchard, J. Phys. B-At. Mol. Opt. **39**, 37 (2006).

[3] E. Neu, D. Steinmetz, J. Riedrich-Möller, S. Gsell, M. Fischer, M. Schreck, and C. Becher, New J. Phys. **13**, 025012 (2011).

[4] A. T. Collins, L. Allers, C. J. Wort, and G. A. Scarsbrook, Diam. Relat. Mater. **3**, 932 (1994).

[5] A. M. Edmonds, Ph.D. thesis, University of Warwick (2008).

[6] K. Iakoubovskii and A. Stesmans, Phys. Status Solidi a **186**, 199 (2001).

[7] K. Iakoubovskii, A. Stesmans, K. Suzuki, J. Kuwabara, and A. Sawabe, Diam. Relat. Mater. **12**, 511 (2003).

[8] J. P. Goss, R. Jones, S. J. Breuer, P. R. Briddon, and S. Öberg, Phys. Rev. Lett. **77**, 3041 (1996).

[9] C. D. Clark, H. Kanda, I. Kiflawi, and G. Sittas, Phys. Rev. B **51**, 16681 (1995).

[10] V. S. Vavilov, A. A. Gippus, A. M. Zaitsev, B. V. Deryagin, B. V. Spitsyn, and A. E. Aleksenko, Sov. Phys. Semiconduct. **14**, 1078 (1980).

[11] J. P. Goss, P. R. Briddon, and M. J. Shaw, Phys. Rev. B **76**, 075204 (2007).

[12] M. V. Gurudev Dutt, L. Childress, L. Jiang, E. Togan, J. Maze, F. Jelezko, A. S. Zibrov, P. R. Hemmer, and M. D. Lukin, Science **316**, 1312 (2007).

[13] R. Hanson, Nat. Mater. **8**, 368 (2009).

[14] J. Wrachtrup and F. Jelezko, J. Phys.- Condens. Mat. p. S807 (2006).

[15] V. M. Acosta, E. Bauch, M. P. Ldbetter, C. Santori, K.-M. C. Fu, P. e. Barclay, R. G. Beausoleil, H. Linget, J. F. Roch, F. Treussart, et al., Phys. Rev. B **80**, 115202 (2009).

[16] G. Balasubramanian, I. Y. Chan, R. Kolesov, M. Al-Hmoud, C. Shin, C. Kim, A. Wojcik, P. R. Hemmer, A. Kreuger, T. Hanke, et al., Nature **455**, 648 (2008).

[17] J. R. Maze, P. L. Stanwix, J. S. Hodges, S. Hong, J. M. Taylor, P. Cappellaro, L. Jiang, M. V. Gurudev Dutt, E. Togan, A. S. Zibrov, et al., Nature **455**, 644 (2008).

[18] A. Beveratos, S. Kühn, R. Brouri, T. Gacoin, J.-P. Poizat, and P. Grangier, Eur. Phys. J. D **18**, 191 (2002).

[19] F. Jelezko and J. Wrachtrup, Phys. Status Solidi a **203**, 3207 (2006).

[20] S. Felton, A. M. Edmonds, M. E. Newton, P. M. Martineau, D. Fisher, D. J. Twitchen, and J. M. Baker, Phys. Rev. B **79** (2009).

[21] J. Harrison, M. J. Sellars, and N. B. Manson, Diam. Relat. Mater. **15**, 586 (2006).

[22] N. B. Manson, J. P. Harrison, and M. J. Sellars, Phys. Rev. B **74**, 104303 (2006).

[23] N. B. Manson and R. L. McMurtrie, J. Lumin. **127**, 98 (2007).

[24] U. F. S. D'Haenens-Johansson, A. M. Edmonds, M. E. Newton, J. P. Goss, P. Briddon, J. M. Baker, P. M. Martineau, R. U. A. Khan, D. J. Twitchen, and S. D. Williams, Phys. Rev. B **82**, 155205 (2010).